Exploration of Acoustic Metasurfaces

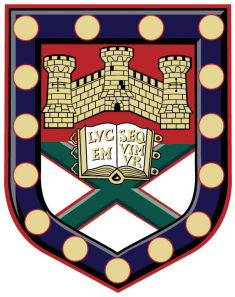

Joseph Graham Beadle

Department of Physics

University of Exeter

A thesis submitted for the degree of

Doctor of Philosophy in Physics

October 2019

Declaration

Submitted by Joseph Graham Beadle to the University of Exeter as a thesis for the degree of Doctor of Philosophy in Physics in October 2019.

This thesis is available for Library use on the understanding that it is copyright material and that no quotation from the thesis may be published without proper acknowledgement.

I certify that all material in this thesis which is not my own work has been identified and that any material that has previously been submitted and approved for the award of a degree by this or any other University has been acknowledged.

I acknowledge financial support from the Engineering and Physical Sciences Research Council (EPSRC) of the United Kingdom, via the EPSRC Centre for Doctoral Training in Metamaterials (Grant No. EP/L015331/1) and QinetiQ.

Joseph Graham Beadle

October 2019

For Mam, Dad, Kara and Shanade. Thank you all for always being there.

Acknowledgements

I would first of all like to thank my supervisors Prof. J. Roy Sambles and Prof. Alastair Hibbins. Without their support and encouragement throughout my PhD, I doubt that I would have been able to complete it. I had so many opportunities that I would never have thought possible when I started my undergrad. They all came from an undergraduate masters project supervised by Roy and Al. During this time, they both saw how much I thrive doing experimental physics, and how much I enjoy to be in the lab. There have been times where I have felt utterly defeated. Both have always helped me during these times, which is something which I will treasure from my PhD experience. Through their feedback, I have become more confident in my ability as an academic researcher. The lessons I have learned through them will stay with me for the rest of my life. Thank you both for everything and believing in me, it is appreciated. I would also like to give a special thanks to Dr. Ben Hodder for the many enjoyable industry meetings which we've had over the years.

Now I would like to mention a few people who have been with me throughout the journey. I could not have asked for two better people to have spent my PhD journey with than Josh Hamilton and Miguel Camacho. Josh, thank you for making this journey such a joyful experience and full of laughs. Miguel, thank you for being such a good friend and such an inspirational physicist. It really has been such a joy over the years to see you come out of your shell and turn into the quick-witted Manuel Sanchez we know today. Charlie-Ray Mann, you have always been the one person who believed and told me not to put myself down, thank you for having confidence

in me as a researcher. During my time as a PhD student, I have not met anyone nicer than Sam Shelley. Sam has often gone out of his way to help, and I cannot thank him enough - but always remember to blame the altitude!

The Electromagnetic and Acoustics group at Exeter has had so many researchers who have helped me throughout the way. I would like to thank Mr Happy himself, Ian Hopper. Thank you for always helping me and asking those oh-so-wonderful questions in the group meetings which have helped me grow as a researcher. Gareth Ward, the self-proclaimed 'King of acoustics' was always willing to spend time to help me understand concepts which I was struggling with. Rhiannon Mitchell and Nina Meinzer, thank you both for being so welcoming at the beginning of my PhD and helping me be more thick-skinned to harsh criticism. Tim Starkey, I truly have appreciated all the help and support which you have given me. Tom Graham, thank you for always willing to have a laugh and helping me with the underwater setup. There are numerous PhD students I would like to thank, but to keep this an acceptable length, I will mention a few. Thank you to Julia and David for keeping the office entertaining. Thank you to the acoustics group students – David, Emily, Ben and Beth for keeping me on my toes during group meetings. I would like to thank Beth Staples in particular, thank you for being there for me during the last few months of my PhD, meeting you for coffee and talking helped me so much.

I would like to thank the rest of the CDT students. While there are far too many to mention by name, you all have made this experience so enjoyable, particularly Joe Morgan, Craig Tollerton, Natalie Whitehead, and Angus Laurenson. A huge thank you m go must to Anja and Deb. Without both of you, the CDT would not have been the same. Anja, thank you for being much more than the program manager, you really care about the wellbeing of each student, and it is really appreciated. I would like to thank the guys down in the workshop, having dealt with my requests over the years. Of all the people I consider friends there are three who need a special

mention, the first being Katherine Hughes. Katherine, you have been my best friend since we met at high school, although we have lived so far apart for all these years our friendship has never changed. The few times a year I get to see you, it is like no time has passed at all. You are always there if I need support, and I cannot thank you enough. I cannot wait to be your bridesmaids at your wedding next year! The second being Olya Kadeshnikova. I was so lucky to have lived with you in student accommodation during our first year at university. You are the only person I have ever met that has the exact same sense of humour as me. I cannot remember the number of times you have made me laugh over these years, which is something that I cannot thank you enough for. Even though we do not speak as often as I would like, you are always there for me and for that I am forever grateful. The last being the wonderful Claire Brimilcombe. From the day we met that fateful day when we met, we instantly clicked. Since that day 6 years ago you quickly became one of my closest friends and someone that I am able share everything with. I feel like I can say anything around you and makes jokes and you will not judge me. Thank you for being such the beautiful person you are and for always being there for me.

I would like to thank the person who put up with me for three and a half years. Thank you so much Narciso, for supporting me throughout my PhD. I will always cherish the years that we had together.

My family have been my biggest support throughout my PhD. Thank you, Mam and Dad, for always being there for me, for accepting me no matter what. I could not ask for better parents than both of you. Ever since I was in school, you both have supported everything that I wanted to do, you have more confidence in my abilities than I do. I love you both so much, and I am so proud to have both of you as parents. Thank you for everything. Kara and Shanade, I really could not have asked for better sisters. Even as we grow older, I feel as close to you as I ever have. You both have grown into such beautiful people, and the love and care which you

have given me have helped me in ways you will never know. I love all you with all my heart, and I am thankful every day that we are a family.

Jason, although we met not so long ago, the love which you have given me since that day has been the most fantastic experience. I never thought it was possible to feel so loved or to love another person the way I do until I met you. I cannot thank you enough for all the support you have given me, you have seen me at my lowest, and you have elevated me to my best. Thank you for everything.

Abstract

The exploration of acoustic metasurfaces presented in this Thesis involves the characterisation and verification through finite element method (FEM) modelling and experimentation of a range of different acoustic metasurfaces. In airborne acoustics, the patterning of sub-wavelength structures on acoustically-rigid material provides the boundary condition that enables acoustic surface waves to exist. These surface waves exist purely in the fluid layer above the rigid material and propagate parallel to the surface, and are evanescent perpendicular to the surface.

The first study explores the radiative and bound acoustic modes supported by a rigid grating formed of three same-depth, narrow grooves per unit cell. One of the grooves is twice the width of the other two, forming a 'compound' grating. The structure supports so-called 'phase' resonances where the phase difference of the pressure field between the grooves on resonance varies by multiples of π. The dispersion of these modes has been measured experimentally by monitoring the specularly reflected signal as a function of the angle of incidence. In addition, by near-field excitation, the dispersion of the non-radiative surface modes has been characterised. The results are compared with the predictions of a finite element method model.

The acoustic surface waves supported by hard surfaces patterned with repeat-period, meandering grooves are next explored. The single, continuous groove forms a glide-symmetric surface, inhibiting the formation of a bandgap at the first Brillouin-zone boundary. Consequently, the acoustic surface waves exhibit an almost constant,

sub-speed-of-sound, group velocity over a broad frequency band. The dispersion of these surface waves has been experimentally measured by a near-field scanning technique and compared to finite element modelling. In addition the influence of covering the straight sections of the channels has been explored. Covering the channel reduces the coupling strength to free radiation which has been shown to significantly alter the standing wave condition at the first Brillouin zone for small channel depths. For such structures, the standing wave condition now comes from an open-ended cavity resonance.

In the final results chapter, underwater acrylic plates are investigated. Due to the change in the fluid, the solid may no longer be regarded as being acoustically-rigid, and acoustic energy propagates into the solid. Because of this, even on a flat surface, surface acoustic waves, Scholte waves are found at the interface of the solid and fluid. Here in particular, so-called soft solid (acrylic) plates are investigated where the shear velocity of the solid is less than the speed of sound in the fluid. The effect of adding structure to thin acrylic plates has been thoroughly explored through FEM modelling. By adding periodic grooves to the plate, unusual dispersion characteristics have been shown. The hybridisation of the modified Scholte-like modes with the cantilever resonances of the solid pillars has been described. The effect of varying grating parameters on the band diagram has been explored, showing that the dispersion of the modes is highly dependent on the structure. Experimental verification was performed on a simple grating (one groove per period) showing good agreement with the FEM model.

Table of contents

List of figures

Chapter 1

Introduction

1.1 Historical Background

Wave propagation in periodic structures has been the topic of studies in many areas of physics. Perhaps one of the most important pieces of literature on periodic systems is '*Wave Propagation in Periodic Structures*' by L. Brillouin.[1] In this work, Brillouin described the mathematics of wave propagation for a variety of physical systems, from solid state physics to the propagation along electric lines. Brillouin described the propagation of waves in periodic structures using the Floquet theorem[2] for 1D, 2D and 3D periodic structures. The concept of the Brillouin zones was introduced that describes the periodicity in momentum space due to the periodic lattice in real space. This work forms a fundamental basis for all related work on periodic systems.

The study of periodic structures in acoustics is analogous to quantum mechanical band theory of solids, where a periodic arrangement of atoms interacts with electronic waves creating a band structure, for acoustics these waves are phonons. From this, the acoustic equivalent of phononic crystals was proposed by Sigalas & Economou in 1993[4]. In this paper, the band structure is investigated for both acoustic and elastic waves. The structure explored comprised 2D arrays of infinite cylinders embedded

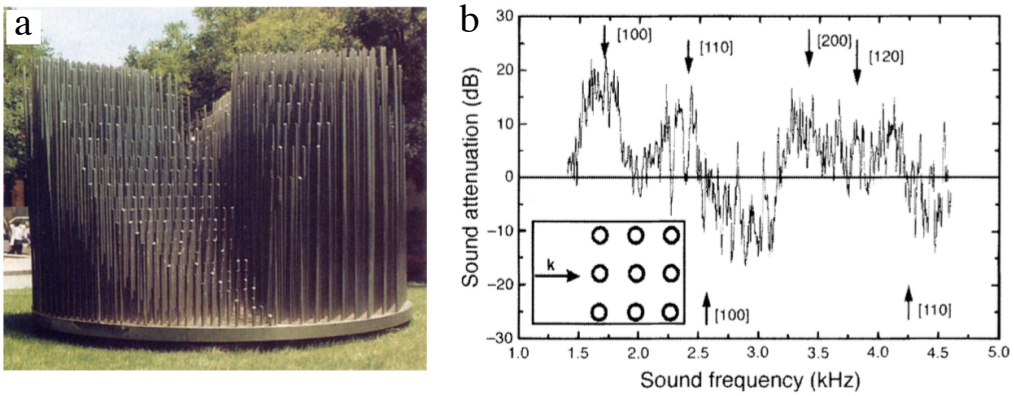

Fig. 1.1 a) Órgano by Eusebio Sempere the sculpture used in the investigation. b) Sound attenuation as a function of frequency, the inset shows the incident wavevector. The labelled arrows show the expected sound attenuation maximum for a given crystal plane. Image taken from Martínez-Sala *et al.*[3]

in a host material, in both rectangular and hexagonal arrangements. Experimental confirmation of the band gaps predicted was by Martínez-Sala *et al.*, where the sound attenuation of acoustic waves propagating through a sculpture consisting of a sub-wavelength array of metallic cylinders was explored.[3] The sculpture and results are presented in Figure 1.1(a-b). Here, the results for an incident wavevector in the [100] direction are presented. The peak at 1670 Hz is attributed to Bragg reflection from the regular lattice and the formation of the first bandgap. Numerous other works have also investigated sound attenuation by sub-wavelength periodic structures.[5–8]. There have been many phenomena investigated using sub-wavelength periodic structures such as guiding of acoustics waves, where transmission through both linear and bent defects have been studied[9–13] as well as refractive acoustic devices, where the periodic structures are implemented to create lenses[14–16].

Sub-wavelength structured materials for controlling sound, acoustic metamaterials, have been the topic of an increasing number of investigations. In 2000 the first artificial acoustic metamaterial was designed by Liu. *et al.*[17] This metamaterial consisted of rubber-coated lead spheres arranged in a simple cubic structure, presented in Figure 1.2(a). This system is analogous to a mass-spring system, the solid lead

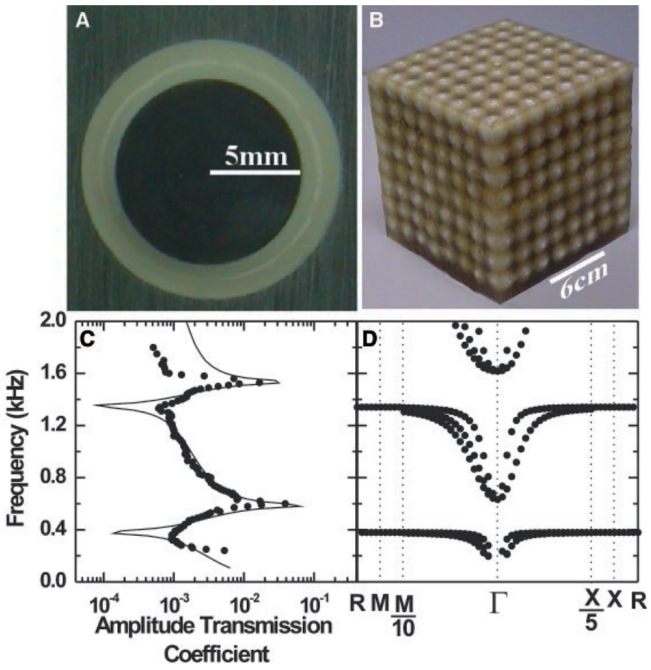

Fig. 1.2 a) Cross-section of the unit to form the metamaterial. A 5mm lead sphere coated by a 2.5 mm layer of silicone. b) A sonic crystal comprised of $8 \times 8 \times 8$ units. c) Calculated (solid line) and measured (circles) amplitude transmission coefficient along the [100] direction. d) The band structure for a simple cubic array of the coated spheres. [17]

sphere is the mass while the rubber acts as the spring. In this metamaterial, the locally resonant and sub-wavelength nature creates an unconventional band structure having flat dispersion curves presented in Figure 1.2(d) that form the lower boundaries of two band gaps. By investigating the frequency-dependent effective bulk modulus (K_{eff}), they found that at frequencies close to resonance, the effective modulus turned negative. One can see from the refractive index ($n^2 = \rho_{\text{eff}}/K_{\text{eff}}$, where ρ is the effective density) that when K_{eff} is negative, n becomes complex. The imaginary component of n means the wave decays exponentially as it enters the material and band gaps form.

Acoustic metamaterials may also take many other forms. One such form is a loaded waveguide, where a one-dimensional array of Helmholtz cavities are attached along the length of the waveguide, as illustrated in Figure 1.3(a). Fang *et al.*

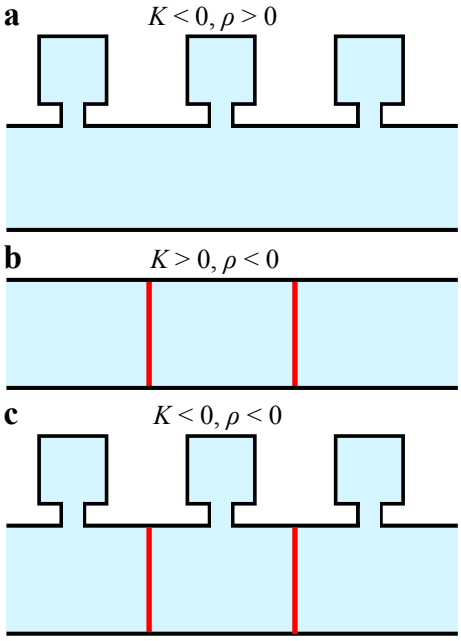

Fig. 1.3 a) Open and closed cavity resonators can be used to design a metamaterial with $K_{\text{eff}} < 0, \rho_{\text{eff}} > 0$. b) A membrane-type metamaterial displays $K_{\text{eff}} > 0, \rho_{\text{eff}} < 0$. c) By combining the previous two examples a double negative metamaterial where $K_{\text{eff}} < 0, \rho_{\text{eff}} < 0$ may be created. Here, the red lines represent the location the membranes.

explored the acoustic response of loaded waveguides in 2006.[18] They found that at the collective resonance frequency of the cavities, a low-frequency stopband occurred. The formation of this stopband was identified to coincide with when K_{eff} goes negative. The frequency at which the stopband exists may be altered by changing the size of the cavities attached. This allows for loaded waveguides to have a low resonant frequency, and to reflect sound until K_{eff} returns to be positive. Lee *et al.* investigated negative ρ_{eff} by designed a membrane-type metamaterial where membranes are placed in parallel in a tube structure, similar to Figure 1.3(b). They experimentally recorded negative ρ_{eff} by directly measuring the negative acceleration of the fluid.[19]. A system where K_{eff} and ρ_{eff} are both negative was explored by Lee *et al.* who expanded their previous work to realise double negativity,[20] using a similar structure as in the previous study; however, there are now small holes that act as cavities giving negative K_{eff} as presented in Figure 1.3(c).

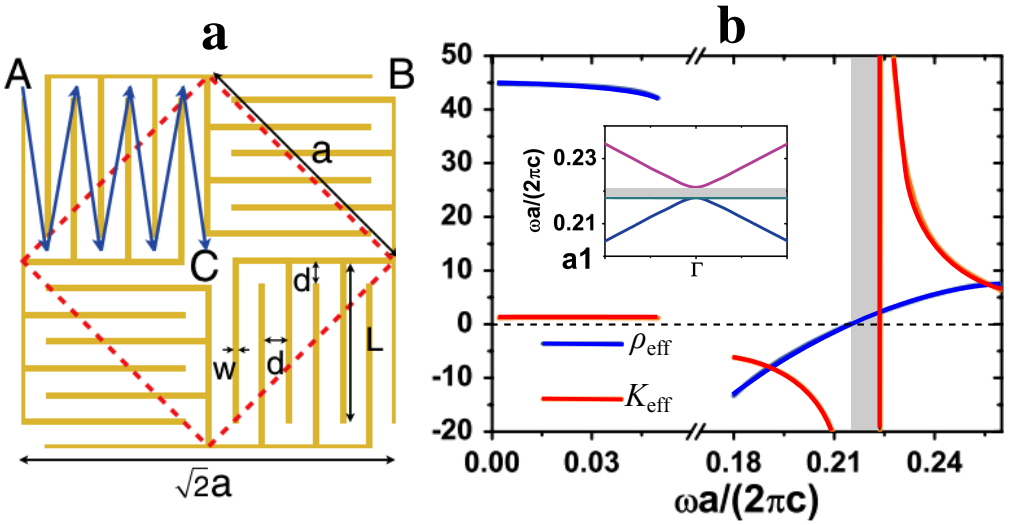

Fig. 1.4 a) Schematic of the structure used by Liang *et al.* The red-dashed line represents the border of the primitive unit cell. The blue arrows represent the propagation path of the sound. b) The effective parameters as a function of normalised frequency. The grey region represents a band gap in the band structure around the Γ point shown in the inset. Image taken and modified from [21]

The previously discussed single and double negative metamaterials have all used resonating elements that give rise to the negative behaviour. Liang *et al.* studied a metamaterial based on the coiling of space into labyrinthine structures presented in Figure 1.4(a).[21] By using space coiled elements in the effective medium regime (where the wavelength of excitation is much greater than the size of the structure, so the structure is non-resonant and behaves like a material), band folding occurs, and the material behaves double negative. Figure 1.4 shows the effective parameters as a function of normalised frequency. The grey region represents a band gap formed at the Γ point, for the frequency range of 0.18-0.218 both ρ_{eff} and K_{eff} are negative. Above the lower edge of the band gap ρ_{eff} turns positive, resulting in a complex n. The upper edge of the band gap is formed when K_{eff} turns positive; therefore, both parameters are positive and n is real allowing the propagation of sound. At specific frequencies the acoustic energy experiences a negative effective refractive index (n), allowing for negative refraction to occur. This was shown numerically.

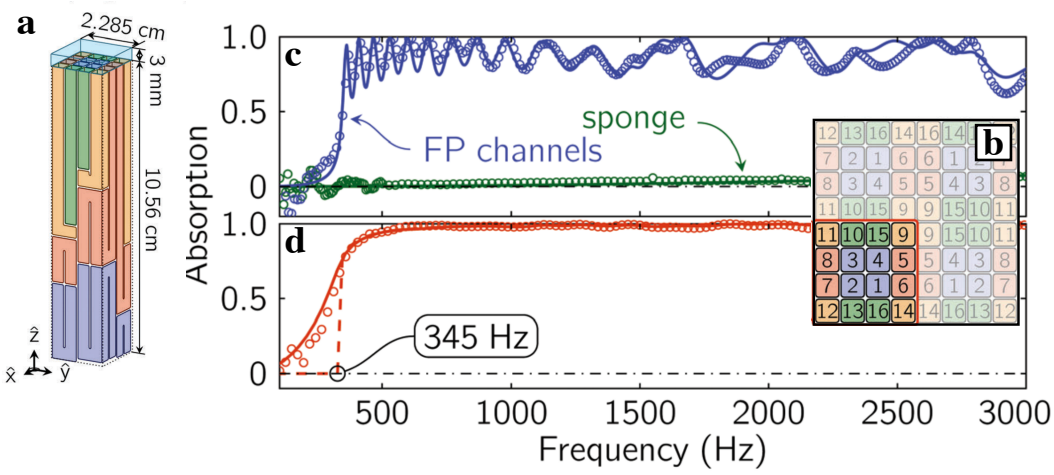

Fig. 1.5 a) Composite unit cell of 16 different length space-coiled resonators, with a layer of sponge on the surface. b) Layout of the channels of the experimental sample. c) The absorption spectrum of only the composite resonators (blue) and only the sponge layer (green). d) The absorption spectrum of the composite structure with the sponge layer placed above the resonators. The coloured solid lines represent theory, and the coloured circles represent experimental data. 345 Hz is the cutoff frequency of the metamaterial. Image from [22].

One substantial issue with creating resonant sub-wavelength metamaterials is the effect of thermoviscous losses in narrow channels.[23–25] These losses potentially can strongly attenuate sound waves as they propagate through the metamaterial preventing use in practice. However, for acoustic metamaterials designed for absorption, these losses are beneficial.

The effect of the thermoviscous losses on periodic structures has been extensively explored. C. Bradley described the propagation of linear, dissipative time-harmonic waves in periodic waveguides. It was shown that if the boundary conditions describe the dynamics of the thermoviscous effects, then a Floquet-like theorem can be applied, and the waves are described as Bloch waves. For a system consisting of a waveguide with rectangular branches, it was shown that the resulting block wave numbers have both a real and an imaginary component. The dispersion diagram of the structure is presented in Figure 1.6. The regions in which the wave number is real are known as pass bands, and the regions where the wavenumber is complex are known as stop

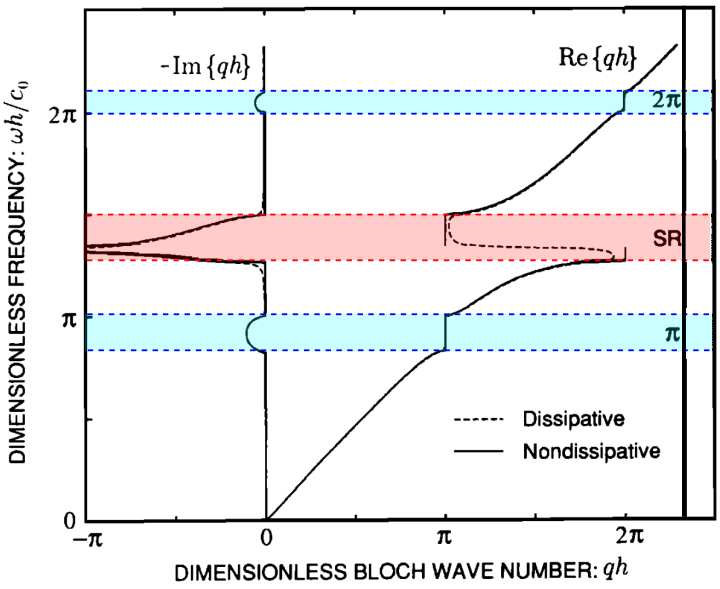

Fig. 1.6 The dispersion diagram of a waveguide with rectangular side branches investigated by Bradley, here both the real and imaginary components of the wavevector are presented. The blue shaded regions represent Bragg stop bands. The red shaded region represents a scatterer resonance stop band. Image taken and modified from [26].

bands, which are associated with exponentially attenuated Bloch waves. Bradley describes two conditions in which a stop band is likely to occur. The first is known as the Bragg stop band condition, $n\lambda_g = nk/2$, where λ_g is the period, and k is the wavevector in the direction of periodicity. The second referred to as scatterer resonance stop bands occur due to the resonance of the rectangular branches of the waveguide. In the dissipative system the previously sharp edges of the stop bands are smoothed out. [26] Furthering the study of thermoviscous effect in periodic structures, Sugimoto and Horioka described the dispersion characteristics of an array of Helmholtz resonators connected to a waveguide. The authors noted that the derived dispersion relation exhibits stop bands in the frequency domain; these stop bands inhibit the propagation of acoustics waves through the structures even in the lossless case. The stopbands are attributed to the resonance and Bragg reflection, which occurs due to the periodicity of the system. Outside of the stopbands, the acoustic

waves show dispersion.[27] More recently, Jiménez et al. designed subwavelength acoustic panels consisting of a structure similar to that presented by Sugimoto and Horioka. They showed that around the resonant frequency of the Helmholtz resonators, near-perfect absorption occurred.

Merely using an array of narrow open-ended resonators to attenuate can potentially result in two problems. Firstly, for low-frequency absorption, these structures become very thick due to a half-wavelength resonance condition, which is often undesirable as lightweight, thin absorbers have more application in cladding to create anechoic conditions. Secondly, due to the resonant nature, these are narrow band. Many investigations have focused on overcoming the narrow band nature of resonant structures. Wu *et al.* investigated profiled absorbers where there are multiple resonators per period of the same widths but different depths.[28–31] Wu *et al.* showed that by including a perforated plate within the profiled absorber broadened the resonances, resulting in a broadband absorber.[28] Romero-García *et al* proposed a different method to increase the bandwidth of resonant structures. by using the mechanism of sub-wavelength multi-resonant scattering. The structure investigated consisted of a viscoelastic porous plate placed in front of a rigid backing. In the regime where the incident wavelength is much larger than the distance between the perforated plate and rigid backing, perfect absorption occurs. Perfect absorption occurs in this system due to destructive interference between the direct reflection from the perforated plate and reflection from the rigid backing. Due to the wavelength being much larger than the phase difference between these two waves is negligible, however, due to waves incident on the porous plate exhibiting a π phase change, and those reflected from the rigid backing exhibiting no phase change, destructive interference occurs.[29] Another method one may implement to create a broadband response is by implementing rainbow trapping structures. Rainbow trapping structures consist of multiple resonators per period, which are graded in

depth. Due to the depths being graded, the resonances of the individual resonators overlap, which creates a broadband response. Jiménez *et al.* investigated the response of sub-wavelength panels composed of graded Helmholtz resonators. The authors showed numerically low-frequency broadband absorption and confirmed the results experimentally. [31]

A metamaterial designed to overcome both the narrow band and size problems was designed by Yang *et al.*[22]. The unit cell of the structure designed comprised of multiple different length space-coiled resonators, topped by a thin layer of sponge, Figure 1.5(a-b). They discovered near-perfect absorption for frequencies above the cutoff frequency in Figure 1.5(c), $f_c = c/d_{\text{min}}$ where d_{min} is the minimum cavity depth needed for the desired frequency range, and c is the speed of sound. Frequencies below the cutoff frequency are unable to propagate into the structure as the pressure-release boundary conditions are no longer satisfied, where the pressure, P, must equal zero.

Having briefly reviewed phononic metamaterials we now go on to look at the key area of this thesis: acoustic metasurfaces. In particular we explore interface modes. Surface acoustic waves (SAWs) exist at the interface between two different media. Rayleigh, Stoneley and Scholte waves exist at solid-vacuum, solid-solid, and solid-fluid interfaces respectively[32–34].

At the interface between a solid half-space and a vacuum half-space, non-dispersive interface waves, Rayleigh waves, exist. In an isotropic solid, for shallow depths the particle motion is elliptical and retrograde (clockwise motion)[32], at greater depths the particle motion becomes prograde (anticlockwise motion). The velocity of Rayleigh waves (c_{R}) has been the topic of many studies[37, 35, 38], P. Malischewsky provided a comparison of the different approximate solutions for the Rayleigh wave velocity[36], with the dependency on Poisson's ratio presented in Figure 1.7.

Stoneley waves may exist at the interface between two dissimilar isotropic solids when the two materials are perfectly bonded; these waves are non-dispersive[33].

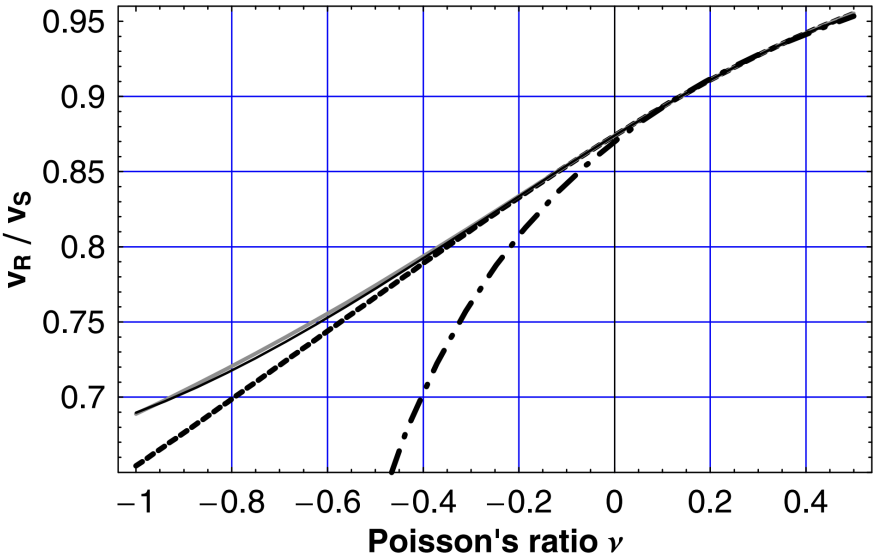

Fig. 1.7 Rayleigh wave velocity normalised to the transverse velocity of the solid. The solid, thick grey line is the exact solution. The dashed black line is the approximation from Scruby *et al.* [35]. The thin solid, black line is the approximation from Malischewsky[36]. The dashed-dotted, black line is the approximation from Bergmann[37]. Figure is taken from[36].

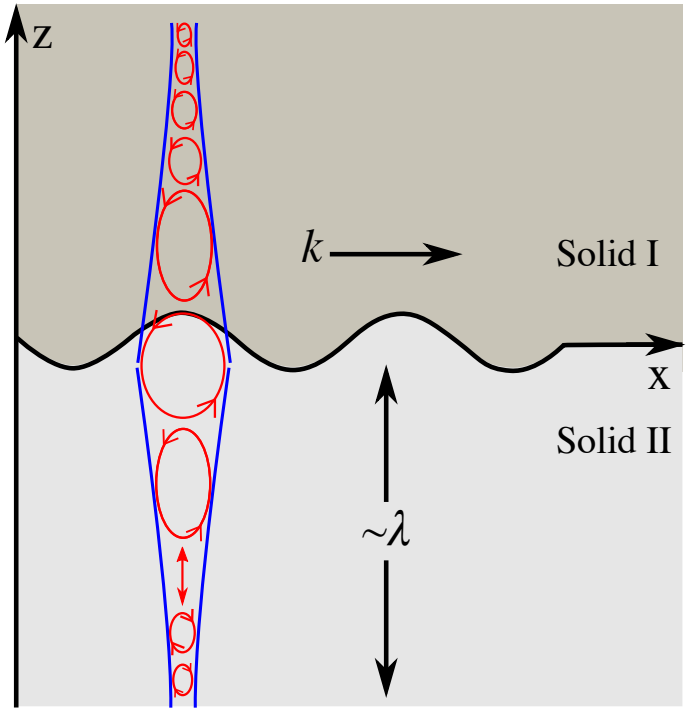

Fig. 1.8 Particle trajectory in both materials for a Stoneley wave. Figure based on [39]. The red lines show the particle displacement.

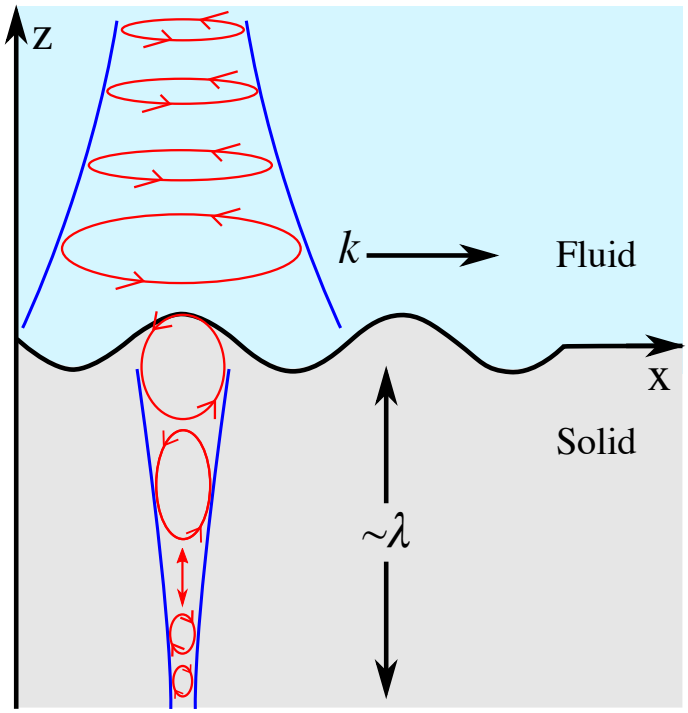

Fig. 1.9 Particle trajectory in both materials for a Scholte wave. Figure based on [39]. The red lines show the particle displacement.

Figure 1.8 shows the particle trajectory in the two elastic materials. In both media, the particle motion is elliptical. In the lower solid, there is a reversal in the direction of the particle motion just below the interface. In the upper solid, the reversal of particle motion does not happen. The characteristics of Stoneley waves, which depend on the stiffness and density of the two solids, has also been explored[34, 40]. The propagation of Stoneley waves at the interface between pre-stressed, incompressible, isotropic elastic materials has been investigated, showing that when a Stoneley wave exists, the velocity of the wave will be higher than that of the slowest Rayleigh wave speed of the solids[41–43]. For the case of loosely bonded elastic halfspaces, the formulas for the velocity of the Stoneley wave has been explored by Vihn *et al.* The formulas derived also show that if a Stoneley wave exists, it is unique[44]. Vihn further expanded this work for the case of bonded interfaces[45].

Introduction

At a solid-fluid interface, two interface waves can exist - leaky Rayleigh waves and Scholte waves. First, a hard solid-fluid interface is considered. A hard-solid−fluid interface is one where the transverse velocity of the solid is greater than the longitudinal velocity of the fluid ($c_{Fl} < c_{St} < c_{Sl}$, where the subscripts F and S represent fluid and solid respectively). For such a system so-called leaky Rayleigh waves[46] propagate with a velocity less than c_{St}, these waves attenuate as they propagate due to radiating into the fluid. Leaky Rayleigh waves have been used to characterise the physical properties of underwater solids [47, 48]. The Scholte wave velocity is less than c_{Fl}, and if the viscoelastic effects are neglected in both the fluid and the solid, the Scholte wave will propagate unattenuated. More Scholte wave energy for a hard solid-fluid system is localised within the fluid than the solid. Scholte waves are a linear combination of longitudinal and vertical shear waves in the solid, and they are evanescent in both directions orthogonal to the interface. The magnitude of the difference between the particle x-displacements in the fluid and solid is proportional to $(1 - c_{sch}^2/c_{Fl}^2)^{-1}$, where c_{sch} is the Scholte wave velocity. It can be seen that this ratio becomes large as the Scholte wave velocity approaches that of the speed of sound in the fluid[39]. A soft-solid−fluid system is one where the transverse velocity of sound in the solid is less than the longitudinal velocity of the fluid ($c_{St} < c_{Fl} < c_{Sl}$). In such systems, there has been some discussion as to whether leaky Rayleigh waves exist[49–51]. Glorieux *et al.* experimentally confirmed the theoretical prediction that the leaky Rayleigh root of the characteristic determinant becomes forbidden for a soft solid-fluid system.[51]. For a soft solid-fluid system, the Scholte wave energy is more localised within the solid, which is in contrast to the hard solid-fluid case. The penetration depth of the wave is deeper for the soft solid-fluid system[52]. Scholte waves are used to characterise soft marine sediments [53–56] and also for non-destructive defect testing[53, 57].

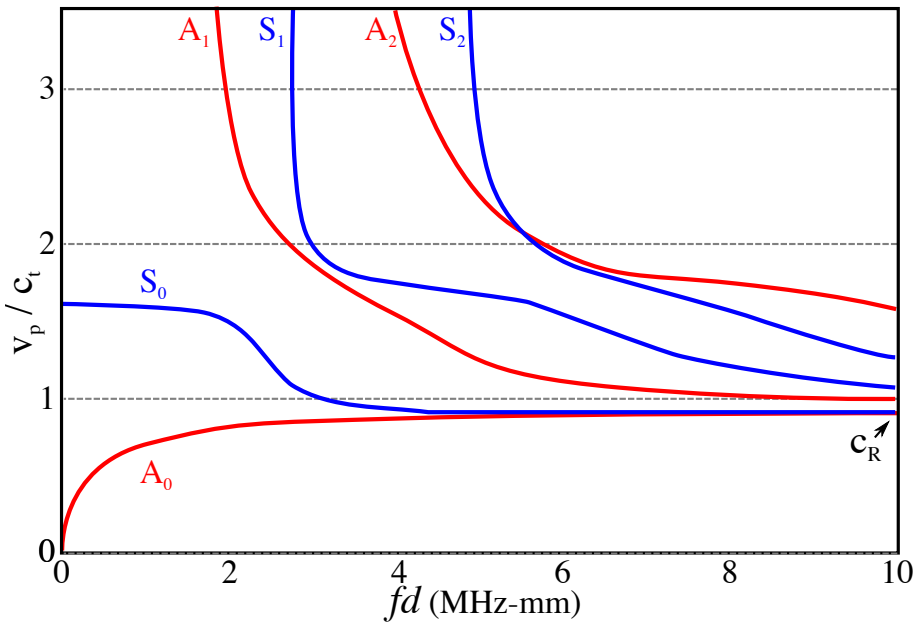

Fig. 1.10 Lamb wave dispersion curve for the three first modes of a finite steel plate. The y-axis has been normalised to the transverse velocity of steel (c_t). Here, d is the thickness of the plate.

Now, moving on to plates rather than semi-infinite substrates Lord Rayleigh first discussed the topic of acoustic waves propagating in elastic plates and this was later expanded by H. Lamb[32, 58]. For a free, infinite plate, there exist two modes which are supported: a longitudinal symmetric mode (S) and a flexural anti-symmetric mode (A). However, when a finite-sized plate is considered, there exists an infinite number of modes. In Figure 1.10, the dispersion curves for the three lowest order modes of a steel plate are shown. For the lowest order modes labelled S_0 and A_0, as the frequency increases they tend to the Rayleigh wave speed (c_R), while the higher-order modes tend to the transverse velocity (c_t) as the frequency is increased. Lamb waves have often been used for the inspection of plates and non-destructive defect testing, due to the property that they can propagate over long distances[59–61]. Lamb waves have also been used to determine the elastic properties of plates[62–65].

In electromagnetism the similar problem of propagation above a plane surface was first explored by Sommerfeld in 1909[66]. This was expanded by Slater[67] who

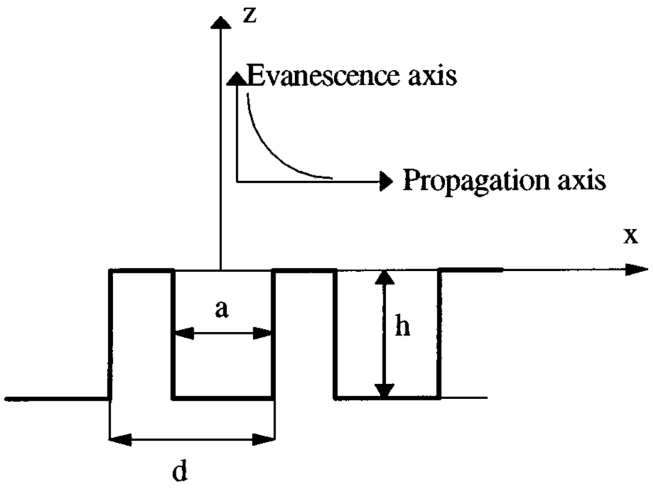

Fig. 1.11 The periodic rectangular groove grating modelled by Kelders *et al.*, evanescent ultrasound surfaces waves propagate above the surface of the solid.

developed an approximate theory of the propagation of waves between two parallel plates, one of which was structured. The surface waves existing at an interface between two media of different impedances was explored by Barlow at Cullen.[68] It is know that the surface impedance contains a resistive and reactive term and is written of the form $Z = R_s + iX_s$. The quantity X_s arises from the skin depth. For a good conductor R_s is slightly larger than X_s. The addition of corrugations on the surface increases the reactance and therefore creates an artificial skin depth which allows surface waves to bind and propagate along the surface.

More recently there has been a wide variety of investigations on periodic electromagnetic structures. Pendry *et al.*[69] developed a theory for structured metal surfaces relating to surface plasmons: collective excitations of the electrons localised to the surface of a metal. So-called designer surface plasmons, exhibit a similar response to optical surface plasmons but at microwave frequencies. The dispersion of these designer surface plasmons can be readily controlled by the parameters of the periodic structure designed. The acoustic equivalent of Sommerfeld's problem was fully realised by Wenzel in 1974.[70] Wenzel found that a surface wave term

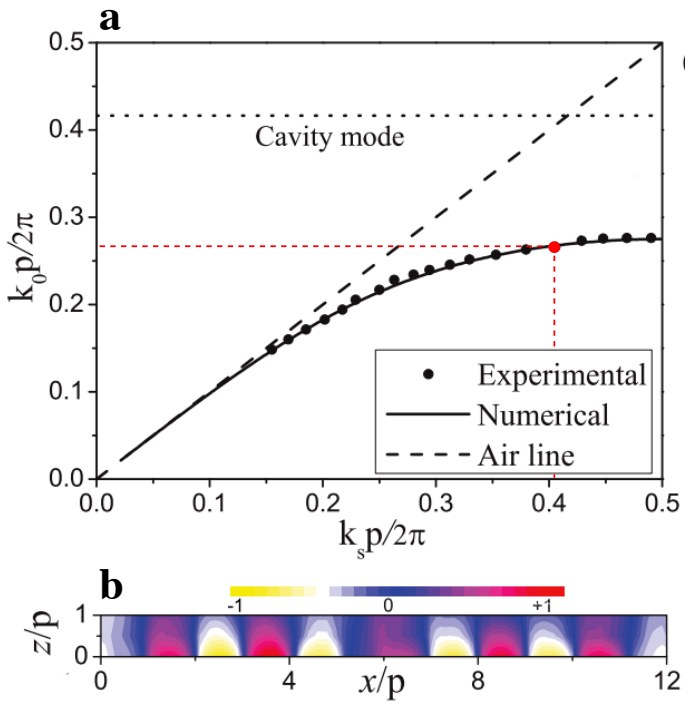

Fig. 1.12 a) Dispersion of an acoustic surface wave above a coarse corrugated rigid surface. b) The pressure fields in the x-z plane where the surface is along z=0. Here, k_0 is the incident wavevector, and p is the size of the unit cell.

existed for the acoustic problem which had previously been omitted by Ingard.[71] Thomasson showed for a surface where the imaginary part of the surface impedance is much greater than the real part surface waves can be excited by near grazing incidence radiation.[72] Raspet and Baird later showed that the surface wave is a true independently propagating wave.[73]

In a system where the solid is acoustically-rigid (no propagation of acoustic energy into the solid), acoustic surface waves arise from diffractive coupling from sub-wavelength periodic structuring resonators into the solid (note that Scholte waves do not exist on the surface due to the solid being acoustically-rigid). These were first described for ultrasonic surface waves by Kelders *et al.* using a modal model and experiment.[74] Figure 1.11 shows the periodic rectangular-groove grating modelled. Here, the surface waves propagate along the surface in the x direction. Kelders then went on to confirm the existence of these surface waves experimentally

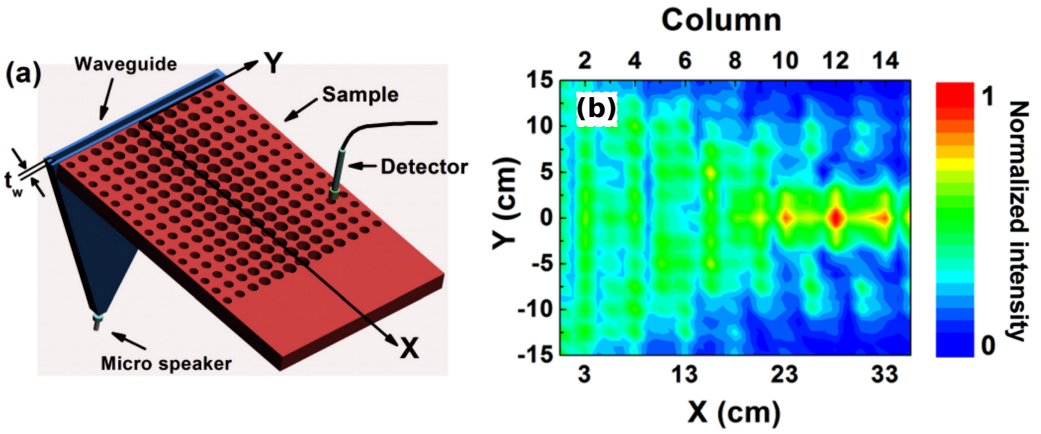

Fig. 1.13 a) The structure investigated by Ye *et al.* Acoustic surface waves propagate along the x direction and due to the grading of the radius of the cylinders in the y direction, the acoustic surface wave is focused. b) Intensity field plot of the focused acoustic surface wave. Image taken and modified from [78].

on the surface of a porous surface.[75] However, the first experimental evidence of acoustic surface waves on periodically structured surfaces was demonstrated much earlier by Ivanov-Shits *et al.* using thin aluminium strips over plywood.[76]. The dispersion above a rectangular grating similar to that described by Kelders *et al.* was experimentally measured by He *et al.*[77], presented in Figure 1.12(a). They showed that by corrugating a rigid surface, highly confined acoustic surface waves are supported over a broad frequency range. Figure 1.12(b) shows the pressure fields at the red point in the dispersion diagram. The evanescent fields were shown to be confined within one period of the surface in the z direction. The dispersion of surface waves are highly dependant on the structure. Christensen *et al.* showed that enhanced transmission could be obtained through a sub-wavelength hole on resonance when the surface has been structured with a periodic groove array. They also showed the transmission collimation of sound.[79]

Schwan *et al.* investigated the complex dispersion of acoustics surface waves of a lossy metamaterial. The complex dispersion is difficult to obtain experimentally; one must separate the attenuation caused by losses from the attenuation from

the geometrical spreading of the source. The complex dispersion can be done by implementing a spatial Laplace transform for complex wavenumbers (SLaTCoW) on the experimental data. The authors theoretically derived a complex dispersion relation that was used to validated the complex experimental dispersion obtained. The metamaterial investigated was a square array of finite depth holes in a wooden plate. It was shown that even with weakly damped resonators around the resonance, the propagation of the surface acoustic waves becomes so highly attenuated that no propagation occurs.[80]

A study by Ye *et al.* showed that acoustic surface waves can be focused by grading the structure on the surface.[78] Such a structure is presented in Figure 1.13(a), where the cylindrical holes are graded in the y-direction but periodic in x. Figure 1.13(b) shows the focusing effect in the direction that the acoustic surface wave propagates. This occurs due to the n being graded in the y-direction. Acoustic surface waves have also be used to exhibit rainbow trapping, where the structure is graded and different frequencies propagate different lengths along the surface.[81, 82]. Sub-wavelength imaging from acoustic surface waves has been reported on two-dimensional metamaterials. Jia *et al.* experimentally and numerically realised such imagining from a square array of holes in a rigid surface.[83] Utilising the broad flat equi-frequency contours of the surface waves supported on the surface, a sub-wavelength image with a full width half maximum of 0.014λ was obtained.

In an underwater environment, Li *et al.* demonstrated experimentally that underwater surface acoustic waves exist above an array of rigid cylinders. Figure 1.14 displays the dispersion diagrams for various r/a, where r is the radius of the cylinders and a is the pitch. For $r/a = 0.25$ and 0.35 only one surface mode can be seen; however, for larger r/a values a second mode can be seen. The mode represented by black dots is a dipolar resonance around the cylinders. The blue dots represent a

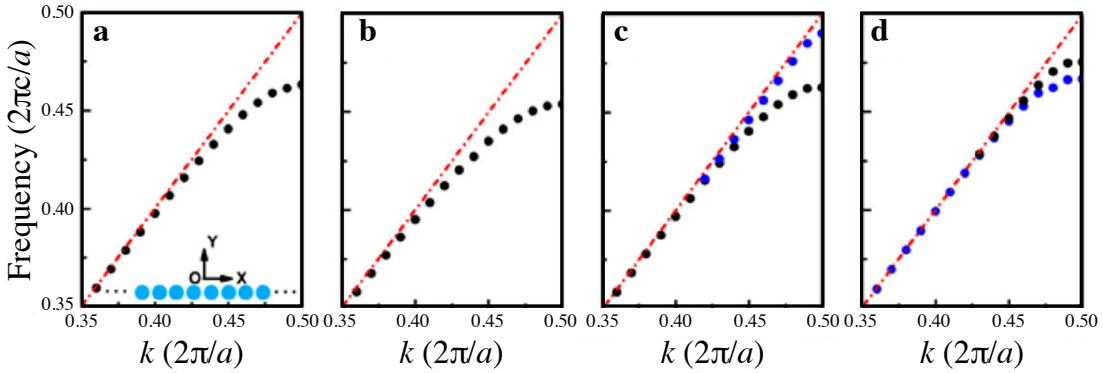

Fig. 1.14 Dispersion diagrams for one-dimension arrays of identical cylinders in the x direction. a) $r/a = 0.25$. b) $r/a = 0.35$. c) $r/a = 0.45$. d) $r/a = 0.49$. r is the radius of the cylinder and a is the pitch. The red dashes line represent the sound line of water. The inset of (a) illustrates the structure. Image from [84].

quadrupole mode around the cylinder where the coupling is stronger as the cylinders are placed closer together.

1.2 Introduction

This thesis will focus on the experimental measurement of acoustic surface waves for airborne acoustics and underwater acoustics. In the literature, while there have been many studies on acoustic metamaterials and metasurfaces, there appear to be very few that directly characterise the propagation of acoustic surface waves through experiments by measuring their dispersion. This is especially prevalent in the case of underwater acoustics, where the direct measurement of the pressure-field through surface scans of metasurfaces remains an unexplored area.

Chapter 2 will focus on essential background physics, which will be referred to throughout the thesis.

In Chapter 3, the experimental and numerical methods used throughout the thesis will be described. Radiative measurements are performed using a reflection experiment where the reflection as a function of angle of incidence can be obtained.

Such radiative measurements will be used in Chapter 4 to obtain the reflectivity spectrum of a phase resonance surface. Near-field surface scans of the pressure fields allow us to experimentally measure the dispersion of acoustic surface waves. The acoustic surface waves have been experimentally measured on a compound grating (Chapter 4), a glide-symmetric metasurface (Chapter 5), and an underwater simple grating (Chapter 6). Finite element method (FEM) models are used to validate the experimental data, and how the models are done will be described in this chapter. FEM models are used throughout the thesis.

Chapter 4, the first of three experimental chapters will explore the radiative and non-radiative modes supported by a compound grating, one with multiple grooves per unit cell. On such gratings, a phenomenon known as phase resonance exists. Phase resonances will be explored for periodic structures where there are more than one resonating element per period. The dispersion diagrams of simple gratings will be investigated through FEM modelling. Expanding on this, compound gratings will be explored. The effect of changing the parameters of the grooves on the phase resonances will be investigated for both two and three-grooves per unit cell. Finally, the experimental validation of both the radiative and non-radiative dispersion will be described using the methods presented in Chapter 3. Alongside the characterisation of acoustic surface waves, the beaming of acoustic energy on the surface will be explored experimentally.

So-called meander structures are the topic of Chapter 5. As discussed previously, the use of space-coiled metamaterials can lead to interesting effects. However, the investigation of the propagation of acoustic surface waves on such a surface had not been undertaken. In this chapter, glide-symmetric meander channels are characterised in full through FEM models and then experimentally validated. These meander channels support slow acoustic surface waves which are broad band due to their near-linear dispersion. The broad band feature is a direct consequence of the surface

possessing glide symmetry which creates a zero band gap at the first Brillouin zone. The decay in intensity of the surface waves will be experimentally measured. Finally, through FEM modelling the dispersion of acoustic surface waves on partially covered meander channels will be explored, showing that there is a change in the resonance condition for shallow grooves compared to the uncovered systems.

Moving from airborne to underwater acoustics, Chapter 6 is a study of the effect of introducing periodic structure to soft-solid plates. In an unstructured plate, two types of interface modes exist within the non-radiative dispersion: symmetric and anti-symmetric Scholte modes. In this chapter simple gratings (one groove per period) are introduces into acrylic plates. The interaction between the Scholte modes and the structural modes now excitable due to the grating is explored extensively through FEM modelling. The dependence on the dispersion curves on the structure is described. Experimental validation using near-field surface scans of an underwater grating is presented.

Finally, possible extensions for this work will be described in Chapter 8. The band structures for underwater soft-solid plates will be explored. Now structure is added to both interfaces. Secondly, the band structure of adding a two-dimensional periodic structure to one of the interfaces will be explored. Thirdly, preliminary results for a method to obtain the radiative dispersion from a surface scan will be presented and described.

Chapter 2

Background Theory

2.1 Introduction

In this chapter, the underlying theory relevant to this thesis will be discussed. Firstly the reflection and transmission through a surface will be described and later for an active surface, one with a frequency dependence reflectivity. Following this, the resonant conditions for acoustic resonators used within this thesis will be defined. The thermal and viscous losses play an essential role in the attenuation of both reflected radiation and of propagating acoustic surfaces modes, these loss mechanisms will be described. In order to characterise the metasurfaces, the band structure will be characterised. In this chapter, the necessary background for these diagrams will be described. Finally, the surface acoustics modes supported on an underwater soft-solid plate will be defined.

2.2 Acoustic Reflection and Transmission

Within this section, an acoustic plane wave incident upon an interface between two different semi-infinite fluids is considered. Here, the angle of incidence is θ_{i}. Such

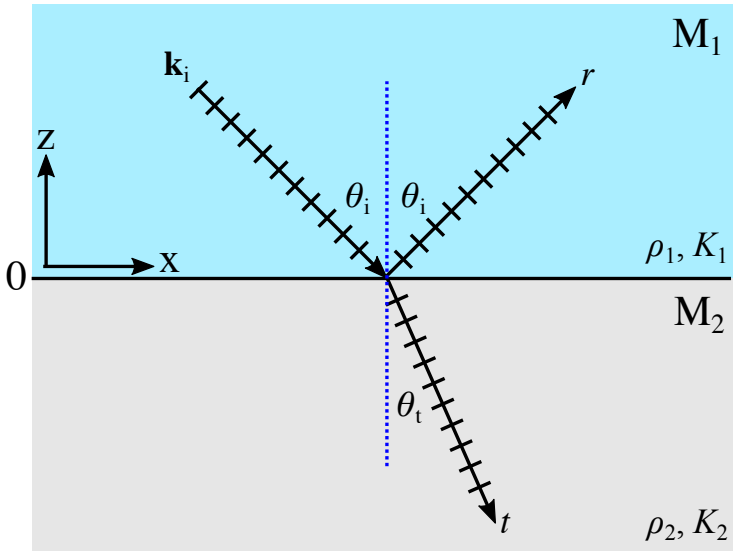

Fig. 2.1 Schematic of the transmission and reflection of a plane wave incident on the interface between two different materials. The interface is located at z = 0.

an interface is shown in Figure 2.1, between two materials, denoted M_1 and M_2, with their respective densities, ρ, and bulk modulus, K. The speed of sound in each material is $c_M = \sqrt{K_M/\rho_M}$. Using this information, one may define the coefficient of reflection amplitude as

$$R = \frac{\rho_2 c_2 \cos(\theta_i) - \rho_1 c_1 \cos(\theta_t)}{\rho_2 c_2 \cos(\theta_i) + \rho_1 c_1 \cos(\theta_t)} \tag{2.1}$$

and the coefficient of transmission amplitude as,

$$T = \frac{2\rho_2 c_2 \cos(\theta_i)}{\rho_1 c_1 \cos(\theta_t) + \rho_2 c_2 \cos(\theta_i)}. \tag{2.2}$$

These can be written in terms of the specific acoustic impedance $z = \sqrt{K_M \rho_M}$, for each material

$$R = \frac{z_2 \cos(\theta_i) - z_1 \cos(\theta_t)}{z_2 \cos(\theta_i) + z_1 \cos(\theta_t)} \tag{2.3}$$

$$T = \frac{2z_2\cos(\theta_\mathrm{i})}{z_1\cos(\theta_\mathrm{t}) + z_2\cos(\theta_\mathrm{i})}. \tag{2.4}$$

If one now considers a surface which has a frequency-dependent characteristic impedance $Z(\omega)$, equation 2.3 may now take the usual form for a locally reactive surface

$$R(\omega) = \frac{Z(\omega)\cos\theta - \rho c}{Z(\omega)\cos\theta + \rho c}. \tag{2.5}$$

Considering a surface where each point acts as a simple harmonic oscillator $Z(\omega)$, for example a simple groove array metasurface, a simple model of the system can be found by equation 2.5 taking on a quadratic form and equation 2.3 can be written as

$$R(\omega) = \frac{\omega_0^2 - \omega^2 - i\omega(\zeta_0 - \eta_0/\cos\theta)}{\omega_0^2 - \omega^2 - i\omega(\zeta_0 + \eta_0/\cos\theta)}, \tag{2.6}$$

where ω_0 is the resonant frequency, ζ_0 is the dissipation and η_0 is the admittance of the surface[80].

The acoustic reflection and transmission has been the topic of many investigations. Such studies explore the control of sound with acoustic metamaterials and surfaces, whereby using such structure the reflected/transmitted waves can be manipulated to achieve acoustic beam steering[85–89] and sound absorption[90–93].

This plane wave analysis of surfaces will be used through finite element method modelling (FEM) to obtain the reflectivity spectrum of a simple grating in Chapter 4. However, once non-radiative modes are considered, Bloch waves must be included, which will be discussed later in the chapter.

2.3 Acoustic Resonators

When sound is incident upon a structured surface, resonances will occur. Simple structures which support acoustic resonances are open and closed air-filled cavities, shown in Figure 2.2(a,d). First consider an open-ended cavity of length L and width w. For these standard 'organ pipe' resonances to be supported, the amplitude of the sound wave pressure field is close to zero at the open ends, where zero here is the deviation from background atmospheric pressure. In contrast to the pressure, the particle displacement is a maximum at an opening. In a physical system, the node in pressure occurs a little distance out of the cavity, increasing the apparent length of the cavity. This additional length leads to an end correction. Now the resonance frequency, f_r, can be defined as

$$f_\mathrm{r} = \frac{nc}{2(L + \Delta L)} \tag{2.7}$$

where n is a positive integer and represents the harmonic, c is the adiabatic speed of sound in air, L is the cavity length and ΔL is the end correction, which to first-order is $\Delta L = 8w/3\pi$ [94].

The first two harmonics of an open-ended cavity are illustrated in Figure 2.2(b-c). For $n = 1$ the pressure field shown as the red line has two nodes just beyond the openings and an antinode at the centre of the cavity. For $n = 2$, there now exists an additional node in the pressure in the centre of the cavity. If a cavity with one end closed is considered, this $n = 2$ mode is not supported, due to the boundary condition of a pressure maximum existing at the closed end. Therefore, only odd harmonics are supported, and the resonance frequency takes the form

$$f_\mathrm{r} = \frac{mc}{4(d + \Delta L/2)}, \tag{2.8}$$

where m is any odd-numbered positive integer, d is the depth of the cavity.

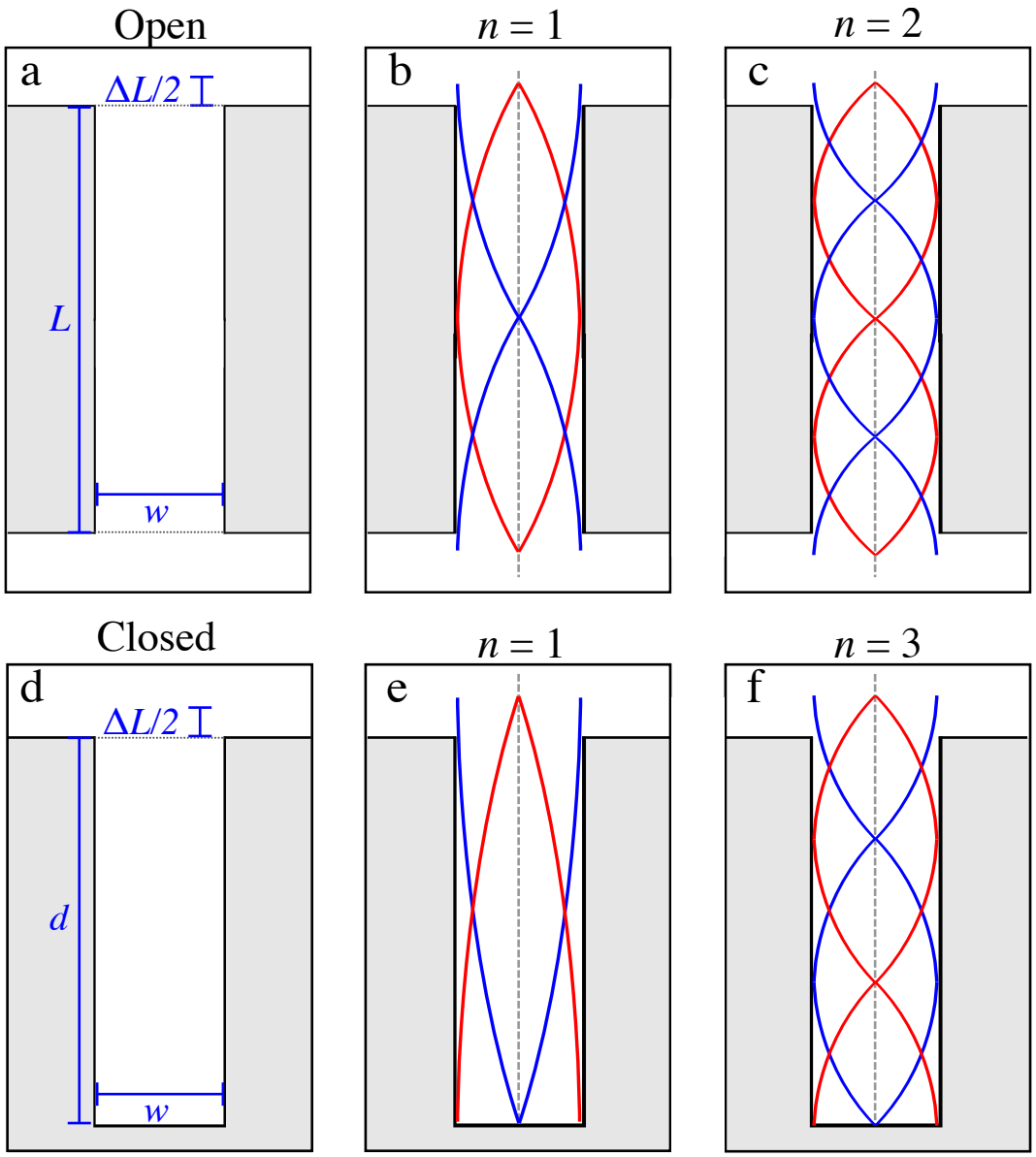

Fig. 2.2 a) An open cavity in an acoustically rigid material (grey) of length L and width w. b) Fundamental harmonic of the cavity. c) The second harmonic of the cavity. d) A closed at one end cavity in an acoustically rigid material (grey) of depth d and width w. e) Fundamental harmonic of the cavity. f) The second mode of the cavity. The red line and blue lines represent the pressure and particle displacement, and their amplitude is respective of the distance from the grey-dashed line, which equals zero amplitude.

2.4 Thermal and Viscous losses

The thermoviscous effects of a propagating acoustic wave can be obtained from the governing equation for acoustic wave propagation – the Helmholtz equation. For some acoustic problems, the equation may be simplified by assuming that the wave propagation is lossless and isentropic. To account for the thermoviscous effects one must consider the effects of viscosity and heat conduction. These are considered by assuming a small harmonic oscillation to the background pressure (p), temperature (T), and velocity field ($\mathbf{u}$). Here the background pressure field and temperature are functions of space, and the velocity field is assumed to be steady (u = 0). By inserting these into the governing equations, one obtained the equation for a propagating acoustic wave, including the thermoviscous losses. Now we will consider the thermoviscous effects near an interface.

At the interface between a fluid and an acoustically-rigid solid, there exist two boundary layers in the fluid which are dependent on the properties of the fluid, the thermal and viscous boundary layers. The study of these two layers was explored by Kirchoff[95] and expanded by Rayleigh[96]. The viscous boundary layer arises from a no-slip boundary condition at the interface; this no-slip condition states that the component of the velocity parallel to the boundary must equal zero at the boundary. A velocity profile now exists at the interface, as at z = 0, $u = 0$, and u must equal that of freely propagating sound u_∞ as z $\rightarrow \infty$. This velocity profile is shown in Figure 2.3(a). If we assume that the particles are organised in layers in the z-direction, it can be seen that each layer has a different velocity to the neighbouring until it equals u_∞. This change in u between each layer leads to viscous effects. These viscous effects cause an irreversible transfer of momentum between the particles where energy is dissipated. The thickness of the boundary layer as a function of incident frequency is given by the following[97]

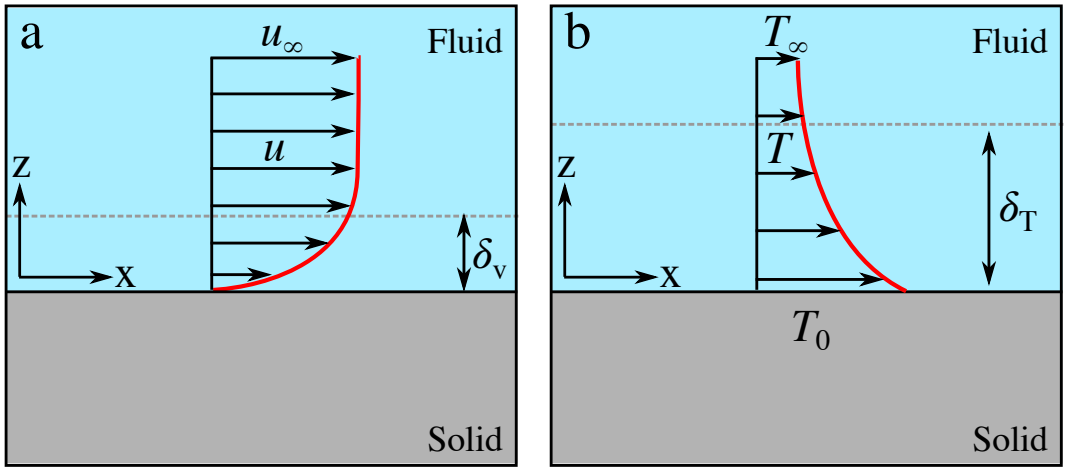

Fig. 2.3 a) Velocity profile (red line) of the component parallel (u) to the interface between a fluid and solid. The length of the arrows represents magnitude. u_∞ is the velocity component of freely propagating sound and δ_ν is the boundary layer thickness. b) Temperature profile (red line) of the temperature in a fluid at an interface of a solid. The length of the arrows represents magnitude. T_∞ is the temperature of the fluid. T_0 is the isothermal temperature of the solid.

$$\delta_v \approx \sqrt{\frac{\nu}{2\pi f}} \tag{2.9}$$

where ν is the kinematic viscosity.

The thermal boundary layer occurs due to an isothermal boundary condition. Here, the solid remains at a constant temperature, T_0, which is different from the temperature of the fluid, T_∞. This is shown in Figure 2.3(b). This change in the temperature between the two materials results in a temperature gradient. This gradient in temperature results in irreversible heat transfer to the solid. The thickness of the boundary layer as a function of incident frequency is given by the following[97]

$$\delta_t \approx \sqrt{\frac{\alpha}{2\pi f}} \tag{2.10}$$

with α being the thermal diffusivity. One can define a ratio between the two boundary layers, known as the Prandtl number

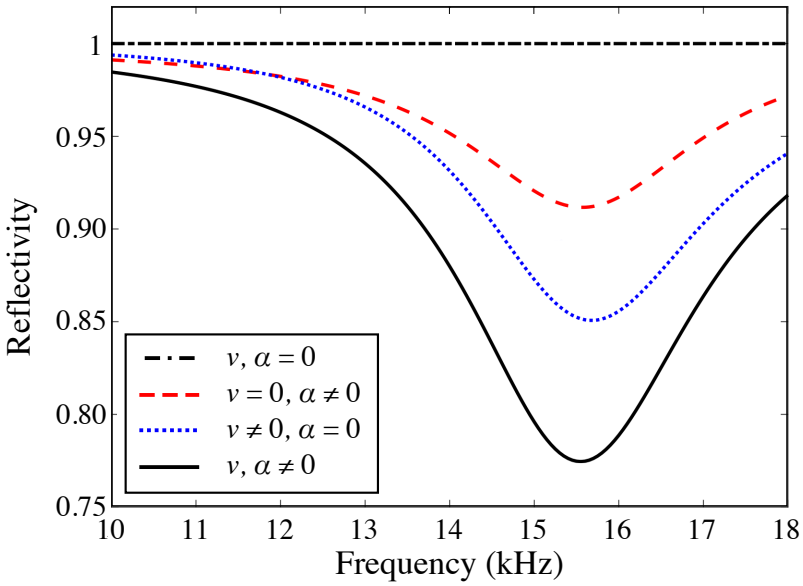

Fig. 2.4 FEM models for normal incidence of a closed-end cavity of parameter $d =$ 5 mm, $w = 1$ mm, and period $(\lambda_g) = 4$ mm, including different losses. No losses (black, dashed and dotted line), thermal losses only (red, dashed line), viscous losses only (blue, dotted line), and both thermal and viscous losses (solid, black line).

$$\mathrm{Pr} = \frac{\delta_v^2}{\delta_t^2} = \frac{\nu}{\alpha}. \tag{2.11}$$

For room temperature air Pr $= 0.71$[98].

In order to see the effect these boundary layers have on a real system, an air-filled simple grating of $w = 1$ mm, $d = 5$ mm, and $\lambda_g = 4$ mm has been investigated with different parameters of the fluid. Here, the fundamental quarter-wavelength resonance of the cavity is explored. Figure 2.4 shows the normal incidence reflectivity as a function of frequency. When both ν, $\alpha = 0$, the reflectivity across all frequencies is unity, this is due to δ_v and $\delta_t = 0$. If now we only consider thermal effects ($\nu =$ 0, $\alpha \neq 0$) the reflectivity is now reduced to 0.92 at a frequency of 15.5 kHz, now comparing this to the viscous only case ($\nu \neq 0$, $\alpha = 0$) the reflectivity is reduced to 0.85 at the same frequency, this highlights that viscous effects are dominant for air-filled cavities. The wavelength on resonance is 0.022 m, for comparison δ_v

= 12 µm and δ_t = 15 µm. The thermal and viscous boundary layers are several orders of magnitude smaller than the incident wave, showing the geometry of the grating is more important than the ratio of wavelength and boundary layer widths. The geometry of the grating also dictates how strongly the resonator will couple to incident radiation, which also affects the losses, which will be discussed later in the chapter.

There have been many studies into the effects of the thermal and viscous boundary layers in acoustics.[99–101] Ward et al.[102] studied the effect that narrowing the width of cavities had on the effective speed of sound. Molerón et al.[103] highlighted the importance of the inclusion of thermoviscous effects on the response of an array of rigid slabs with sub-wavelength slits embedded in air. They showed that when these effects were considered 100% reflection occurs; however, in the lossless case, perfect transmission was predicted. The authors stated that the losses are not merely a refinement, but a dominant feature in narrow-cavity resonant structures. These boundary layer effects have also been studied in porous media.[104, 105].

One important feature of the losses is the quality factor (Q-factor) of a resonance. The quality factor relates the internal losses of a surface, the thermal and viscous losses, to the external losses of a surface, the coupling between neighbouring resonators and also free radiation. Figure 2.5 shows a reflectivity spectrum for a simple grating of w = 0.5 mm, d = 5 mm, and λ_g = 6 mm. One can define the quality factor as

$$Q = \frac{f_r}{\Delta f}, \tag{2.12}$$

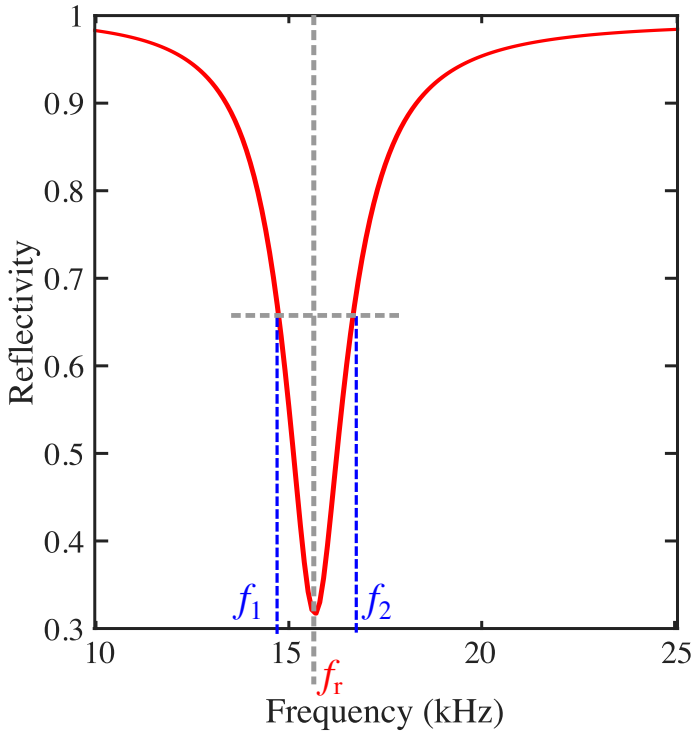

Fig. 2.5 FEM model of the normal incidence reflectivity spectrum for a simple grating of parameter $w = 0.5$ mm, $d = 5$ mm, and period $(\lambda_g) = 6$ mm. f_r is the frequency which the minimum reflectivity occurs. The full width at half maximum is defined by $f_2 - f_1$.

where f_r is the frequency where the minimum value of reflectivity occurs. $\Delta f = f_2 - f_1$ is the full width at half maximum (FWHM). Q also measures how well coupled the system is, with three distinct cases:

$$Q < 1, \qquad \text{Under-coupled} \tag{2.13a}$$

$$Q = 1, \qquad \text{Critically-coupled} \tag{2.13b}$$

$$Q > 1. \qquad \text{Over-coupled} \tag{2.13c}$$

For $Q < 1$, the system is described as under-coupled as the internal losses are higher than the external losses. For $Q > 1$ the system is over-coupled, and the external losses are more prevalent than the internal losses. When $Q = 1$, the system is critically-coupled, and the internal and external losses are equal. [106–108] In acoustic systems, critical-coupling has been the topic of many studies in perfect and broadband absorption[109–112]. One may consider the coupling by investigating the damping of the system. For a grating being excited by incident radiation, this radiation acts as the driving force for the resonance of the grooves. A damping ratio (ζ) is defined as the damping in the system γ over the damping needed for critical damping γ_c, which is related to the Q-factor by ($\zeta = 1/2Q$). In an undamped system, the exciting field would excite a resonance in the grating by a perturbation (δp) from the background field pressure (p_0). The pressure field in the grooves of the grating would then oscillate about the background pressure field with the minimum and maximum value given by $p_0 \pm \delta p$. Due to no damping being present, this would then oscillate around the background field infinitely with the same amplitude. By including a small amount of damping into the system, energy is now dissipated. Now the amplitude of the oscillation will decrease with time until the pressure field

return to p_0. Here, the internal dissipation is low, and the system is over-coupled. By increasing the damping so that $\gamma = \gamma_c$, the pressure within the groove will return to p_0 in the shortest time possible from the initial perturbation; this is a critically coupled resonator. Finally, when the dissipation is high, the system is under-coupled. The system does not oscillate about the background pressure field, and the decay in amplitude from the initial perturbation is slower than that of a critically-coupled system.

2.5 Acoustic Metasurfaces

If some 1D sub-wavelength periodic structure similar to the one shown in the inset of Figure 2.6 is considered, where material 1 is a fluid and material 2 is an acoustically-rigid material, surface modes will be supported at the interface z = 0. It is instructive to investigate the dispersion relation for such modes. One may analyse the dispersion of such surfaces by accounting for Bloch waves. Bloch waves are plane waves which are modulated by a periodic function. One can solve the eigenvalues of Bloch waves to obtain the dispersion diagram.

A dispersion relation relates the wavenumber (or frequency) of the exciting field (k_0) to the wavenumber in the direction of the periodicity (k_x). An example of a dispersion relation can be seen in Figure 2.6. Here, a grating wavevector is defined as $\mathrm{k_g} = 2\pi/\lambda_\mathrm{g}$, where λ_g is the periodicity of the sample. The region extending from $-\mathrm{k_g}/2 \leq k_\mathrm{x} \leq \mathrm{k_g}/2$ is known as the first Brillouin zone. There are two distinct regions of a dispersion relation. The radiative regime, shown in blue, is the region where $k_0 > k_\mathrm{x}$, due to the conservation of energy $k_0^2 = k_\mathrm{x}^2 + k_\mathrm{z}^2$, k_z is real and therefore, modes which exist in this region propagate energy away from the surface. The non-radiative regime, shown in yellow, is the region where $k_\mathrm{x} > k_0$, now k_z must be purely imaginary in order to conserve energy. This purely imaginary k_z signifies

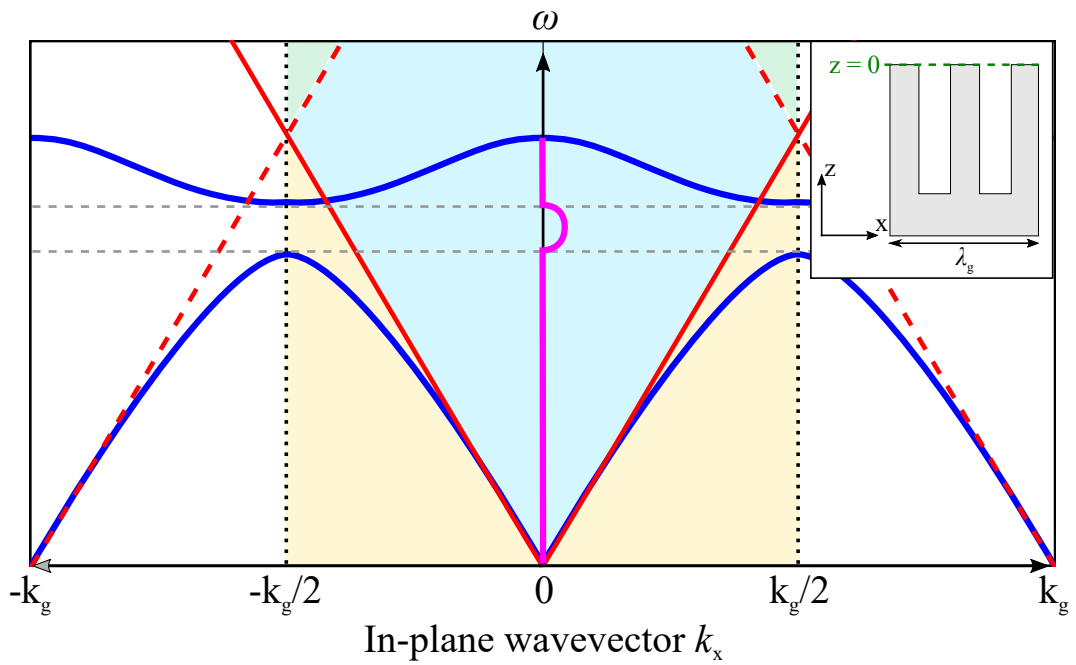

Fig. 2.6 Schematic of a dispersion relation having two supported modes (solid, blue lines), the sound line and diffracted sound line (solid and dashed, red lines, respectively). The solid, magenta line shows the magnitude of the imaginary component of k_x. The yellow region represents the non-radiative regime of the first Brillouin zone. The blue region represents the radiative regime of the first Brillouin zone, and the green region represents the radiative regime where first-order diffraction modes may exist. The dashed, grey lines show the top and bottom of a band gap formed by the two standing wave solutions at the Brillouin zone boundary. Inset: a diagram a unit cell of a periodic surface which would have a dispersion diagram similar to the schematic shown. An acoustically-rigid compound grating (grey) with two resonators per period (λ_g) is presented.

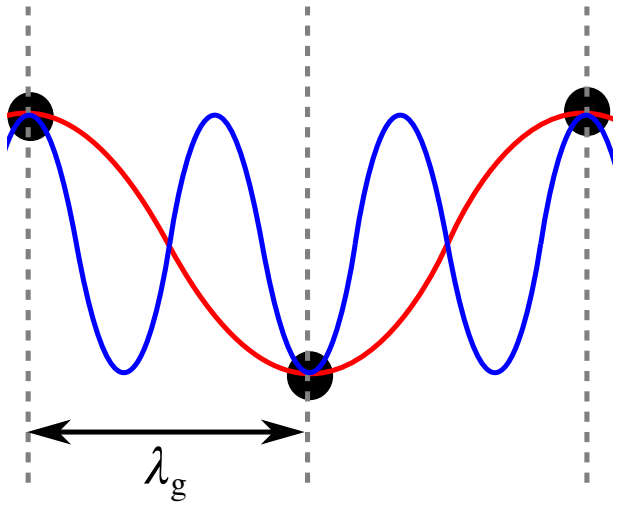

Fig. 2.7 1D mono-atomic chain of particles of periodicity λ_g. Particle displacement at $k_g/2$ (red line), and at $3k_g/2$ (blue line).

that modes within this region are bound to the surface and have an evanescent field in the z-direction. These two regions are separated by a line where $k_0 = k_x$, and this line represents waves where the group and phase velocity are the same. In airborne acoustics, this is known as the sound line (solid, red lines). The diffracted sound lines originating from $-k_g$ and k_g are shown as the dashed, red lines. The in-plane wavevector (k_x) in reality is complex, and written as $k_x = k'_x + ik''_x$. In a lossless system, the regions of the dispersion diagram where k_x is purely real are known as passbands. When k_x is purely imaginary, regions known are stop band exist. In the stopband regions no propagating surface mode on the surface exists. The solid, blue lines in Figure 2.6 shows k'_x. The solid, magenta line shows k''_x which is zero everywhere except between the two dashed, grey lines. When losses are included in the system, k_x is complex throughout the dispersion diagram where the magnitude of the imaginary component signifies the attenuation of the propagating wave.

Dispersion relations are periodic through multiples of k_g in k_x

$$k_x = k_0 \sin\theta \pm N k_g \tag{2.14}$$

where N is an integer, θ is the angle of incidence of the exciting field. For simplicity Figure 2.7 shows a mono-atomic chain of particles rather than the previous grating, and their displacement for two different values of k_x, $k_g/2$ and $3k_g/2$. Since the smallest periodicity in the system is λ_g, any k_x with a value of more than that of k_g will have additional maxima between the neighbouring particles. For the case presented in Figure 2.7, the particle displacement for two standing wave solutions can be seen. Although there are two different λ_x, the particles experience the same displacement.

Within this thesis, non-radiative dispersions are obtained through FEM modelling by solving for the eigenvalues of the Bloch waves supported on a given surface. This analysis was used for simple gratings in Chapter 4 and 6, for more complex compound gratings in Chapter 4, and for glide-symmetric meander metasurfaces in Chapter 5.

2.6 Acoustic Surface Waves

As discussed, modes which exist in the non-radiative regime are confined to the surface since k_z is purely imaginary. For a system comprised of an acoustically rigid material and a fluid, the modes which exist are called acoustic Surface Waves (ASWs). These ASWs propagate parallel to the surface and are evanescent orthogonal to the surface. The number of ASWs supported per cavity resonance of a surface is determined by the number of degrees of freedom on a given surface. A 1D array of blind holes is considered with parameters, $d = 5$ mm, radius $(r) = 1.5$ mm, and $\lambda_g = 4$ mm, the unit cell is shown in Figure 2.8(a). Since there is only one degree of freedom per unit cell, only one surface mode exists. Figure 2.8(b-c) shows the dispersion of the fundamental cavity mode and the fields in two unit cells at $k_g/2$ obtained through finite element method modelling which will be discussed in detail in Section 3.7.2. If an additional resonator is added into the unit cell at the same x

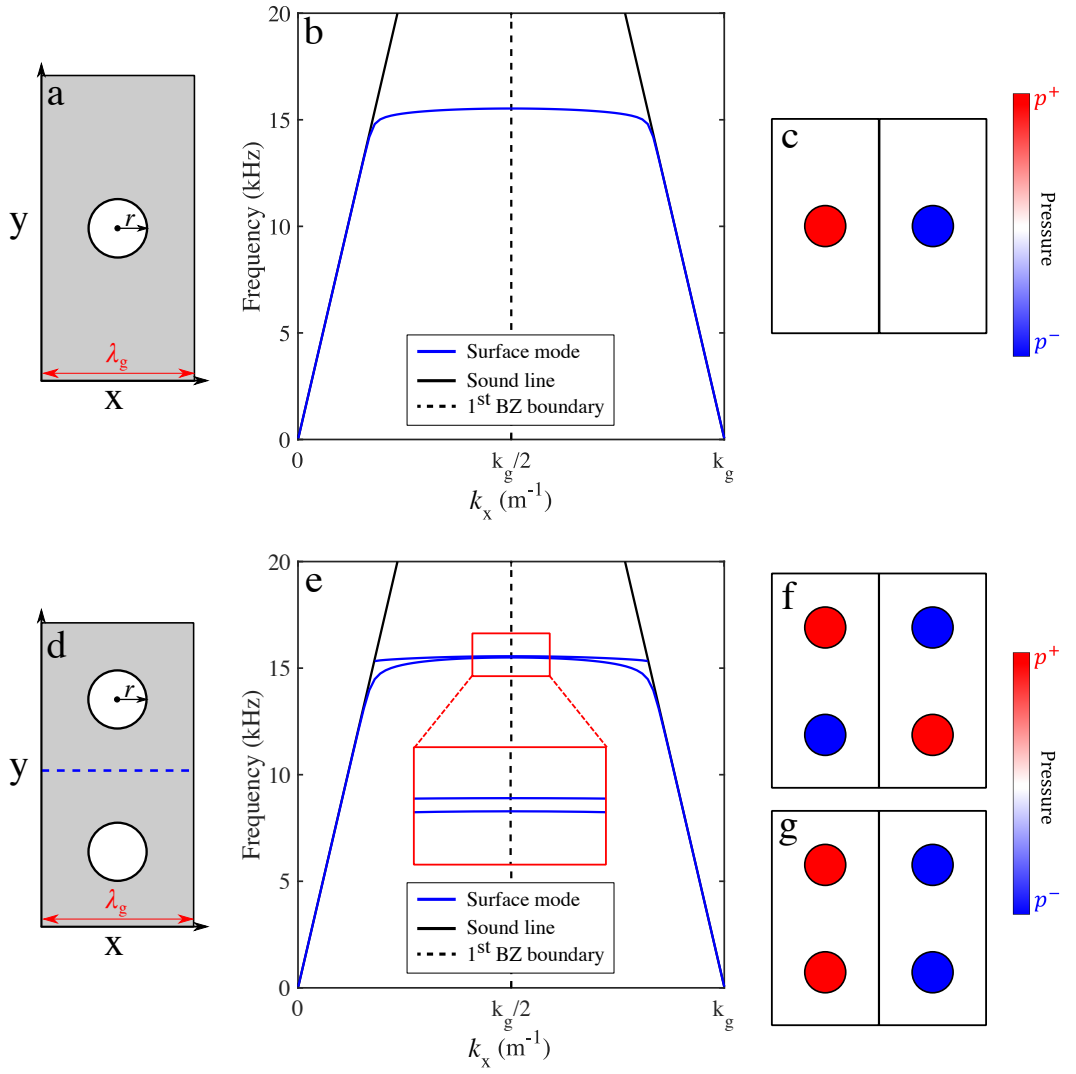

Fig. 2.8 a) Unit cell of 1D periodic array consisting of a blind hole of depth (d) = 5 mm, radius (r) = 1.5 mm, and λ_g = 4 mm. b) FEM model dispersion for the structure in a. c) Instantaneous pressure fields within two adjacent holes at $k_g/2$. d) A unit cell of a 1D periodic array consisting of two blind holes (with the same parameters as a), here, the centre-centre separation is 4 mm. e) FEM model dispersion for the structure in d. f) Higher energy standing wave solution at $k_g/2$. g) Lower energy standing wave solution at $k_g/2$.

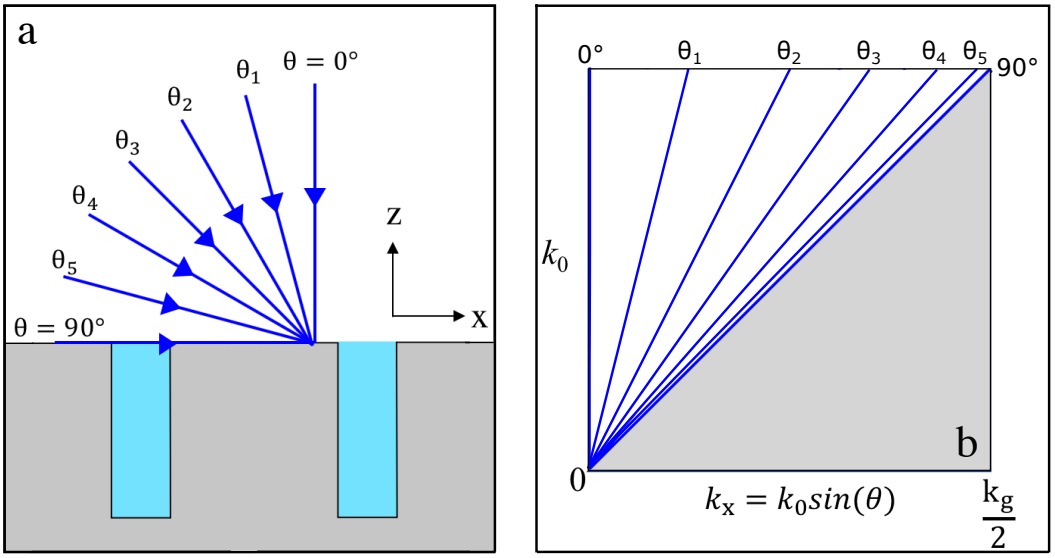

Fig. 2.9 a) Schematic of the angle of incidence (θ) upon a surface. b) Schematic of how θ relates to the dispersion diagram.

position, but with a y-separation of 4 mm, Figure 2.8(d), an additional mode is now supported.

2.6.1 Radiative Dispersion

As seen previously k_x is dependent on the angle of incidence, θ, such that $k_x = k_0 \sin\theta$. It is easy to see at normal incidence ($\theta = 0°$) that $k_x = 0$, on a dispersion diagram the normal incidence data is a slice of data at $k_x = 0$. At grazing incidence ($\theta = 90°$), $k_x = k_0$ which is the sound line. Angles of incidence between these two values, are slices of data with different gradients. A visual representation of this relationship is shown in Figure 2.9

2.6.2 Band Gaps and Anti-crossings

Another feature of Figure 2.6 is the presence of a band gap, represented by the region between the two grey dashed lines. If we consider the mode which originates at $k_x = 0$ and the mode which originates at $k_x = k_g$, it is seen that as they reach the first

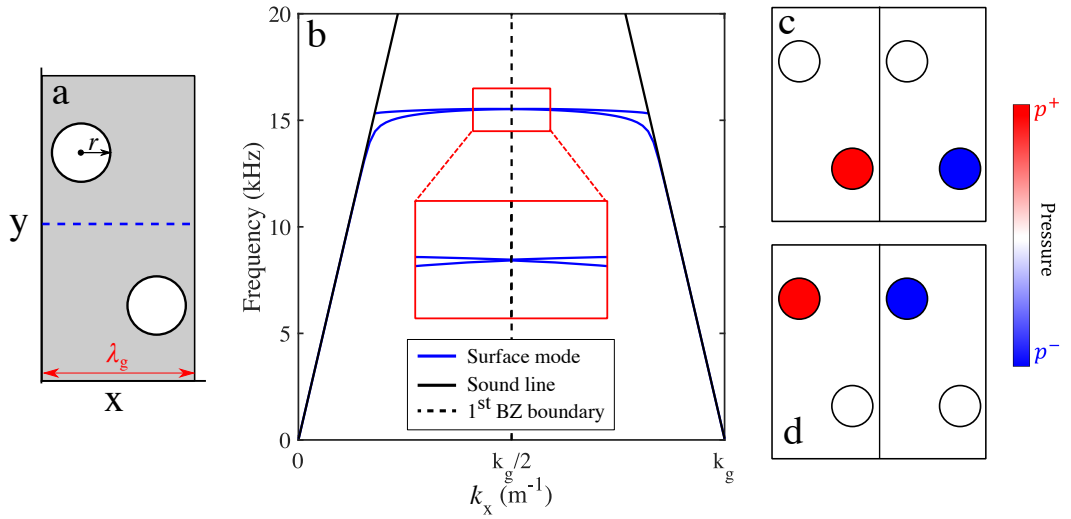

Fig. 2.10 Unit cell of 1D periodic array consisting of glide-symmetric, blind holes of depth (d) = 5 mm, radius (r) = 1.5 mm, λ_g = 4 mm, and a y-separation of 4 mm. The blue dashed line represents the mirror plane. b) FEM model dispersion for the structure in a. c-d) Standing wave solution at $k_g/2$.

Brillouin zone boundary ($k_x = k_g/2$), rather than crossing they split, forming a lower energy mode and a higher energy mode. Between these two modes is a region where no mode can exist known as a band gap. The dispersion presented in Figure 2.8(e) shows two modes and a band gap at $k_g/2$. This band gap exists as the two standing wave solutions have two different field configurations Figure 2.8(f-g). For the lower energy mode, the acoustic fields within the two resonators in the unit cell are in phase; however, for the higher frequency mode, there is now a phase difference of π between the two cavities. As indicated above not all structures have a band gap at the first Brillouin zone boundary, one such structure possesses a symmetry known as glide symmetry[113, 114], Figure 2.10(a) shows such a structure. Glide symmetry is defined as a reflection along a mirror plane (dashed, blue line) and a half-period translation in the direction of periodicity (x). As can be seen in Figure 2.10(b) glide symmetric periodic structures remove the band gap at the Brillouin zone boundary [115, 116]. Figure 2.10(c-d) show the pressure fields of the two modes at $k_g/2$. For both of the modes, it is seen that only one line of resonators is excited and that the

field configurations in both cases are identical, with no fields interacting with the unexcited line of resonators.

The first studies of glide symmetry were in the '60s and '70s, along with studies of twist symmetry which is a translation followed by a rotation.[113, 114, 117, 118]. More recently, glide-symmetric metasurfaces have been investigated with microwaves[119, 120], such structures being employed to minimise leakage. They have also been investigated to mimic the dispersion of surface plasmons [121, 122], and also to prevent stop bands[123]. However as regards glide-symmetric metasurfaces in acoustics, there is little research; this will be the topic of Chapter 5.

Band gaps are not the only splitting of modes to exist. Consider a simple grating of parameters $d = 5$ mm, $\lambda_g = 6$ mm, and allow the slit width w to vary. The grating will have a specific resonance frequency, given by the depth of the grooves, which would appear as a line of constant frequency if the interaction with free radiation is ignored. However, for a system where this interaction is considered, the resonance mode interacts with the sound line, and an anti-crossing occurs. Figure 2.11 show the full dispersion for gratings of different w. For the narrowest case $w = 0.02$ mm, these cavities are highly isolated, and the coupling between neighbouring unit cells is weak, it can be seen that an anti-crossing occurs between the sound line and the resonant mode; however, the modes only disperse over a small frequency range. As w is increased the frequency range which the mode disperse over increases as does the size of the anti-crossing. When $w = 3$ the mode disperses over a broader frequency range, demonstrating that the coupling between neighbouring until cells has increased. In addition the band gap at the Brillouin zone boundary also increases in magnitude. These anti-crossings are not just isolated between the mode resonances and the sound line; they may also occur between different modes in the dispersion.

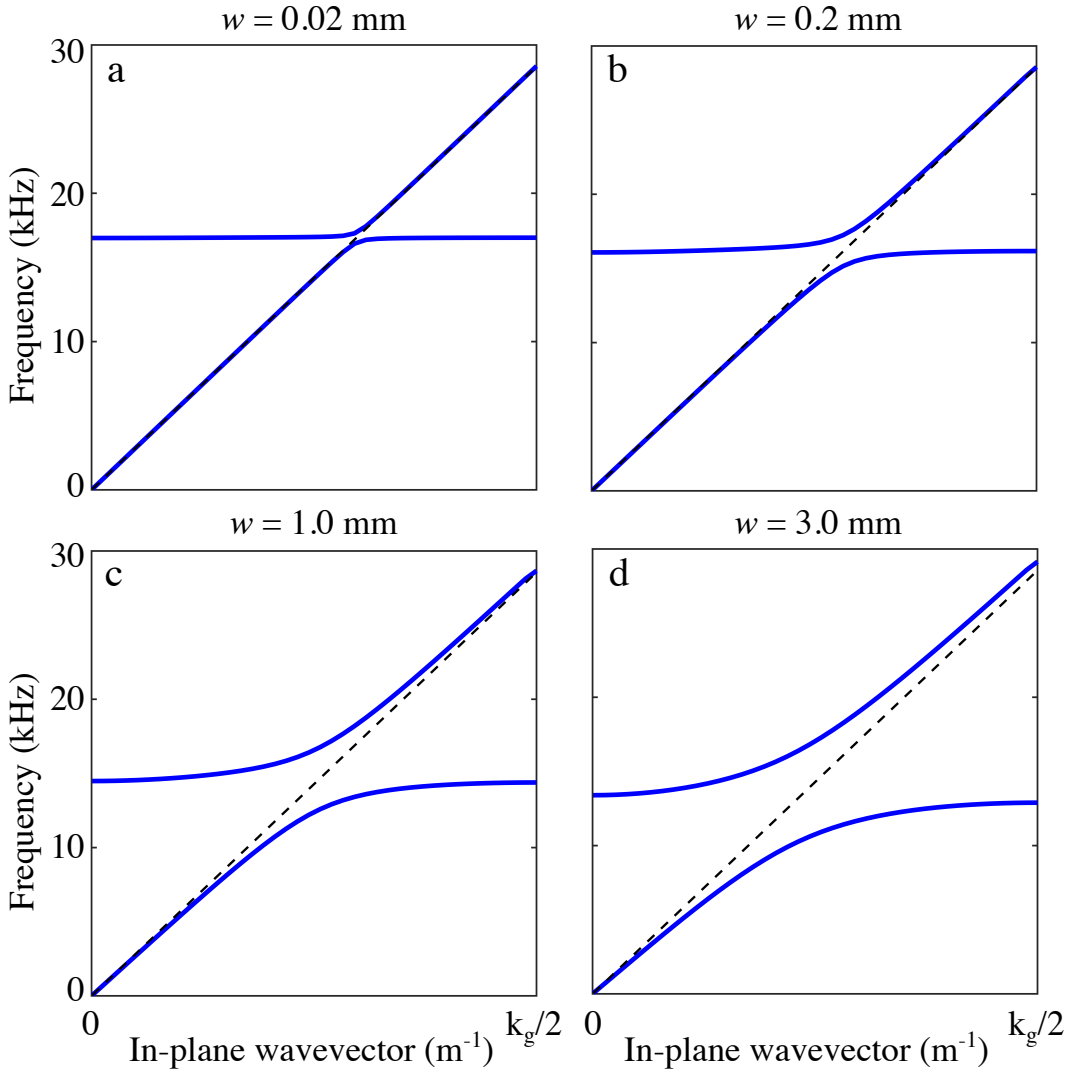

Fig. 2.11 Dispersion relations for various groove widths of 1D periodic gratings of parameters $d = 5$ mm, $\lambda_g = 6$ mm. As the groove width increases, the anti-crossing between the two modes increases. The dashed, grey line represents the sound line.

The band-structure of periodic structures has been the topic of numerous investigations.[4, 124, 125] Kushwaha et al.[126] presented the first calculation of a full band structure for periodic elastic composites.

2.7 Elastic Materials

So far only airborne acoustics has been considered, where the solid is acoustically rigid. Acoustic waves in elastic media are defined by their elastic properties, namely the Young's (E), bulk (K) and shear (G) moduli, and the Poisson's ratio (ν). From these parameters and the density (ρ), both the longitudinal and transverse velocities may be defined

$$c_\mathrm{l} = \sqrt{\frac{K + \frac{3}{4}G}{\rho}} = \sqrt{\frac{E(1-\nu)}{\rho(1+\nu)(1-2\nu)}}, \tag{2.15}$$

$$c_\mathrm{t} = \sqrt{\frac{G}{\rho}}. \tag{2.16}$$

There are two other useful elastic moduli used to relate the three previously stated and also c_l and c_l. These are know as Lamé constants

$$\lambda = \rho(c_\mathrm{l}^2 - 2c_\mathrm{t}^2) \tag{2.17}$$

$$\mu = \rho c_\mathrm{t}^2 \tag{2.18}$$

These Lamé constants will be used later when describing the Lamb modes supported on a fluid-loaded plate.

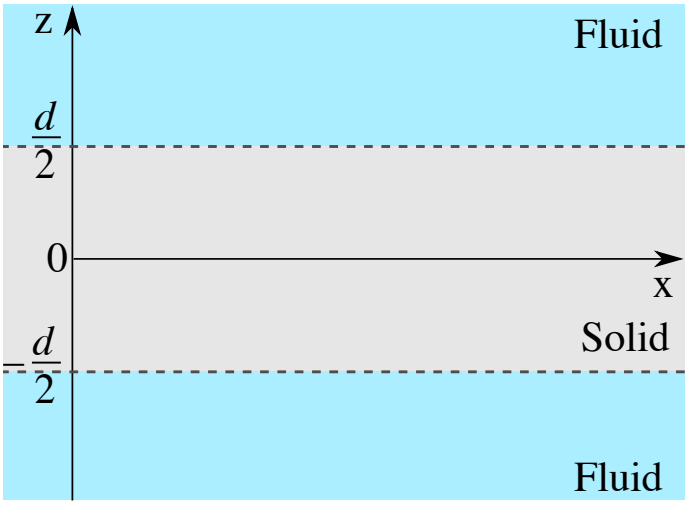

Fig. 2.12 An underwater plate of thickness d loaded with fluid on both sides.

2.7.1 Elastic Modes on Fluid-Loaded Plates

In this section the modes supported on a fluid-loaded, elastic plate of thickness d is considered as shown in Figure 2.12, here the plate interfaces are located at $z = \pm\frac{d}{2}$. There exist two pairs of modes on fluid loaded elastic plate, symmetric and anti-symmetric coupled interface waves. The characteristic equations for both these modes are as follows[127]

$$\begin{aligned}(k_{\mathrm{Tz}}^2 - k_{\mathrm{x}}^2)\tan(k_{\mathrm{Tz}}d/2) + 4k_{\mathrm{x}}^2 k_{\mathrm{Lz}}k_{\mathrm{Tz}}\tan(k_{\mathrm{Lz}}d/2) - \\ i\frac{\rho_{\mathrm{liq}}k_{\mathrm{Lz}}\omega^4}{\rho_{\mathrm{s}}k_{\mathrm{liq,z}}c_{\mathrm{t}}^4}\tan(k_{\mathrm{Lz}}d/2)\tan(k_{\mathrm{Tz}}d/2) = 0,\end{aligned} \tag{2.19}$$

and the characteristic equation for the anti-symmetric modes is

$$\begin{aligned}(k_{\mathrm{Tz}}^2 - k_{\mathrm{x}}^2)\tan(k_{\mathrm{Lz}}d/2) + 4k_{\mathrm{x}}^2 k_{\mathrm{Lz}}k_{\mathrm{Tz}}\tan(k_{\mathrm{Tz}}d/2) + \\ i\frac{\rho_{\mathrm{liq}}k_{\mathrm{Lz}}\omega^4}{\rho_{\mathrm{s}}k_{\mathrm{liq,z}}c_{\mathrm{t}}^4} = 0.\end{aligned} \tag{2.20}$$

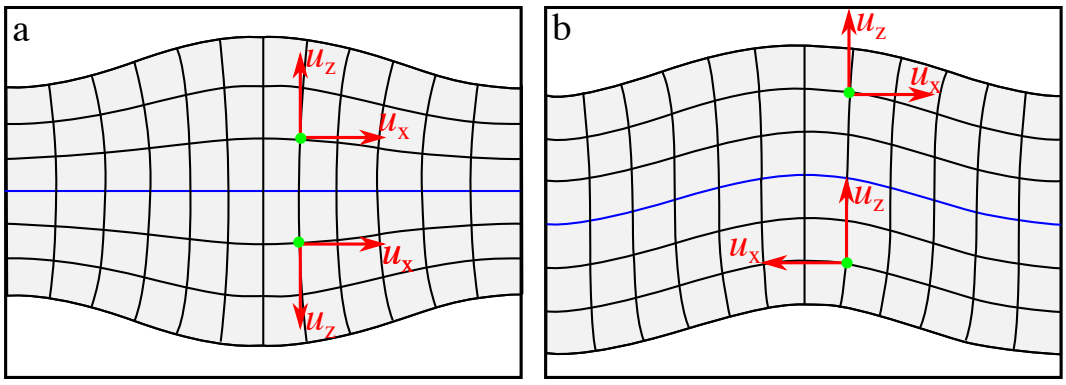

Fig. 2.13 Exaggerated total deformation of a $d = 6$ mm fluid-loaded, acrylic plate. a) The symmetric coupled-Scholte mode. b) The anti-symmetric coupled-Scholte mode. Each element represents a 1 x 1 mm area. The blue line represents the line at z = 0 in the undeformed system.

In these equations $k_{\mathrm{Lz}} = \sqrt{\omega^2/c_l^2 + k_{\mathrm{x}}^2}$ and $k_{\mathrm{Tz}} = \sqrt{\omega^2/c_t^2 + k_{\mathrm{x}}^2}$ are the z-component of the wavevector of the longitudinal and transverse waves in the solid respectively. While the z component of the wavevector of the longitudinal wave in the fluid is $k_{\mathrm{liq,z}}$. The densities in the solid and fluid are represented by ρ_{s} and ρ_{liq}.

For both the symmetric and the anti-symmetric equations, the real part is the equations for free waves in a plate, known as Lamb's equations. The additional term is the imaginary term which describes the effects of fluid loading. Figure 2.13(a-b) shows the deformation of the plate. The two green circles show the z-displacement (u_{z}) and x-displacement (u_{x}) of one particle in the top half ($\mathrm{z} \geq 0$) and one in the lower half ($\mathrm{z} \leq 0$) of the plate. In the symmetric case, it is seen that deformation is symmetric around the reflection plane z = 0 (blue line), as u_{z} are in opposite directions and u_{x} are in the same direction. In the anti-symmetric case at a particular x position, u_{z} is in the same direction and magnitude. However, in the upper and lower half of the plate, u_{x} are in opposite directions (I would like to thank Beth Staples for help with these equations).

The dispersion relation for a $d = 6$ mm, water-loaded acrylic plate is shown in Figure 2.14. The dashed, blue-line is the symmetric coupled-Scholte mode. At low

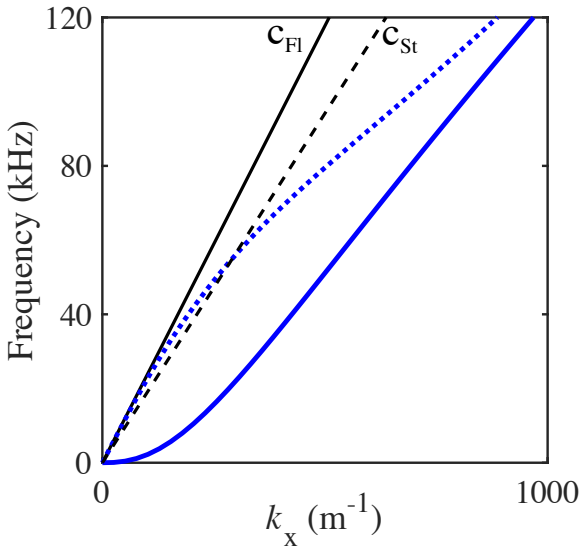

Fig. 2.14 Dispersion relation for a 6 mm, water-loaded acrylic plate. c_{Fl} represents the water sound line, and c_{St} represents the solid transverse speed.

k_x, the symmetric mode follows the water sound line and then begins to disperse. In contrast, at low k_x the group velocity of the anti-symmetric mode begins at zero, and increases until the mode become linear at high k_x. Both of these modes tend towards the Scholte wave speed as k_x increases.

2.8 Conclusions

In this chapter, the properties of radiative and non-radiative modes supported on both structures and unstructured surfaces have been discussed. The reflectivity and transmission at an interface have been explored and expanded to the case of a system composing of resonators. Various structures supporting acoustic resonances have been discussed alongside the thermal and viscous boundary layers where losses occur. Periodically structuring a surface has been shown to allow for bound surface modes to couple to the surface, these modes disperse in frequency and can exhibit phenomena such as band gaps and anti-crossings. Adding structure in one period of

such a surface allows for additional modes to be supported, while certain symmetries such as glide symmetry remove the band gap at the first Brillouin zone boundary.

Interface waves between two differing media have been discussed. A solid-fluid interface has been shown to support Scholte waves. This discussion was expanded to the case of fluid-loaded plates where symmetric and anti-symmetric modes are supported. These modes are shown to be coupled Scholte modes. In the following chapter I will discuss the experimental methods and numerical methods which will be used extensively throughout the thesis.

Chapter 3

Methods

3.1 Introduction

Within this chapter the methods of experimentally and computationally characterising acoustic surfaces are presented. Experimentally such surfaces are analysed in both the radiative and non-radiative regimes so they may be fully characterised. The reflection experiments used to obtain the radiative dispersion are discussed in section 3.4. Surface scans from which the dispersion relation and iso-frequency contours are obtained are discussed in section 3.5. Both of the methods use Fourier analysis which is discussed in section 3.6.

Finite element modelling is used to obtain both the reflectivity spectrum in the radiative regime and also the dispersion relation in the non-radiative regime.

3.2 Sample Fabrication

Within this thesis, multiple experimental samples were fabricated in house. The sample discussed in Chapter 4 was fabricated from milled acrylic using 1 ± 0.02 mm milling cutters. The effect on the results due to the error in the cutting is

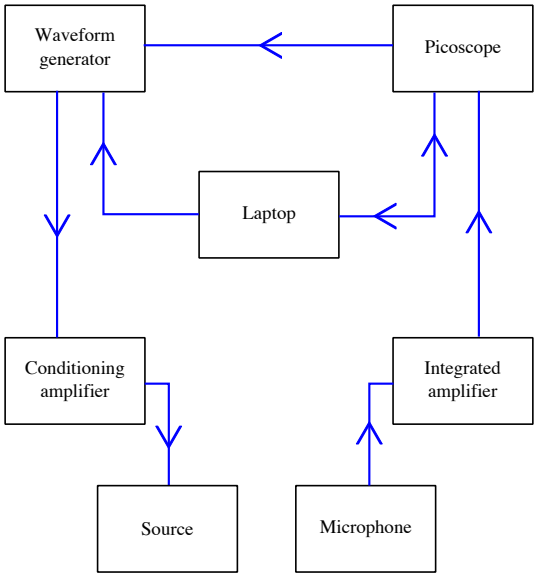

Fig. 3.1 Schematic of the equipment used in both the radiative and scan experiments.

negligible, as the width has little effect om resonant frequencies of the channels. In Chapter 5, a similar milling process was used; however, these samples were milled out of aluminium. The errors in fabrication remain the same and have a negligible influence on the results. In the underwater case, the same milling process was used. However, the effect on the results is more significant than the air case, due to the bulk modes being considered. This increased sensitivity of the geometry of the structure is explained in detail in Chapter 4.

3.3 Data Acquisition

To experimentally measure acoustic metasurfaces the hardware used is illustrated in Figure 3.1. Depending on whether a radiative or non-radiative measurement was taken it was connected to the relevant experimental setup, both of which use a Labview interface which has been designed especially for experiments. A laptop is the connected to a Picoscope 4262 which allows for the real-time signal acquisition where the resolution of the time data can be set and also the amount of data points.

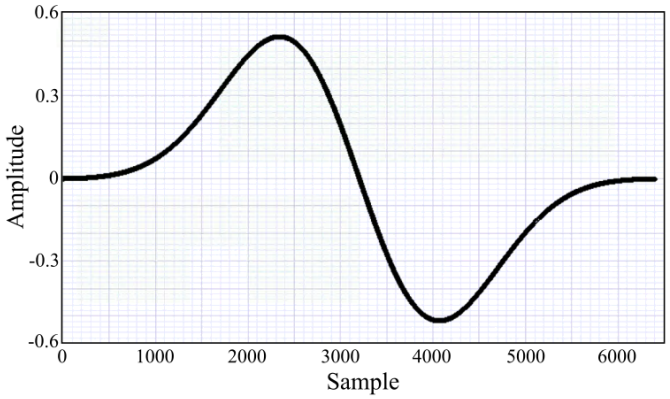

Fig. 3.2 The pulse shape used in all experiments (near-single-cycle Gaussian-envelope sound pulse).

An Agilent 33500B series waveform generator is connected to the laptop which is used to generate a pulse with the desired central frequency, length and shape. In all of the following experiments near-single-cycle Gaussian-envelope (broad-band) sound pulses were used shown in Figure 3.2. To ensure that the data is acquired correctly the waveform generated is synchronised with the picoscope . The generated pulse is then passed through a Cambridge audio topaz AM5 integrated amplifier, the pulse is then passed to a source and emitted for measurement. An acoustic receiver detects the acoustic pulse, this signal is then fed through a Brüel & Kjær nexus conditioning amplifier in order to increase the strength of the detected signal. This signal is then sent to the picoscope for the data acquisition and then to the laptop. This process is then repeated for a desired number of repeats.

3.4 Radiative Measurements

To experimentally explore the radiative regime the equipment shown in Figure 3.3 was used. A speaker (Tucker-Davis Technologies MF1) was placed on a moveable arm at a distance of 1 m away from a collimating mirror. The acoustic wavefronts incident upon this mirror were reflected as plane waves onto a sample placed 2 m

away. The reflected signal was then incident on to a second collimating mirror which then focused the beam onto a microphone (Brüel & Kjær 4190) which was placed on a second moveable arm. In order to ensure that the microphone and speaker did not directly impede the acoustic beam they are placed below the central plane of the experiment. The smallest angle of incidence (θ) that could be measured was a pseudo-monostatic measurement where the microphone was placed on top of the speaker and only one mirror was used ($\theta << 1°$). By contrast the smallest angle that could be measured by using both the mirrors was 8.3° due to the physical size of the mirrors (diameter of 44 cm), the equipment can theoretically be used to measure up any angles within the range 8.3° - 90° but at the higher angles of incidence the projected beam area onto the sample becomes much larger than that of the sample, and the reflected signal becomes weak due to most of the beam not being incident upon the sample. At the largest angles measured ($\theta = 70°$), direct transmission becomes increasingly prevalent due to the width of the beam and the mirrors being close to 180° apart.

There is a minimum frequency that can be measured in this setup due to the finite size effects of the mirrors (radius = 220 mm, focal length = 1 m). As the acoustic wavelength approaches the diameter of the mirrors, diffraction begins to occur. However, in this thesis, the wavelength used is always smaller than the diameter of the mirrors. The maximum wavelength used for radiative measurements is 34 mm.

To obtain the reflectivity at a given angle two measurements had to be taken one with the sample and a reference. The reference used was a flat metallic plate, an acoustic mirror, the size of the sample. The signal form this reference plate was used for normalisation. It should be noted that the reference measurements had to be taken with great care as any divergence from the original orientation of the sample rendered the reference unreliable. To decrease the effect of background noise repeats

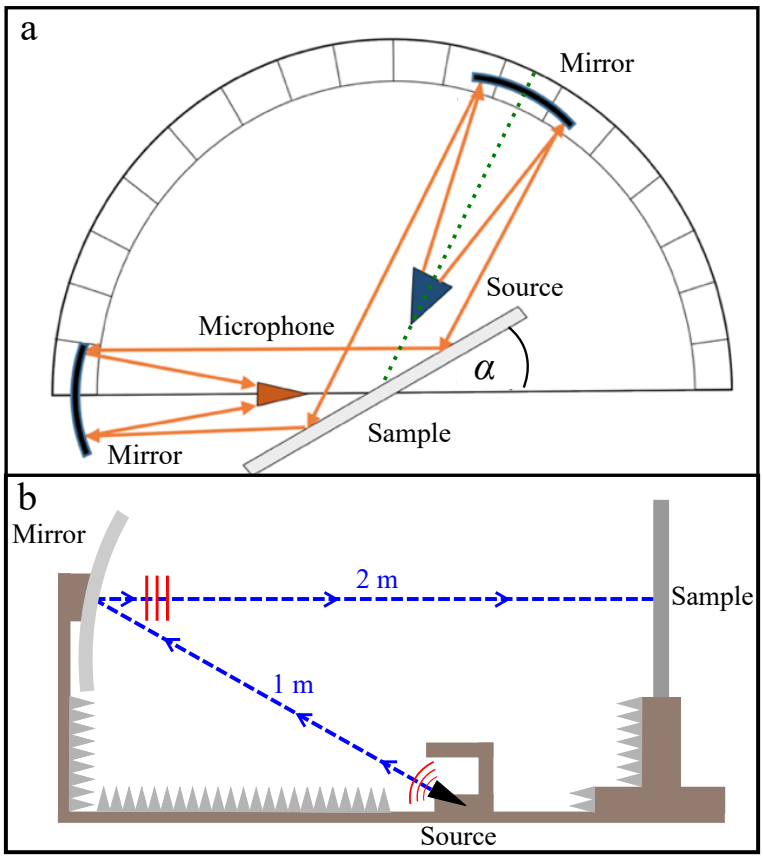

Fig. 3.3 a) Schematic (not to scale) of the experimental setup, consisting of a speaker at the focus of a collimating mirror giving a plane wave incident onto the sample, the reflected signal being then focused by a second mirror onto the microphone. The speaker and microphone are placed below the central plane of the mirrors and sample such that they do not directly impede the acoustic beams. Here, $\alpha = 90° - \theta$, where θ is the angle of incidence. b) Side view of the experimental setup along the green dotted line in (a). The red lines represent the shape of the phase fronts.

were taken, in all radiative measurements taken 100 repeats proved to be sufficient. A typical signal to noise ratio from such measurements is 31.5 dB.

3.5 Non-Radiative Measurements

The measurement of the non-radiative, surface bound modes was undertaken by recording the propagation of an acoustic pulse in time over a line or surface. These scans were performed using scanning stages. For measurements in air, an XY

scanner was used which allows for one and two-dimensional scans to be performed. Underwater measurements used an XYZ scanner where three-dimensional scans could also be performed. In order to set up an experiment a sample was held in place within the scan area. A detector was then placed close to the surface (< 0.5 mm) so that the evanescent fields of the bound surface waves could be detected. The detector was then moved to the beginning of the scan range and then moved slowly to the extremes of the scan area. This was to ensure that the detector distance from the surface remained constant, as any variation in the distance resulted in inequivalent intensities being recorded. Figure 3.4 shows an unstructured sample which has been placed and aligned, the microphone in the lower right corner is at the start position of the scan. In order to excite surface waves two excitation methods were used: diffractive and direct. For airborne measurements 3 repeats were used as the signal intensity was much stronger than in the radiative case. Typical signal to noise ratio for airborne non-radiative measurements is 20 dB. In the underwater non-radiative measurements 50 repeats were used with a signal to noise ratio of 15 dB.

In diffractive excitation a hole was drilled into the required position on the sample. An acoustic source was then placed on the unstructured side of the sample so that there was minimal distance between it and the hole. This was done as any distance between the source and the plate resulted in a standing wave being formed which in turn affects the intensity content of the pulse emitted from the hole. The emitted acoustic pulse propagates through the hole and then diffracts, some of this diffracted acoustic energy will couple to surface waves which are then measured. Diffractive excitement was used in Chapters 4 and 6.

In direct excitation a source was placed at an angle ($< 10°$) to the surface and a pulse is emitted directly onto the structured surface. This method proved to be beneficial when measuring samples which support surfaces waves that rapidly decay, as the microphone was able to be placed directly next to the source. One slight

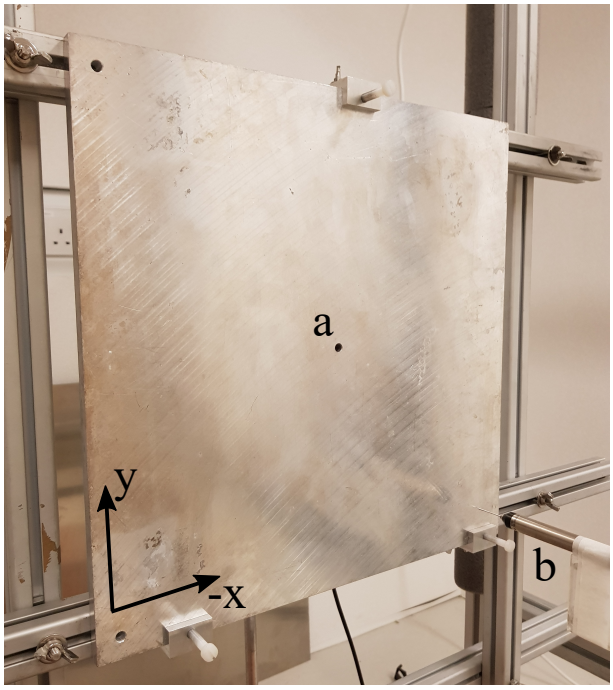

Fig. 3.4 An unstructured sample with a central hole (a) placed in the XY stage. The sample has been aligned so that the microphone (b) remains at a fixed distance from the surface while performing the scan.

disadvantage to this method is that a substantial amount of radiation leaves the structured surface. Direct excitation was used in Chapter 5.

In both cases, the same data acquisition method was used as discussed in section 3.3. For air, a needle microphone (Brüel & Kjær Probe Microphone Type 4182) was raster scanned at the required resolution over the predefined scan area. It is important that both the resolution and scan size area are chosen carefully as the resolution in space determines the maximum values in momentum-space which can be measured, and the total scan length in a direction determines the resolution, this is discussed in more detail in section 3.6. A slight complication is the scan of high-momentum, rapidly-decaying waves where a high resolution scan is needed in order for them to be recorded due to the decay lengths being small. At each position a fluctuation of the acoustic pressure exists corresponding to the propagation of acoustic energy over the surface, this varying pressure was then transduced into an

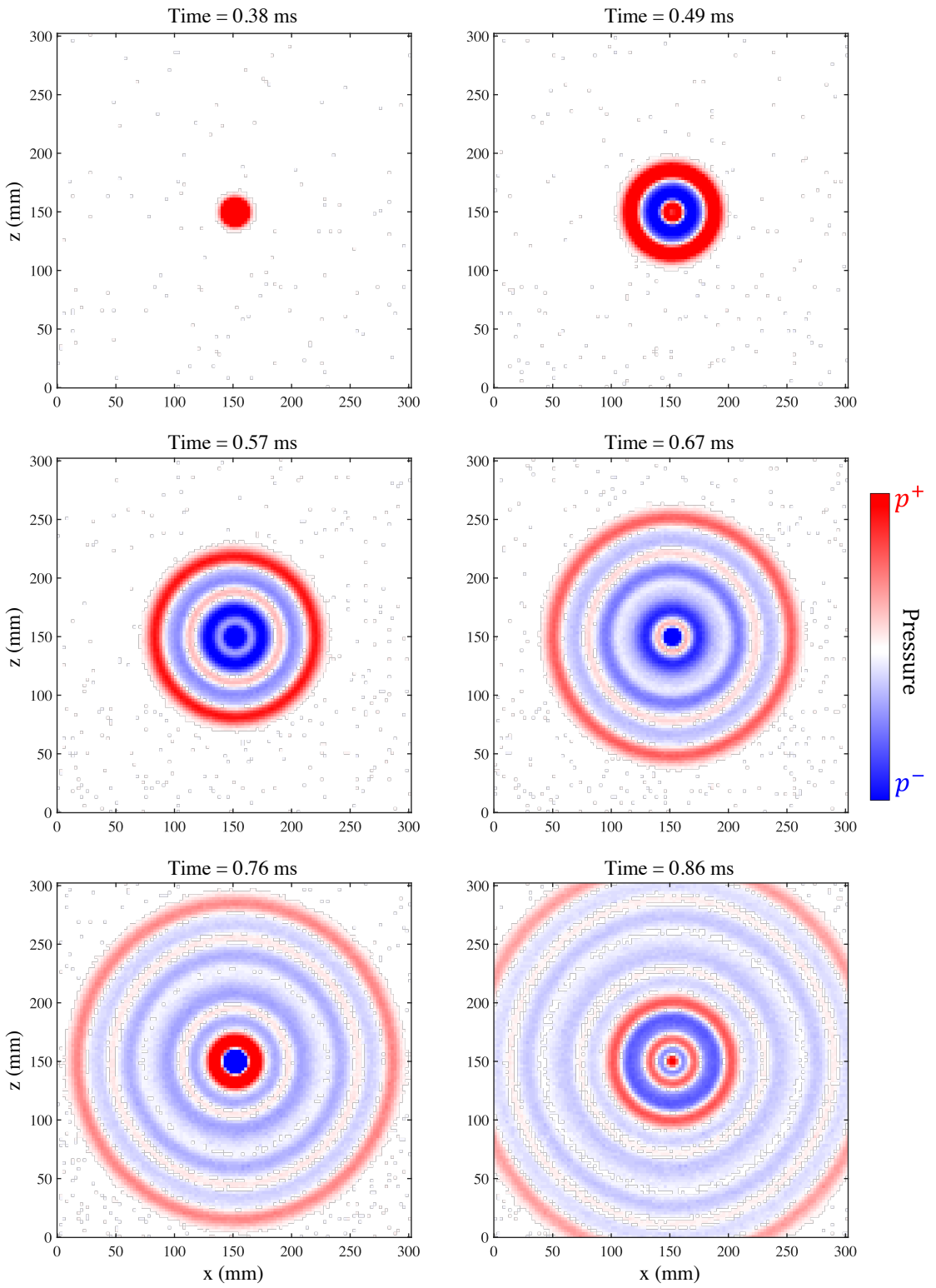

Fig. 3.5 Progression of an acoustic pulse excited by diffraction through a central 6 mm diameter hole on an unstructured plate. Note that the intensity in the centre is saturated due to the acoustic energy density being larger directly above the speaker.

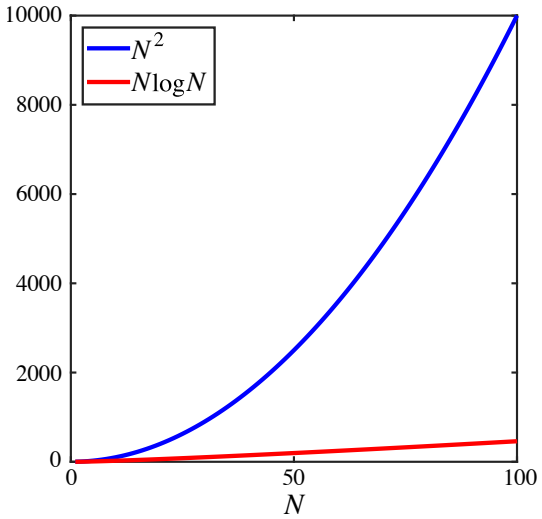

Fig. 3.6 Computational complexity growth with the number of samples. DFTs scale with N^2. FFTs scale with $N\log N$.

electrical signal which was recorded as a function of time. In order to demonstrate this more clearly, a surface scan of an unstructured plate of dimensions 360 × 360 × 10 mm was measured with a spatial resolution of 2.5 mm over a length of 300 mm in both directions. Whilst no surface waves are supported on this surface, due to diffractive excitation the diffracted wave fronts propagate over the surface and were recorded. For this sample shown in Figure 3.4 the central hole was 6 mm in diameter. Figure 3.5 shows the acoustic pulse propagating over the surface. At a time of 0.38 ms the pulse is emitting and diffracting from the hole. It should be noted that the intensity of the radiation above the centre of the hole is much larger than that anywhere else, as directly above the hole there is more acoustic energy per unit area than above the structured surface due to the diffractive wave being hemispherical in nature. As the time (t) progresses the wave propagates evenly in all directions and falls in intensity.

3.6 Fourier Analysis

Fourier analysis is an essential method for the analysis of the experimental data, it is used to decompose a function in time $f(t)$ into its spectral components of frequency $F(\omega)$. Likewise, it is also used to decompose a function in space $f(x)$ into the spectral components of wavevector $f(k)$. In the case of non-periodic functions in t the Fourier transform and the inverse are defined as the following[128]

$$F(\omega) = \frac{1}{\sqrt{2\pi}} \int_{-\infty}^{\infty} f(t) e^{-i\omega t} dt \tag{3.1}$$

$$f(t) = \frac{1}{\sqrt{2\pi}} \int_{-\infty}^{\infty} F(\omega) e^{i\omega t} d\omega. \tag{3.2}$$

The equivalent expressions for non-period functions in x are

$$F(k) = \frac{1}{\sqrt{2\pi}} \int_{-\infty}^{\infty} f(x) e^{-ikx} dt \tag{3.3}$$

$$f(x) = \frac{1}{\sqrt{2\pi}} \int_{-\infty}^{\infty} f(k) e^{ikx} dt \tag{3.4}$$

In the analysis of the experimental data discrete Fourier transforms (DFT) are used[129]. The DFT creates a periodic signal by repeating the original, non-periodic signal. This periodic signal results in a spectrum of data which occur at specific frequencies at small intervals proportional to $1/N$, where N is the total amount of samples. To compute DFTs in Matlab a fast Fourier transform (FFT) algorithm is used[130]. If a DFT is performed on a data set with N samples the computational complexity is of order N^2. However, by using a FFT the complexity is now $N\log N$. The relation between computational complexity and N is shown in figure 3.6. If two data sets $Y(k)$ and $X(j)$ are related such that Y = FFT(X) and its inverse X = IFFT(Y) these function are defined by:

$$Y(k) = \sum_{j=1}^{N} X(j) W_n^{(j-1)(k-1)} \tag{3.5}$$

$$X(j) = \frac{1}{N} \sum_{k=1}^{n} Y(k) W_n^{-(j-1)(k-1)} \tag{3.6}$$

where

$$W_n = e^{\frac{-2\pi i}{N}}. \tag{3.7}$$

Using the above equations the frequency domain data is obtained from the time domain data.

At each spatial position a 1D FFT was applied to the time signal. A typical experimental time signal is shown is Figure 3.7(a), the whole time signal is not shown for clarity purposes but the main feature is that the whole pulse emitted from the speaker is measured within the first 6 ms. It may appear that the rest of the data is somewhat irrelevant but it actually serves a very useful purpose - due to the nature of FFTs the longer in time which a signal is measured ($t_{\max}$): the higher the frequency resolution will be, $\Delta f = \frac{1}{t_{\max}}$. Likewise, the resolution in time (Δt) dictates the maximum frequency $f_{\max}$ which can be measured as $f_{\max} = \frac{1}{\Delta t}$.

Examples of these relations can be seen in Figure 3.8 where the left column shows the time domain functions and the right column the respective Fourier transforms in frequency space $|F(\omega)|$. The time domain functions are all sine waves of periods $T = 0.1$ s and of the form $f(t) = \sin\left(\frac{2\pi t}{T}\right)$. The range of t is defined $t = 0 : \Delta t : nT$, where n is a positive integer. The top row shows a 10 Hz sine wave with $\Delta t = 0.010$ s and $n = 2$. The resulting Fourier transform has been shifted around the central axis y = 0 so that the zero-frequency components are in the centre of the spectrum, it is also symmetric and defined within the following regions depending on the length of the data set:

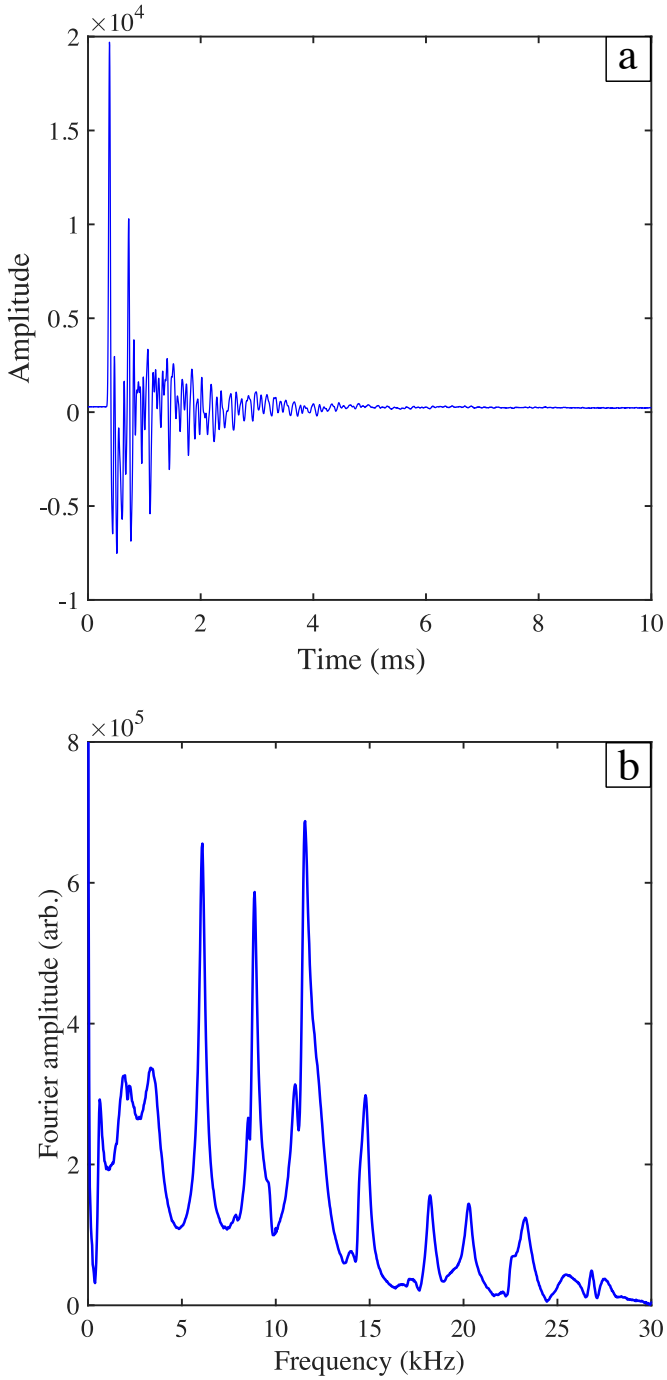

Fig. 3.7 **(a)** Direct transmitted time domain signal for one position, in this case directly above the hole used for diffractive excitation. Only a section of the time signal is shown, so that the pulse can be seen more clearly. **(b)** Part of the frequency spectrum obtained from the Fourier transform $|F(\omega)|$ of the above time signal, note the periodic peaks which correspond to a standing wave forming in the system between the plate and detector holder.

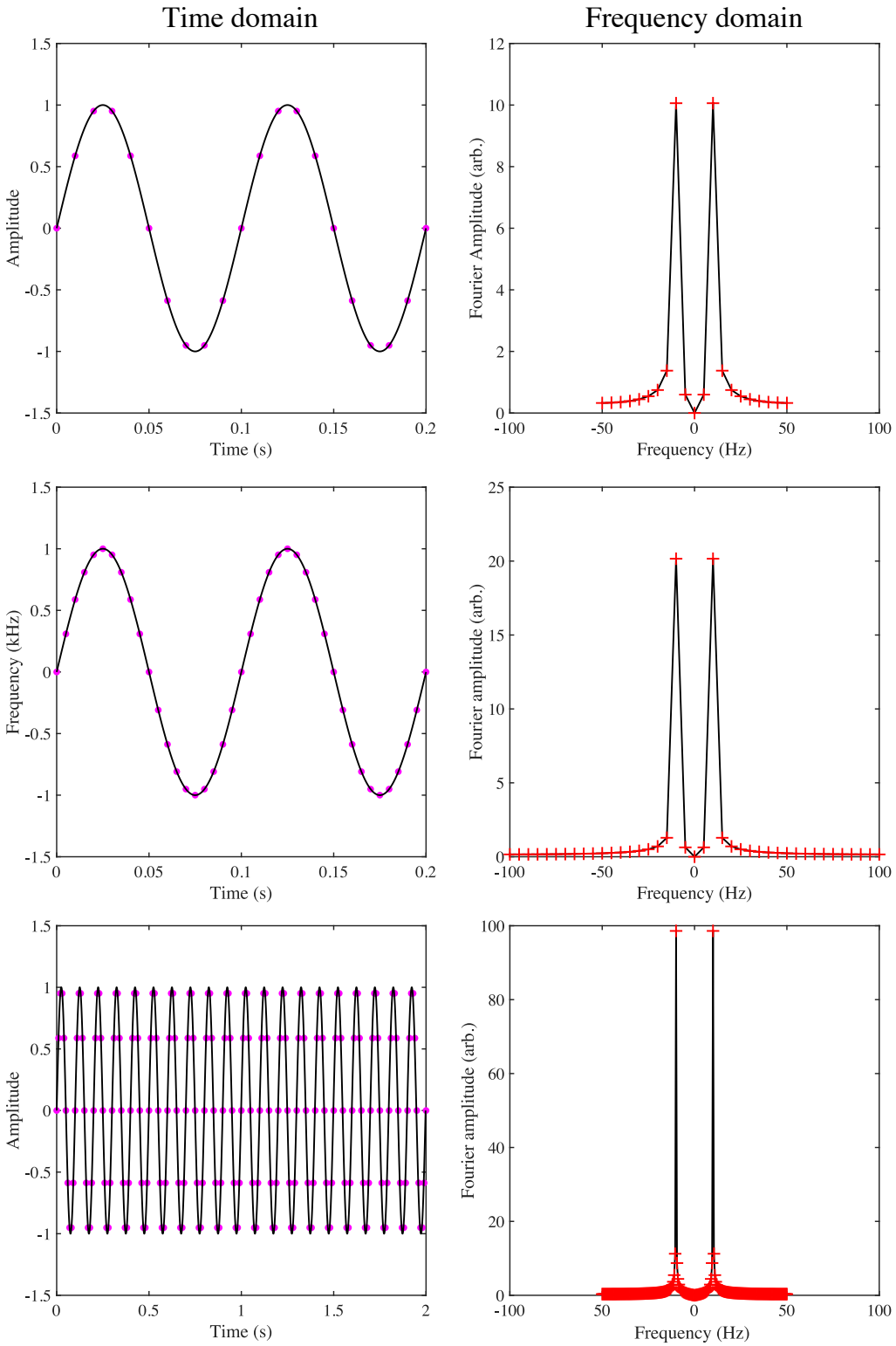

Fig. 3.8 Time domain: Top. Two periods of a 10 Hz sin wave with a $\Delta t = 0.010$ s. Middle. Two periods of a 10 Hz sin wave with a $\Delta t = 0.005$ s. Bottom. Ten periods of a 10 Hz sin wave with a $\Delta t = 0.010$ s. In all of the above the magenta markers show the actual data, the black line is only a guide to show the sin wave. Right side shows their respective Fourier transforms.

$$\text{even:} \qquad -\tfrac{f_{\max}}{2} : \Delta f : \tfrac{f_{\max}}{2}$$
$$\text{odd:} \quad -\tfrac{f_{\max}}{2} + \tfrac{\Delta f}{2} : \Delta f : \tfrac{f_{\max}}{2} - \tfrac{\Delta f}{2}$$

Due to low temporal resolution the maximum frequency recorded ($\frac{f_{\max}}{2}$) is only 50 Hz, in the case of a sine wave this does not present any issue; however, for more complex functions or experimental data a larger $f_{\max}$ may be required. To increase $f_{\max}$ an increase in time resolution is needed. An example of an increased time resolution can be seen in the middle row. Here $t_{\max}$ has been kept the same as in the first case but the resolution has been halved to $\Delta t = 0.005$ s. After Fourier transforming, it is now possible to measure up to an $\frac{f_{\max}}{2} = 100$ Hz. This is particularly useful when the experimental data is expected to exist over a broad range of frequencies. In both the previous discussed cases it can be seen that measuring over a small total time results in poor resolution in frequency space. This leads to the expected peak at 10 Hz being ill defined. The bottom row shows a 10 Hz sin wave with a $\Delta t = 0.010$ s and $n = 20$. In the frequency space it is immediately obvious that the peak at 10 Hz is much better resolved compared to the previous two examples. In the case of measuring over an infinite number of periods this peak would be a delta function. Both the length and resolution of the temporal data need careful consideration; having too high time resolution over a large time results in exceeding the amount of data the data acquisition system can store. This is particularly important in experiments where a large number of repeats are necessary.

After the first Fourier transform has been performed at each position the resulting complex data $\Big(F(\omega)\Big)$ is used to plot the spatial fields. $F(\omega)$ is complex as the imaginary component contains information about the phase. Examples of such fields are shown in Figure 3.9 for two arbitrary frequencies. The top row shows the instantaneous pressure field at one phase and is defined as the real components of $F(\omega)$. In these figures the amplitude has been saturated due to the high acoustic energy density that exists directly above the hole used for excitation. The middle

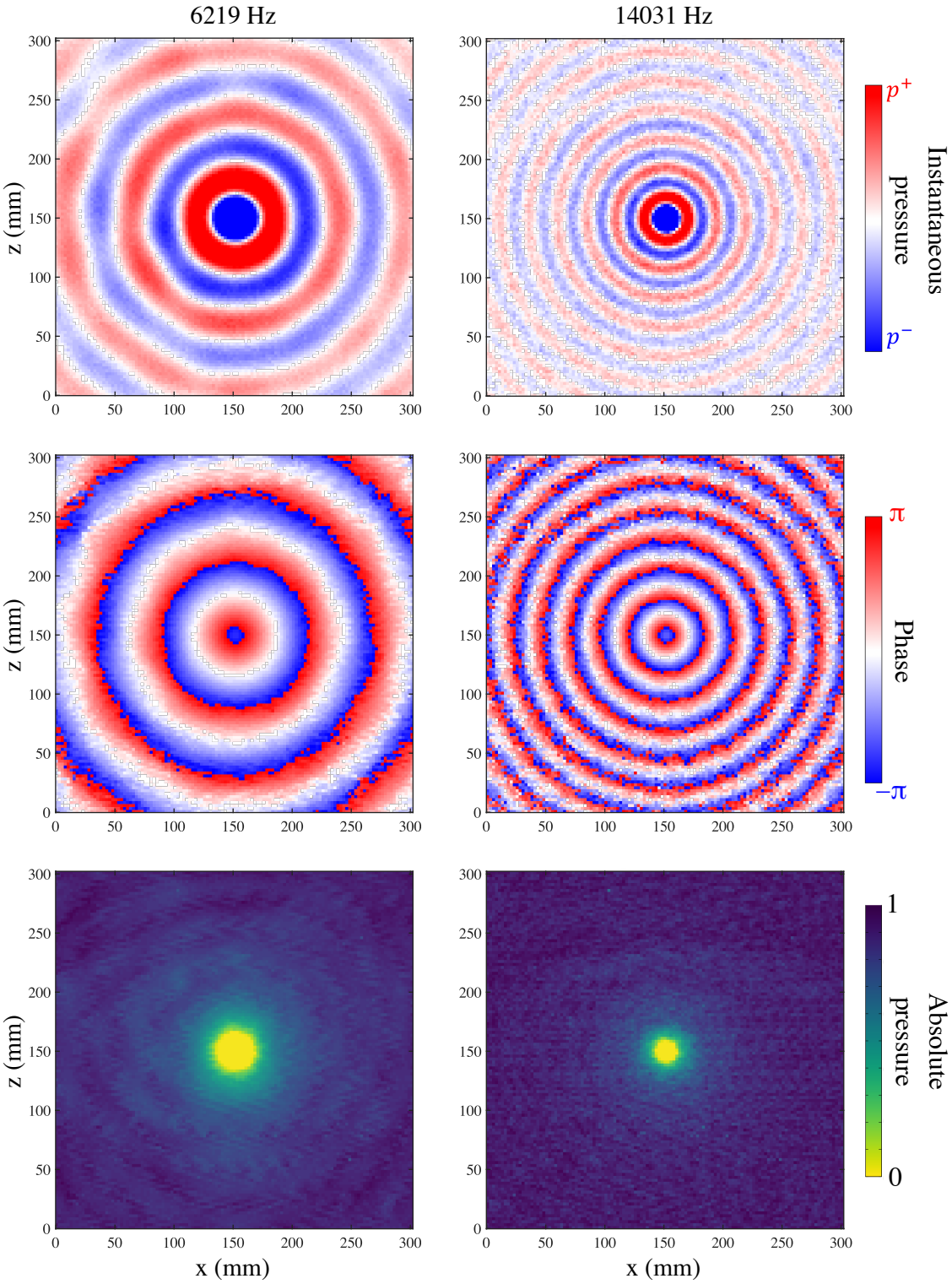

Fig. 3.9 Spatial acoustic fields for an unstructured sample excited by diffraction through a hole. The top row is the instantaneous pressure $\mathrm{Re}\big(F(\omega)\big)$, the middle row is the phase $\arg\big(F(\omega)\big)$, and the bottom row is the absolute pressure $|F(\omega)|$. Note the scales on the instantaneous and absolute pressures have been saturated due to acoustic energy density being larger directly above the speaker.

row shows the phase (θ) which is defined as the argument of $F(\omega)$. The bottom row show the absolute pressure defined as the modulus of $F(\omega)$. It is expected that the absolute pressure should decay evenly in all directions; however, this is not the case which can be seen more strongly in the 6219 Hz plot. This intensity variation come from reflections within the experimental setup such as off the frame which holds the sample into place. This is resolved by time gating the data. Time gating is the process of shortening the time of recording the individual signal pulses to remove unwanted data. One unwanted effect of shortening the time signal is that the frequency resolution will be reduced. This can be counteracted by zero-padding the data, whereby zeroes are added to the temporal data to increase the frequency resolution; however, this can create artefacts in the resulting Fourier data due to sharp changes in data where the data begins to be padded. It should be noted that zero-padding will not resolve any features below the original resolution. One method to overcome this is applying a window function to the data.

Since DFTs treat non-periodic data as periodic, it may affect how the resulting frequency data will appear. In the case of time-gated data, when repeated at each point where the data is repeated a sharp change in the data may now exist, this results is spectral leakage: where the signal is spread to higher frequencies. Some examples of window functions and their respective Fourier transforms are seen in Figure 3.10. The first is a top-hat function which always results in a sharp transient region of data. It is seen that while the mainlobe width (MLW) is small at 0.021% (MLW is defined as the width where the peak is reduced by 3 dB) the leakage factor (LF): the ratio of power in side lobes to total power is 9.35%, is high. Another factor is the ratio of the power in the mainlobe peak compared to that of the sidelobes, which is known as the relative side lobe attenuation (RSLA). In the case of the top-hat function this is low at -13.3 dB. If we now consider the middle row a Hamming window is shown. It is immediately obvious that the MLW is larger than that of the

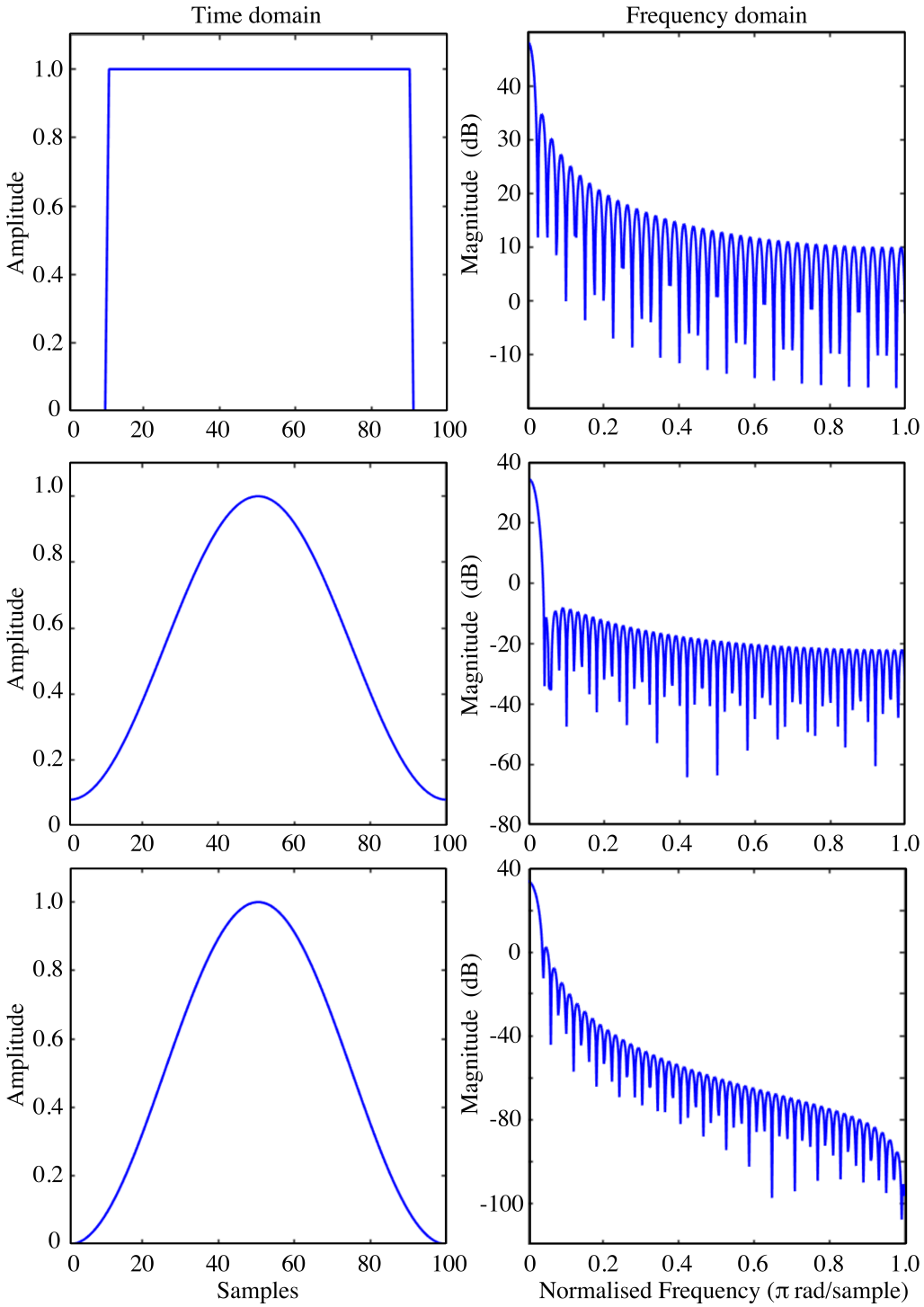

Fig. 3.10 Various window functions and their frequency spectra. Top: Top-hat function. Middle: Hamming window function. Bottom: Hanning window function. Note that the frequency has been normalised to the total number of samples.

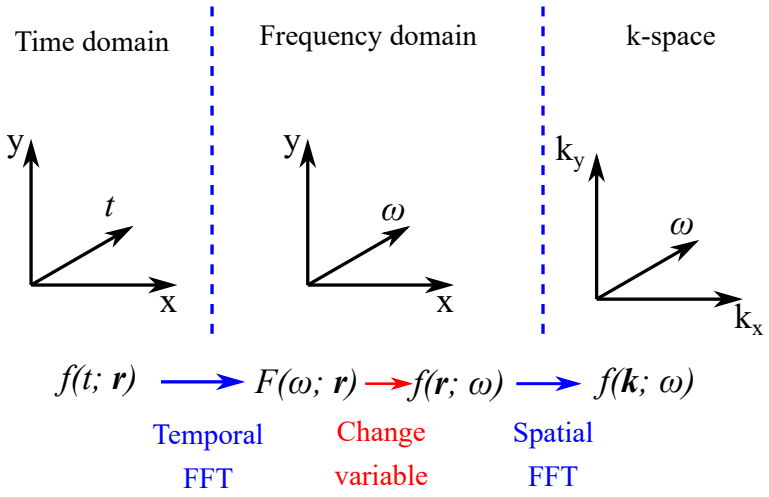

Fig. 3.11 A schematic of the Fourier analysis process. Firstly a temporal FFT is performed on the raw data at each position ($\mathbf{r}$) time domain, resulting in complex frequency domain data. The second process is a subtle change of variable from temporal to spatial, which is in practice a restructuring of the data matrix. A spatial FFT is then performed on the spatial data at a given frequency, resulting in k-space data. Cross-sections of the k-space data matrix are then taken in order to plot the dispersion diagrams.

top-hat function at 0.025%, but both LF and RSLA have been improved at 0.03% and -42.6 dB respectively. Finally, the third window function shown is a Hanning window. Here, the MLW is 0.027%, the LF is 0.05%, and the RSLA is -31.5 dB. It is seen that the use of a window function reduces the spectral leakage but at the cost of the resolution of the data being reduced. The characteristics of the mode under investigation determines which window function is used.

The next process is to perform a 2D FFT on the spatial field data which will allow for the data to be analysed in momentum space. As for the discussion of the temporal Fourier transform in the spatial Fourier transform we have similar relations between the size and resolution. The resolution in momentum space in a given direction is defined by $\Delta k_x = \frac{2\pi}{L}$ where L is the total length of the scan in a particular direction. The maximum momentum measurable is $k_{max} = \frac{\pi}{\Delta l}$ where Δl is the spatial resolution. The range of k values defined depends on whether the number of data points is even or off. For a particular direction:

$$\text{even:} \qquad -k_{\max} : \Delta k : k_{\max}$$
$$\text{odd:} \quad -k_{\max} + \tfrac{\Delta k}{2} : \Delta k : k_{\max} - \tfrac{\Delta k}{2}$$

Two slightly different spatial FFTs were used to obtain the results in this thesis: one by performing the FFT on the complex spatial data; the second by performing the FFT on $e^{(i\theta)}$. The choice between these two depends on the experiment being performed. In experiments where the ASW's signal is strong the first was used. The second was used when trying to detect much weaker signals. If we write the full complex spatial data as $R = |R|e^{(i\theta)}$, by only analysing $e^{i\theta}$ the amplitude is removed. This results in the decay of the fields over distance being removed from the Fourier data; however, this has limitations where the amplitude of the signal is required. Examples of these two different Fourier transforms are shown in Figure 3.12. The top dispersion shows the Fourier transform of the full complex data and the lower shows the Fourier transform of $e^{(i\theta)}$. In the full complex dispersion the data at higher frequencies is very weak which is directly related to a weak frequency response of the speaker at these frequencies. It is also seen that there is a periodic increase in intensity of the mode in frequency, this is equivalent to what is seen in the frequency spectrum of Figure 3.7. This is due to a standing wave between the plate and the detector holder. The resulting data can be plotted as dispersion relations or as isofrequency contours. A schematic of the whole Fourier analysis process is presented in Figure 3.11.

Isofrequency contours are seen in Figure 3.13 for two different frequencies, the data represents a slice of the dispersion relation for a given frequency. Due to the experiment being for an unstructured plate, the ring of data represents the sound line. The radius of the ring is given by the free space wavevector $k_0 = \frac{2\pi f}{v}$, where v is the speed of sound in air. This explains why as the frequency increases so does the radius of the ring. It is also seen that contrary to what is expected the intensity is not uniform around the ring, this arises from the scan area being a square. In

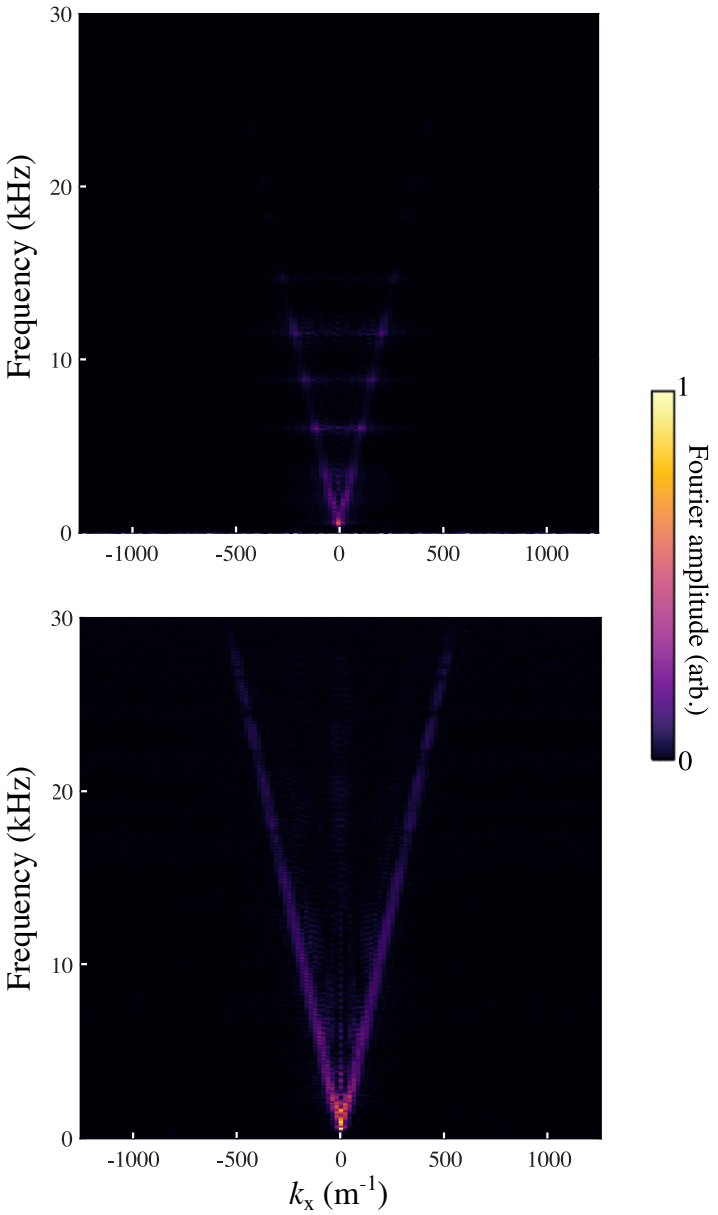

Fig. 3.12 Dispersion relations obtained from the unstructured plate along the line $k_z = 0$. Top: dispersion relation of the complex data Fourier transform. Bottom: dispersion relation of $e^{(i\theta)}$.

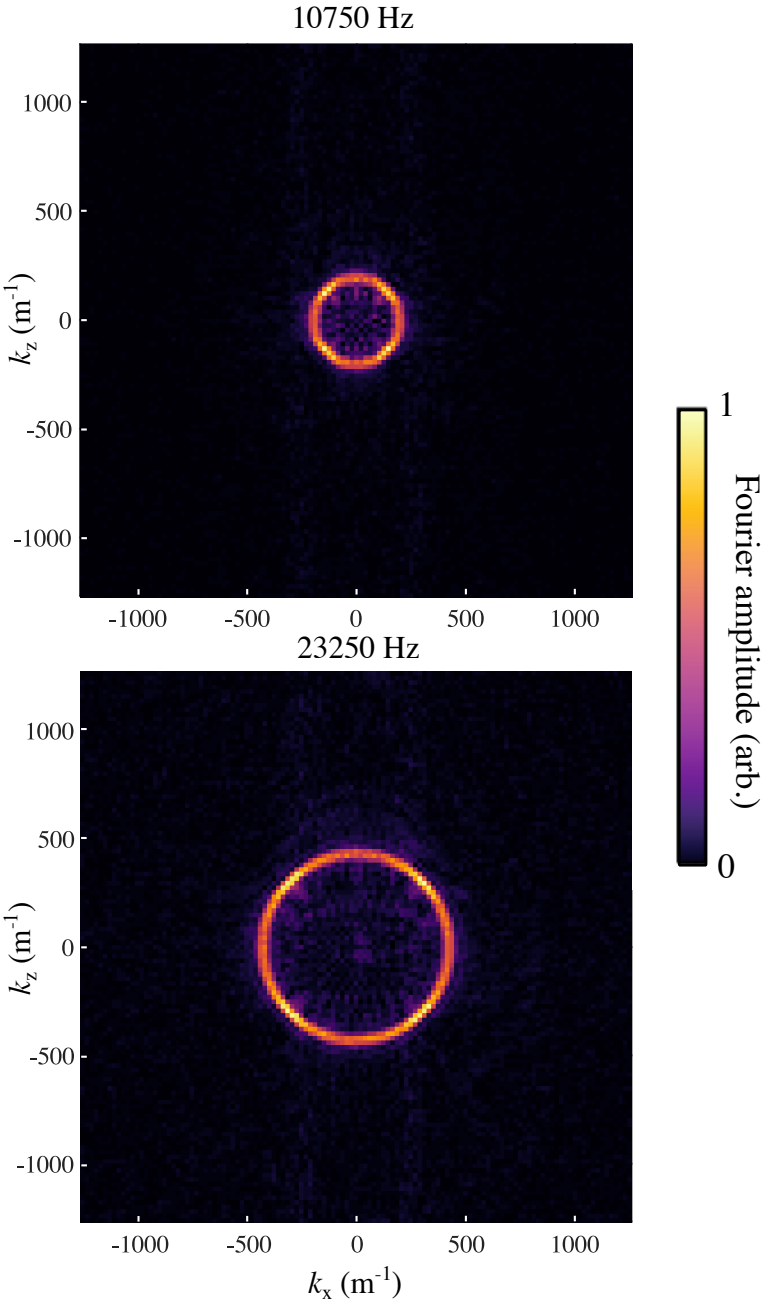

Fig. 3.13 Isofrequency contours for an unstructured plate. The ring of data present in both diagrams represents a waves propagating over the surface with a wavevector equal to that of free radiation.

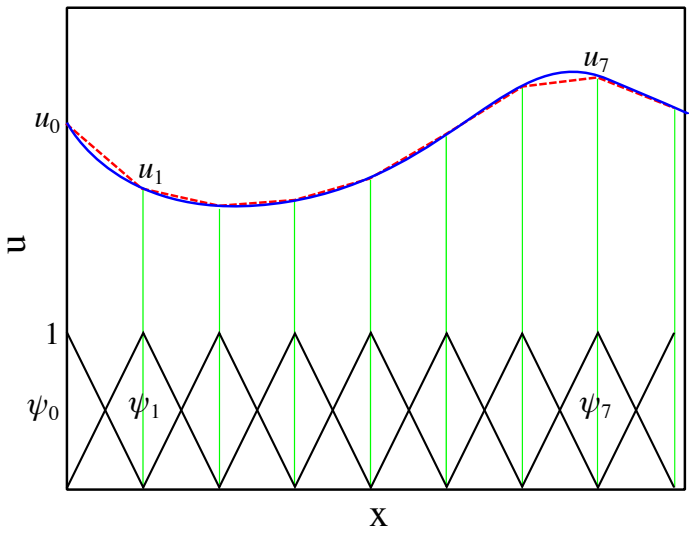

Fig. 3.14 The function u (blue line),the approximate solution (red dashed line) which is a combination of linear base functions (black line).

turn, more data being measured of waves propagating with momentums that have components in both k_x and k_z, that with pure k_x and k_z.

3.7 Finite Element Method

The Finite element method (FEM) is a useful tool when trying to solve partial differential equations (PDEs) for geometries where they cannot be analytically solved by splitting the geometry into many smaller elements. Approximate equations are constructed based on various discretisations by using numerical model equations to approximate the PDE which are then solved using numerical methods[131]. The solutions obtained from such equations are approximations of the real solutions of the PDE. If a function u is defined to be a dependent variable in a PDE, it is possible to approximate the function $u \approx u_h$ using linear combinations of basis functions ψ_i:

$$u_h = \sum_i u_i \psi_i. \tag{3.8}$$

Here, u_i are the coefficients of the functions that approximate u with u_h. An example of how the discretisation works is shown in Figure 3.14. Here the function u is shown as a blue line which is being approximated by u_h (red line) which itself consists of 8 basis functions. Depending on the solution required this discretisation does not have to be linear, a distribution of basis function may be used to resolve parts of the function where a higher resolution is required. One such finite element method program used is COMSOL Multiphysics, where the discretisations are defined by mesh elements. All mesh elements were triangular for 2D models or tetrahedral in 3D models, except in the PMLs (perfectly matched layer) where the mesh elements were swept from the boundary of the model to the end of the PML. The solutions are approximated along the boundaries of the mesh elements which are then interpolated between the boundaries.[132] The following discussion will briefly explain the construction of the models used within this thesis. In the modelling of the thesis, two conditions were used to define the maximum mesh size, the first being that there must be a minimum of 5 mesh elements per wavelength, the second being that there must be 10 mesh elements per period so that the fields may be resolved. The smaller of these two conditions was used.

3.7.1 Radiative Model

Within this thesis only periodic systems have been investigated. One use of FEM is modelling the reflectivity spectrum of periodic surfaces. When modelling periodic structures only one unit cell needs to be modelled. This is advantageous as it reduces the amount of discretisation (mesh elements) and reduces the overall solve time of the model. One such unit cell of a 2-dimensional monograting (periodic, infinitely-long cavities of a depth) is shown in Figure 3.15(a). Here, an air-filled cavity in an acoustically-rigid solid is modelled. Air was treated as an ideal gas, with the following physical parameters: density = 1.2754 kg/m^3; dynamic viscosity = 1.983 $\times$

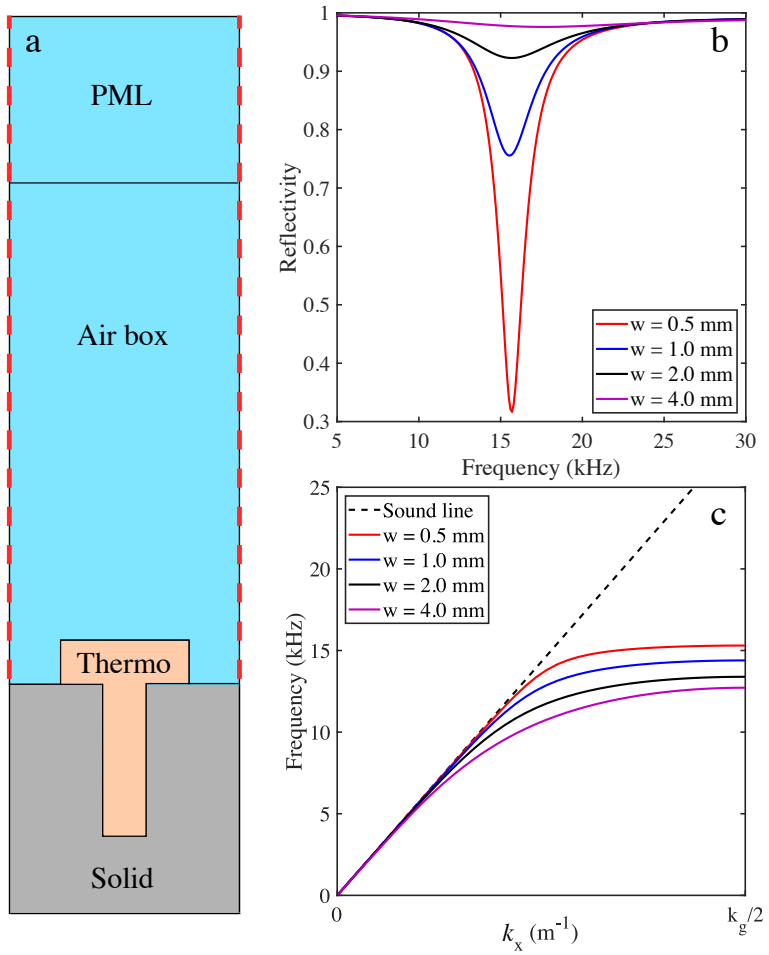

Fig. 3.15 a) Schematic of a radiative finite element model. Pressure acoustics is represented by blue, thermoviscous acoustics is represented by the orange, and grey represents solid mechanics. b) Example of reflectivity data obtained from a radiative model. c) Example of dispersion relations obtained from an eigenvalue model.

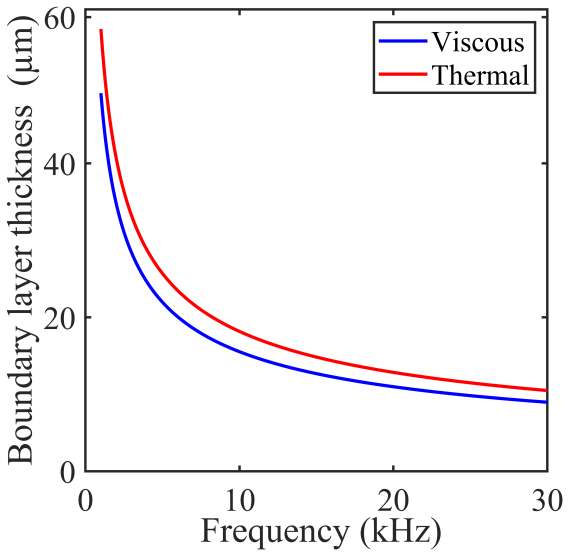

Fig. 3.16 Boundary layer thickness in air as a function of frequency. Here the frequency range is 1 kHz - 30 kHz.

10^{-5} Pa s; thermal conductivity = 0.0257 W/m K; and the specific heat capacity = C_P = 1.005 kJ/kg K. [133] Note however, when modelling a system of a water-filled cavity there is now a transfer of energy at the boundary. Therefore, the physics of the solid must be included. Water was modelled with the following physical parameters: density = 0.998 kg/m^3; dynamic viscosity = 1.002×10^{-3} Pa s; thermal conductivity = 0.598 W/m K; and the specific heat capacity = C_P = 4.182 kJ/kg K. [133] The cavity and the surrounding surface is modelled using the thermoviscous acoustics, which models variations in pressure, velocity, and temperature. This is important as the thermal and viscous boundary layers are where the losses occur, which arise from an isothermal and no-slip boundary condition, respectively. These boundary conditions are explained in detail in section 2.4. However, including thermoviscous acoustics is computationally heavy. Therefore, it is only placed in the model where needed. In this thesis, thermoviscous losses were only used in Chapter 4.

Figure 3.16 shows the thermal and viscous layer in air thicknesses as a function of frequency. A convergence plot of the reflectivity from a grating with various

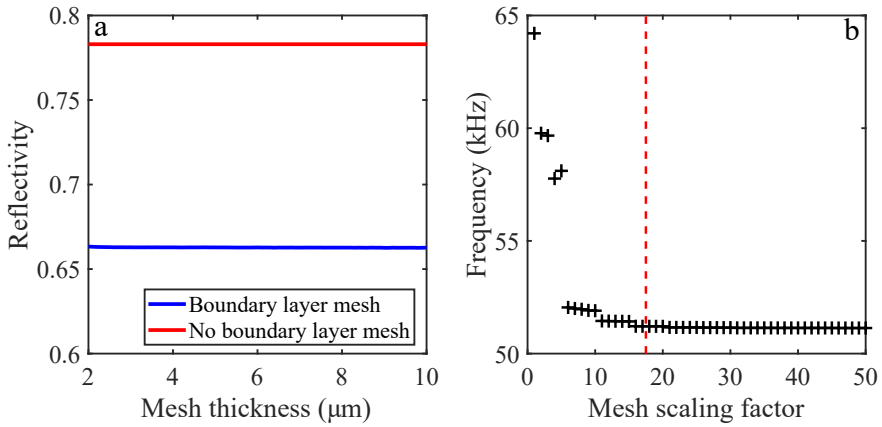

Fig. 3.17 a) Convergence plot of the reflectivity from a grating as a function of boundary layer mesh thickness (blue line). Note that 10 boundary layer mesh elements were used in all models. The reflectivity from the same grating with no boundary layer mesh included (red line). b) Convergence plot of an eigenvalue model of an unstructured elastic plate. Here, the mesh scaling factor is the factor of which the wavelength is divided by to obtain the maximum mesh size. The dashed red line represents the size of the mesh, which equals the maximum mesh size equal to the period/10.

boundary layer mesh thicknesses at 15 kHz is presented in Figure 3.17(a). A no boundary layer mesh curve has been included for comparison. For an incident wave at 15 kHz frequency, the boundary layer thicknesses are around 15 µm. In this simulation 10 layers of the boundary layer mesh at the thickness stated were used with a growth factor of 1.2 between each layer. It can be seen that the solution is converged over the range presented. It should be noted that defining a too large mesh for the structure results in the meshing failing. In comparison to the case where the boundary layer mesh was excluded, there is a significant difference in the reflectivity. In all the thermoviscous modelling in this thesis, five boundary layer mesh elements per wavelength were used.

Above the surface, pressure acoustics is modelled. This only models variations in the pressure fields and is where the background pressure field is defined. At the thermoacoustic and pressure acoustic boundary certain conditions are included

to keep the system physical. A dynamic condition at the boundary that there is continuity of total normal stress. A kinematic condition of continuity of total normal acceleration, and finally an adiabatic condition for the temperature. The background pressure field is modelled as plane waves where the angle of incidence is defined as needed. Finally, a perfectly matched layer (PML), also using the pressure acoustics module, is added to the top of the model to acts as an absorber. A PML is an artificial absorbing layer that is used to reduced the size of numerical models. [134] Any radiation which enters is attenuated and cannot be reflected back into the model. The red-dashed line on the sides of the air box and PML represents where the Floquet boundary conditions exist. This condition allows for the wavevector to be maintained at the boundaries. Therefore, there is no discontinuity at the boundary of two neighbouring unit cells, and an infinite system is modelled. The mesh on both of these boundaries must be identical so that the solutions are solved in the same place on each boundary. In such models, a frequency and angle range are chosen, and the model computes the results using parametric sweeps. The scattered pressure field intensity is then calculated and normalised to the incident pressure field intensity for each frequency and angle of incidence to give the reflectivity, allowing us to plot a numerical radiative dispersion plot. Figure 3.15(b) shows the normal incidence reflectivity obtained for various parameters, these results will be discussed later in Chapter 4.

3.7.2 Eigenvalue Model

Eigenvalue models allow the calculation of the eigenvalues of particular surface. These models are very similar to the previously discussed radiative models except that due to the fact that the surface characteristics are being analysed the thermoviscous acoustics may be removed and replaced with pressure acoustics. Due to thermoviscous acoustics being computationally expensive and that it is not required to calculate

the eigenvalues, it is omitted. Through the inclusion of Floquet periodic boundaries where wavevectors have been defined for all directions, it is possible to find particular eigenvalues for a given wavevector and numerically find the dispersion relation, Figure 3.15(c) shows dispersions which have been obtained by the eigenvalue solver, to be discussed in Chapter 4. In this figure, the in-plane wavevector (k_x) has been swept to the first Brillouin zone. For each individual wavevector eigenvalue of the system is found, and the frequency at which it occurs is stored. In post-processing, the eigenfrequencies can be plotted against the in-plane wavevector. A convergence plot for a typical eigenvalue model can is presented in Figure 3.17(b).

The interaction between pressure acoustics and solid mechanics module is only used in eigenvalue models of Chapter 6. The solid mechanics module models the stress, strain, and displacement of the structure. In order to couple with the pressure acoustics, two effects are taken into account. The first being the fluid load on the structure, and the second being the effects of the structural acceleration on the fluid. It is from these conditions that the dispersion of the Scholte waves discussed in Section 2.7 may be solved. These effects are implemented using the Acoustic-Structure Multiphysics model.

3.8 Conclusions

The experimental setup and methods for obtain both radiative an non-radiative have been discussed. After this the data analysis techniques used on the experimental data such as time gating and the application of window functions have been described. A numerical method known as finite element method has been introduced. FEM modelling will be used in all the following results chapters to explore potential metasurfaces and to validate experimental results.

The first results chapter will explore the phenomenon of phase resonance on compound grating (more than one groove per unit cell). Both of the radiative and non-radiative experimental techniques introduced in this chapter will be used, as well as FEM models.

Chapter 4

The Acoustic Phase Resonances and Surface Waves Supported by Compound Rigid Gratings

4.1 Introduction

In the previous chapters the background physics and methods have been discussed. Within this chapter, the dispersion is fully explored, through finite element method (FEM) modelling and experimentally using the methods discussed previously, of the acoustic surface modes supported by a compound grating (multiple grooves per unit cell) with three grooves per unit cell of two different widths and all of the same depth.

Throughout the chapter band diagrams of simple gratings are fully investigated through Finite Element Method (FEM) modelling. Expanding on this, more complicated, multiple grooves per unit cell compound gratings are investigated. The addition of the extra degrees of freedom allow so-called phase resonances to be sup-

ported. The effect of changing the parameters of the grooves on the phase resonances was also explored. This was done for both two and three grooves per unit cell.

4.2 Background

Recently, a number of works [135–137] have shown that enhanced acoustic transmission of sound through sub-wavelength perforations (open-ended holes or grooves) can be achieved. These studies are somewhat analogous to the extraordinary optical transmission found in the electromagnetic domain explained by coupled surface wave and evanescent diffraction phenomena.[138] Work by Skigin and coworkers [136, 139] has shown that transmission of electromagnetic radiation through a so-called 'compound grating', comprising of more than one groove per unit cell, is significantly different to that for a simple groove grating. The additional complexity of the unit cell typically broadens the existing resonant mode (due to increased radiative and non-radiative losses), while a new, narrow (i.e., high-Q-factor) 'phase' resonant mode is observed. These phase resonances are characterised by the resonant acoustic fields in adjacent grooves varying in phase by odd multiples of π with strong field enhancement on resonance. [139]

Analogous behaviour in the acoustic domain was predicted by Wang et al.[137] and then experimentally verified by Ward et al.[25], who demonstrated phase resonances in compound-groove-gratings with different structure factors. Narrow resonant dips within the band of the broad transmission maxima were observed and attributed to evanescent diffractive coupling between fields in adjacent grooves. More recently, Zhang et al. [140] investigated the acoustic transmission for compound gratings comprising of different square and triangular shaped elements; they reported some degree of control of the resonance frequencies.

In addition to transmission-type gratings, similar phase-resonance effects in reflec-

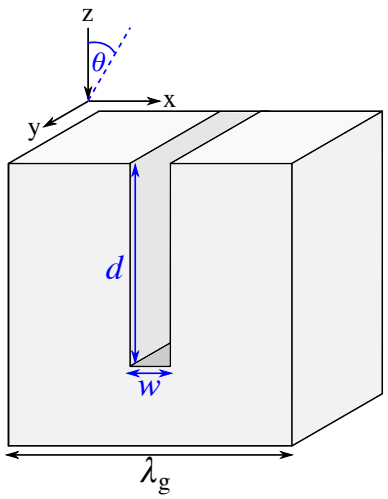

Fig. 4.1 Schematic of a simple grating unit cell of width w, depth d, and a periodicity in $\hat{\mathrm{x}}$ of λ_{g}, the grooves are infinitely long in y. θ is the polar angle of incidence.

tion compound gratings have also been studied in the electromagnetic domain.[141–143] In a study by Fantino et al.[141], several different metallic compound gratings were numerically investigated. For a transverse-magnetic-polarised incident beam, phase resonances were observed as maxima in the reflectivity spectrum of the surface, with strongly enhanced fields within the grooves. A similar phenomenon for reflection gratings has yet to be recorded in the acoustic domain.

4.3 Simple Gratings

Within this section, the reflectivity and surface modes of simple gratings will be investigated. The unit cell of a simple grating is seen in Figure 4.1, here, a single air-filled groove of depth d, width w, and infinitely long in the y - direction is shown within an acoustically-rigid material. The properties of the modes in both the radiative and non-radiative regimes can be altered by changing the parameters of the grooves, w, d and the periodicity, λ_{g}.

Each groove of the simple grating supports a quarter-wavelength ($\lambda/4$) resonance with frequencies given by

$$f_n = \frac{(2n+1)v}{4(d+\Delta L)} \tag{4.1}$$

where the end-correction (ΔL) is approximately $8w/3\pi$[102], d is the groove depth, v is the speed of sound in air, and n is a positive integer. This resonance condition comes from the boundary condition that the displacement field of the particles must be equal to zero at the bottom of the groove, and therefore, an antinode in the pressure field exists. If we consider the opening of the groove, ignoring end effects, the displacement field of the particles is maximum, and there is a node in the pressure field. However, when end-effects are considered this node is located slightly above the surface.

In the radiative regime, these resonances appear in the reflectivity spectrum as minima: as the frequency approaches that of the resonance the intensity of the pressure fields within the groove increase. When the pressure field is increased within the groove so are the losses from the thermal and viscous boundary layers. The viscous boundary layer exists at a solid/air interface where a gradient in the particle velocity is present. For further discussion of the boundary layers please refer to Section 2.4.

The effect of changing the groove depth is shown in Figure 4.2, here, $w = 1$ mm and $\lambda_g = 6$ mm. Figure 4.2(a) displays the normal incidence reflectivity for depths $d = 2.5$, 5.0 and 10.0 mm. As expected, the effect of increasing the groove depth reduces the resonance frequency. Another feature of varying the depth is that as it is increased the width of the respective reflectivity minima decrease to values: 0.79, 0.75, 0.69 respectively. As the grooves increase in depth, the fields become less over-coupled hence increasing the Q-factor with values of 4.37($\pm$0.24), 4.46($\pm$0.13) and 4.85($\pm$0.008). Here, the uncertainties arise from the frequency resolution. [144] This increase in Q-factor is also evident within the non-radiative regime as seen in

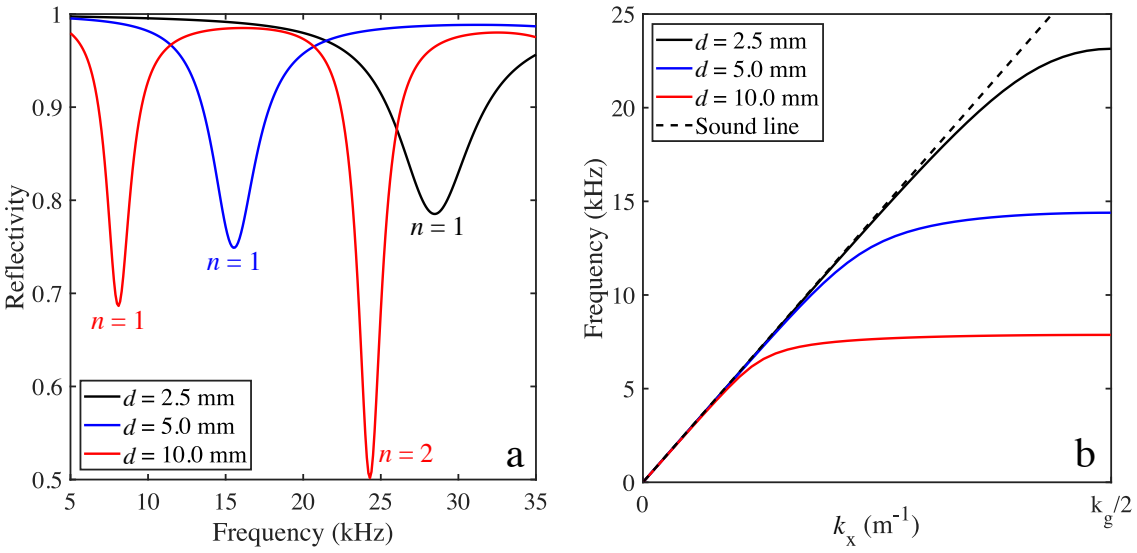

Fig. 4.2 a) Normal incidence reflectivity of simple gratings with $w = 1$ mm, $\lambda_g = 6$ mm and various depths. n is the mode number. b) Non-radiative dispersion of the fundamental surface waves supported by simple gratings of various depths. Here, $k_g/2$ is the first Brillouin-zone boundary. All data has been obtained through FEM models.

Figure 4.2(b), which shows the dispersion of the fundamental mode of surface waves supported by such simple gratings. As the depth increases the mode disperses over a much narrower frequency range. Further information on the Q-factor can be found in Section 2.4.

Another way to change the properties of the modes supported is by varying the width of the groove. The normal incidence reflectivity is shown in Figure 4.3(a) for different groove widths. If the $w = 0.5$ mm and $w = 4$ mm spectra are compared; it is seen that in the wider case where the groove is occupying 2/3 of the unit cell the mode has a Q-factor of 0.996($\pm$0.008) and barely any loss with a minimum reflectivity of 0.98. This is due to being highly over-coupled resulting in the pressure fields within the grooves being weak. In comparison, the Q-factor for the $w = 0.5$ mm is larger at 14.0($\pm$1.3), and its higher losses are present with a minimum in the reflectively of 0.32. The effect of w on the reflectively minimum is shown in Figure 4.4. A minimum value occurs when $w = 0.25$ mm, this is as the system

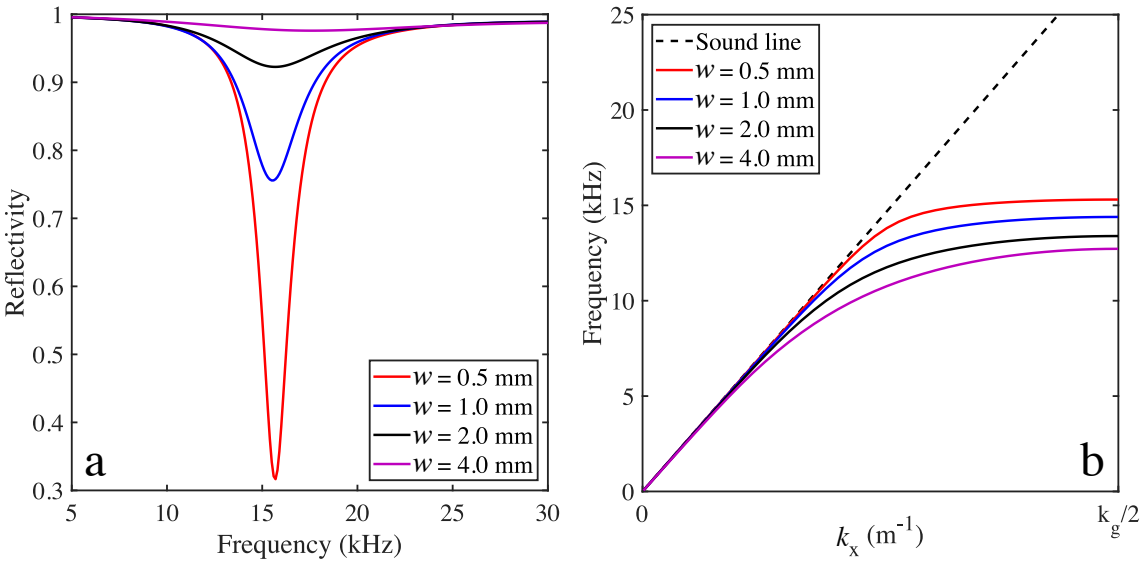

Fig. 4.3 a) Normal incidence reflectivity of simple gratings with $d = 5$ mm, $\lambda_g = 6$ mm and various groove widths. b) non-radiative dispersion of the fundamental surface waves supported by simple gratings of various groove widths. Here, $k_g/2$ is the first Brillouin-zone boundary. All data has been obtained through FEM models.

becomes critically-coupled: where the internal losses of the resonator are equal to the radiative losses resulting in perfect absorption. At values of w below this, the system is under-coupled. In the non-radiative regime as w is increased the modes disperse over a larger frequency range as they couple more strongly to free radiation as seen in the previous discussion with the fundamental mode of $d = 10$ mm. The frequency at which the modes reach the Brillouin zone boundary decreases with w as expected. As the width increases, so does the end-correction resulting in the groove appearing longer, which decreases the resonant frequency.

In order to explore the reflectivity from a resonant surface, the following equation taking the usual form is used:

$$R(\omega) = \frac{\omega_0^2 - \omega^2 - i\omega(\zeta_0 - \eta_0/\cos\theta)}{\omega_0^2 - \omega^2 - i\omega(\zeta_0 + \eta_0/\cos\theta)}, \tag{4.2}$$

where ω is the angular frequency, ω_0 is the resonant frequency, ζ_0 is the dissipation and η_0 is the admittance of the surface. Figure 4.5(a) shows the normal incidence

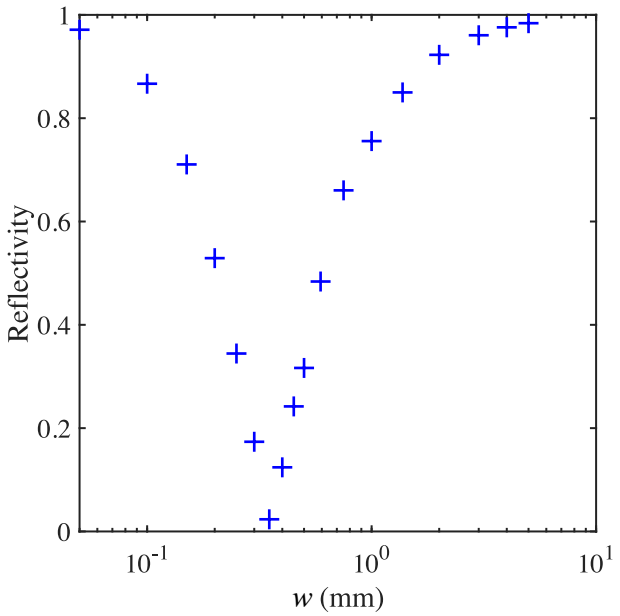

Fig. 4.4 Relation between w and the reflectivity for a simple grating of $d = 5$ mm and $\lambda_g = 6$ mm. At small w the system in under-coupled, the surface becomes critically-coupled as w approaches 0.25 mm. At larger w the mode is over-coupled. All data has been obtained through FEM models.

reflectivity spectra obtained from $|R(\omega)|$. Three distinct cases are shown for under-coupled, $\eta_0 > \zeta_0$ which is satisfied when $\eta_0 = \omega_0/200$; critically coupled $\eta_0 = \zeta_0$, and finally over-coupled, $\eta_0 < \zeta_0$ satisfied by $\eta_0 = \omega_0/2$. Here, ω_0 takes the value 30000π, and $\zeta_0 = 2000$. All three cases show the expected behaviour as previously discussed. One may also look at the phase on reflection. If the phase of reflected waves at a given distance from an acoustic mirror is considered, as the frequency is increased the phase of the reflected wave would decrease at a constant rate as the wavelengths shorten.

However, as soon as any structure is present on the reflecting surface, additional phase changes occur as the frequency moves across the resonance of the structure. It is expected that as ω approaches ω_0 a phase shift of π occurs. This results in a total phase shift of 2π over the full frequency spectrum for each resonant mode. The phase shift for the critically coupled case occurs over a very narrow frequency band. The over-coupled system is much different as the phase change now occurs

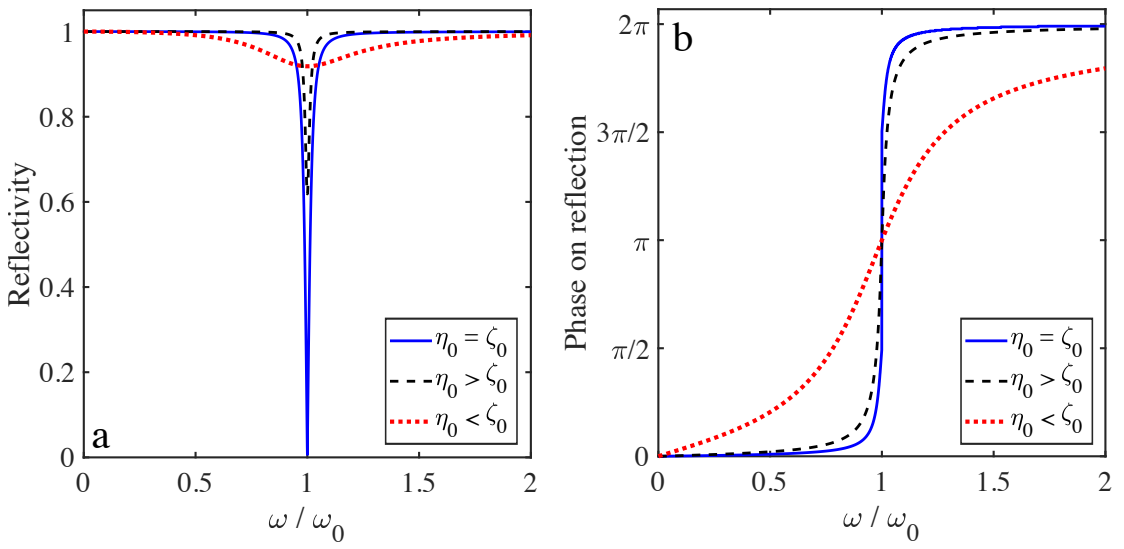

Fig. 4.5 a) Normal incidence reflectivity spectrum calculated using equation 4.2 for critically (solid, blue line), under (dashed, black line) and over-coupled (dotted, red line) surfaces. b) Normal incidence phase on reflection for critically (solid, blue line), under (dashed, black line) and over-coupled (dotted, red line) surfaces.

over a much broader frequency band, and an important feature is that the phase change is less than 2π over the frequency range shown, this occurs as the internal losses (the dissipation) of the surface are less than that of the external losses (the admittance). However, due to the mode being broad in frequency a phase change of 2π will be accumulated as ω approaches infinity. A full FEM modelled dispersion of a simple grating with $w = 1$ mm, $d = 5$ mm and $\lambda_g = 6$ mm is shown in Figure 4.6. In all modelling presented in this chapter, the frequency resolution is 100 Hz, and an angle resolution of 2∘. The non-radiative dispersion was calculated at a resolution of $k_g/40$. The colour data represents the radiative regime for angles of incidence up to grazing; the reflectivity minimum weakens at higher angles of incidences due to weaker coupling to free radiation. The blue line represents the acoustic surface mode supported by the surface, due to there only being one resonator per unit cell, only one mode exists per groove resonance.

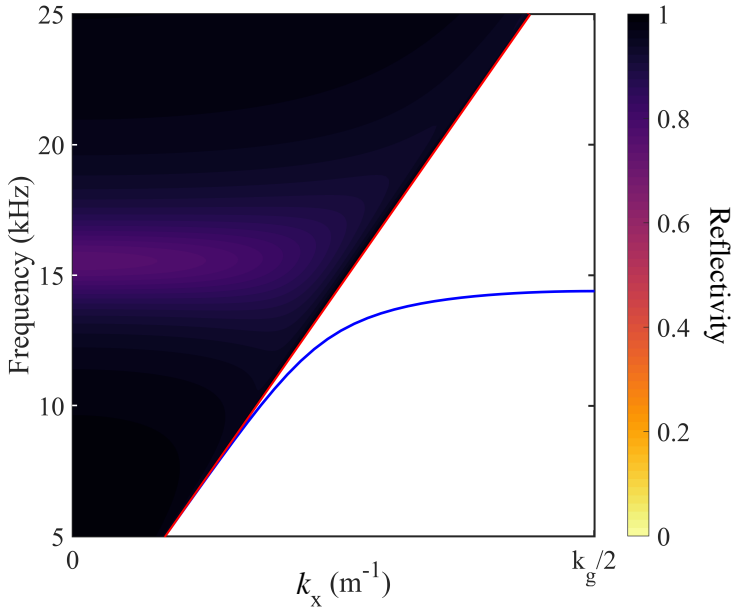

Fig. 4.6 Full FEM mode dispersion for a simple grating of $w = 1$ mm, $d = 5$ mm and $\lambda_g = 6$ mm. The colour plot represents the radiative regime ($k_0 > k_x$). The blue line represents the dispersion of the non-radiative surface mode ($k_x > k_0$). The red line is the sound line ($k_x = k_0$).

4.4 Two-resonator Compound Grating

More resonators per unit cell create additional degrees of freedom. With higher degrees of freedom more than one resonance will be found at every wavevector. One such unit cell is shown in Figure 4.7 which has two identical grooves with a separation of l. However, the grooves are unevenly separated such that $l \neq \lambda_g - l$. If they were evenly spaces, the periodicity would reduce to a simple grating. If a unit cell is considered where $w_1 = w_2 = 1$ mm, $d_1 = d_2 = 5$ mm, $l = 3$ mm and $\lambda_g = 10$ mm, then the resonance condition for both the grooves is the same. Therefore, in isolation they have the same resonance frequency. The full dispersion for this structure has been modelled in Figure 4.8(a), it is clear that in the non-radiative regime, two coupled modes now exist for the fundamental resonance of the grooves. Figure 4.8ii shows the phase of the lower frequency mode at the first Brillouin-zone boundary. It is seen that acoustic fields in both of the grooves are in phase with each other.

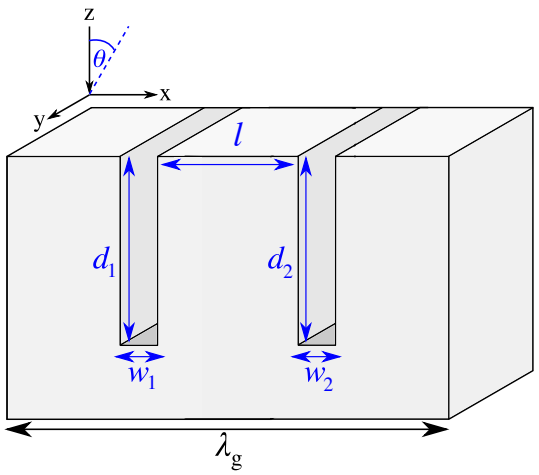

Fig. 4.7 Schematic of a two resonator compound grating unit cell. Here, two grooves of widths: w_1 and w_2, and depths: d_1 and d_2; separated by l, within a pitch of λ_g.

However, when the higher frequency mode is considered, now there appears a phase difference of π between the acoustic fields in the grooves. These two standing wave solutions are of slightly different energies, which results in a band-gap existing at the first Brillouin-zone boundary. This newly excited, high-frequency mode is a phase resonance mode. Within the radiative regime, there are also two modes: one broad mode at 16 kHz at normal incidence; and a second, much narrower mode which lowers in frequency as the angle of incidence is increased. This mode originates from the higher frequency radiative mode which has been folded back into the first Brillouin zone, therefore, it does not interact with the sound line. This mode is also not excitable at normal incidence due to the configurations of the fields; this is a characteristic feature of a true phase resonance mode. The first mode is the non-phase resonance mode, while the second is the phase resonance mode.

One may change various parameters of the system to increase the separation in the frequency of the modes, or to increase the losses so that the system is critically coupled. Consider a system where the width of one of the grooves has been doubled, $w_1 = 2$ mm and $w_2 = 1$ mm, and the depths of the grooves have been kept the same. Now the resonant frequency of each groove is slightly different as the end-correction

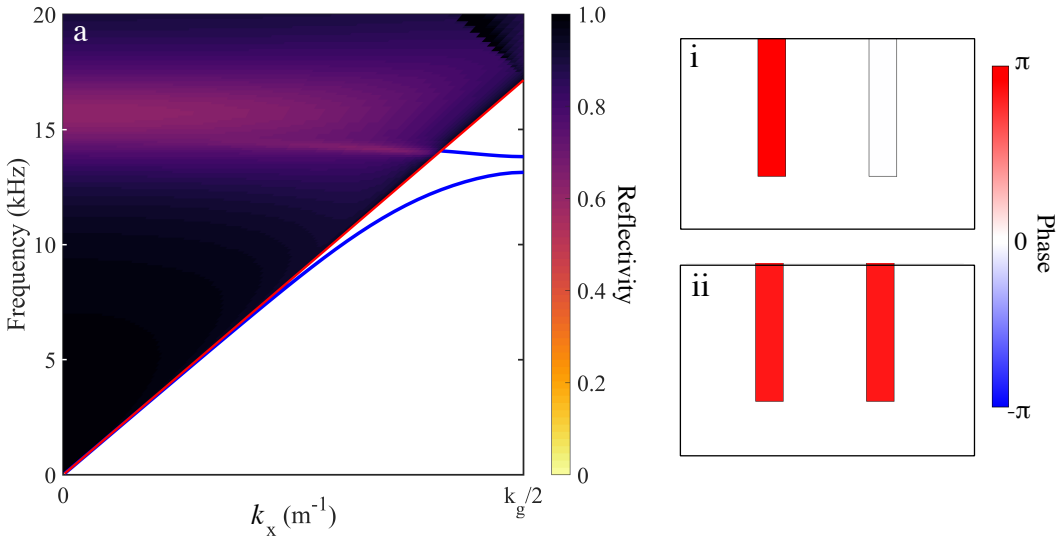

Fig. 4.8 a) Full FEM dispersion for a two-resonator compound grating with parameters $w_1 = w_2 = 1$ mm, $d_1 = d_2 = 5$ mm, $l = 3$ mm and $\lambda_g = 10$ mm. i) Phase within the grooves of the higher frequency mode at $k_g/2$. ii) Phase within the grooves of the lower frequency mode at $k_g/2$. The blue lines represent the dispersion of ASWs. The red line represents the sound line. The phase here is arbitrarily chosen to highlight the phase difference between the cavities.

increases with groove width, as discussed in Section 2.3. The full dispersion is shown in Figure 4.9. In the non-radiative regime, the effect of the different groove widths is that a larger band-gap exists at the first Brillouin-zone boundary, compared to the equal-width system. This increased band-gap width is expected as there is now a more significant difference in the energies of the two standing wave solutions at $k_x = k_g/2$. In the radiative dispersion, it is immediately clear that the narrow, low-frequency mode is much deeper in reflectivity. The minimum reflectivity is 0.19 as compared with 0.70 for the case of two grooves of the same width. This reduction in reflectivity signifies that this system is much closer to the critical coupling condition while the same width case is under-coupled. It is important to remember that any mode which exists in the radiative part of the dispersion diagram inherently radiates energy away from the surface due to k_z being real. These losses associated with these radiative modes arise purely from the thermoviscous losses. An example of this is

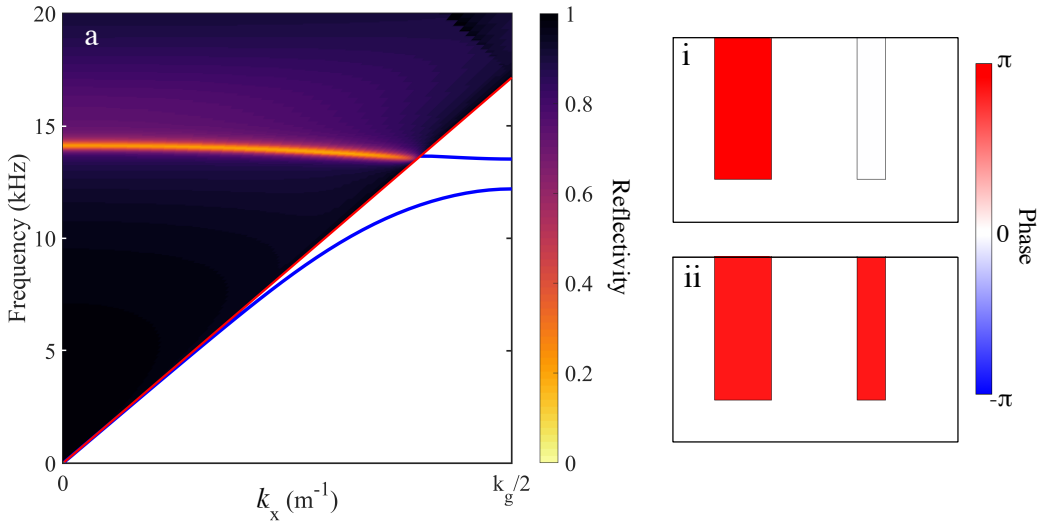

Fig. 4.9 a) Full dispersion for a two-resonator compound grating with parameters $w_1 = 2$ mm, $w_2 = 1$ mm, $d_1 = d_2 = 5$ mm, $l = 3$ mm and $\lambda_g = 10$ mm. i) Phase within the grooves of the higher frequency mode at $k_g/2$. ii) Phase within the grooves of the lower frequency mode at $k_g/2$. The blue lines represent the dispersion of ASWs. The red line represents the sound line. All results are from FEM modelling. The phase here is arbitrarily chosen to highlight the phase difference between the cavities.

shown in Section 2.4 in Figure 2.4 where the normal incidence reflectivity from a simple grating was shown. By completely removing the thermoviscous effects from the model, a reflectivity of unity was obtained. A feature of this mode is that the reflectivity remains almost constant as θ is varied until just before reaching the sound line. It is expected that the reflectively will increase to unity as the mode approaches the sound line, as the exciting radiation becomes grazing in nature. The higher frequency, over-coupled, radiative mode is also seen and is similar in characteristic to the equivalent mode of the equal-width case.

Another way in which one may change the unit cell is to vary the groove depth. The dependence on depth is more significant than the dependence on width. Consider the case where $d_1 = 5.5$ mm and $d_2 = 5$ mm, defining a new variable, p, as d_1/d_2. For this structure $p = 1.1$ and $w_1 = w_2 = 1$ mm. The dispersion diagram of the $p = 1.1$ system is shown in Figure 4.10(a). The radiative dispersion is similar

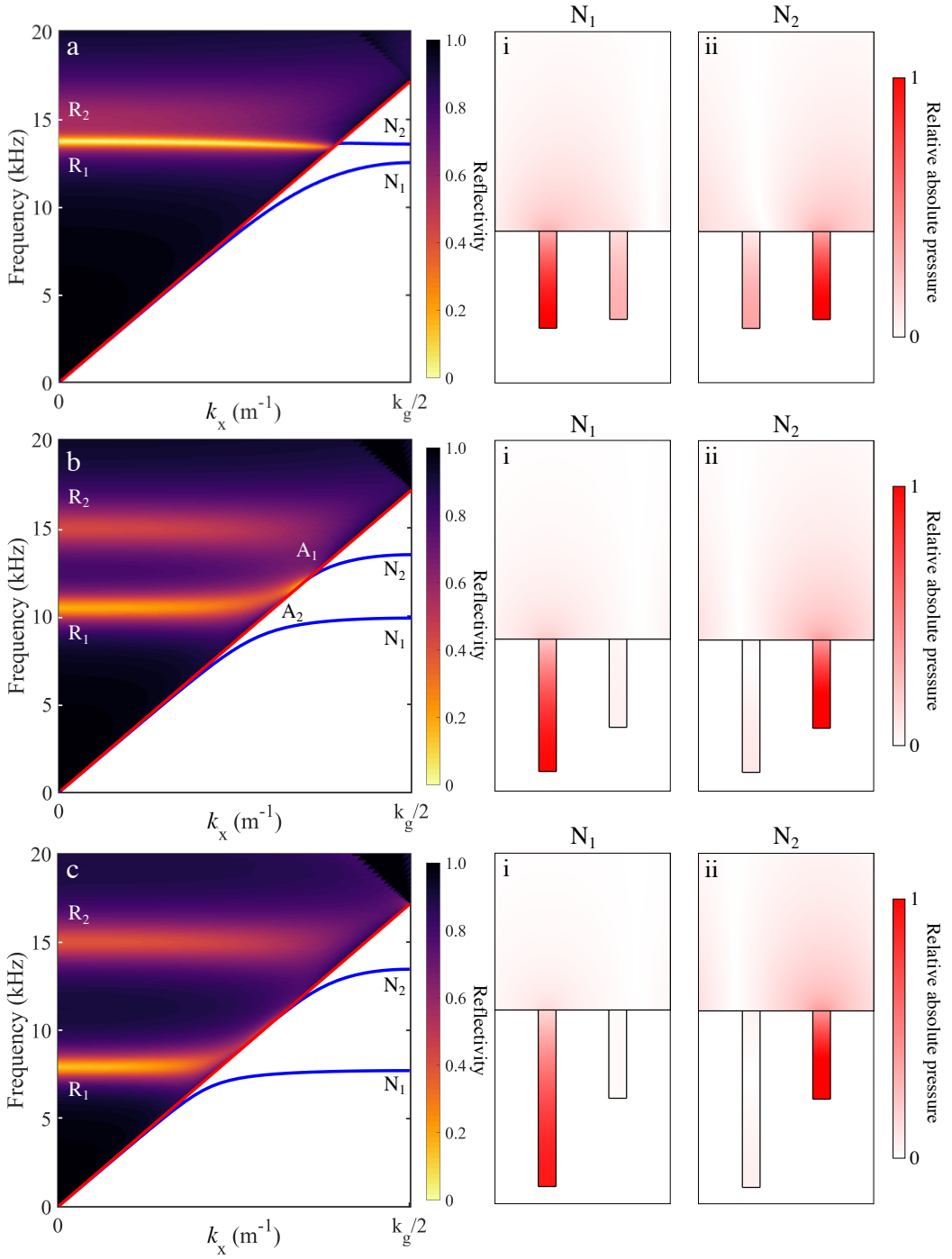

Fig. 4.10 a) Full dispersion for a two-resonator compound grating with $d_1 = 5.5$ mm, $d_2 = 5$ mm. b) Full dispersion for a two-resonator compound grating with $d_1 = 7.5$ mm, $d_2 = 5$ mm. c) Full dispersion for a two-resonator compound grating with $d_1 = 10$ mm, $d_2 = 5$ mm. i) Relative absolute pressure field within the grooves of N_1 at $k_g/2$. ii) Relative absolute pressure field within the grooves of N_2 at $k_g/2$. The blue lines represent the dispersion of ASWs. The red line represents the sound line. All results are from FEM modelling.

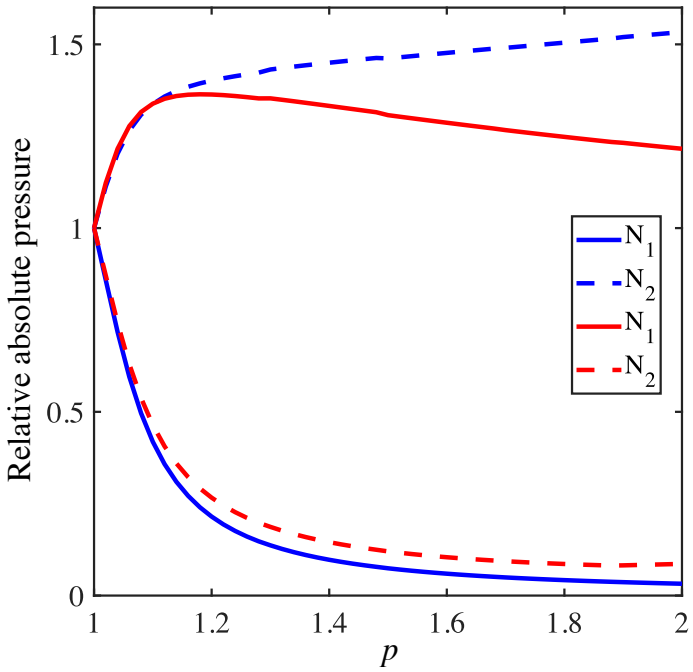

Fig. 4.11 FEM model of relative absolute pressure (p_r) field within the grooves at $k_g/2$ as a function of p. The blue lines represent p_r fields within the groove whose depth remains constant. The red line represents p_r for the groove of varying depth. The solid line represent p_r for the N_1 mode, and the dashed line represent N_2 mode.

to the system shown in Figure 4.9. The non-radiative regime is also similar; a band gap still exists at the first-Brillouin zone boundary due to the difference in energies of the standing waves of modes N_1 and N_2. When the difference in depths is increased, these two modes slowly begin to stop acting as a pair and begin to act as independent resonances. This is shown in Figure 4.10(b) for the case where $p = 1.5$ and $w_1 = w_2 = 1$ mm. The flat, broad mode labelled R_2 at 15 kHz in the radiative region remains, which is related to the resonance frequency of the $d_2 = 5$ mm groove; however, the narrow, phase resonance mode characteristic has changed. Now R_1 is a flat, broad mode relating to the resonance of the $d_1 = 7.5$ mm groove.

One additional feature is that the mode labelled N_2 now anti-crosses with R_2 at the point labelled A_1. N_2 crosses into the radiative regime becoming R_1 and anti-crosses with N_1. This anti-crossing occurs in the region labelled A_2. This anti-crossing provides evidence that N_1 and N_2 are acting as separate resonator

modes. One may notice that as p increases, R_1 moves further out of the wings of the resonance R_2.

Further evidence for this is found by considering the absolute pressure field within the grooves at $k_g/2$. In the case of equal groove depths, for N_1 and N_2 there is equal intensity within each groove. From now on, the relative absolute pressure will be considered in each groove, $P_r = P_g/P_{equal}$, where P_g is the absolute pressure in one of the grooves, and P_{equal} is the pressure in the grooves for the equal depth system. Considering the surfaces shown in Figure 4.10, it is seen that as p is increased the difference in the absolute pressure between the two grooves increases. For the surface in 4.10(c), considering the fields of the N_1 mode the majority of the absolute pressure is located within the $d = 10$ mm groove. However, for the N_2 mode, the majority of the absolute pressure is located in the $d = 5$ mm groove.

The relative absolute pressure within each groove was measured as a function of p. The results as presented in Figure 4.11. Here, the blue line represents the cavity whose depth remains constant (C_1), and the red lines represent the cavity of varying depth (C_2). The solid line represents the data for the N_1 mode, while the dashed line represents the data for the N_2 mode. Firstly considering the N_1 data, it is seen that as p increase P_r decreases in C_2 and increases in C_1. Interestingly, P_r in C_2 has a maximum value around $p = 1.12$ and then gradually decreases at a constant gradient over the p range presented. This will be discussed in further detail later. The data for the N_2 mode shows a similar behaviour to the N_1 mode; however, as p increases P_r now increases in C_2 and decreases in C_1. From this, we can see that as p increases, the acoustic energy which started evenly distributed between the two cavities, becomes more confined to one of the cavities (depending on the mode). This further provides evidence that as p increases, the cavities are acting as isolated resonators within the unit cell as the coupling between the cavities decreases.

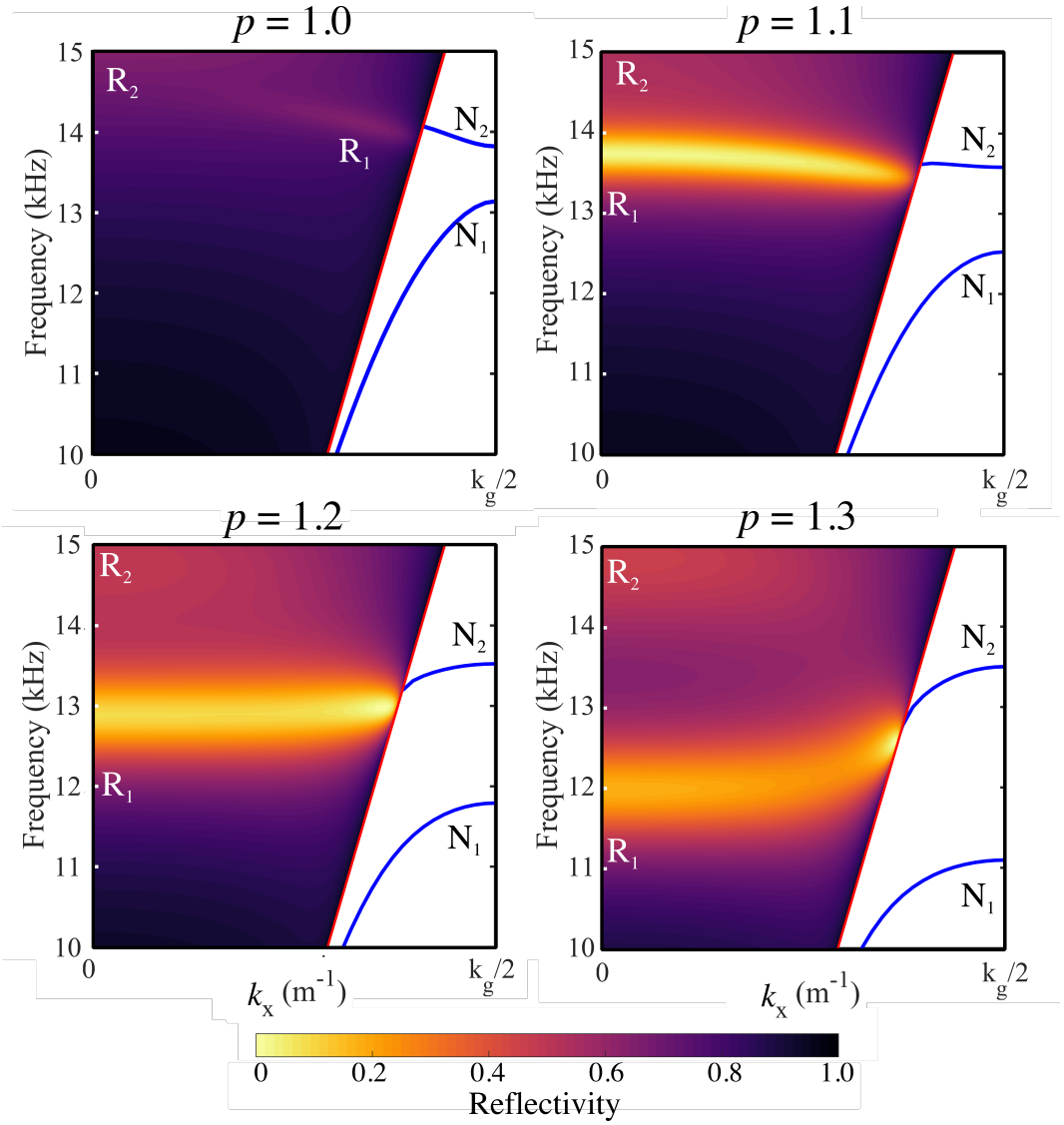

Fig. 4.12 Full dispersion for a two-resonator compound gratings with $p = 1.0$, 1.1, 1.2 and 1.3. The blue lines represent the dispersion of ASWs. The red line represents the sound line. All results are from FEM modelling.

To explore more this apparent isolation of the cavity modes surfaces with smaller p are considered. Figure 4.12 shows the band diagrams for $p = 1$, 1.1, 1.2, 1.3. It can be seen that as p is increased R_1 lowers in frequency and also broadens. The intensity of the mode also changes as p is increased. For the $p = 1.0$ case this mode is not excitable at normal incidence, but as p is increased the mode becomes excitable at all angles of incidences. The weakening intensity and broadening of the mode are indicative of the mode becoming over-coupled. Within the non-radiative regime, the change in dispersion as p is increased is more subtle that in the radiative regime. As p is increased, the gradient of the upper mode becomes less negative until it is almost flat in the $p = 1.1$ case. This gradient changes sign in the $p = 1.2$ case.

For a system where the modes are acting independently ($p > 1.2$), the surface wave dispersion for both the modes begins on the sound line. As k_x is increased, the modes disperse until the first Brillouin zone boundary where standing wave resonances across the unit cell occur. In Figure 4.11, the fields above the surface can be seen to only exist above one of the grooves for each resonance, with the other groove not influencing the form of the surface wave above the surface. If we now consider a system where the grooves are coupled, at $k_g/2$, both grooves now influence the fields above the surface. This is in contrast to only one for the independent systems. The surface waves for the independent system physically act like surface waves above a monograting of the relevant groove depth; this is not the case for the coupled system. It is shown for the coupled system that one of the modes is close to critical coupling (high absorption due to losses occurring in both grooves). In the independent system, due to only one groove being strongly excited per resonance, lower absorption occurs.

Using a similar analysis to that of the simple gratings the phase on reflection is investigated for 2-resonator compound gratings. Figure 4.13(a) shows the normal-incidence phase on reflection for a two-unit compound grating with various p values

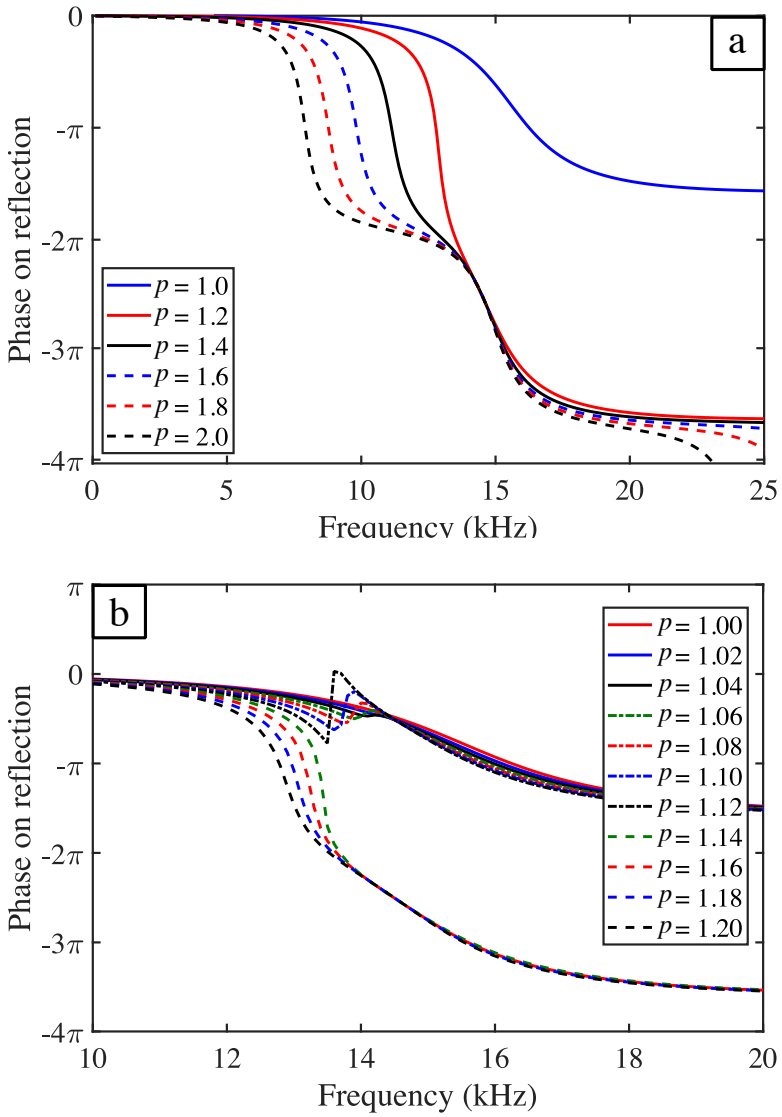

Fig. 4.13 a) Normal incidence phase on reflection for various p values of two-resonator compound gratings. b) Phase on reflection for surfaces with p values close to 1.0. All results are from FEM modelling.

where the background phase change has been removed. For a surface with $p = 1.0$, only one mode is expected at normal incidence: R_2. It is seen that as the frequency varies over the resonance region (radiative dispersion is shown in Figure 4.7) there occurs a phase shift associated with this mode between 10 - 22 kHz. As soon as p is increased to 1.2 the phase change has now more than doubled, this suggests another resonance is occurring within the system, and this is consistent with the previous consideration that the resonators are acting in isolation. The phase on reflection allows one to further analyse this sudden change from the resonators coupling together to becoming independent. Structures were modelled for values of p between 1.0 - 1.2. Two distinct mode behaviours occur, one for p values of 1.00 - 1.12, and the other between values of 1.14 - 1.20. It is seen for p values of 1.08, 1.10, and 1.12 that there is a sudden increase in the phase on reflection occurring at around 14 kHz. For the $p = 1.10$, this occurs at the same frequency as the phase resonance mode seen in Figure 4.12. It would appear that this sudden phase change occurs when there is only a slight difference between the two groove depths, where the phase resonance exists within the wings of the broader mode. The change in behaviour occurs around $p = 1.12$, which is the same p value as where the maximum pressure field in C_2 for the N_1 mode occurs. This again relates to the coupling between fields of the cavities reducing, until they begin to act independently.

4.5 Three-resonator Compound Grating

The final configuration of compound gratings investigated are those with three-resonators per period. As expected, the addition of an additional degree of freedom allows for a third mode to be excited. Figure 4.14 shows a schematic of the unit cell used. For consistency, the distance between the centre of the grooves remains constant for all the following cases.

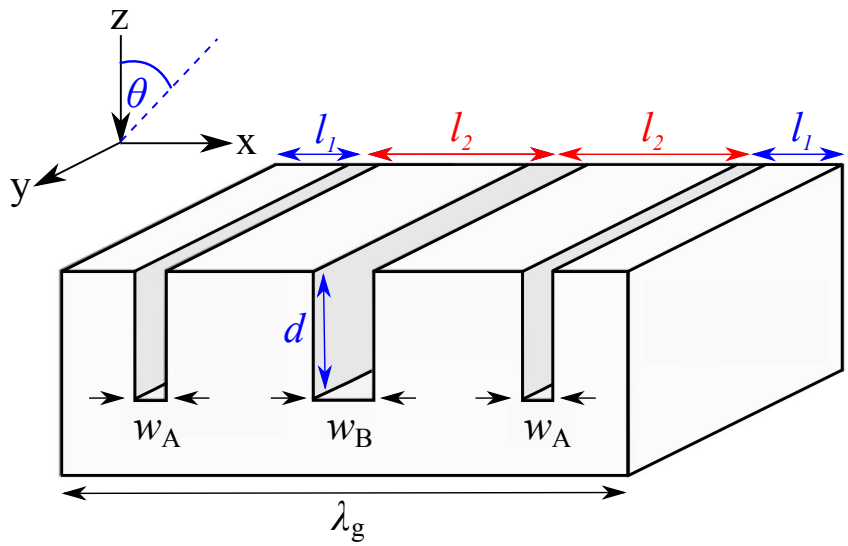

Fig. 4.14 Schematic of a unit cell comprising of three resonators per period ($\lambda_g = 19$ mm). In all discussed gratings $\lambda_g = 19$ mm, $l_1 = 3$ mm, $l_2 = 6.5$ mm. θ is the polar angle of incidence.

Using FEM models, the band diagrams have been investigated for five different systems: two keeping the width of the central groove constant and varying the width of the outer grooves, and three keeping the width of the outer grooves constant and varying that of the central groove. The results are shown in Figure 4.15. The first case shown in Figure 4.15(a) shows the computed dispersion for a compound grating with $w_A = 0.5$ mm and $w_B = 2$ mm. It is apparent that there is an absence of the expected three modes in the non-radiative regimes; however, this is only because the third mode does not exist in the frequency regime shown. The two modes which do appear are both phase resonance modes. The pressure field configurations for these two modes at $k_x = k_g$ are shown in Figure 4.15(a,i-ii). The upper mode field configuration is seen in 4.15(a-i). Here, the fields in the two outer grooves have a phase difference of π, and there no pressure field within the central groove. The lower frequency mode's pressure field configurations are shown 4.15(a,ii), the fields in the two outer grooves are π out of phase with the central groove. The modes within the radiative dispersion are hard to distinguish; this is due to one of the phase resonance

modes existing very close to the central frequency of the non-phase resonance mode. The lower frequency, phase resonance mode can be seen clearly and is becoming over-coupled.

In contrast to the previously discussed dispersion, the radiative dispersion shown in Figure 4.15(b) (for a surface where $w_{\mathrm{A}} = 3$ mm and $w_{\mathrm{B}} = 2$ mm) shows the two phase resonance modes clearly. Interesting, at normal incidence the higher frequency mode may now be excited but the lower frequency mode is only able to be excited off-normal incidences. This change from the previous case of which mode may be excited at normal incidence is explained by the resonance frequencies of the grooves. All the grooves are of the same depth but their widths are different to perturb their resonance frequencies. For the phase resonance between the outer grooves, the frequency of the mode is higher than the other. As the widths of the outer groove are more narrow than that of the central ($w_A < w_B$), the resonant frequency is increased due to the end-corrections. However, in the other phase resonance, the central groove is now being excited. As a result of the groove's width being larger, the resonance frequency is lowered, when the opposite case is considered where $w_A > w_B$, the previous discussion is reversed. The phase resonance between the outer cavities now occurs at a lower frequency than the other due to the grooves having a lower resonance frequency. Due to the configuration of the pressure fields, the mode where the phase resonance exists between the two outer grooves will always be non-excitable at normal incidence.

To find a surface where one of the modes is critically-coupled, the width of the central groove is kept constant ($w_A = 1$ mm) and the widths of the outer grooves are varied. In order for the lower mode to always be excited at normal incidence, the width of the groove has been increased so that $w_A < w_B$ is always true.

The band diagrams in Figure 4.16 show the influence of varying the width of the central groove: $w_B = 1.5$ mm, 2.0 mm, and 2.5 mm. In all of these cases, the

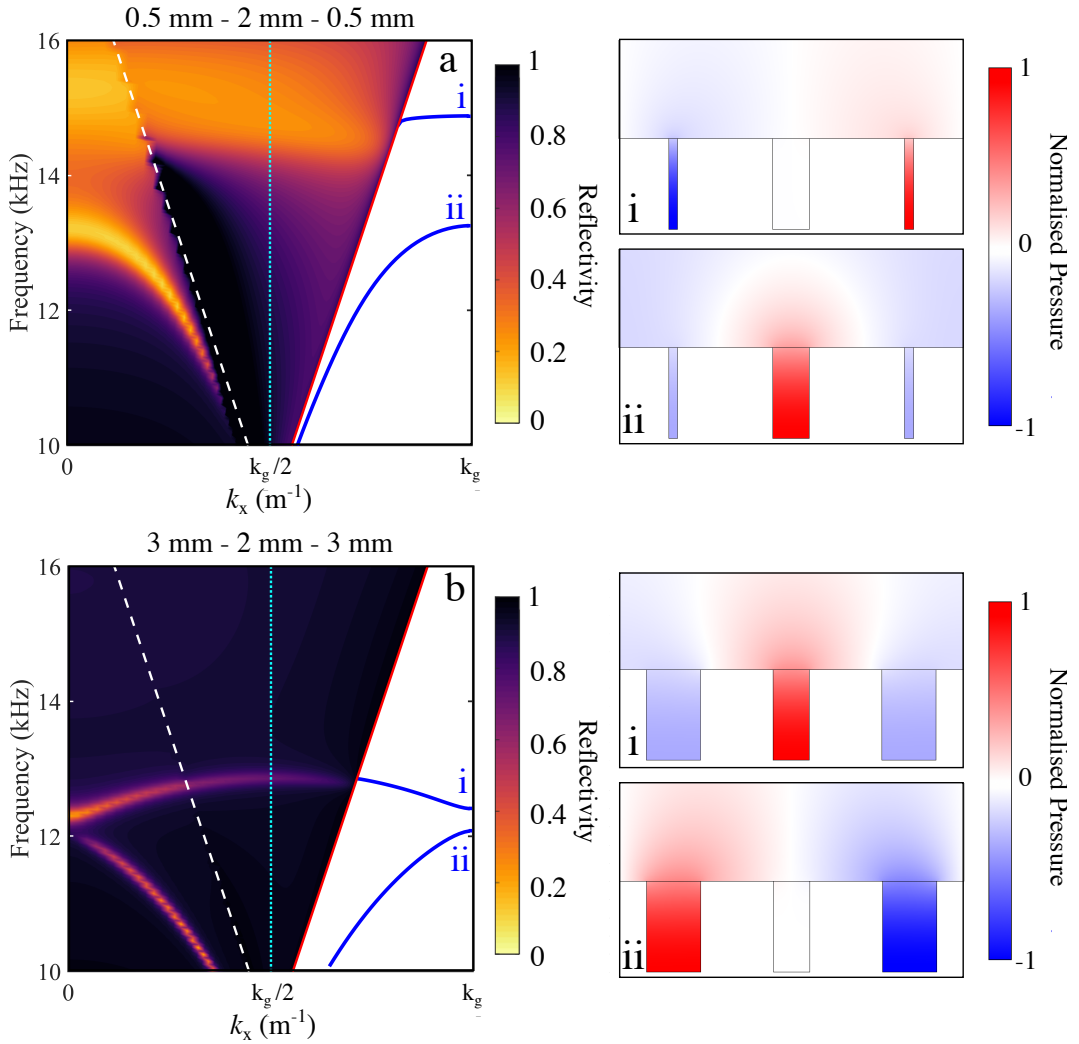

Fig. 4.15 Full dispersion for various configurations of three-resonator compound gratings. Here, the width of the central groove remains constant $w_B = 2$ mm. a) $w_A = 0.5$ mm. b) $w_A = 3$ mm. The solid blue lines represent the dispersion of ASWs. The solid red line represents the sound line. The dashed white line represents the diffracted sound line. The dotted blue line represents the first Brillouin zone boundary. i & ii. Instantaneous pressure fields for the respective modes. All results are from FEM modelling.

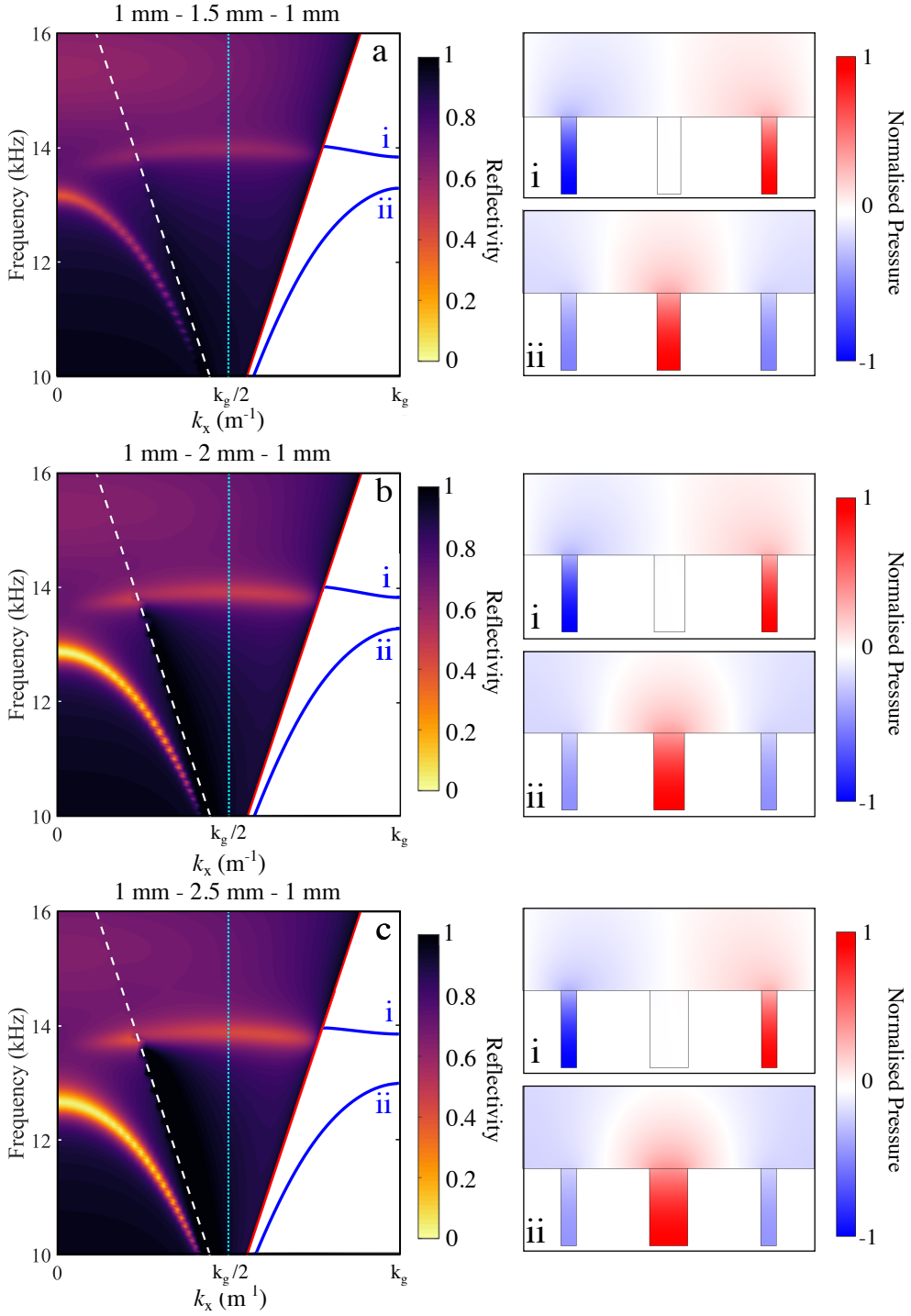

Fig. 4.16 Full band diagrams for various configurations of three-resonator compound gratings. Here, the widths of the outer grooves remain constant, $w_A = 2$ mm. a) $w_B = 1.5$ mm. b) $w_B = 2$ mm. c) $w_B = 2.5$ mm. The solid blue lines represent the dispersion of ASWs. The solid red line represents the sound line. The dashed white line represents the diffracted sound line. The dotted blue line represents the first Brillouin zone boundary. i & ii. Instantaneous pressure fields for the respective modes. All results are from FEM modelling.

lower mode is where the fields in the outer grooves are π out of phase with the fields of the central groove. The first case in Figure 4.16(a) shows that mode ii is under-coupled, as the width is increased to 2 mm the mode becomes near-critically coupled as evidenced by the sharp minimum in Figure 4.16(b). The mode becomes over-coupled, as the width is increased further and the mode begins to broaden. As the width is increased, the reflectivity of the higher frequency mode (i) decreases suggesting that the mode is approaching becoming critically coupled. For more discussion on critical coupling, please refer to Section 2.4.

4.6 Experiment

To experimentally investigate phase resonances on a compound grating, a 23-unit sample with the unit cell shown in Figure 4.16(b) was made. Here, $\lambda_g = 19$ mm, $d = 5$ mm $w_A = 1$ mm, and $w_B = 2$ mm. The sample's dimension are 450 mm $\times$ 450 mm. The grooves extend the whole y-length of the sample. The experiments were performed using the reflection experiment discussed in Section 3.4. A 12 kHz centred single-cycle Gaussian enveloped pulse was used for all measurements. In the experiment a pseudo-normal incidence measurement was performed followed by $\theta = 8.3°$ which was the minimum angle able to be measured using two mirrors due to their physical size. Finally an angle range of $\theta = 10° - 60°$ was measured at 5° intervals. At each angle, 100 repeat measurements were recorded in the time-domain, and subsequently averaged. The time domain signals are then Fast Fourier Transformed (FFT) and the resulting frequency domain response is normalised to that of an unpatterned, rigid plate.

The reflectivity as a function of frequency is shown in Figure 4.17(a). The rather broad and shallow mode at 15.5 kHz (C) corresponds to a resonance where all the fields in the three grooves in a unit cell are in-phase. The fundamental mode of

the grooves is the quarter-wavelength ($\lambda/4$) condition plus an end correction. The dependence of the modes' resonant frequencies on the angle of incidence is shown in Figure 4.17(b): off-normal excitation also reveals a third mode (B) that cannot be excited at normal incidence, to which there is increased coupling strength with increasing angle of incidence. Also of interest is the angle dependence of the resonance frequency of mode (A) that shows a decrease in frequency as the angle of incidence is increased.

The phase on reflection for normal incidence is shown in Figure 4.18. Here, the broad, over-coupled mode (C) features a very sharp change in phase at 13 kHz relating to the phase resonance mode (A). As expected, there is no feature of the off-normal mode (B) as only normal incidence data is shown.

From such data, one obtains a mapping of much of the dispersion curve in the radiative region for the plane containing the grating wavevector k_g. Figure 4.19 shows the experimental data obtained for the reflectivity measurements demonstrating the dispersion of the three modes, compared to the predictions of the reflectivity from a FEM model.

Also explored is the excitation of the bound surface modes supported by the sample. The dispersion of the bound surface was experimentally measured using the surface scan method described in Section 3.5. In this experiment, a scan area of 400 mm $\times$ 400 mm was used; this allowed for sufficient k-space resolution. A resolution of 1 mm was used in both x and y. At each position of 3 repeats were taken. The data was then Fourier analysed to obtain the dispersion diagram and isofrequency contours. Figure 4.20 demonstrates that the acoustic surface mode dispersion is close to being isotropic at the lowest studied frequencies but becomes highly anisotropic as the frequency rises, and the mode approaches the Brillouin zone boundaries.

Fourier-transformed field information for any selected frequency in any direction in k-space can be extracted to yield the mode's dispersion. This is shown for the

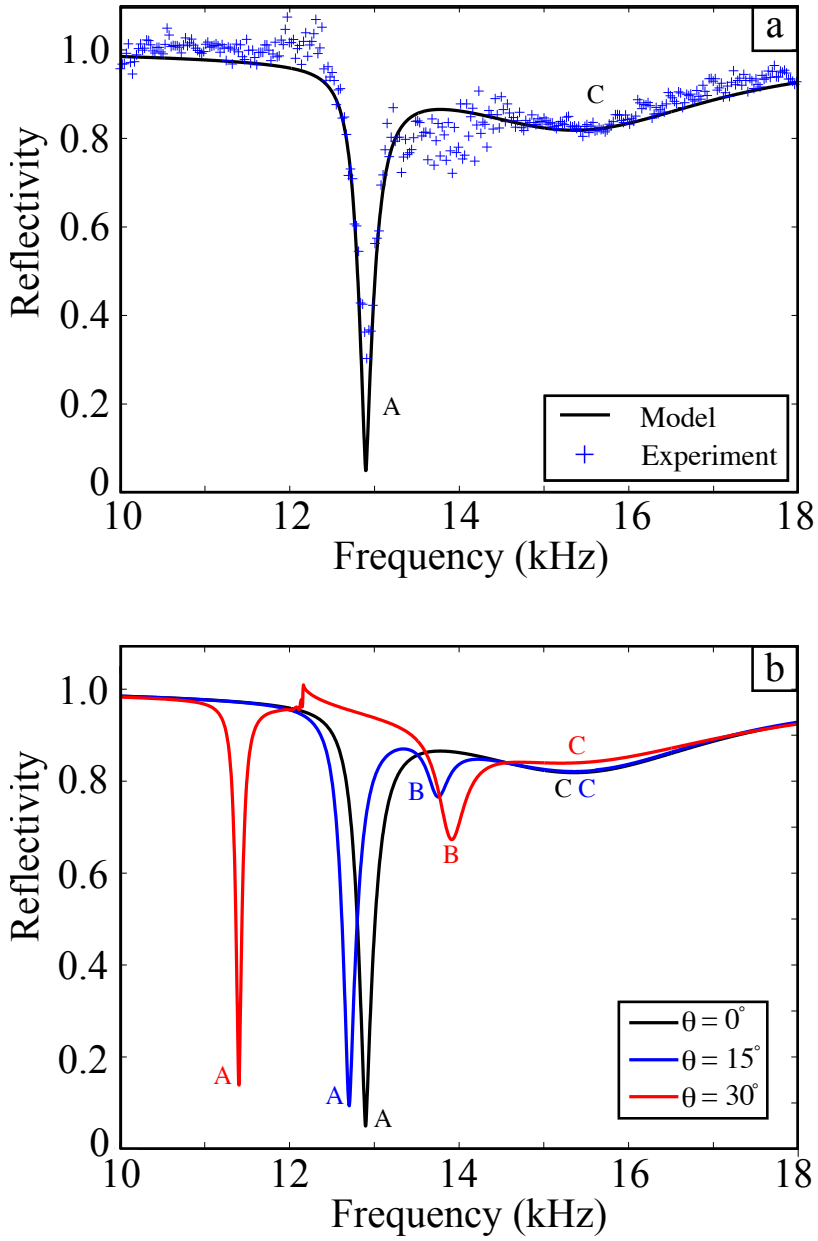

Fig. 4.17 (a) Experimental reflectivity data for near-normal incidence (blue crosses) compared with the FEM model (solid line). (b) FEM model predictions of the reflectivity showing the reflectivity spectrum for different angles of incidences. The sharp feature at ∼12 kHz for $\theta = 30°$ corresponds to the onset of diffraction where the in-plane component of the incident radiation λ_{0x} is comparable to λ_g. As this condition is met, radiation is diffracted into unwanted loss channels rather than coupling to the surface mode.

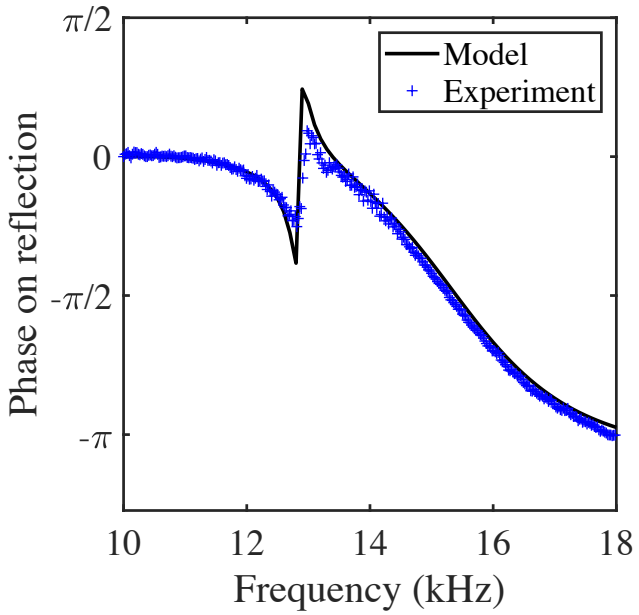

Fig. 4.18 Experimental near-normal incidence phase on reflection (blue crosses) compared with the FEM model (solid line).

plane containing the grating vector in Figure 4.20, where the experimental data is the colour scale, and the points are the eigenvalues predicted by the FEM modelling. Note here the weak modulation of the intensity of the experimental signal along the dispersion curve: this arises from the finite size of the sample defining a limiting k-space resolution.

The first supported mode is the broad and shallow branch (C) for which the field in each of the three grooves has the same phase in any given unit cell. Its frequency is approximately given by its wavelength being four times the groove depth, d - the fundamental resonance of the groove. When grooves are excited on resonance, evanescent end-effects occur at the opening of each groove these near-fields couple the groove resonances together over the surface in the form of a wave. For an ASW mode within the first Brillouin zone (BZ), only one pressure antinode per unit cell is allowed. This mode can be excited in the case of a simple grating because the ASWs wavelength (λ_x) approaches that of twice the grating wavelength (λ_g): with one

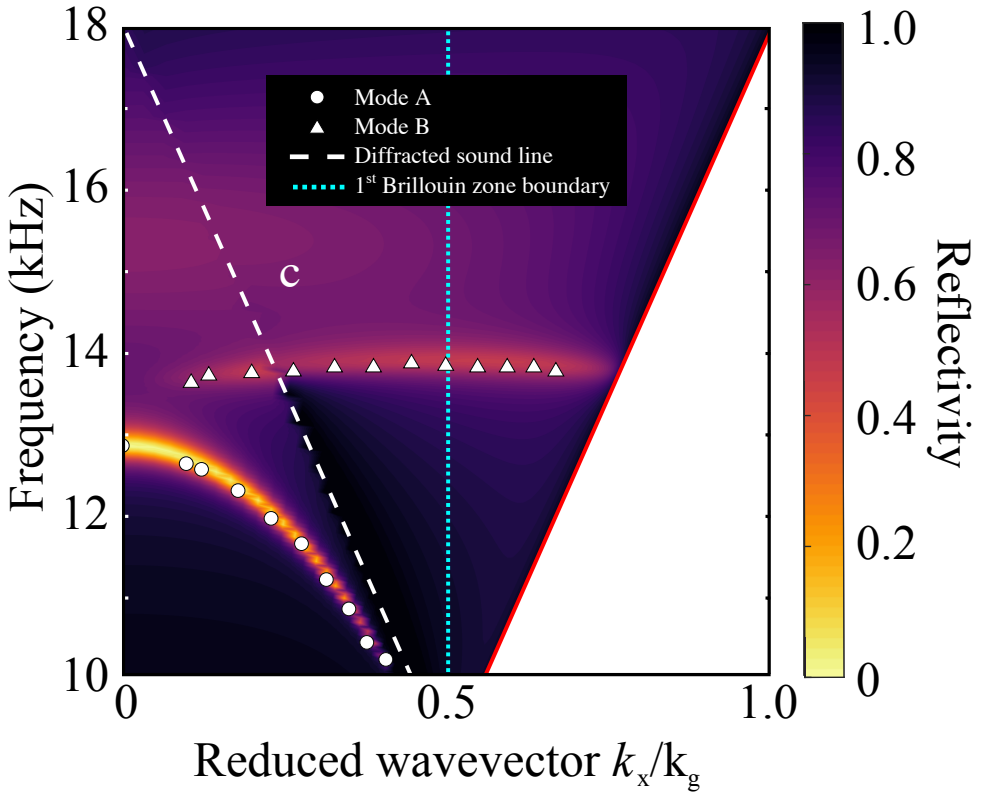

Fig. 4.19 Radiative domain in blue - frequency of reflectivity minima from experimental measurements (symbols) compared with predictions of the reflected intensity from the FEM model (colour-scale). The broad and shallow mode C has also been labelled for completeness.

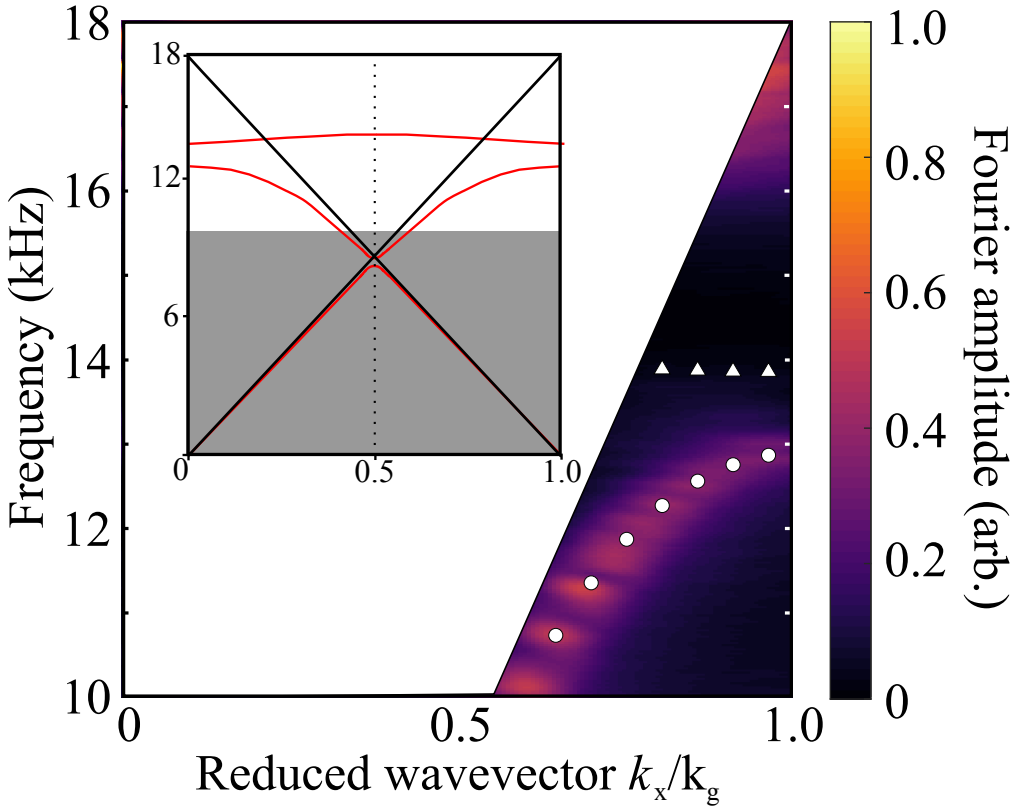

Fig. 4.20 Non-radiative region in blue - Fourier transform of the spatial near-field maps (colour-scale) compared with the predictions of the surface wave eigenmodes from the FEM model (symbols). Inset: Predictions of the dispersion obtained from the FEM model across a broader range of frequencies. The surface eigenmodes are shown in red, the solid black lines represent the sound line and onset of diffraction, and the shaded area represents frequency below our measured range (i.e., only the unshaded region of wavevector-frequency space is depicted in the main part of this figure).

resonator per unit cell as the condition of one antinode per unit cell is satisfied. In the case of shorter ASW wavelengths (in the second BZ) two antinodes are required per unit cell with one being required over the rigid surface, this cannot occur. With the addition of an additional degree of freedom, i.e. a second groove per unit cell, the condition of two antinodes per unit cell may now be met. Then, by the process of first-order diffraction, this mode is observed in the radiative region of the first BZ. Extending the discussion to the case of the sample measured, with three resonators per unit cell a third mode existing within the third BZ can be excited. Hence, with the extra degree of freedom, ASWs with smaller wavelengths than $\lambda_x = \lambda_g$ can now be excited as an eigenmode with three antinodes per unit cell is now available. Similar to the second mode, this mode is also scattered by diffraction into the radiative region of the first BZ. These modes can be seen in the inset of Figure 4.20 as the two red lines in the radiative region.

The acoustic field configurations for modes A, B and C are represented in Figure 4.22. As evidence of the previous discussions, notice that the ASW wavelength λ_x, matches the associated wavevector of the Brillouin zone boundary from which it was scattered; and note that mode C is a radiative mode and not confined to the surface. The relative pressure field in comparison to the non-resonant case, for modes A, B and C are 32.4, 21.7 and 3.5, respectively. When a comparison is made between the absorption and the relative pressure field strength, it becomes apparent that as the pressure field within the grooves increases the amount of absorption, seen as a reduction in reflectivity in Figure 4.17, also increases.

The increased field on resonance is similar to the case of transverse-magnetic light incident on a metallic compound grating; however, the difference is that in the electromagnetic case the feature of the phase resonance gives a maximum in the reflectivity while in the acoustic case a minimum is observed. This is due to the relative backgrounds in the two cases: for p-polarised light, the phase resonance

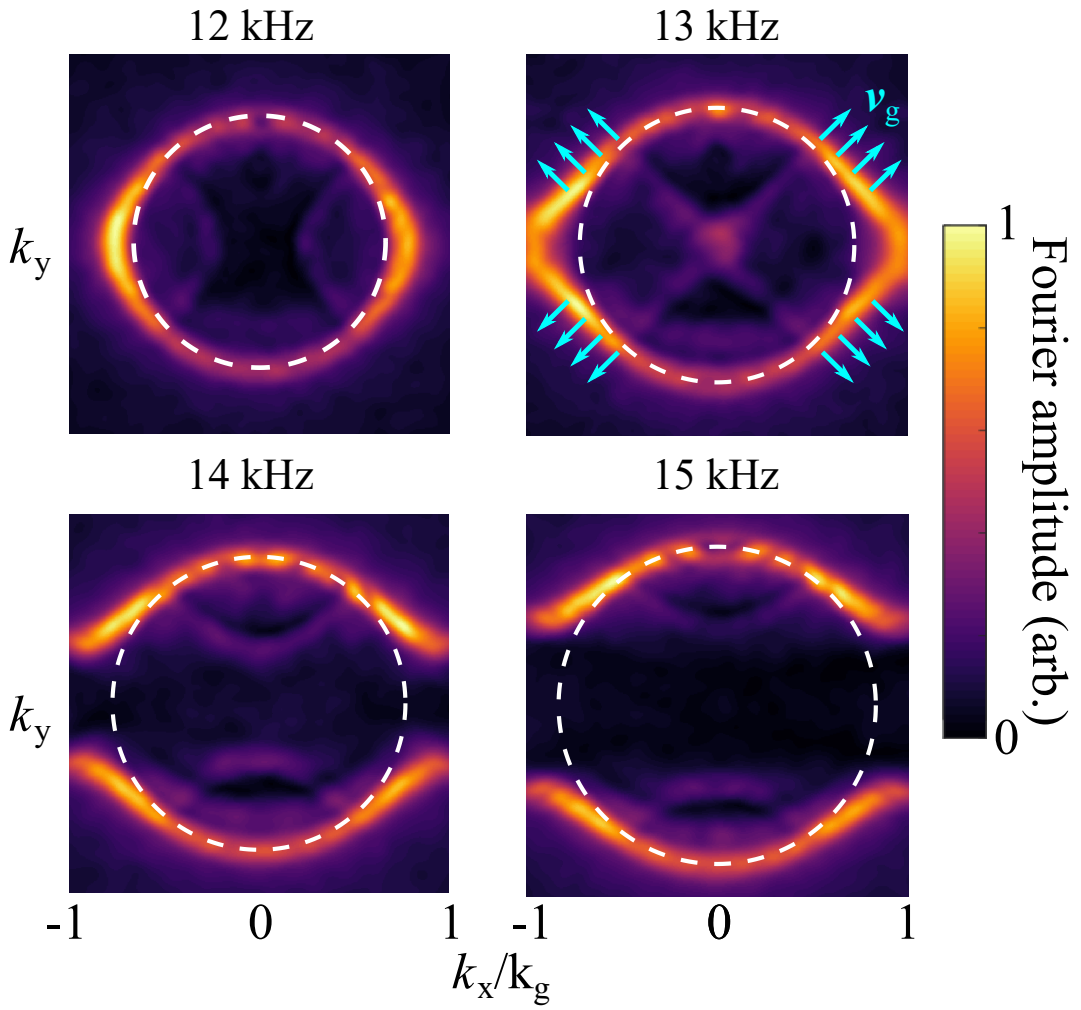

Fig. 4.21 Experimental equifrequency contours within the first Brillouin zone (in k_x) for 12, 13, 14 and 15 kHz. There is no periodicity in y, but the k_y axis is plotted on the same scale as k_x. The dashed, white line represents the sound line. The blue arrows represent the direction of the group velocity ($\mathbf{v}_g$).

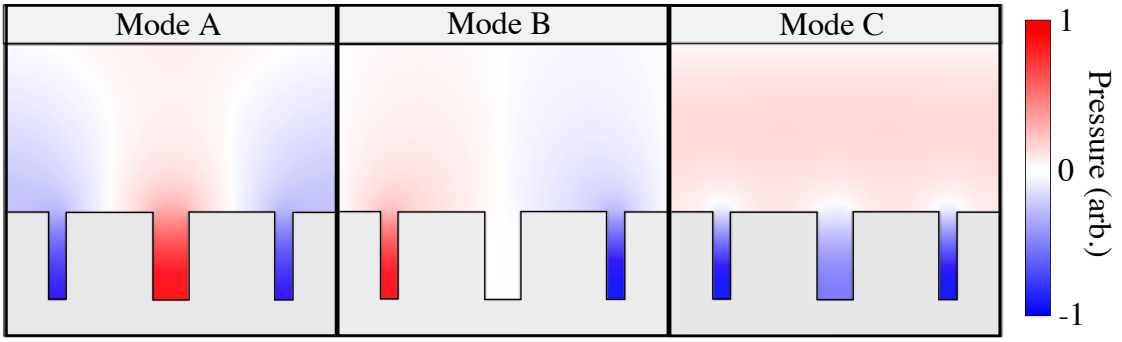

Fig. 4.22 Pressure fields for phase resonances A (the central groove fields being in antiphase with the outer two), B (fields in the outer two grooves being in antiphase, with the central one having zero amplitude), and C, the normal in-phase resonance. The scaling factors for the limits of the colour scale are 32.4, 21.7, and 3.5 respectively.

features as a sharp maximum in a low background.[141] For acoustic waves, the resonance is a sharp minimum in a high background.

From Figure 4.19 it is apparent that mode B is not excited at normal incidence. This arises simply because the fields in the outer two grooves have to be in antiphase for this mode with the central groove fields having zero amplitude at normal incidence. It is thus impossible to excite with a plane, normal incidence wave. Away from normal incidence, there is a phase difference across a unit cell, and this mode may now be excited.

Note from Figure 4.21 how the surface wave propagation becomes progressively more anisotropic as the frequency is increased. The equi-energy circle distorts first into an ellipse and then at frequencies above the first resonance of the system (at normal incidence) a band gap occurs where no mode is excitable in the x-direction, and the equi-energy contour splits into curved lines. (The weaker features shown towards the centre of each image are modes scattered into the first BZ by first-order diffraction, there are also reflections present due to the finite sample size). From these isofrequency contours, the direction of the group velocity ($\mathbf{v}_g$) (determined by $\mathbf{v}_g = \nabla_k \omega$, ω being angular frequency) is obtained, and if it has a region which

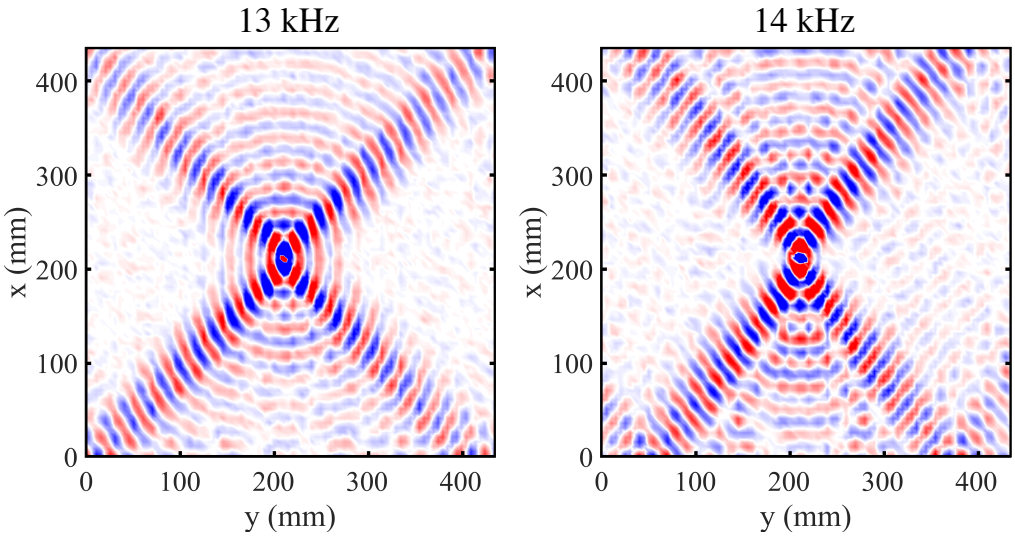

Fig. 4.23 Experimental data for the instantaneous pressure fields at 13 and 14 kHz, showing that the power flow is strongly confined in four directions.

is straight, acoustic beaming occurs where a range of wavevectors have the same $\mathbf{v}_g$. The direction of the acoustic beaming is the direction that is normal to the isofrequency contours; an example of this is shown by the blue arrows in Figure 4.21. An example of this effect in the frequency domain is shown in Figure 4.23. Interestingly, for different frequencies, the acoustic power is directed in different directions allowing for a frequency dependent directivity of acoustic power on the surface.

4.7 Conclusions

In this chapter, the characteristics of the radiative and non-radiative modes supported by simple and compound gratings have been explored.

It was discovered for a surface with two grooves per period that as p increases (the ratio of the groove depths) the resonators become less coupled and begin to behave more like isolated resonators. Investigating the absolute pressure fields in each groove for each surface mode supported, showed that as p increases the difference in pressure between the grooves increases. However, for $p = 1.12$ the maximum value of pressure

is the deeper groove. This maximum value of pressure in conjunction with a larger phase shift presented in the phase on reflection supports the idea that the resonators are becoming less coupled. One potential application of the independently coupled sets would be a near-angle independent frequency-selective filter that operates for two frequencies; this could be turned into an active frequency selective filter by adjusting the depth of the cavities.

A compound groove grating having three grooves per period has been modelled and the results verified experimentally, showing a sharp minimum in the reflectivity spectrum for a phase resonant mode where the outer grooves are out of phase with the central, giving the possibility of a frequency-specific acoustic filter. The surface was also found to support acoustic surface modes whose dispersion has been obtained and which, for a range of frequencies, exhibit frequency-dependent directional acoustic power beaming due to a range of wavevectors having the same group velocity.

In the following chapter, the surface waves supported by a so-called meander structure will be explored. These glide-symmetric surfaces present interesting band diagrams due to a degeneracy of the modes at the first Brillouin zone boundary. These surfaces have been modelled through FEM modelling and their predicted response verified experimentally.

Chapter 5

Broadband, Slow Sound on a Glide-Symmetric Meander-Channel Metasurface.

5.1 Introduction

In this chapter, so-called meander structures are investigated. The dispersion of the surface modes supported by such glide-symmetric labyrinthine channels features a zero magnitude band gap at the first Brillouin zone boundary and a region of constant group velocity (v_g). The dispersion of such structures has been thoroughly investigated through FEM modelling and then experimentally verified. In addition, the propagation length of the surface modes has been quantified. Finally, a variation of the meander channel where the straight channels have been covered has been explored through FEM modelling. A groove depth-dependent change in the resonance condition of the standing waves at the first Brillouin zone between the two systems will be explored.

5.2 Background

A number of works have shown that it is possible to control the propagation of sound waves using arrays of sub-wavelength elements (phononic crystals) as first proposed by Kock and Harvey[145], or more recently the study of labyrinthine structures[146, 147]. Recently Liang et al.[21] demonstrated that, by using curled perforations to coil up space, large effective refractive indices (n) can be achieved. This allows the potential to spatially engineer n and create arrays of such structures of various different acoustic path lengths to control phase-gradients allowing for the focusing, absorption and directing of acoustic waves, as well as 'doubly negative' material properties and those with effective 'density' near zero. Other structured surfaces have been used to control waves, such as a sub-wavelength corrugated surface demonstrated by Zhu et al. where, by manipulating the dispersionless phase fronts, ultra-broadband extraordinary reflection could be obtained[148]. Fan et al. found that by enclosing a monopole sound source in a structure comprising of various space-coiled elements allows for the device to be 1/10th the size of the wavelength emitted[149].

Whilst being able to reduce the velocity of propagation of acoustic energy over a surface is itself interesting and undoubtedly useful, for some applications one may require this to be maintained over a broad frequency band. In general, this is difficult to achieve with a periodically patterned or resonant surface because of diffraction and mode-hybridisation, the former being particularly dominant on approach to the first Brillouin zone boundary. Glide symmetric structures[113, 114] offer an opportunity for broadband low-group-velocity acoustic surface waves, as has been demonstrated in electromagnetism[150]. They comprise of a geometry that has reflection symmetry about a mirror plane when the unit cell is displaced by half a period. In this way, these structures do not present a band-gap at the

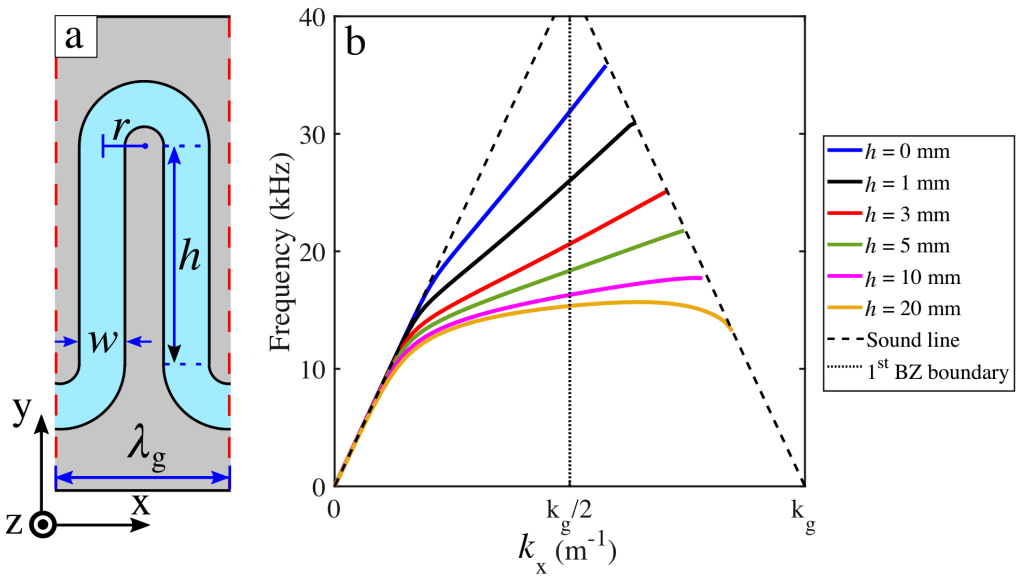

Fig. 5.1 (**a**) Schematic of the surface of a unit cell used in this investigation, comprised of an air-filled channel (blue) of depth $d = 5$ mm in an acoustically-rigid material (grey). The depth is in the negative z direction, and the acoustic surface wave propagates in the positive x-direction. Here, $\lambda_g = 4$ mm, $w = r = 1$ mm, and $h = 5$ mm. (**b**) FEM model non-radiative dispersion for different values of h.

first Brillouin zone boundary since the two normally different energy standing wave solutions are now degenerate[121, 116], resulting in a near-linear dispersion over a broad bandwidth.

5.3 Theory

The dispersion of the bound surface modes supported by different meander channels is explored. Such meander channels have depth d, and width w, as illustrated in Figure 5.1(a). The channel is space-coiled in a glide-symmetric unit cell with repeat period of λ_g along the direction of propagation. To first order this may be modelled through a simple geometrical approach, a wave following the channel across one unit cell will propagate along a path-length of

$$l_{\mathrm{p}} = 2(\pi r + h) \tag{5.1}$$

where r is the radius of the curved channel sections and h is the length of the straight sections of the channels. This increase in path length in relation to the unit cell can be thought of as creating an effective waveguide index, given by

$$n_{\mathrm{wg}} = \frac{l_{\mathrm{p}}}{\lambda_{\mathrm{g}}} \tag{5.2}$$

If the power propagation is confined to the grooves, then this is directly related to the group index. A simple dispersion relation for such a structure can be established since, to first order the wavevector in the vertical direction (depth of grooves) is given by the quarter wavelength resonator condition, $k_{\mathrm{z}} = 2\pi/4d$ (ignoring end effect corrections [151]). With the wavevector in the propagation direction given by k_{x} it follows that the dispersion relation is simply

$$f = \frac{v}{2\pi}\sqrt{\left(\frac{k_{\mathrm{x}}}{n_{\mathrm{wg}}}\right)^2 + \left(\frac{2\pi}{4d}\right)^2} \tag{5.3}$$

The effect of varying h on the dispersion is considerable, as seen by FEM models in Figure 5.1(b). The surface wave dispersion was obtained by modelling an infinite system using Floquet boundary conditions. Solving the eigenvalues of the system and performing a parametric sweep of the in-plane wavevector in the direction of periodicity (k_{x}), results in the dispersion curves shown. This is discussed in further detail in Section 3.7.2. It is shown that as h is increased, the mode lowers in frequency and the linear region's gradient is decreased. It can also be seen for $h = 10$ mm and 20 mm, that the extent in k_{x} for which the linear region exists is now reduced, as the curved region of the dispersion is much more prominent than for smaller h values, this is due to coupling strongly to free radiation.

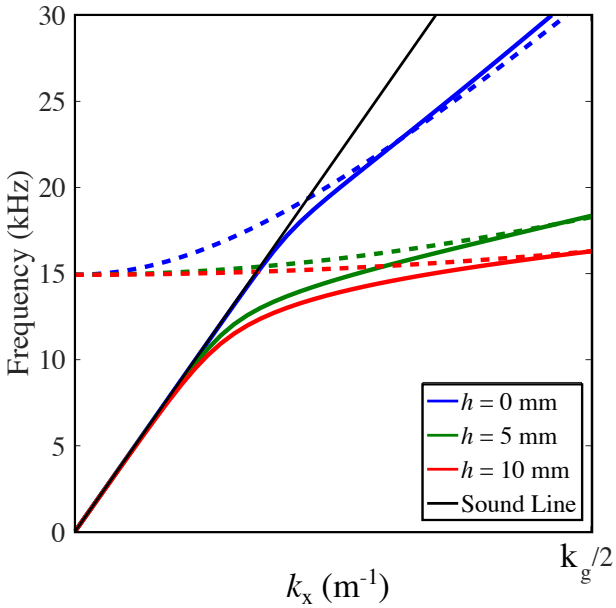

Fig. 5.2 Waveguide approximation from equation 5.3 (dashed coloured lines) and finite element model (solid lines) dispersion for different values of h. The solid black line corresponds to the maximum wavevector of an incident plane wave.

Now the FEM model results are compared with those obtained by the simple analytic model, as shown in Figure 5.2. The simple analytic model neglects any interactions with free-space sound modes and diffractive coupling between adjacent grooves so there is significant disagreement between the two models at wavevectors within and close to the sound line. However, at values of $k_x > k_0$, the mode becomes more confined to the surface and therefore the channel, and hence equation 5.3 provides a good approximation. Of course, Equation 5.3 does not include any diffraction effects, but it is clear from the FEM model that the modes have a linear dispersion (and uniform group velocity) approaching the first Brillouin zone boundary ($k_g/2$) – a consequence of the glide symmetry of the system[114].

We also wish to investigate the effect of the channel width on the dispersion. Figure 5.3 shows the FEM model for three channel widths: $w = 0.5$ mm, 1.0 mm and 1.5 mm. The effect of changing the channel width is much more subtle than varying h. Firstly, as one may expect the narrowest channel, $w = 0.5$ mm, couples

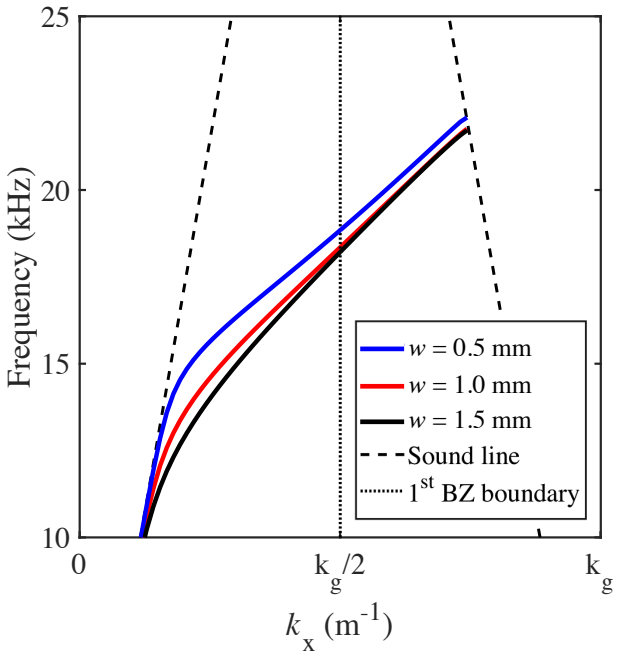

Fig. 5.3 FEM model non-radiative dispersion for different values of w. Here, $h = 5$ mm, $d = 5$ mm, and $\lambda_g = 4$ mm.

less strongly to free radiation as much less of the surface is occupied by the channel. Secondly, as the channel width is increased the gradient of the linear region also increases, this increase in group velocity suggests that the path-length (l_p) has now decreased. However, this is a very small effect. Finally, as discussed previously in Section 2.4, as the channel width increases so does the the end-correction making the channels appear deeper, which decreases the resonance frequency.

Varying the depth of the meander has a very significant effect by shifting the fundamental resonance resonance in the vertical (depth) direction. However this is not the only effect as shown in the resulting dispersion illustrated in Figure 5.4. Here we show the non-radiative dispersion relations for $d = 2.5$ mm, 5.0 mm and 10 mm. The dispersion for $d = 2.5$ mm shows no near-linear region, this is because the modes are coupling strongly to free radiation (explained more thoroughly in Section 2.4). As d is increased to 5.0 mm, the dispersion shows a near-linear region as there is in this case weaker coupling to free radiation. For $d = 10$ mm, the mode shows even

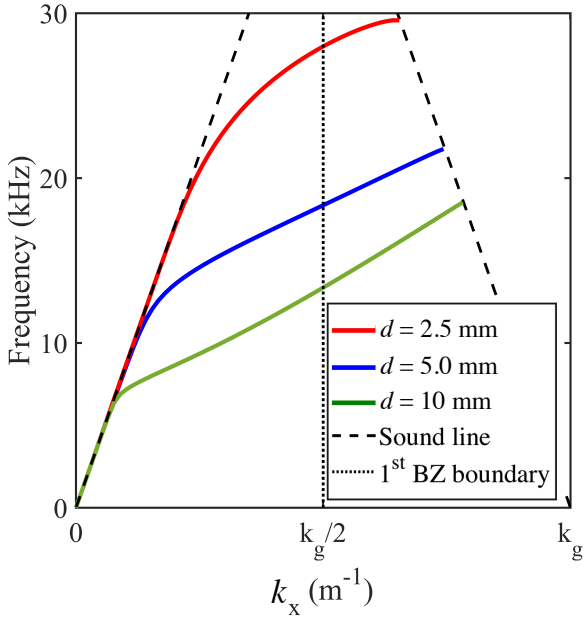

Fig. 5.4 FEM model non-radiative dispersion for different values of d. Here, $h = 5$ mm, $w = 1$ mm, and $\lambda_g = 4$ mm.

weaker coupling to free radiation, which results in the near-linear region being over an even broader k_x region. In addition, as anticipated, as the depth is increased the frequency at which the mode starts dispersing lowers, due to the quarter wavelength resonance condition.

5.4 Experiment

To experimentally determine the dispersion of the ASWs, a loudspeaker with a sound-launching conical attachment was positioned so that the sound emitted was angled onto the surface, such as described in section 3.5. Figure 5.5 is a schematic of the setup. The narrow exit hole of the cone and close proximity to the surface leads to strong diffraction enabling the creation of high in-plane momentum components and near-field coupling to the ASW. One of the main difficulties with obtaining results was due to the signal from the surface mode being dominated by free radiation. To avoid this the needle microphone (Brüel & Kjær Probe Microphone Type 4182)

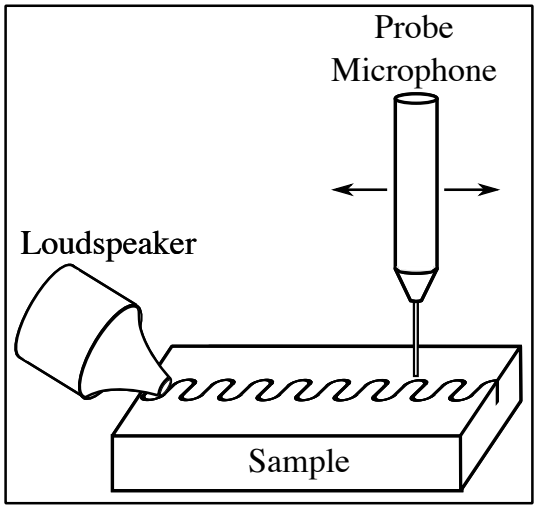

Fig. 5.5 Schematic of the experimental setup. A loudspeaker with conical attachment emits a broadband-pulse that excites the ASW. This then propagates over the surface and the arriving pulse is recorded using a near-field probe that is raster scanned over the surface.

had its tip positioned about 0.5 mm from the surface. This was then raster-scanned over the sample to detect the near-fields with a resolution of 1 mm over a total scan length (x) of 300 mm. The signature of free radiation appears on the dispersion along the sound line ($k_{\mathrm{x}} = k_0$). This signal eventually dominates at high k_{x} when the surface modes become progressively more confined and their intensity at long distances from the source becomes very low. For each microphone position, a 30 kHz near-single-cycle Gaussian-envelope (broadband) sound pulse was emitted from the loudspeaker and subsequently detected by the microphone. For each spatial position an average of three pulses was taken to improve the signal to noise. Subsequently a temporal Fourier transform was performed to obtain the amplitude and phase for each frequency at each spatial position, resulting in a spatial field-map for each frequency. A two-dimensional Fast Fourier Transform (FFT) was then performed on each of the spatial field maps. By plotting the Fourier amplitudes as a function of wavevector from each of these two-dimensional FFTs for each frequency one obtains the dispersion diagram of the ASWs supported [152]. The group velocity

($v_g = d\omega/dk$, where ω is the angular frequency) was calculated by fitting a straight line to the near-linear region of the surface mode.

Five aluminium samples have been characterised each 600 mm in length (x): three samples comprise of 150 unit cells, each with $\lambda_g = 4$ mm, $w = 1$ mm, and straight line sections of $h = 0$ mm (i), 5 mm (ii), 10 mm (iii); a further sample (iv) (100 unit cells) has $\lambda_g = 6$ mm, $w = 2$ mm and $h = 5$ mm. As will be discussed later, a fifth sample (v) is a modified version of (ii) with tape placed over part of the meander to remove the glide symmetry.

5.5 Height Dependence

Figure 5.6(a) shows a typical experimentally determined dispersion plot for the $\lambda_g = 4$ mm and $h = 5$ mm surface. Below 10 kHz the mode is essentially non-dispersive and propagates as a grazing mode at the speed of sound. From 10 to 14 kHz there is strong frequency dependence of both the phase and group velocity as the mode moves from being a lightly-bound surface wave to being more like a waveguide mode confined to the channel. Then, at higher frequencies up to 21 kHz, the mode has a nearly constant gradient, corresponding to a constant group velocity, but a changing phase velocity (v_p). For this particular sample in the vicinity of 20 kHz the group velocity is $v_g = 55.6$ ($\pm$ 4.1) ms^{-1}, a reduction by a factor of 6 below that of the speed of sound in air. Note that the FEM model predicts $v_g = 57.1$ ms^{-1} which is in excellent agreement with the experimental data. These surface modes propagated over the sample at a reduced velocity compared to waves propagating over an unstructured surface, as these would propagate at the speed of sound. The sound waves propagating over such a structured surface are described as slow, as they propagate slower than the speed of sound in the surrounding fluid medium (air).

The frequency range for which a near constant group velocity is observed is extended in k_x due to the absence of a band gap at the first Brillouin zone boundary, a consequence of the glide symmetry of the structure. This glide symmetry condition may be readily broken by applying a tight membrane over part of the meander sample. This was done using parcel tape with the tape edge aligned parallel to the propagation direction with the tape covering 20% of the meander of the $h = 5$ mm sample, as seen in the inset of Figure 5.6(b). The resulting ASW is now very different; a band gap has opened between 16 and 18 kHz resulting in the mode no longer having a constant group velocity over a wide band.

5.6 Channel Length Dependence

The effect of changing l_p on the dispersion of the ASW is seen in Figure 5.6(c-d). Using the simple analytic equation (3) we predict that n_{wg} at high k_x has values of 1.57 and 8.14 for the $h = 0$ and 10 mm samples respectively. For the $h = 0$ sample, the analytical result compares favourably with that from the full modelling shown in Figure 5.1(b), which gives 1.76. For the 10 mm sample, the full model value of 10.70 agrees less well since the analytic treatment neglects end effects as well as interactions with the free-space sound. For these two surfaces, v_g has been measured as the group velocity ($v_g = d\omega/dk$, where ω is the angular frequency) is the gradient of the mode. It was calculated by fitting a straight line to the near-linear region of the surface mode. The experimental index can then be calculated as $n_{ex} = v/v_g$, where v is the speed of sound in air. Experimentally v_g had values of 192.4 ($\pm$ 15.1) ms^{-1} and 33.4 ($\pm$ 3.1) ms^{-1} were found for $h = 0$ mm, and $h = 10$ mm respectively, giving n_{ex} values of 1.78 ($\pm$ 0.14) and 10.28 ($\pm$ 0.96). The experimental values are in close agreement with the FEM model of 1.76 and 10.70, respectively. As h increases, the section of the band diagram where the mode disperses away from the sound

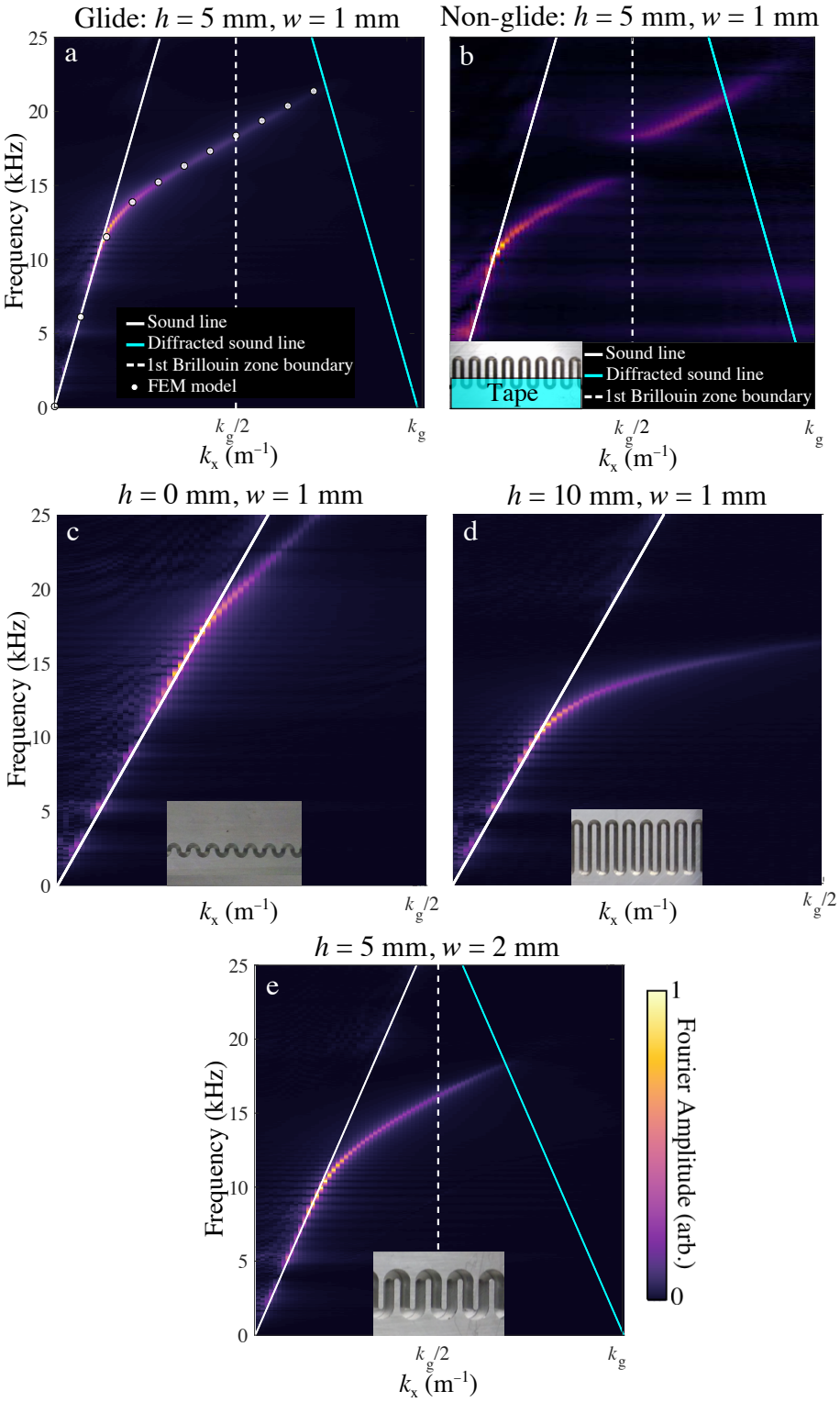

Fig. 5.6 a-e) Two-dimensional FFT of the experimental field data recorded at a height of 0.5 mm across the surface, illustrating the dispersion of the surface mode supported by each of the investigated structures: a) $h = 5$ mm, $w = 1$ mm, also shown are predictions from the FEM model (symbols). b) $h = 5$ mm, $w = 1$ mm, but with the glide-symmetry broken. c) $h = 0$ mm, $w = 1$ mm. d) $h = 10$ mm, $w = 1$ mm. e) $h = 5$ mm, $w = 2$ mm. Note the different x-axis extent in (c) & (d).

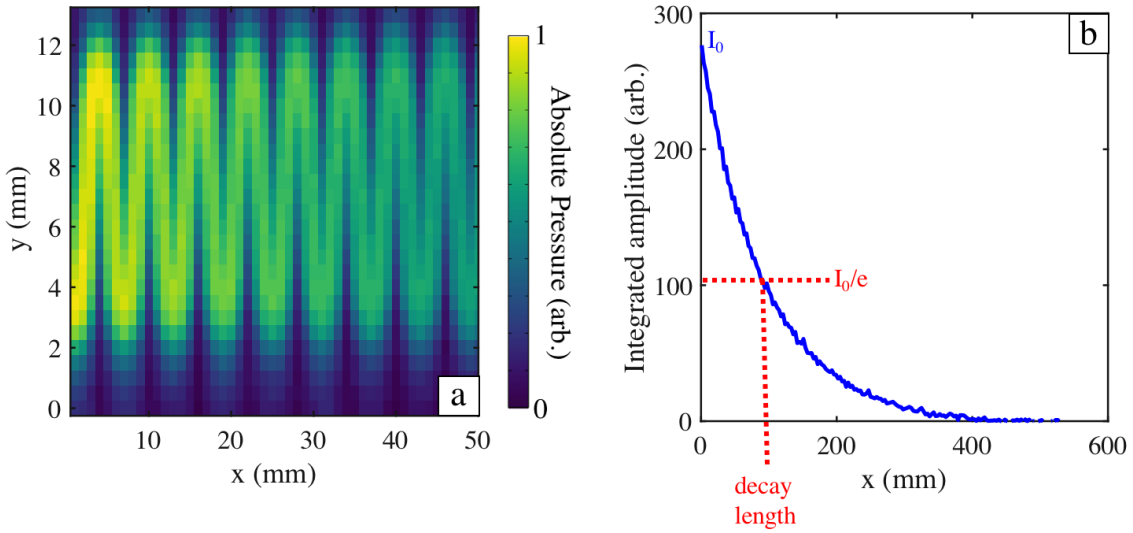

Fig. 5.7 a) Experimental absolute pressure field plot for a frequency 16.2 kHz over 50 mm in the x-direction of the sample. b) Calculation of the decay length from the absolute pressure field.

line to where it becomes near-linear increases, reducing the bandwidth of the linear region. As discussed in Section 2.6.2, this occurs as the mode couples more strongly with free radiation.

5.7 Propagation Length

Also of interest is the propagation length of the ASWs along the x-direction of the meander surface. Attenuation will occur due to the thermal and viscous boundary layers within the channel, see Section 2.4. One may characterise the decay of the ASW as the distance over which the amplitude of the absolute pressure field decays to 1/e.

In order to calculate the decay length as a function of frequency, the absolute pressure field at every third x position was integrated in the y-direction, this was to ensure that the same part of every unit cell was being integrated over. An example of such a field plot is shown in Figure 5.7(a) for a frequency of 16.2 kHz. The result of the integrated amplitude as a function of x is shown in Figure 5.7(b). Here, the decay

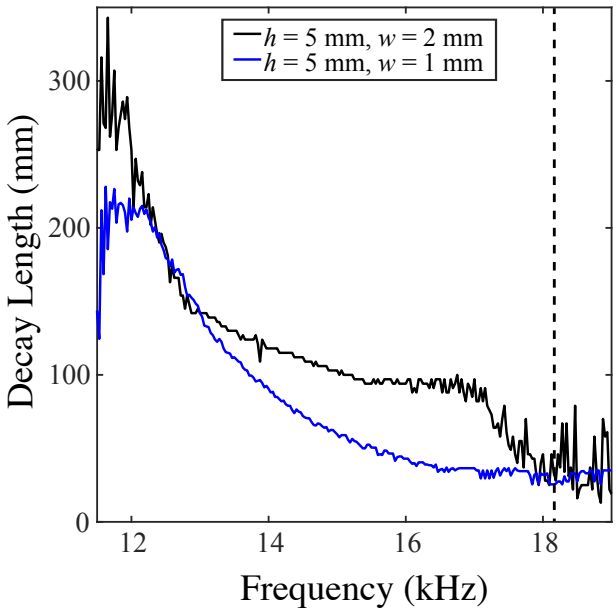

Fig. 5.8 Decay length as a function of frequency for the two different widths and h = 5 mm samples. The vertical dashed line indicates the diffraction edge for the h = 5 mm, w = 2 mm sample.

length is calculated when the maximum value (I_0) is reduced to I_0/e; this was then repeated for all frequencies. One should note, that this calculation is only undertaken when the mode is away from the sound line and only up to frequencies for which the signal is still well resolved at long distance from the source. To further investigate the decay length, one sample (v) with a wider channel (w = 2 mm) was fabricated. The dispersion plot for the ASW on this sample is shown in Figure 5.6(e) with the inset showing a section of the sample. Notice that the dispersion of the mode curves away from the sound line more slowly before becoming linear. This arises from diffractive coupling between adjacent grooves. Similar coupling has been described by Zhu et al.[148] for the case of isolated cavities supporting zero-velocity (trapped) modes, however, the coupling in the presented structure becomes dominated by the direct propagation along the groove as the mode becomes more strongly confined at higher frequency. This results in the dispersion curve for the channel with the largest h having the least near-linear region. Figure 5.8 shows the decay lengths as a

function of frequency for the two different width $h = 5$ mm samples. With decreased channel width the attenuation of the surface waves increases; this is expected as the thermal and viscous boundary layers ($\sim$ 15 μm) now occupy a larger proportion of the channel. It is clear from the results that the width of the channel affects the decay length of surface waves, with the narrow channels attenuating the waves faster. The increased localisation of the pressure fields in the grooves (due to a larger imaginary component of k_z at a given frequency, due to smaller unit cell) directly results in more energy being absorbed in the thermoviscous boundary layers of the groove. In addition, the decay of the ASW for the $w = 2$ mm sample shows a second, steeper, decay beyond 17 kHz. At these frequencies, the fields are becoming more strongly localised in the curved ends of the channels. Eventually, nodes in the pressure field form in the straight section in the channel and the fields begin to resemble a glide-symmetric array of holes in place of the curved ends. With the fields in the transverse direction falling to zero over a distance of about 5 mm (the channel length in the transverse direction) then the characteristic wave dimension in the transverse direction is of order 20 mm. Thus these localised strong fields may now give rise to free radiation of this wavelength. This extra loss channel appears to come in at about 17 kHz. Up until that frequency once the dispersion has deviated from the sound line the decay length in the wider channel is more than twice that in the narrower channel.

The progression of the localisation of the absolute pressure field as the frequency is increased is shown in Figure 5.9 for the $h = 5$ mm, $w = 1$ mm sample. The three frequencies shown are 13.5 kHz ($k_x << k_g/2$), 17.5 kHz ($k_x \approx k_g/2$) , and 19.5 kHz ($k_x > k_g/2$). As expected, the absolute pressure field for the 13.5 kHz is interacting with the surface, but the fields are weakly confined to the surface due to the small imaginary k_z. The phase plot in Figure 5.9(d) shows that the surface wave wavelength is long compared to the unit cell ($\lambda_{sw} >> \lambda_g$). For the absolute field close

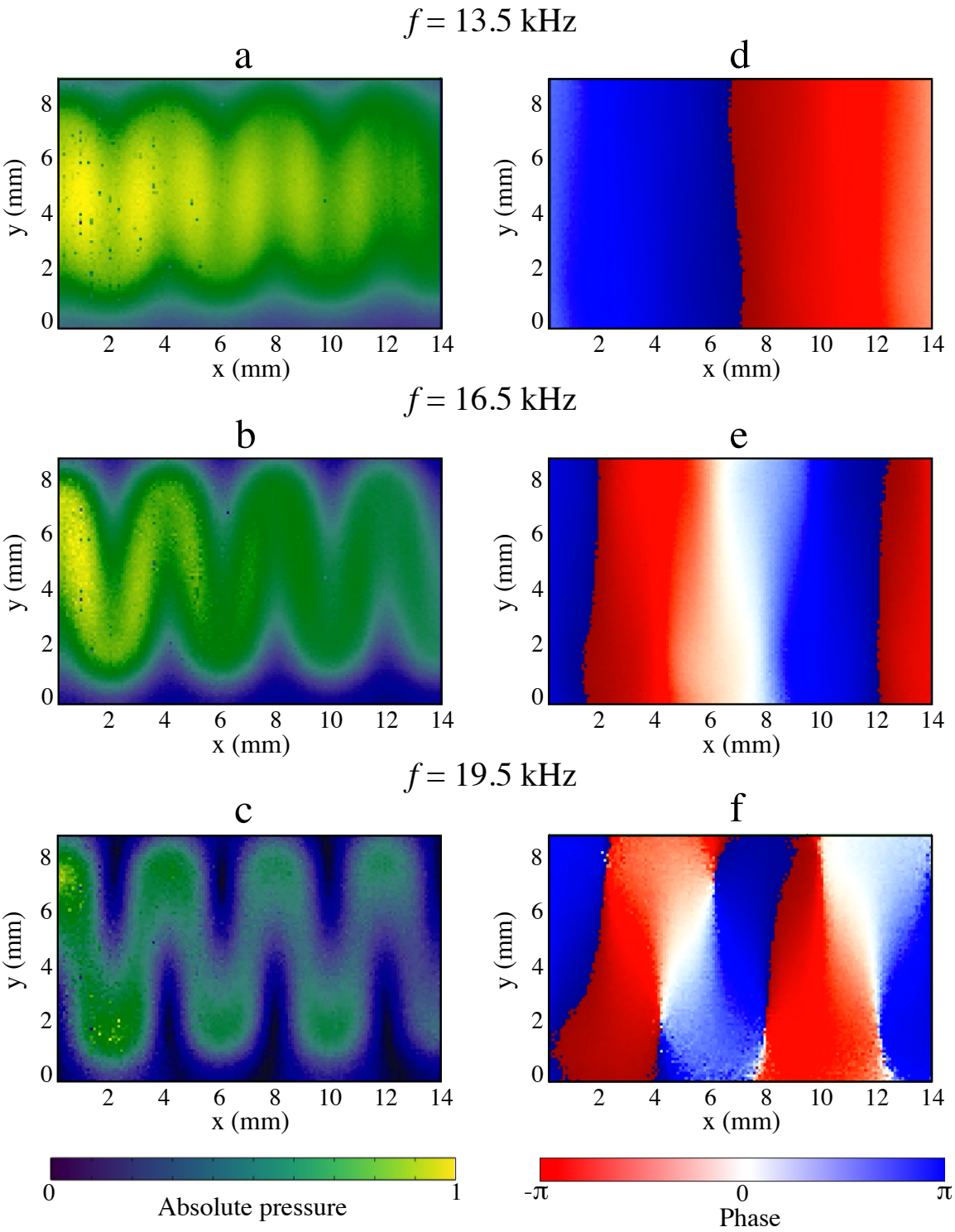

Fig. 5.9 a-c) Absolute pressure fields over 3.5 periods. d-f) Phase maps over 3.5 periods.

to the Brillouin zone boundary, it is evident that the modes are more confined with a reduced field strength above the walls of the meander. Interestingly, when the phase plots are investigated shown in Figure 5.9(d-f), it appears that the modes contain a component in the y-direction as the fields are following the meander, even though the only periodicity is in the x-direction. Figure 5.9(c,f) show the fields in the second Brillouin zone. The wavelength of the surface wave is approaching that of the grating period corresponding to the second Brillouin zone boundary ($\lambda_{sw} = \lambda_g$), compared to being half the grating period at the first Brillouin zone boundary. Here, the maxima in the absolute pressure are located in the curved sections of the meander channel, with the straight sections having reduced intensity, suggesting that there are now nodes in the pressure fields within these sections. The 19.5 kHz phase plot shows a larger y-component of the field than that at 16.5 kHz, this is to be expected as both the fields are more confined to the channel, and λ_{sw} is smaller than the previous case.

Figure 5.10 shows FEM isophase contours at various depths in the meander channel for $h = 5$ mm, $w = 1$ mm, and $d = 5$ mm. At the bottom of the channel (z $= -5$ mm), the contours are straight and orthogonal to the walls of the channel. The contours remain unchanged until z $= -1$ mm. Here, the isophase contours in the straight section are starting to curve; this is shown more prominently at z $= -0.5$ mm. On the surface (z $= 0$ mm), the origin of the warped isophase contours can start to be seen. The isophase contours no longer have the constraint of being perpendicular to the walls of the channel, instead the field couples with the free radiation where the isophase contours are parallel with the straight sections of the meander channel. This is shown further as the contours are investigated above the surface. The further away from the surface, the less influence the ASWs have on the free fields, due to their evanescent nature.

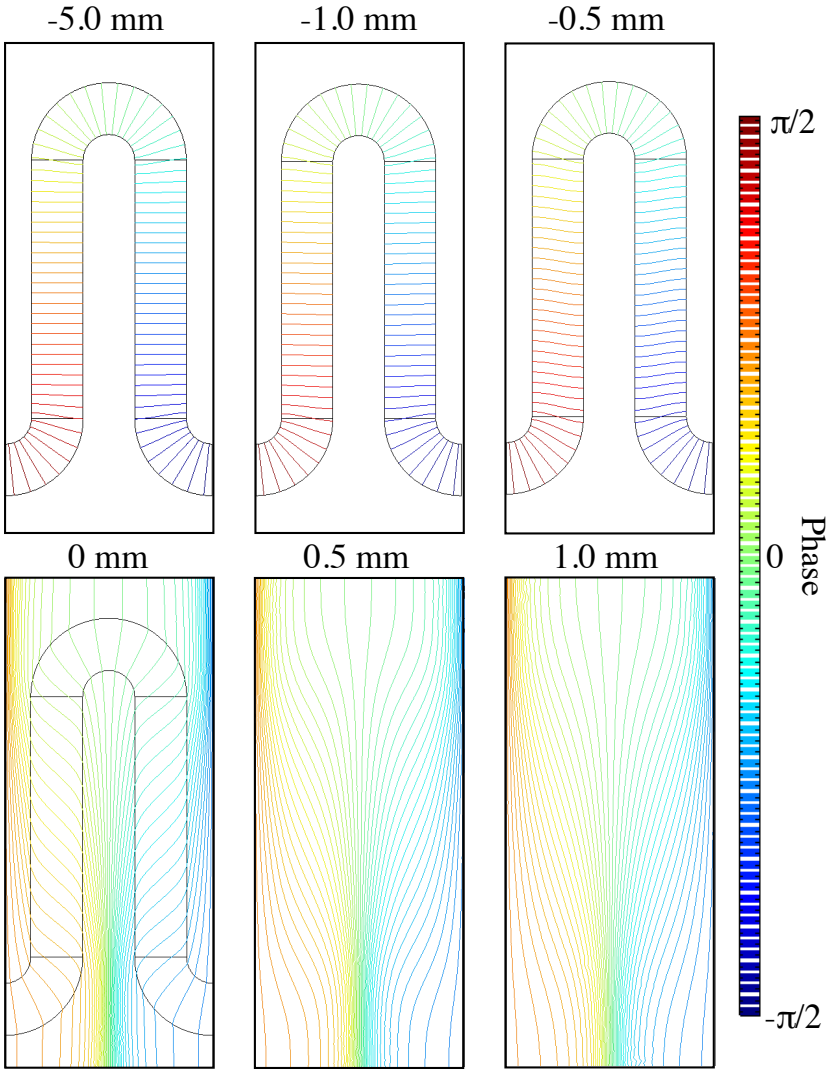

Fig. 5.10 Isophase contours at various depth within the grooves of a $h = 5$ mm, $w = 1$ mm, $d = 5$ mm meander channel. The surface is at z = 0 mm, and the bottom of the channel is at z = −5 mm.

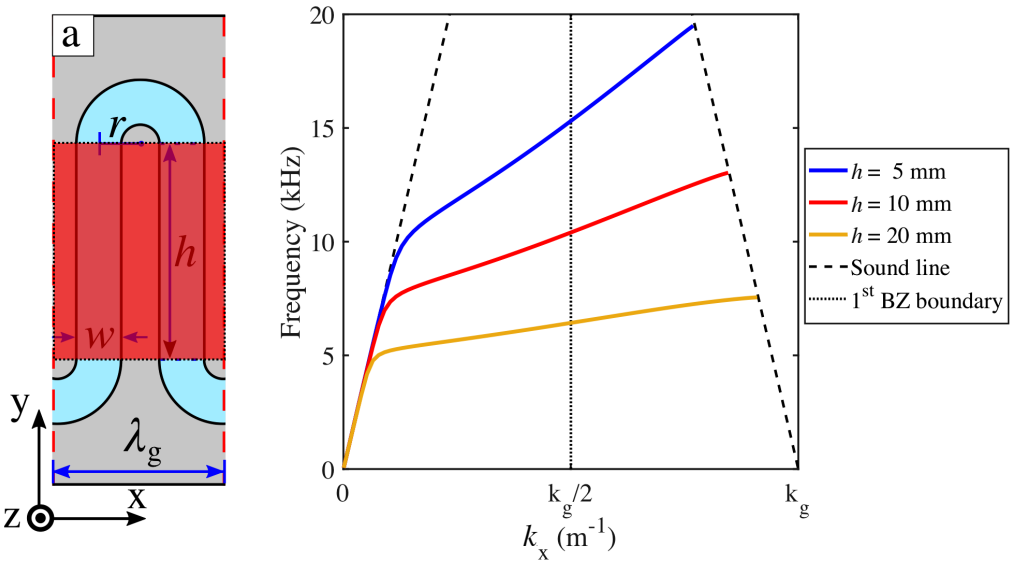

Fig. 5.11 (**a**) Schematic of the surface of a covered meander unit cell comprised of an air-filled channel (blue) of depth $d = 5$ mm in an acoustically-rigid material (grey), covered by a thin (0.1 mm) acoustically rigid material (red). The depth is in the negative z direction, and the acoustic surface wave propagates in the positive x-direction. Here, $\lambda_g = 4$ mm, $w = r = 1$ mm, and $h = 5$ mm. (**b**) FEM model non-radiative dispersion for different values of h.

5.8 Covered Meander

In the previous section, one characteristic of channels with a large h is the strong coupling to free radiation, reducing the size of the near-linear region of the dispersion. A simple way to reduce the strength of coupling is to reduce the area of the surface which can directly couple to free radiation. One way to achieve this is to place a thin, acoustically-rigid material over the vertical sections of the meander channel. Figure 5.11(a) shows such a structure. Note, due to how the thin covering has been placed the structure maintains its glide symmetry. As the height is increased only the curved sections of the channels are open; therefore, for all values of h the same area is open which allows similar coupling to free radiation. The effect of varying h can be seen in Figure 5.11. All curves show little coupling to free radiation and large near-linear regions. However, in contrast to the uncovered system, as h is increased

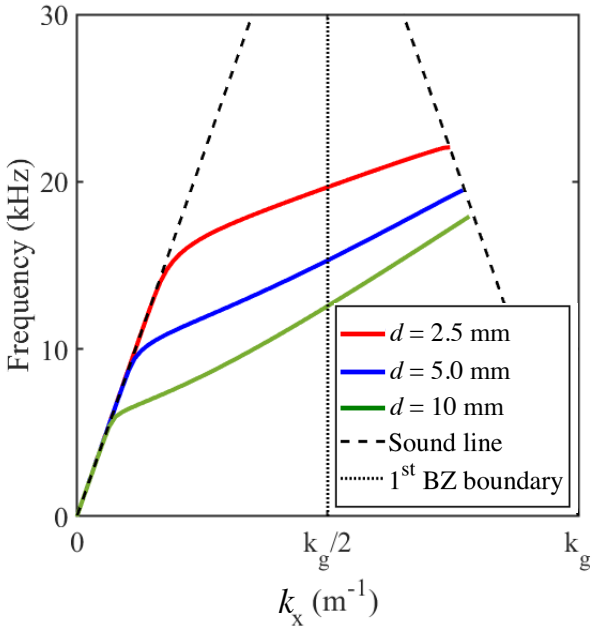

Fig. 5.12 FEM model non-radiative dispersion for different values of d for a covered meander of parameters $h = 5$ mm, $w = 1$ mm, and $\lambda_g = 4$ mm.

the frequency where the mode starts to disperse lowers substantially. To explore this further, d will now be varied.

The effect of varying d for covered meanders has been explored. The resulting dispersion relations are shown in Figure 5.12. The effect of changing the depth is much more subtle than the uncovered case, as coupling to free radiation is not as prevalent. Interestingly the frequencies where the mode begins to disperse and cross the first Brillouin zone boundary are all smaller than the equivalent uncovered structure. To explore this further, the frequency of the modes at $k_g/2$, have been calculated as a function of d, for both the covered and uncovered meanders in Figure 5.13. For $d > 15$ mm, there is little difference between the two systems, suggesting the standing wave at $k_g/2$ arise from the same condition. Figure 5.14(a-d) shows the fields for the two systems for $d = 19.5$ mm. At the bottom of the channel (a,c) it can clearly be seen that $\lambda_{sw} = 2l_p$. For the systems considered $\lambda_{sw} = 32.6$ mm; therefore, $f_{sw} = 10.5$ kHz. While this is below the frequency which the FEM model

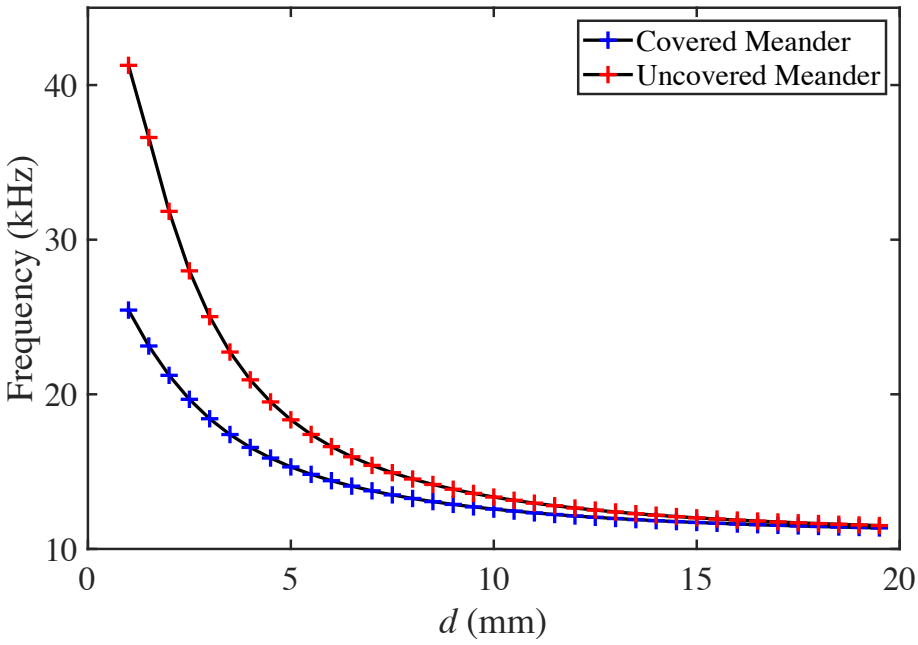

Fig. 5.13 FEM model of the frequency of the modes at $k_g/2$ for both a uncovered and covered meanders. Both of parameters $h = 5$ mm, $w = 1$ mm, and $\lambda_g = 4$ mm.

in Figure 5.13 predicts of 11.5 kHz, naively the longest l_p was chosen by considering the path length directly along the centre of the channel, Figure 5.15(a). However, considering the experimental fields shown in Figure 5.9(b), this is not the case. It can be see that the fields in fact take the shortest route available, being essentially a straight line from the centre of one curved channels to the centre of the next half a period away, Figure 5.15(b). With this shorter path, one can assume that near the first Brillouin zone boundary a l_p of 29.1 mm may be used, giving $f_{sw} = 11.8$ kHz, which is in better agreement with the model.

For $d < 15$ mm the frequencies of the two systems start to diverge, with the uncovered meander increasing in frequency at a faster rate as d decreases. If the uncovered system is considered for $d = 0.5$ mm, the FEM model data in Figure 5.13 predicts $f_{sw} = 41.2$ kHz. Figure 5.14(g-h) shows the fields of the modes at the bottom and on the surface of the channel. At the bottom of the channel, the field appears similar to the previously discussed large d system. However, the fields on the surface show a subtle, but important difference. If we consider k_z, for both depths

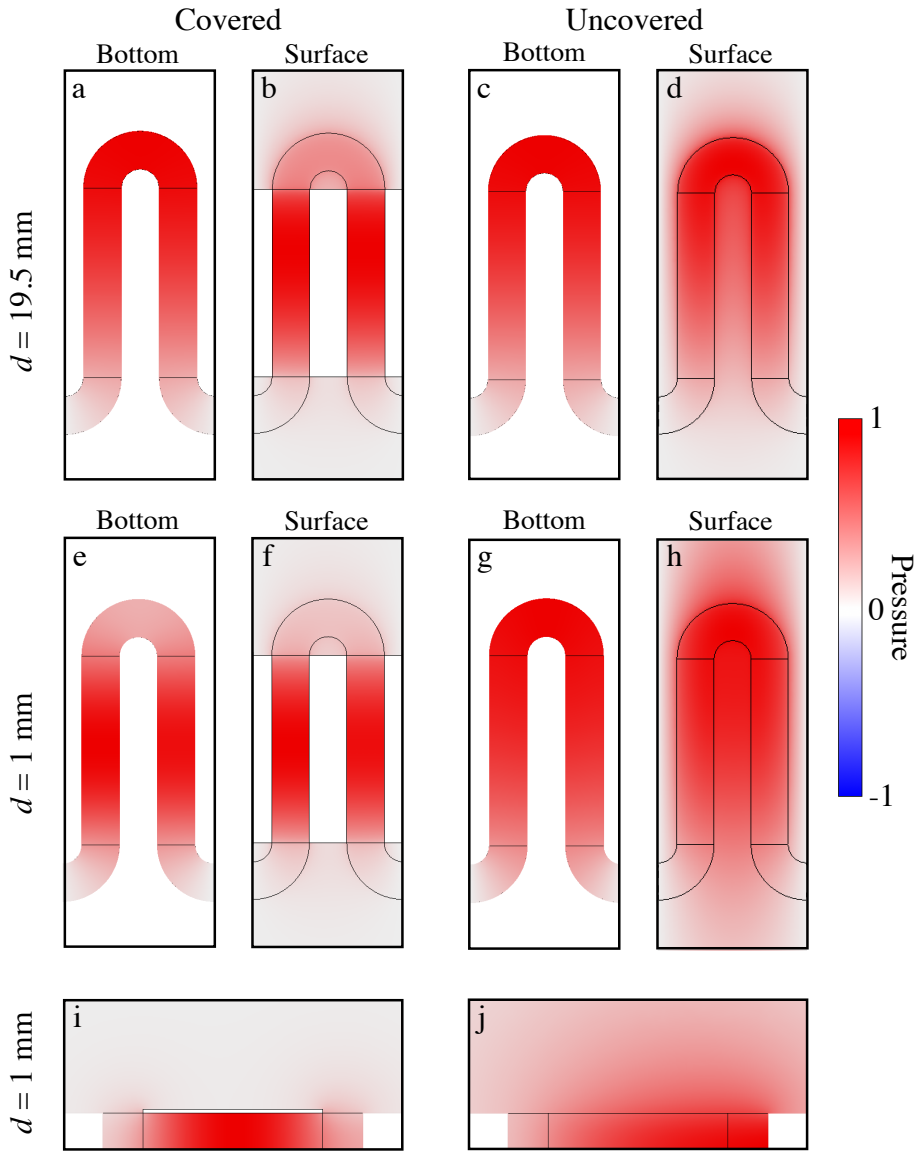

Fig. 5.14 Instantaneous pressure fields at $k_g/2$ for $d = 1$ mm and $d = 19.5$ mm. a,c,e,g) Pressure fields at the bottom of the channel ($z = -d$. b,d,f,h) Fields on the surface of the channel ($z = 0$). i-j) Pressure field of a surface in the y-z plane in the centre of one of the straight channels ($x = 1$ mm).

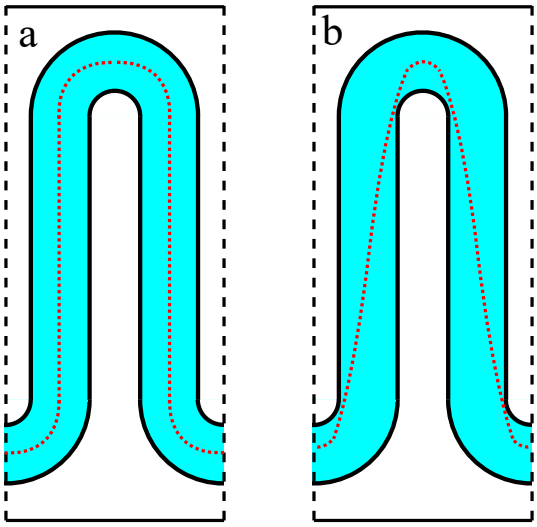

Fig. 5.15 Schematic of different l_p in a meander unit cell (red, dotted lines). a) Shows the path where the wave propagates in the centre of the channel At kg/2, $\lambda_{sw} = 2l_p$. b) A shorter l_p where the wave propagates diagonally across the vertical sections.

of the uncovered meander, it is obvious that the k_z is purely imaginary due to it being an ASW. When $d = 19.5$ mm, k_z is larger than for $d = 1$ mm, due to the data being taken at $k_x = k_g/2$ and due to the conservation ($k_0 = \sqrt{k_x^2 + k_z^2}$, assuming no y component) of energy, a lower frequency indicates a larger k_z component. Therefore, the fields are more confined in the channel for $d = 19.5$ mm. The fields in Figure 5.14(d) show a clear reduction in the pressure between the two straight channel. In contrast, for $d = 1$ mm this reduction does not exist. From this it is assumed that $\lambda_{sw} = 2\lambda_g$, resulting in $f_{sw} = 42.9$ kHz.

For the covered meander where $d = 1$ mm, the FEM model data in Figure 5.13 predicts $f_{sw} = 25.4$ kHz. Figures 5.14(e-f) show the pressure fields at the bottom of the channel and on the surface. It is immediately obvious that the maximum pressure is located in the centre of the straight channels, reducing in intensity near the uncovered sections suggesting an open-ended cavity resonance. Figure 5.14(i) shows a cross-section in the centre of one of the straight channels, which displays this resonance more clearly. Here, $\lambda_{sw} = 2(h + e.c)$, where $e.c$ is an end correction

for the cavity. If one naively assumes $e.c = 2$ mm, this then gives an estimate of f_{sw} = 24.5 kHz, which is similar to what the FEM model predicts.

The difference between frequencies of the mode at $\mathrm{k_g}/2$ for small d arises from different standing wave conditions. For the uncovered meanders, the standing wave condition is $\lambda_{\mathrm{sw}} = 2\lambda_{\mathrm{g}}$. For covered meanders, the standing wave condition comes from an open-ended cavity resonance of the form $\lambda_{\mathrm{sw}} = 2(h + e.c)$. For large d, the standing wave condition for both systems is $\lambda_{\mathrm{sw}} = 2l_{\mathrm{p}}$.

5.9 Conclusions

In this chapter, glide-symmetric metasurfaces composed of space-coiled (meandering) cavities have been studied and show a broadband reduction in the group velocity of the supported acoustic surface waves. We have shown that, as the length of the meander is increased, the group velocity decreases, with values of 192.4 ($\pm$ 15.1) $\mathrm{ms^{-1}}$, 55.6 ($\pm$ 4.1) $\mathrm{ms^{-1}}$ and 33.4 ($\pm$ 3.1) $\mathrm{ms^{-1}}$ obtained for different length channels. An increase in the channel width also results in a decreased attenuation of the ASWs due to the thermoviscous boundary layers occupying a smaller proportion of the channel. Covering the straight sections of the channels reduces the coupling strength to free radiation and changed the standing wave condition at $\mathrm{k_g}/2$ for small values of d. For the uncovered meanders, the standing wave condition is $\lambda_{\mathrm{sw}} = 2\lambda_{\mathrm{g}}$. For covered meanders, the standing wave condition comes from an open-ended cavity resonance of the form $\lambda_{\mathrm{sw}} = 2(h + e.c)$. For large d, the standing wave condition for both systems is $\lambda_{\mathrm{sw}} = 2l_{\mathrm{p}}$. This work may lead to novel structures for controlling the propagation of acoustic power over such surfaces.

In the following chapter we will move from airborne to underwater acoustics. The dispersion of surface acoustic waves supported on soft-solid plates structured with

simple gratings (one groove per period) will be investigated through FEM modelling and experimentally verified.

Chapter 6

Modified Coupled-Scholte Waves on Thin Structured Plates

6.1 Introduction

In this chapter, simple acrylic gratings (one groove per period) will be investigated. While similar to Chapter 4, these gratings will be investigated in an underwater environment. The change from airborne to underwater acoustics no longer allows for the solid to be treated as acoustically-rigid, as the impedances of the acrylic and the water are similar. This allows for the propagation of acoustic energy along the solid-fluid interface, with fields decaying in both materials. The dependence on the characteristics of the surface waves on the structure of the simple groove will be explored. The dispersion of acoustic surface waves will be characterised experimentally on a sample of parameters $h = 2.70$ mm, $w = 1$ mm, $d_\mathrm{p} = 5.63$ mm, and $\lambda_\mathrm{g} = 4$ mm.

In this chapter, the dependence of the dispersion characteristics on the structure of simple gratings are investigated through FEM modelling and experiments.

6.2 Background

Acoustic metamaterials for underwater sound absorption have been the topic of many investigations. One common method to increase the absorption of acoustic energy, is to use periodic inclusions within a soft material – such as rubber. Ivansson investigated the sound absorption of a thin viscous-elastic anechoic coating with spherical air-filled cavities in a 2D periodic array, both theoretically and numerically. The losses occur due to the multiple scattering by air-filled cavities, and it is shown that the majority of the losses occur within the vicinity of the cavities. Here, coatings much thinner than quarter-wavelength were described, this means that the absorber is much thinner that the incident wavelength used.[153] Leroy et al. investigated the absorption from a bubble metascreen - a sub-wavelength layer of bubbles immersed in a soft elastic matrix. The results showed that by using only one layer, broadband super absorption could be achieved.[92] Recently, pentamode materials (PM) have been the topic of many studies. These structures were first proposed by Milton and Cherkaev [154]. They exhibit fluid-like properties since the effective bulk modulus is orders of magnitude greater than the shear modulus[155]. Due to their non-resonant nature these materials are inherently broadband in nature. These structures have been shown to have applications in cloaking [156–159].

The modes supported on a fluid-loaded elastic plate have been the focus of many studies[160–162]. These modes, sometimes called quasi-Scholte modes may be used to extract the material properties of the fluid.[160, 163] The dispersion of these modes appears not to have been experimentally characterised at least to a similar extent to the band diagrams obtained in the previous chapters. Furthermore, to the authors knowledge there appears to be no experimental studies on the effect of adding structure to the interfaces. In this chapter, the effect that structuring one of the interfaces has on the dispersion will be investigated.

6.3 Coupled Scholte Waves on Thin Plates

As discussed in Section 2.7.1, a thin solid plate immersed in a fluid will support two coupled surface modes: a symmetric and anti-symmetric mode. These modes are coupled Scholte waves, as due to the narrow thickness, the two Scholte modes on both of the interfaces interact. Here, acrylic plates in water are explored. As discussed in Section 2.7.1 acrylic can be describe as a soft-solid material. The transverse (shear) wave speed is less than the speed of sound in water, this means that both modes exist in the non-radiative domain. The parameters of the acrylic-based material used in the FEM model are $\rho = 1190$ kgm^{-3}, $E = 4.5$ GPa, $\nu = 0.35$ [164]. With these parameters the wave speed in the acrylic are $c_\mathrm{t} = 1184$ ms^{-1} and $c_\mathrm{l} = 2464$ ms^{-1}. One should note the viscoelastic losses are negligible for Scholte modes propagating along the plate, as lossless transmission occurs through the plate.[162] Another feature is the frequency dependant Young's modulus. Previous measurements have shown that for the frequency range of interest, a Young's modulus of 4.5 GPa proved to be suitable, this is larger than the standard value of E 3.2 GPa literature[164]. For all the systems modelled within this chapter, the viscous effects of the fluid can be neglected as at the frequency range of interest (<150 kHz) the Reynolds numbers are greater than the critical value where they would have to be considered.[165] The FEM modelling presented in this chapter neglects both the viscoelastic effects of the solid and the thermoviscous effects of the fluid.'

The effect of the plate thickness (d_p) on the dispersion of the modes is shown in Figure 6.1. It is noticeable that as the plate thickness is increased, the anti-symmetric mode (solid line) disperses over a smaller surface wavevector (k_x) range. For example, for the case of $d_\mathrm{p} = 1$ mm the mode disperses for all values of k_x; however, as the thickness is increased further the mode has almost constant group velocity. For a plate of $d_\mathrm{p} = 12$ mm, the anti-symmetric mode disperses over a very small k_x

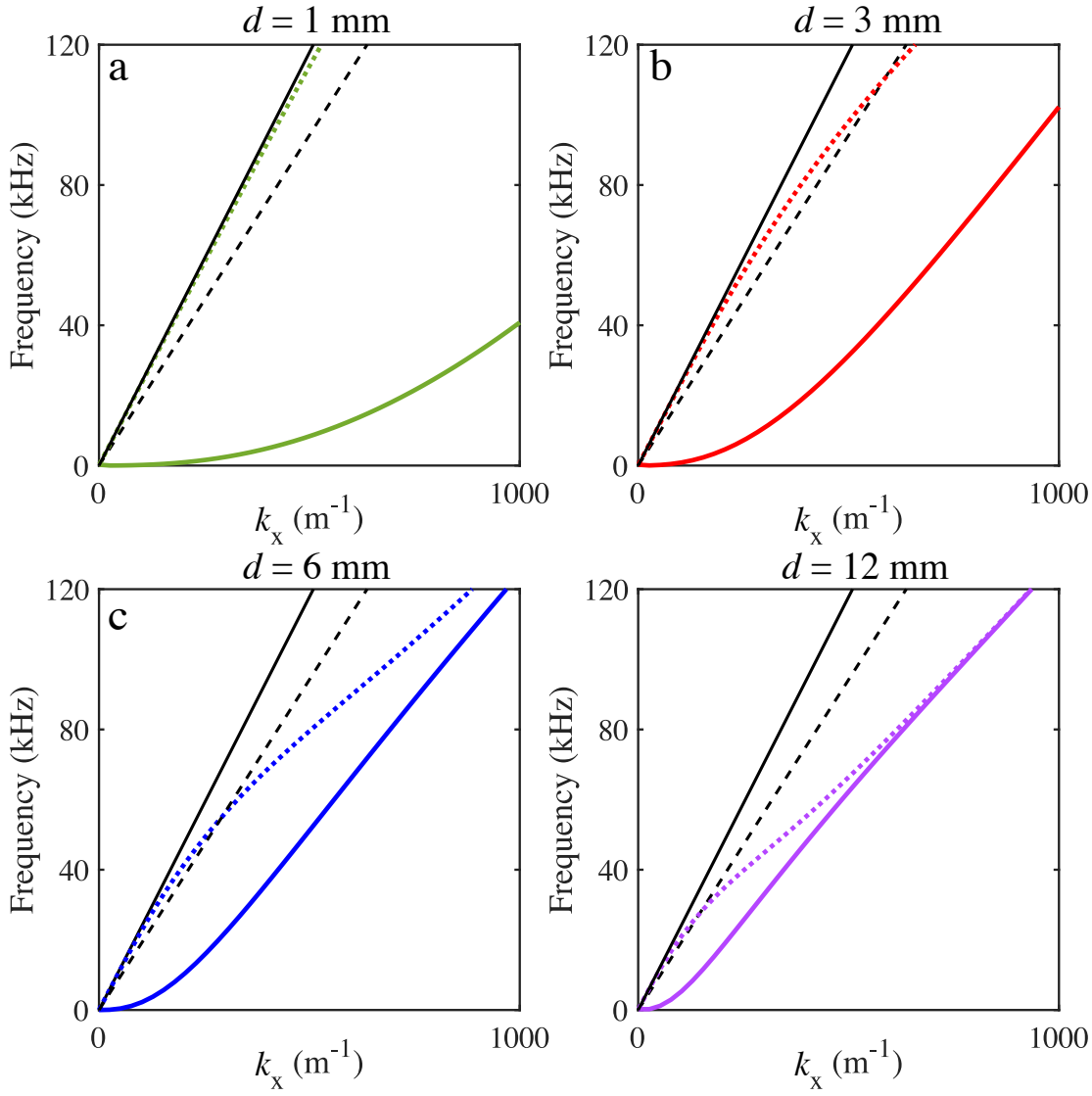

Fig. 6.1 FEM non-radiative dispersion of acrylic plates of varying thicknesses (d_p). The solid, black line is the water sound line. The dashed, black line is the transverse velocity of acrylic. The coloured, solid line is the anti-symmetric mode, and the coloured, dotted line is the symmetric mode.

range. Considering the symmetric mode, for $d_{\mathrm{p}} = 1$ mm the mode is located at the sound line up to a frequency of about 80 kHz and disperses at higher frequencies. As d_{p} is increased, the frequency at which the mode appears to begins to deviate away from the sound line reduces. When the plate of $d_{\mathrm{p}} = 12$ mm is considered, it can be seen that the symmetric mode asymptotes to the same constant gradient as the anti-symmetric mode. This constant gradient is the Scholte interface wave speed. One may understand why both of these modes approach this line when the penetration depth of the individual Scholte waves on each interface is considered. It is known that the penetration depth is on the order of one wavelength (λ_{sw})[34]. Due to the inverse relationship as k_{sw} increases the surface wavelength decreases then, once the plate thickness becomes larger than $2\lambda_{sw}$, the modes on each interface no longer interact. Each interface supports a single interface Scholte wave. Therefore, the modes tend to the Scholte wave velocity of a mode that exists on the interface between a solid half-space and fluid half-space. As d_{p} is decreased, the k_{sw} at which both modes tend to the Scholte wave velocity increases. Now, the effect of adding structure to thin acrylic plate will be explored.

6.4 Surface Acoustic Waves on Monogratings

The introduction of a periodic structure to a plate supporting SAWs leads to interesting characteristics. A shallow simple grating (one groove per period) is explored to investigate the effect of adding structure to an acrylic plate.

Consider a 6 mm thick acrylic plate with a zero depth 4 mm periodicity, the expected dispersion diagram is shown in Figure 6.2. The periodicity of the system introduces diffraction and band-folding about the Brillouin zones. In the unstructured system, there existed two coupled Scholte modes: one symmetric, and the other anti-symmetric. However, once periodicity is introduced into a system, there now exists

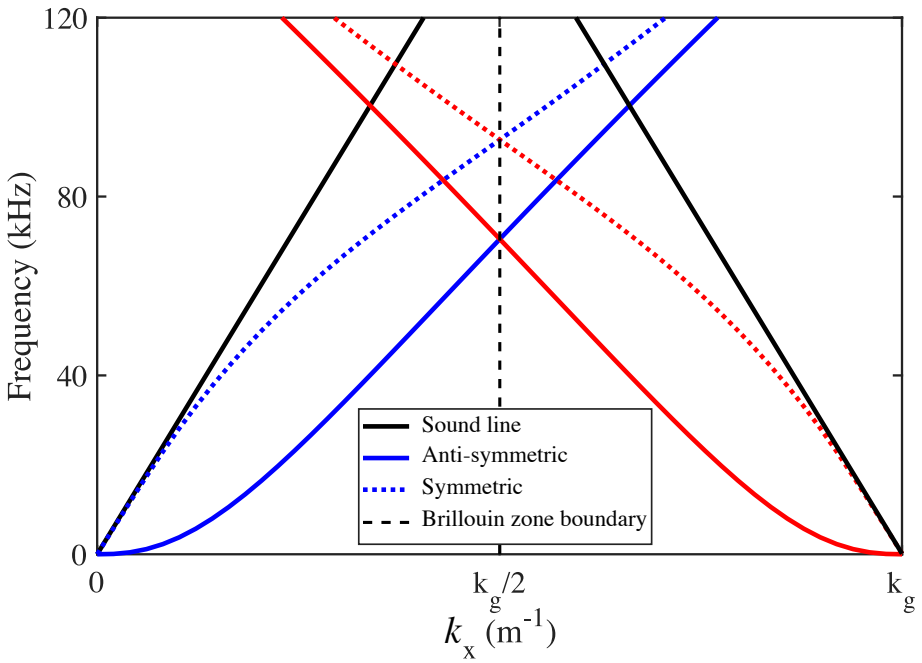

Fig. 6.2 FEM model band structure for a 6 mm thick acrylic plate of thickness with a zero depth 4 mm periodicity. Blue lines represents modes originating for $k_x = 0$. Red lines represents modes originating for $k_x = k_g$. One should note that due to the infinitesimal perturbation added, the coupling into the diffracted modes will be infinitely weak.

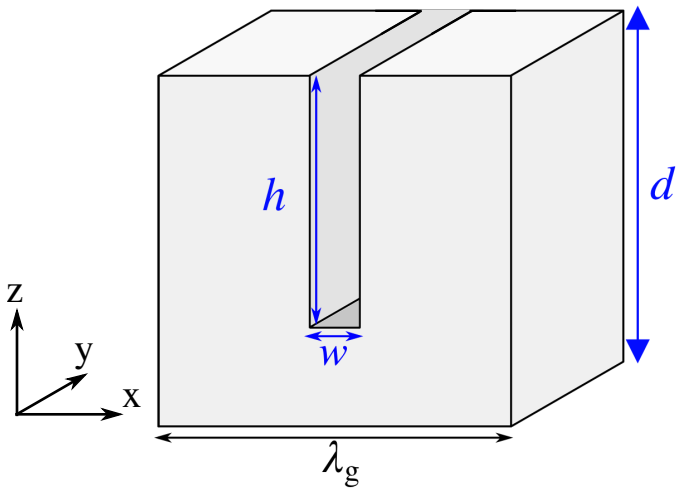

Fig. 6.3 Schematic of the unit cell of the monogratings considered in this chapter. λ_g is the pitch, h is the groove depth, d_p is the plate thickness, and w is the groove width. The sample is infinite in the y-direction.

two symmetric and two anti-symmetric modes. These additional modes originate from Bragg scattering. Now, at the first Brillouin zone boundary ($k_x = k_g/2$) there exist two standing waves on the surface. In the first Brillouin zone, there is a simple crossing between the diffracted anti-symmetric mode (solid-red line) and the undiffracted symmetric mode (dashed-blue line), in a system with finite perturbation with real grooves added these two modes would anti-cross and a band-gap would form. However, when a non-zero perturbation is added, caution needs to be taken as adding structure may add more degrees of freedom to the surface; therefore, new modes may be supported.

6.5 Groove Depth Dependence

The structures which will be investigated are monogratings. A unit cell of a monograting of groove height, h, is shown in Figure 6.3. Firstly a monograting with a

shallow groove is considered, such that $h \ll d$, with parameters ($h = 0.1$ mm), $d_{\mathrm{p}} = 6$ mm, $w = 1$ mm and $\lambda_{\mathrm{g}} = 4$ mm.

For the shallow grating considered, the band diagram is shown in Figure 6.4(a). For the lower two modes shown (blue and red curves), as k_{x} approaches $\mathrm{k_g}/2$ the modes behave as expected for an unstructured plate. However, at the region labelled A, there is an anti-crossing which arise due to mode repulsion. Two modes may cross only if there exists exact symmetry between the two modes, which allows for degenerate eigenvalues. However, when the modes are not symmetric, the modes become coupled, and the degeneracy no longer exists; therefore, the modes 'repulse' each other. An example of this can be seen in Figure 6.5 where a system where mode crossing occurs (the structure in Figure 6.2) and one where mode repulsion occurs (the structure in Figure 6.4). If we compare the total displacement fields ($A = \sqrt{u_{\mathrm{d}}^2 + w_{\mathrm{d}}^2}$, where u_{d} is the x-displacement, and w_{d} is the z-displacement), of the points labelled i and ii, to the fields at the same k_{x} for the system presenting mode repulsion, labelled iii and iv, we see that they are near identical. Here, we have gone from a system of two modes which do not interact and cross, to an upper and lower mode, which has split due to the coupling of the two modes. Considering the fields of the lower mode in the mode repulsion system, we can see that the mode changes characteristic either side of the crossing, which is a characteristic feature of mode repulsion.[166].

Next, a change of language is necessary, since unstructured plates are no longer being investigated - there are no true symmetric and anti-symmetric modes, as the addition of structure onto only one of the interfaces inherently makes this impossible; therefore, these modes will be referred to as the modified symmetric (MS) and the modified anti-symmetric (MA) coupled-Scholte modes. This anti-crossing arises from the MS mode originating from $k_{\mathrm{x}} = 0$ coupling to the diffracted MA mode originating from $k_{\mathrm{x}} = \mathrm{k_g}$. At $\mathrm{k_g}/2$, there now occur two additional anti-crossings, as the modes

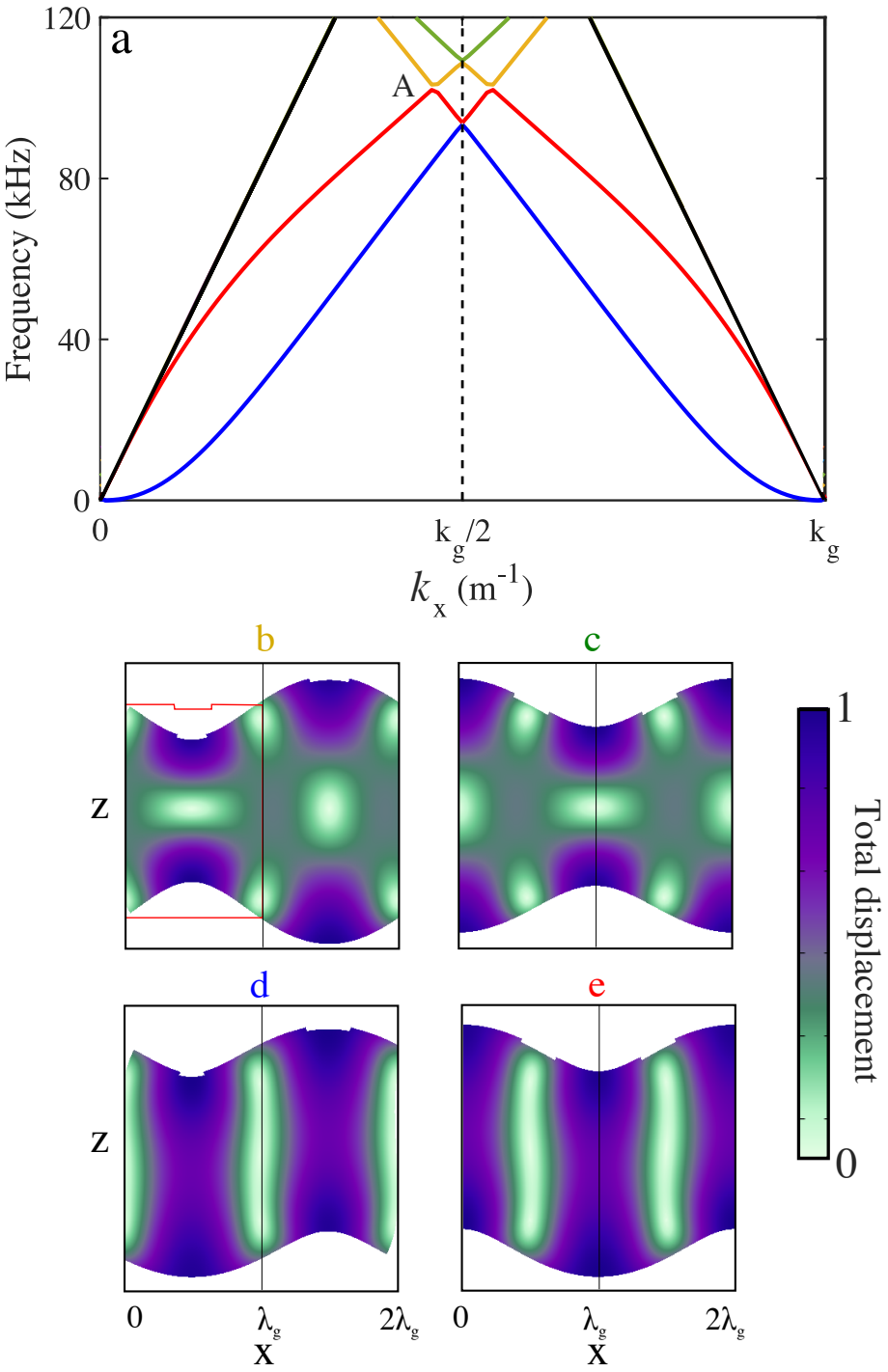

Fig. 6.4 a) FEM model of the non-radiative dispersion for a shallow monograting with parameters $d_\mathrm{p} = 6$ mm, $\lambda_g = 4$ mm, $w = 1$ mm, and $h = 0.1$ mm. b-e) Total displacement fields ($A = \sqrt{u_\mathrm{d}^2 + w_\mathrm{d}^2}$, where u_d is the x-displacement, and w_d is the z-displacement). of the modes at the first Brillouin zone boundary ($k_x = \mathrm{k}_g/2$). The solid red line in (b) represents the outline of the undisplaced plate. Note: the amplitudes have been normalised to the maximum values, and also the physical displacement shown has been greatly exaggerated.

from $k_x = 0$ couples with the mode from $k_x = k_g$, for both the MA modes, and both the MS modes. Therefore, four standing-wave states now exist at $k_g/2$, two symmetric-like states and two anti-symmetric-like states.

The normalised total displacement fields ($A = \sqrt{u^2 + w^2}$) of the four standing waves are presented in Figures 6.4(b-e). The lower frequency pair relate to the MA modes, at $k_x = k_g/2$ there is a splitting of 297 Hz. The origin of this splitting is explained by the difference in the displacement fields of the two modes. These modes differ by a half-wavelength displacement in the x-direction. In Figure 6.4(d) the maximum displacement in the z-direction occurs at $x = \lambda_g/2$ for the low-frequency MA mode, where the centre of the groove is located. For the high frequency MA mode [Figure 6.4(e)], there is a zero in the z-displacement at $x = \lambda_g/2$. The splitting arises from a mass-loading effect from the added structure, which lowers the frequency of the mode. For the pair of MS modes, this is also the case. The mode with the maximum z-displacement at $x = \lambda_g/2$, Figure 6.4(b), is the low frequency MA mode, while the high frequency MA mode has zero z-displacement at $x = \lambda_g/2$.

It is of interest to increase h and observe how the band structure is perturbed. By increasing h, the effect of the mass loading will increase, which will increase the size of the splittings at $k_g/2$. To investigate the effect that varying h has on the band structure, the modes for gratings of $d_p = 6$ mm, $w = 1$ mm, $\lambda_g = 4$ mm, and $h = 1$ mm, 2 mm, 3 mm, and 4 mm are investigated. Figure 6.6 shows the evolution of the modes as the depth is increased. For $h = 1.0$ mm there is an additional resonance in the system compared to the previously discussed $h = 0.1$ mm. One may notice that there is an anti-crossing between the red and blue curves (labelled A) which lowers in frequency as h is increased; also the mode becomes near flat-banded for an increasing k_x range. There is a second anti-crossing (labelled B) between the yellow and green curves. As h is further increased, it becomes more difficult to identify each mode just from the band structure. To aid in the identification of the modes,

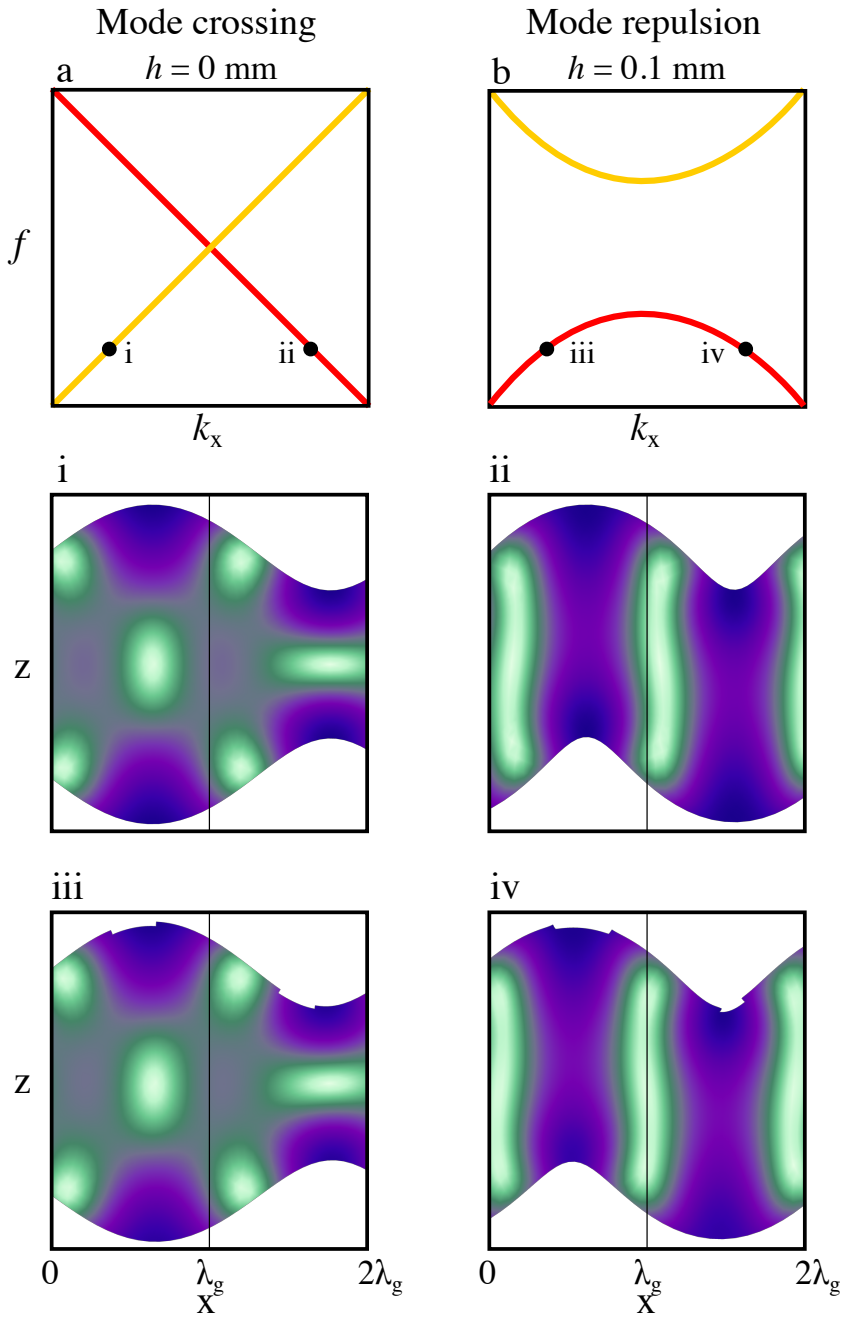

Fig. 6.5 a) Schematic of a dispersion showing mode crossing from a symmetric system (an unstructured plate). b) Schematic of mode a dispersion showing mode repulsion for a non-symmetric system ($h = 0.1$ mm, $\lambda_g = 4$ mm). i-iv) Total displacement fields ($A = \sqrt{u^2 + w^2}$, where u is the x-displacement, and w is the z-displacement for the eigenvalues labelled in (a) and (b). Note: the amplitudes have been normalised to the maximum values, and also the physical displacement shown has been greatly exaggerated.

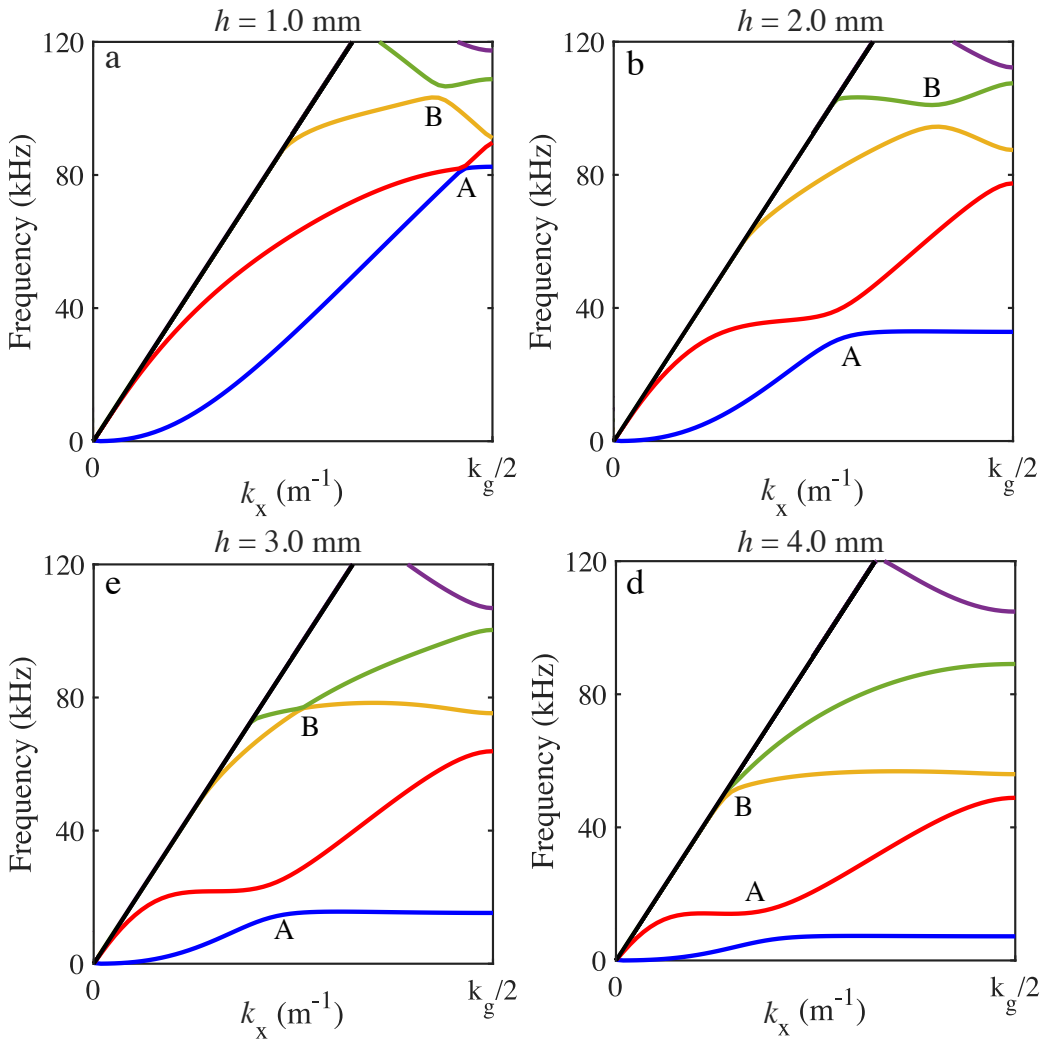

Fig. 6.6 FEM model dispersion for gratings of various groove depths, $d_p = 6$ mm, $w = 1$ mm, $\lambda_g = 4$ mm. a) $h = 1$ mm. b) $h = 2$ mm. c) $h = 3$ mm. d) $h = 4$ mm.

the fields at $k_g/2$ for the $h = 4$ mm grating are displayed in Figure 6.7. For the first mode shown 6.7(a), much of the displacement occurs in the solid pillars between the grooves. This movement of the pillars is characteristic of a cantilever mode (CM); however, coupling between each pillar through the supporting plate is shown. A higher order cantilever mode can be seen in 6.7(c). The MA mode can be seen in 6.7(b) and 6.7(d). The field in 6.7(e) is the MS_1 mode. The other symmetric-like mode (MS_2) does not appear in the frequency range shown. Notice how the fields of mode 6.7(e) are very similar to the fields of the unstructured system shown in Figure 6.4(c), this is due to them being the equivalent modes in each system.

One method to aid identification of the modes is to observe the frequency at which the modes cross the first Brillouin zone as the groove depth is increased. The results from such modelling can be seen in Figure 6.8. The first immediately obvious feature is that as h increases CM_1 lowers in frequency. If the pillars are to be treated as cantilevers, one may naively assume that the resonance frequency will reduce proportionally to $1/\sqrt{h^4}$.[167] This mode as h is increased, anti-crosses with MA_2, labelled A. Here, one may have noticed for $h = 0.1$ mm that the mode where the maximum z-displacement occurring at $x = 0$ is the second high-frequency MA mode. However, for $h = 4$ mm, the mode with maximum z-displacement occurs at $x = 0$ is now the low-frequency MA mode. The anti-crossing with CM_1 explains this change, which shifts the frequency higher than the original, low-frequency MA mode for $h = 0.1$ mm. Also, MA_2 does not anti-cross with the mode but exists in the gap formed by MA_1 and CM_1. At $k_g/2$ these modes are standing wave solutions of the same pair, the difference between the two if that the maximum in the displacement field is shifted by $\lambda_g/2$. One of the modes disperses little with h. This mode is MS_1. It is understandable why the modes are near dispersionless at small h values, as the fields of these modes have a node in the displacement field at the location of the pillar. Therefore, the introduction of the groove barely, if at all, affects the frequency of the

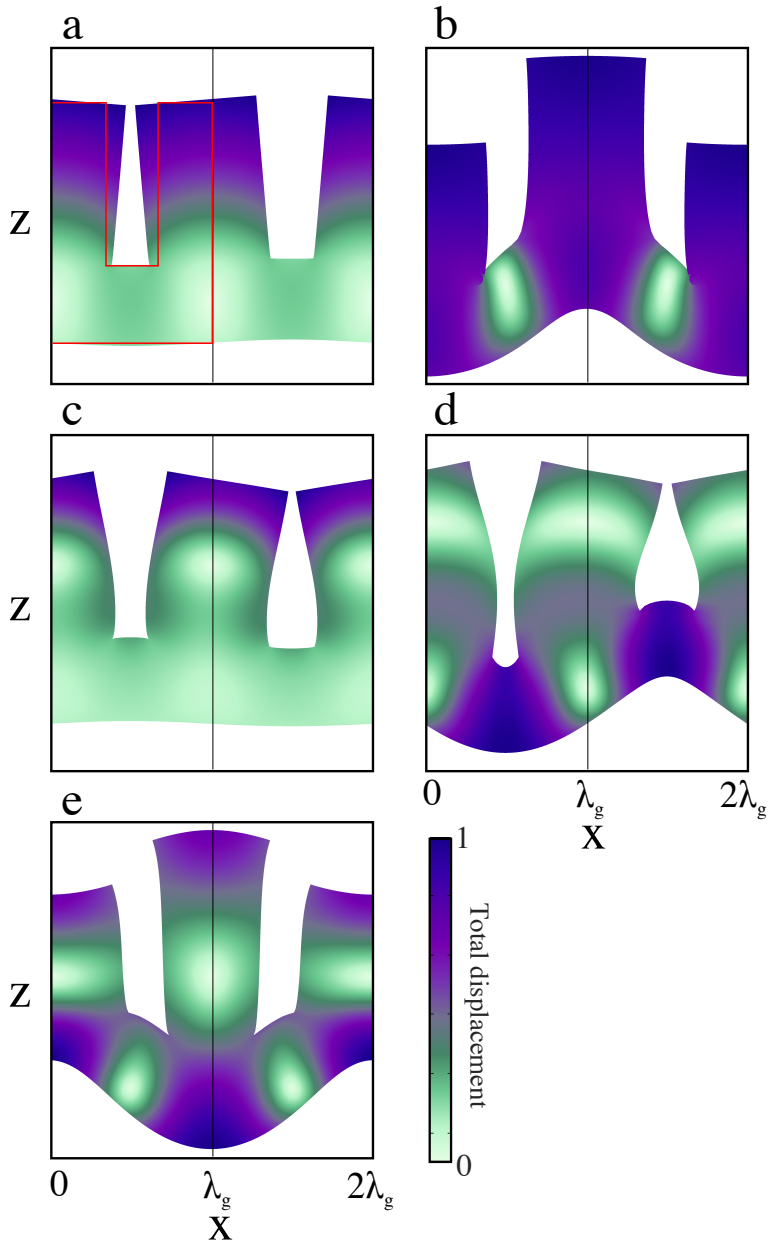

Fig. 6.7 FEM model total displacement fields for a grating of parameters $w = 1$ mm, $h = 4$ mm, $d_\mathrm{p} = 6$ mm, and $\lambda_\mathrm{g} = 4$ mm. In order, they are CM_1, MA_1, CM_2, MA_2, and MS_1. The solid red line in (a) represents the outline of the undisplaced plate.

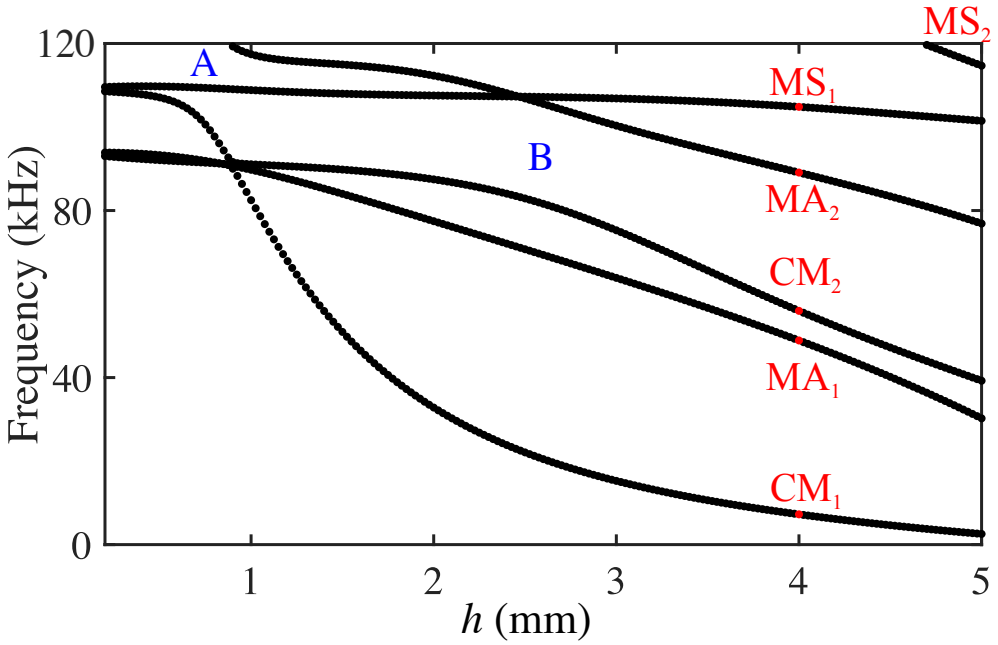

Fig. 6.8 Frequency of the modes at $k_g/2$ as a function of h. $MA_{1,2}$ are the modified anti-symmetric modes, $MS_{1,2}$ are the modified symmetric modes, and $CM_{1,2}$ are the fundamental and first order cantilever modes. The modes are labelled for the displacement fields at $h = 4$ mm.

standing wave solution. A second anti-crossing labelled B occurs between CM_2 and MA_2. It can be seen in the fields shown in Figure 6.7 (c-d) that the fields of these two modes are somewhat similar. For MA_2, the highest displacement is located in the plate; however, for CM_2, the maximum displacement is located in the pillar. For each of these modes, when the mode is excited a characteristic displacement of the other mode is also seen. For MA_2, the pillars displace similarly to how they displace for CM_2. For CM_2, there occurs a small anti-symmetric displacement of the field. These common features explain the anti-crossing. As h increases, some modes lower in frequency. Ignoring the cantilever modes, this also happens for MA_1 due to the locations of the displacement anti-nodes. These anti-nodes are located at $x_{\text{a-node}} = n\lambda_g$ ($n \in 0,1,2,3...$) because the displacement maxima are located at the pillars, we observe that increasing the effect of the mass-loading is a lowering of the frequency.

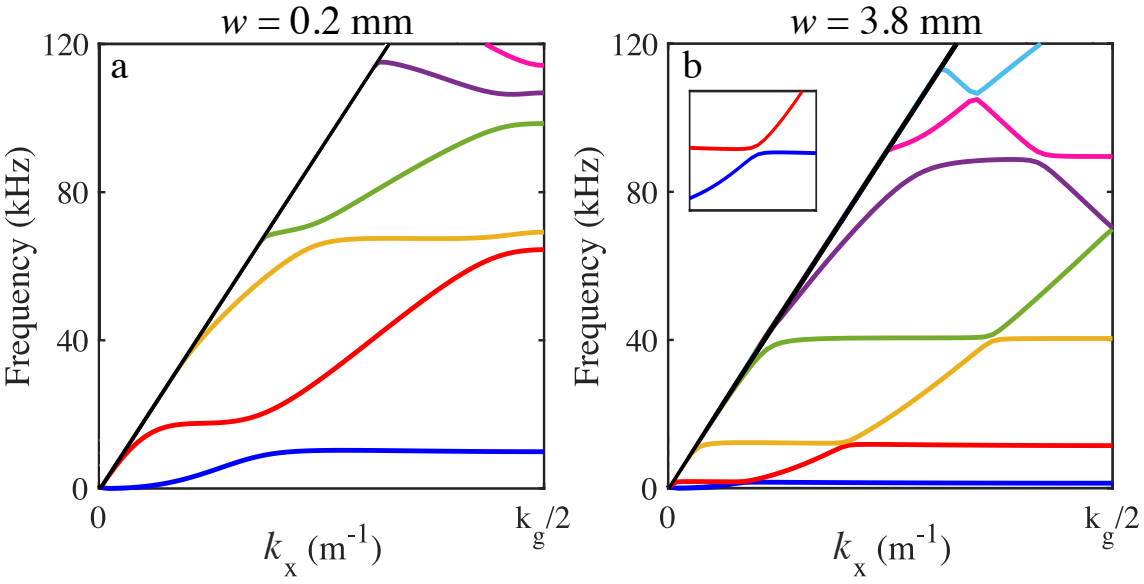

Fig. 6.9 a) FEM model non-radiative band diagram for a grating of parameters $w = 0.2$ mm, $d_p = 6$ mm, $h = 3$ mm, $\lambda_g = 4$ mm. b) FEM model non-radiative band diagram for a grating of parameters $w = 3.8$ mm, $d_p = 6$ mm, $h = 3$ mm, $\lambda_g = 4$ mm. Inset: a view of the anti-crossing between the red and blue curves.

6.6 Groove Width Dependence

Here we explore the effect of varying just the groove width while keeping the other parameters fixed at $h = 3$ mm, $d_p = 6$ mm, $w = 1$ mm, and $\lambda_g = 4$ mm. Initially, two gratings will be considered, where $w = 0.2$ mm and 3.8 mm. In the small width case, the width of the groove compared to the unit cell width is $w/\lambda_g = 0.05$. The band diagram for this system is shown in Figure 6.9(a). The lower two modes disperse similarly to the sample in Figure 6.6(c), where $w = 1$ mm; however, the CM_2 mode appears at a lower frequency and anti-crosses with the MS_1. The yellow and green curves represent the two MA modes at $k_g/2$. The magnitude of the band splitting is 29.3 kHz. Since the two MA modes maxima displacement are translated by half a period, it is understandable that the mode where the maxima in displacement are located beneath the pillar, will be heavily perturbed by the pillar - as the pillar is now occupying 95% of the backplate. For the MS modes, the gap at $k_g/2$ is 7.4 kHz,

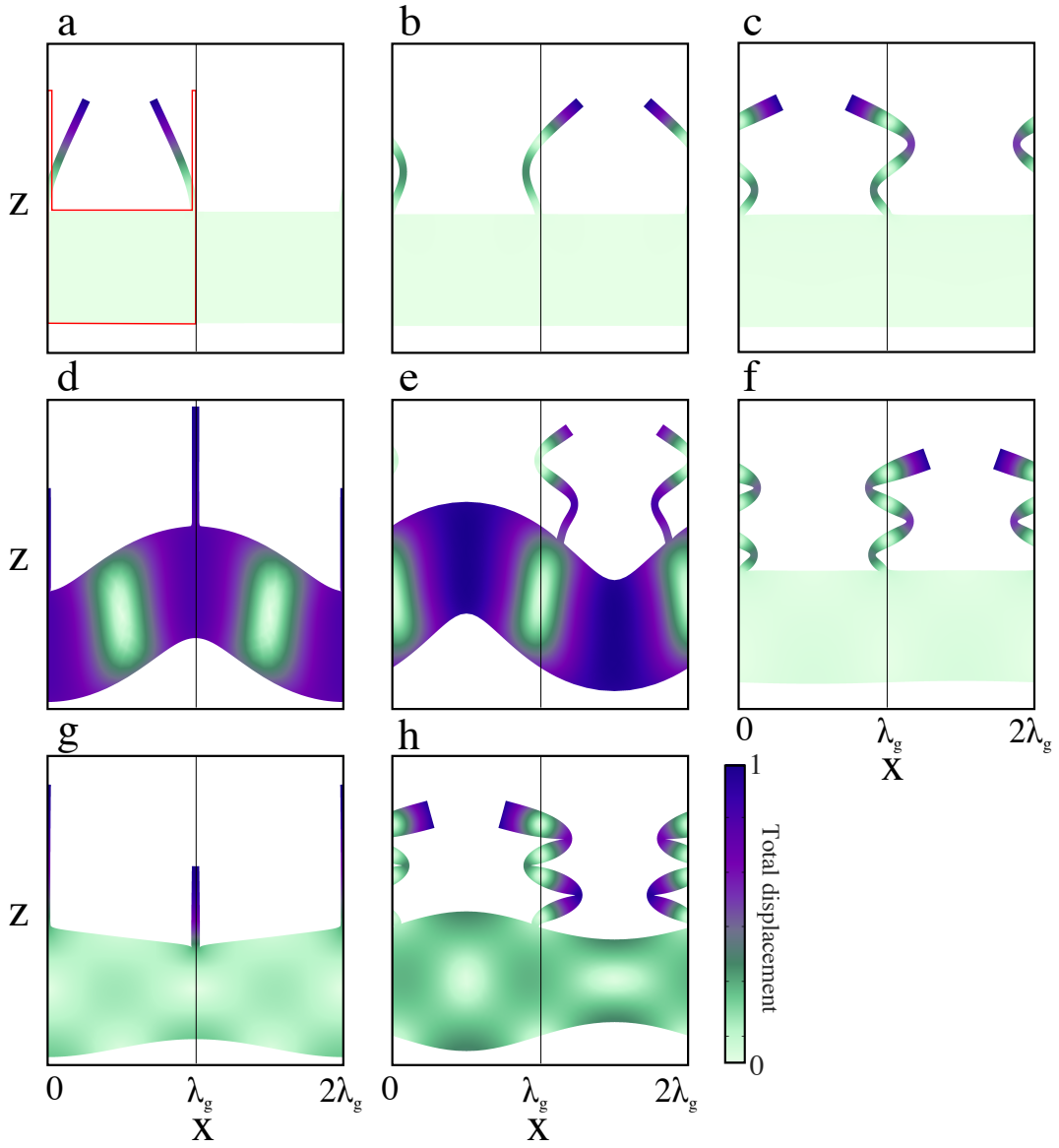

Fig. 6.10 Total displacement fields for a wide groove grating of parameters $w = 3.8$ mm, $h = 3$ mm, $d_p = 6$ mm, and $\lambda_g = 4$ mm. In order, they are CM_1, CM_2, CM_3, MA_1, MA_2, CM_4, MS_1, and MS_2. The solid red line in (a) represents the outline of the undisplaced plate.

this suggests that due to the symmetry of the displacement, these modes are less sensitive to the mass-loading effect of the pillars.

For the wider groove, $w/\lambda_g = 0.95$, the band diagram is much more different, as seen in Figure 6.9(b). In the frequency range there now exist eight modes. Upon investigation of these modes both the MA and MS modes can be seen at the Brillouin zone, much smaller gaps exist between the modes than the previous case. For the MA pair the gap is 180 Hz, and for the MS pair, the gap is 1090 Hz. The reduction of gap width at $k_g/2$ is easily understood as the narrow pillars reduce the effect of the mass-loading on the standing wave solutions, hence, creating a smaller splitting at $k_g/2$. The fields of the anti-symmetric modes at $k_g/2$ are presented in Figure 6.10(d-e), the mode shown in 6.10(d) is the lower frequency mode occurring at 70 kHz, while mode 6.10(e) displays the high-frequency mode at 70.3 kHz. For the low-frequency mode the pillar is located at an anti-node in the displacement of the plate. In contrast, for the high-frequency mode, the pillar is located at a displacement node; however, the pillar is displacing also.

The remaining modes are all cantilever modes of increasing order with frequency, the three lowest, CM_1, CM_2, CM_3, all anti-cross with MA_1 and disperse little in frequency, hence they are flat-banded. The highest frequency cantilever mode, CM_4 disperses more with frequency and anti-crosses with MS_1. The two highest frequency modes are the MS pair at $k_g/2$. The fields in Figure 6.10(g-h) display similar characteristics to the MA modes, where the pillar for the low-frequency mode (132.1 kHz) is located at an anti-node in the displacement. For the high-frequency mode (134.1 kHz), the pillar is located at a node. For both the high-frequency MA and MS mode, the pillar is resonating with the first cantilever mode which is lower in frequency than the high-frequency modes.

The frequency of the modes at $k_g/2$ as a function of w is presented in Figure 6.11(a-b). As mentioned previously, for small values of w, there exists a large splitting

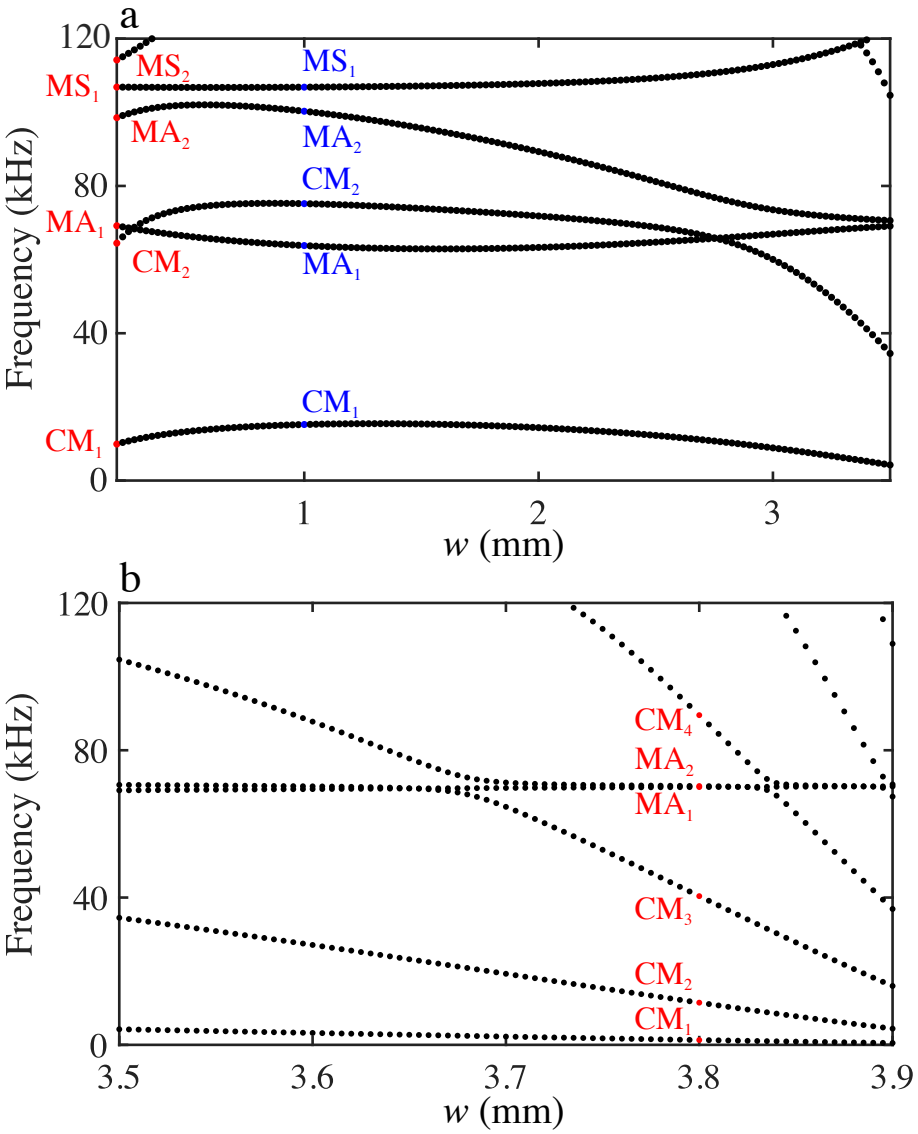

Fig. 6.11 a) FEM model of the frequency of the modes at $k_g/2$ as a function of w, for 0.2 mm $\leq w \leq$ 3.5 mm. b) FEM model of the frequency of the modes at $k_g/2$ as a function of w, for 3.5 mm $\leq w \leq$ 3.9 mm.

at $k_g/2$; however, as w is increased this decreases in size and both modes tend to the same frequency of 70.3 kHz for $w = 3.9$ mm. For values of w less than 0.5 mm, four of the six modes displayed show a decrease in frequency as w is decreased. These modes are CM_1, CM_2, MA_2 and MS_2. The MS modes increase in frequency as w is increased because the effective thickness of the plate is decreased. As seen in the unstructured plate, as d_p is decreased, the frequency at which the symmetric Scholte mode asymptotes to the Scholte velocity increases. If this were to be the case for the MA modes, we would expect a decrease in frequency with increasing w. However, this only occurs for one of the MA modes, for MA_1, the frequencies for the $w = 0.2$ mm and 3.5 mm samples vary little. With MA_2, there is a decrease in frequency as w is increased. The rate of this decrease is similar to the rate of increase of the MS modes. This is rather like a previous discussion where the modified Scholte modes and the cantilever modes exhibit similar displacement fields.

Next, the case where $w/\lambda_g > 0.875$ is considered, the band structure is shown in Figure 6.11(b). Here, there are multiple CM modes of various order decreasing in frequency as w is increased. This is expected because as $\lambda_g - w$ tends to zero, there are no pillars; therefore, no cantilever resonances are supported. It is interesting that with increasing order of cantilever resonance, the gradient of the modes increases, suggesting that the higher-order modes are much more dependent on frequency than the lower order modes. It can be seen that the CM modes decrease in frequency with increasing w, and they anti-cross with one of the MA modes.

6.7 Plate Thickness Dependence

As a final model exploration the plate thickness d_p will be increased, while the other parameters will remain constant. Here, the parameters of the unit cell are $h = 3$ mm, $w = 1$ mm and $\lambda_g = 4$ mm. Figure 6.12(a) displays the FEM model of the

frequency of the modes at $k_g/2$ as a function of d_p. For values of d_p greater than 9 mm, the modes become almost fully independent of the thickness. However, for values of d_p less than 9 mm, all the modes disperse in frequency with decreasing d_p. For the MA and MS modes, it is expected that the anti-symmetric modes will decrease in frequency, and the symmetric modes will increase in frequency as the plate thickness decreases. One expects this as an unstructured plate displays similar behaviour. There is however, an interesting difference between the MA and MS modes. The gap between the two MA modes remains relatively constant as d_p is varied, this is expected as the mass-loading effect remains constant for MA_1 as the pillars do not change in size. However, the MS modes tend to the same frequency. This suggests that the structure on one of the surfaces only has a small effect on the dispersion of these modes. The dispersion of CM_1 displays a similar trend to that of the MA modes. From previous discussions, the field of CM_1 is influenced by MA_1, where the backing plate shows a MA_1 like displacement. The displacement of this backing plate will change as d_p is varied, which will result in a lowering of the frequency similar to that of the MA_1 mode.

As the value of d_p approaches that of h for a particular system, the dispersion behaves very differently. In this system, $h = 3$ mm, and the behaviour of the modes markedly changes for $d_p < 4$ mm. The displacement fields shown in Figure 6.12(b-e) are for a system where $d_p = 3.1$ mm. The modes shown are the same except for the lowest frequency mode shown in Figure 6.12(a), as this mode was the CM_1 mode. The modes 6.12(b-c) represent the MA modes, in 6.12(b) this is easily seen as the neighbouring pillars are at the anti-nodes in the displacement field. The displacement field shown in 6.12(c), however, is not as clear. If the backing plate between the two pillars is considered, in 6.12(b) there is a node in the displacement field at $x = \lambda_g/2$, in 6.12(c) the node is located in the centre of the pillars at $x = 0$ and λ_g, this is characteristic of the two anti-symmetric pairs. If the mode in 6.12(d) is now

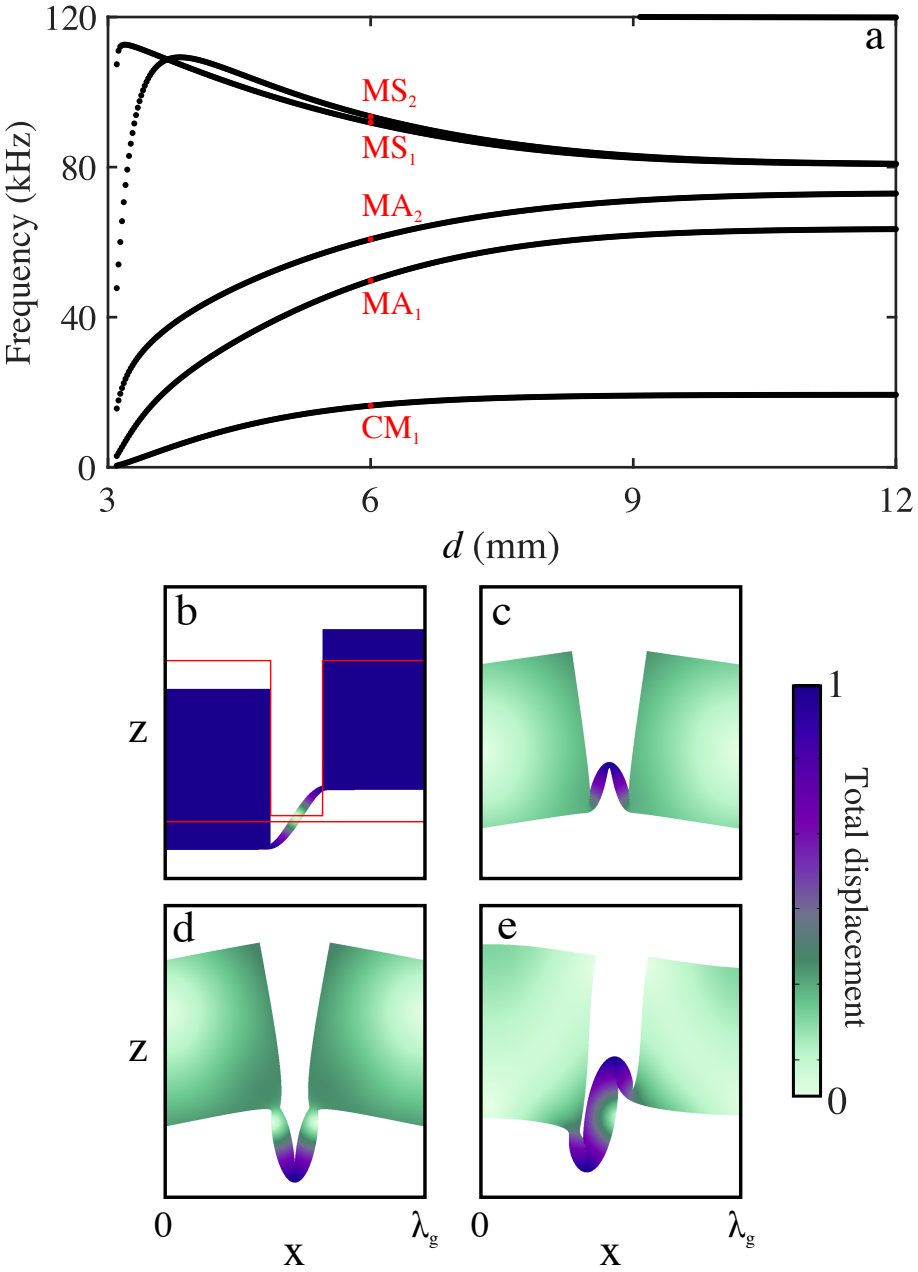

Fig. 6.12 a) FEM model of the frequency of the modes at $k_g/2$ as a function of d_p, for 3.1 mm $\leq d \leq$ 12 mm. b-e) Total displacement fields for the four highest frequency modes at $d_p = 3.1$ mm. The lowest frequency (CM_1) is omitted as it is addressed earlier. The solid red line in (b) represents the outline of the undisplaced plate.

considered, the fields resemble those of the mode in 6.12(c); however, there is a subtle difference that the displacement field nodes exist at the edges of the plate connecting the two pillars. It now appears that a new resonance not previously discussed in this chapter is occurring. This new resonance is a standing wave in the elastic material connecting the two pillars. This mode is similar to the fundamental mode of a string fixed at both ends; however, in this system the ends are not fixed and can displace. The next resonance of the connecting plate is shown in 6.12(e), and nodes exist in the centre and in the two pillars. The anti-nodes are located halfway between the node and the pillars; therefore, the pillars are being displaced.

So far, the modes on thin acrylic plate has been thoroughly investigated through FEM modelling. The dispersion of the modes supported on such surfaces are highly dependent on the grooves geometry. To verify the previous results, the band structure of an experimental structure will be characterised using near-field scanning.

6.8 Experimental Sample

The experimental sample was made in house from milled acrylic, the dimensions of the unit cell of the sample were chosen to be $h = 2.70$ mm, $w = 1$ mm, $d_{\mathrm{p}} = 5.63$ mm, and $\lambda_{\mathrm{g}} = 4$ mm. The parameters of the acrylic-based material are $\rho = 1190$ kgm^{-3}, $E = 3.7$ GPa, $\nu = 0.35$, Note due to the frequency dependence of the Young's modulus; this value was obtained from fitting of the experimental data, while keeping the other parameters constant to the standard values[164]. Over the frequency range explored, E is constant. One may notice that this value is smaller than that given at the beginning of the chapter, this arises from the samples coming from different sources, hence the discrepancy between the two values. A schematic of the unit cell is presented in Figure 6.13(a). A thin plate was chosen as the separation of the MA and MS modes then exists over a large range in k_{x}. The experimental

sample consists of 101 periods in a 450 × 398 mm plate, where 23 mm has been left unstructured in the x direction. The grooves extend the whole length of the sample. As discussed previously, acrylic was chosen due to the transverse wave velocity being less than the velocity of sound in water. In Figure 6.6(c) the expected dispersion can be seen. The model displacement fields of the modes at $k_g/2$ are shown in Figure 6.13(b-f), where the modes are CM_1, MA_1, MA_2, MS_1, and MS_2 respectively.

6.9 Experimental Method

To experimentally measure the non-radiative dispersion where the surface modes exist, a similar technique was implemented as discussed for the case of air in Section 3.5. A schematic of the experimental setup is displayed in Figure 6.14. Firstly, the sample was slowly submerged into the water, so that any air bubbles which remained on the sample were gently removed. The sample was then moved into the centre of the tank to be aligned with the detector. To align the sample the scanning arm with the hydrophone (Brüel & Kjær 8130) attached was placed roughly 1 cm away from the surface. The hydrophone was slowly moved in intervals along the surface in a line, if the microphone moved toward/away from the sample, the sample was realigned so that it moved parallel to the surface. Once this initial alignment was complete, the hydrophone was moved as close as possible to the sample without touching ($<$ 0.5 mm). The source (Neptune Sonar D70) was placed on the unstructured side of the sample. For this experiment, it was directly behind a small hole (diameter 2 mm) in the sample. This was to ensure that the acoustic energy diffracted and coupled to the surface modes. The source was part shrouded in absorbing foam to increase the directivity of the acoustic energy, as shown in the inset of Figure 6.14. For these experiments, the hydrophone was placed at the centre of the sample. Once the source was in place, the transducer was aligned to give maximum signal strength,

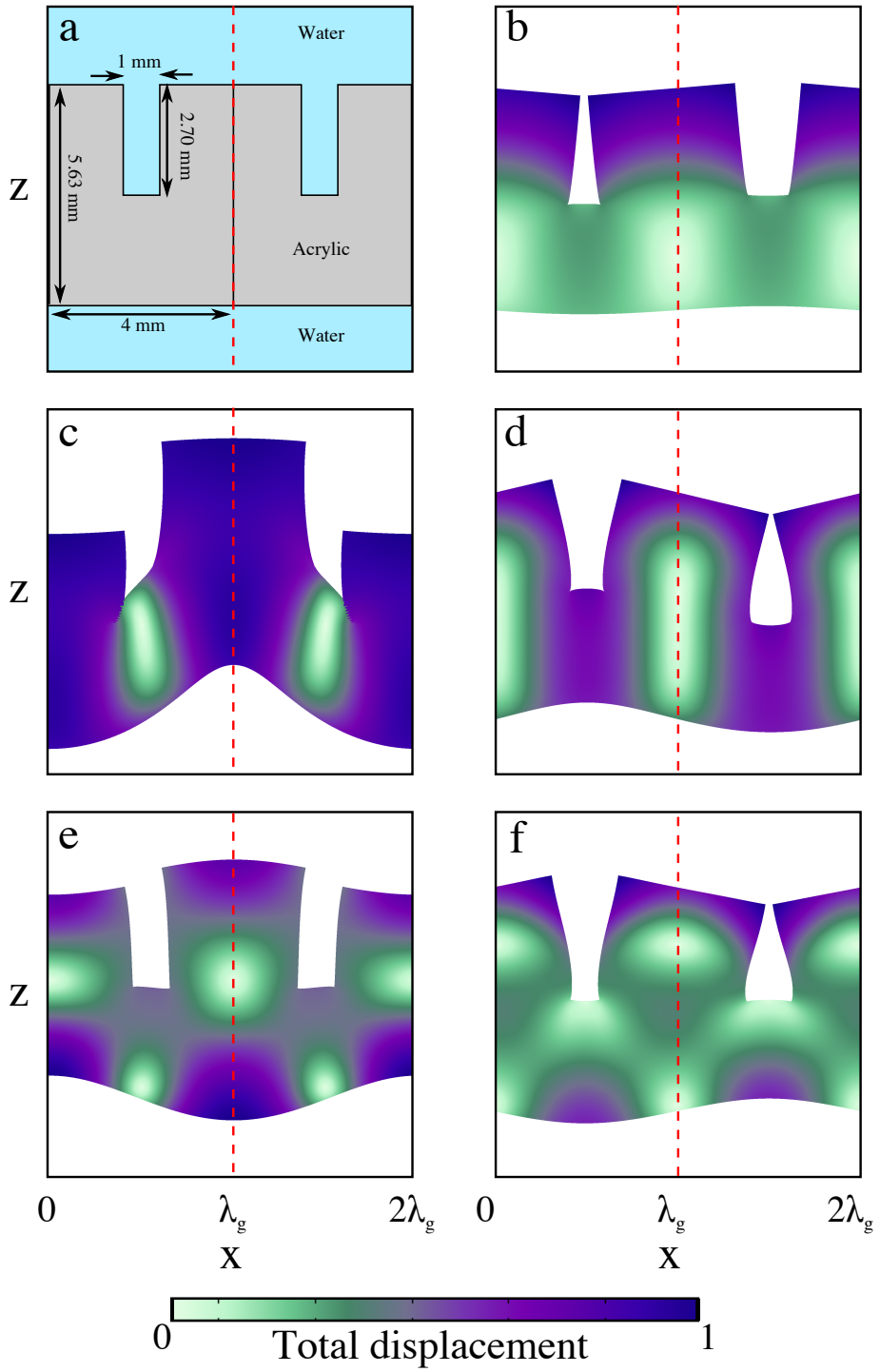

Fig. 6.13 a) Schematic of the unit cell used for the experimental sample. b-f) Displacement field for the modes at $k_g/2$, from lowest to highest in frequency. In order these modes are: CM_1, MA_1, MA_2, MS_1, and MS_2.

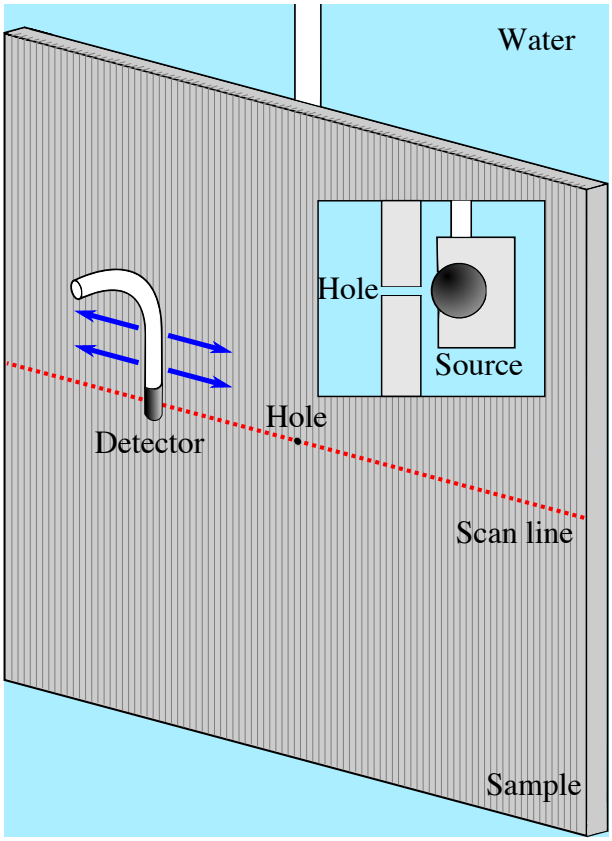

Fig. 6.14 Schematic of the underwater experimental setup (not to scale). The sample is placed in a tank, and the hydrophone is aligned, ensuring that it moves parallel to the surface at a constant distance away from the surface. Along the red dotted line is where the scan is performed. The inset shows the source's placement behind the sample. The source has been shrouded in absorbing foam to increase the directivity of the acoustic energy.

directly in front of the source. The hydrophone was then moved so that it was placed at the edge of the sample so that the whole length of the sample could be measured.

In this experiment it was necessary to perform two separate line scans to cover the frequency range needed. The only difference between the two experiments were the pulse length and central frequency. Both experiments used single-cycle Gaussian enveloped pulses shown in Chapter 3. The low-frequency scan had a pulse length of 40 μs and 25 kHz central frequency. The high-frequency scan had a pulse length of 20 μs and 50 kHz central frequency. Each spatial scan was 300 mm in length (x_l) with a resolution (x_res) of $1/2\pi$ mm. At each position 50 repeats were taken

and averaged to increase the signal to noise ratio. Temporal, followed by a spatial, Fourier transforms were applied to the raw experimental data.

6.10 Results

The results of the experiments are displayed in Figure 6.15. Here, the results of the low and high-frequency scans are separated by the red dashed line. The white-dotted lines represent the results from the FEM model. For the lowest frequency mode, at small values of k_x the mode displays an anti-symmetric Scholte-like dispersion (MA_1), the mode then anti-crosses with the lowest order cantilever mode (CM_1) and becomes flat until $k_g/2$. In the experimental results, this mode is not visible. It is very difficult to observe modes with a flat dispersion, as $v_g = 0$; however at small k_x this mode does have a non-zero value of v_g. However the lowest frequency which could be produced with the equipment available was 15 kHz. Thus the signal strength at these frequencies at which this mode should be found was extremely low. For this reason we did not find any clear experimental evidence for this lowest order very slow mode.

The second mode begins at low k_x as CM_1, it then anti-crosses with MA_1 and becomes linear with a constant v_g. As the mode approaches $k_g/2$, v_g tends to zero due to the band splitting at $k_g/2$. This mode can be seen in the experimental data for small values of k_x, the curve in the dispersion due to the anti-crossing (labelled A) is also seen for positive k_x and agrees well with the FEM model. The reason for the difference between positive and negative directions is due to a small curvature of the sample. While due care was taken to make the sample planar, it appears that some curvature was present. This results in the hydrophone in one of the directions (negative x-direction) moving away from the surface. Notice that a small section of the band diagram was recorded in the region B. Below this region there is a 10 kHz

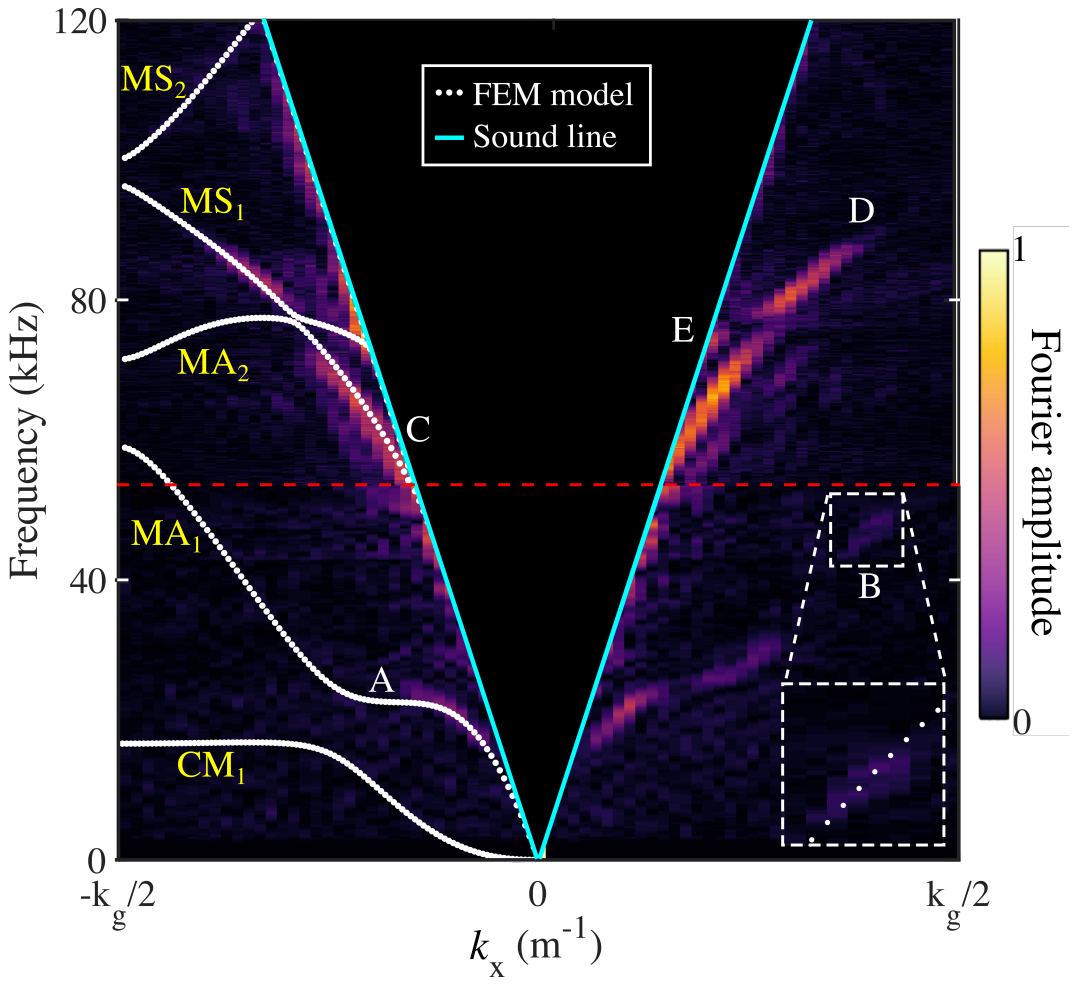

Fig. 6.15 Experimental non-radiative dispersion. The red-dashed line shows the boundary between the low-frequency and high-frequency scan data. The cyan lines represent the sound lines of water.

gap of little experimental data, this is likely due to the source being weak in signal strength at these frequencies.

The next two modes will be considered together. In region C, the symmetric Scholte-like mode (MS_1) starts to disperse away from the water sound line. Here, the model is in good agreement with the experimental results. This mode then anti-crosses with the diffracted anti-symmetric-like mode (MA_2). The mode can then be seen to extend towards $k_g/2$. In the experimental data, for higher k_x values than the label D, the intensity of the mode rapidly decays, due to the diffracted radiation used to excite the surface not containing high k_x components. While this appears to be similar to the frequency region below B, there is intensity recorded on the water sound line showing that the source signal was present. To increase the range in k_x a smaller hole should be used; however, by using a smaller hole less signal strength will propagate through the hole and couple by diffraction to the surface modes. For MA_2, as v_g is negative as the mode approaches $k_g/2$, the mode was not measured by the experiment. A small section of MA_2 can be seen near the water sound line in region E.

Finally, the highest frequency mode presented in the FEM result is the diffracted symmetric-like mode, MS_2. This mode, as with MA_2 can not be measured experimentally due to v_g being negative.

6.11 Conclusions

In this chapter, the effect of adding structure to the surface modes supported by acrylic plates has been thoroughly explored through FEM modelling. By adding periodic grooves to the plate, unusual dispersion characteristics have been shown. The hybridisation of the modified Scholte-like modes with the cantilever resonances of the solid pillars has been described. The characteristic of these acoustic surface waves have

been presented to be highly dependent on the dimensions of the grating used. The splitting at the first Brillouin zone boundary of the modified anti-symmetric−Scholte modes was shown to decrease as the width of the pillars decrease, this was expected as the mass loading effect which creates the splitting vanishes as the pillars become infinitesimally small. For the modified anti-symmetric−Scholte modes this effect was much more subtle. As the thickness of the plate becomes similar to the groove depth, a resonance in the thin plate connecting the pillars was found, showing displacement fields similar to standing waves on a string bound at both ends.

A monograting of parameters $h = 2.70$ mm, $w = 1$ mm, $d_{\mathrm{p}} = 5.63$ mm, and $\lambda_{\mathrm{g}} = 4$ mm, has been fabricated and measured experimentally through the use of line scans. A low- and high-frequency scan were used to obtain the frequency range necessary.

Chapter 7

Conclusions

At the interface between two different materials, surface, acoustic waves exist. However in contrast to the wealth of studies for elastic materials, for an interface between a fluid and an acoustically-rigid material, these waves are rarely observed. A material can be defined as acoustically rigid if its surface impedance is much greater than that of the surrounding fluid. By adding periodic structure to an acoustically-rigid material, acoustic surface waves may propagate on the structured interface. These acoustic surface waves have too much in-plane momentum to radiate directly into the fluid half space Thus to obey momentum conservation laws these modes are evanescent in the direction normal to the surface. The evanescent waves do not propagate energy away from the surface (as long as no defects are present). The characteristics of acoustic surface waves are highly dependent on the periodic structure which they exist over. Within this work, acoustic surface waves have been characterised over various metasurfaces.

The first surfaces explored were simple (one groove per period) and compound gratings (multiple grooves per period) in Chapter 4. By adding complexity to the unit cell, new, narrow 'phase resonant' modes were observed. Phase resonances are characterised by the resonant acoustic fields in adjacent grooves varying in phase

by odd multiples of π with strong field enhancement on resonance, and therefore, the potential for high losses. It was discovered that for a surface with two grooves per period that as the ratio of the groove depths increases the individual grooves become less coupled and begin to behave more like isolated resonators. For the first time, the dispersion of the modes supported by a compound grating with three grooves per period, where the outer two grooves are twice the width of the central groove, were investigated experimentally. A sharp minimum at 13 kHz associated with the excitation of a phase resonance where the outer grooves are out of phase with the central groove was recorded at normal incidence in the reflectivity spectrum presenting high absorption. This mode dispersed strongly with frequency. A second, weaker mode associated with a second phase resonance between the two outer grooves was also measured. The acoustic surface mode dispersion was obtained. Frequency-dependent directional acoustic power beaming was observed experimentally and occurs due to linear regions in the iso-frequency contours where a range of wavevectors have the same group velocity.

The acoustic surface waves supported by glide-symmetric metasurfaces composed of space-coiled (meandering) cavities were the topic of Chapter 5. While space-coiled metamaterials have been used in previous investigations, this chapter presents the first experimental realisation and characterisation of acoustic surface waves on meander surfaces. The surface modes supported on such narrow grooved structures were shown to have broadband, near-linear dispersion (near-constant group velocity) that was dependent on the length of the meander channels. The broadband behaviour of these surfaces arises from the glide symmetry of the structure, that removes the band gap at Brillouin zone boundaries because a degeneracy of modes exists. The narrow cavities and resonance behaviour of the acoustic surface modes naturally creates high attenuation as modes propagate along the surface. It was shown that by increasing the channel width, the attenuation of the modes was reduced. Covering

the straight sections of the meander channel was shown to reduce the coupling to free radiation. The standing wave condition at first Brillouin zone for small values of the depth was explored showing a change in behaviour when the meander channel was partially covered. It was discovered that for partially covered meander channels, the standing wave condition now comes from an open-ended cavity resonance (of the form $\lambda_x = 2\lambda_g$) in the structure compared with the resonance condition being the length of the channel in a unit cell for the uncovered case ($\lambda_x = 2\lambda_g$). For large d, the standing wave condition for both systems is $\lambda_x = 2l_p$.

In underwater acoustics, the solid materials previously considered acoustically-rigid can no longer be described as such. A soft solid-fluid system is one where the transverse velocity of the solid is less than the longitudinal velocity of the fluid. Such a system is acrylic surrounded by water. In a flat soft-solid plate a pair of surface acoustic waves (coupled-Scholte waves) exist in the non-radiative dispersion. Structuring such plates hybridises the coupled-Scholte modes with the locally resonating structures. In Chapter 6, the effect of adding structure to soft-solid plates on the characteristic of acoustic surface waves was investigated. Structuring one interface of the plate with a simple groove grating (one groove per period) induces cantilever resonances in the pillars. These cantilever resonances hybridise with the coupled-Scholte waves to form modified coupled-Scholte waves. The characteristic of these acoustic surface waves was shown to be highly dependent on the dimensions of the grating used. The splitting at the first Brillouin zone boundary of the modified anti-symmetric−Scholte modes was shown to decrease as the width of the pillars decrease, this was expected as the mass loading effect which creates the splitting vanishes as the pillar become infinitesimally small. As the thickness of the plate becomes similar to the groove depth, a resonance in the thin plate connecting the pillars was found, showing displacement fields similar to standing waves on a string bound at both ends. A monograting of parameters $h = 2.70$ mm, $w = 1$ mm, d

= 5.63 mm, and λ_g = 4 mm, was fabricated and measured experimentally using pressure field line scans. The experimental dispersion of the surface modes gave good agreement with the FEM model. However, the low-frequency mode could not be measured due to equipment limitations, and high-momentum waves were not able to be measured. This chapter presents the first experimental realisation of the acoustic surface waves on an underwater grating and the discussion of the hybridisation of the Scholte-like modes with the structural resonances of the grating.

Chapter 8

Future Work

8.1 Introduction

In this chapter a set of modelling studies and a further experimental study are outlined. These are essentially extensions of the previous work and could form the basis of more in depth work. In the Chapter 6, the surface acoustic waves supported by an underwater acrylic plate with a simple monograting on one of the interfaces was investigated. In this chapter, this work will be expanded to plates where both of the interfaces are now structured. Two different systems will be discussed. Firstly, a system where the structure is symmetric with respect to the mid plane will be considered, following that a glide-symmetric system will be explored where the structure on one interface is displaced by half a pitch. It is proposed that by implementing glide-symmetry into the system, will lead to a degeneracy of the modes at the first Brillouin zone boundary which may allow broadband, slow surface waves to exist on the surface.

The next preliminary study expands the previous 1D grating work to 2D or bigratings in both soft- and hard-solids. It is expected due to the extra degree of

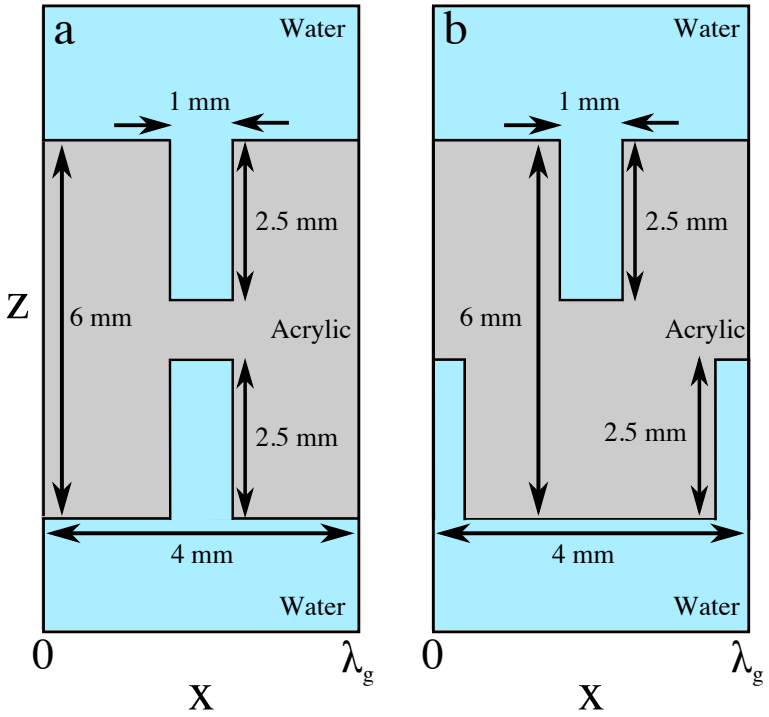

Fig. 8.1 Unit cells for acrylic plates where both interfaces are structured with simple gratings. Here, $\lambda_g = 4$ mm, $d = 6$ mm, $h = 2.5$ mm, and $w = 1$ mm a) The structure is symmetric about a mirror plane through the centre of the plate. b) Glide symmetric system where there is a translation of $\lambda_g/2$ and a reflection about the mirror plane.

freedom present in the 2D systems, that additional, torsional modes will be supported on such surfaces.

Finally, preliminary measurements for a method to obtain the reflectivity spectrum of samples using angle scan measurements will be shown and discussed.

8.2 Structured Underwater Plates

In the Chapter 6, simple underwater acrylic gratings were investigated. For those gratings, only one of the interfaces was structured. In this section, acrylic plates where both of the interfaces have been structured will be investigated through FEM models.

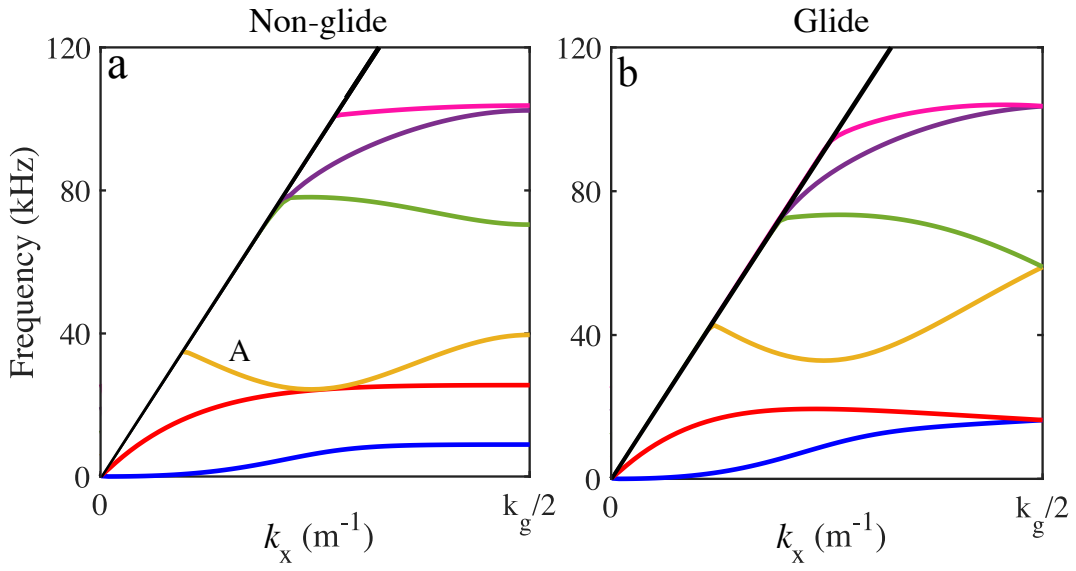

Fig. 8.2 a) FEM model dispersion of the non-glide symmetric system. b) FEM model dispersion for the glide-symmetric system.

The unit cells for the two systems which will be investigated are shown in Figure 8.1(a-b). For the first system in 8.1(a), each interface has been structured with a simple monograting of parameters $\lambda_g = 4$ mm, $d = 6$ mm, $h = 2.5$ mm, and $w = 1$ mm. The structure is symmetric about a mirror plane at the centre of the plate. This system will be described as the non-glide symmetric case. The second system in 8.1(b) shows a glide-symmetric system of the same parameters, here the structure on each interface is displaced by half a pitch with respect to the opposite interface. The idea behind choosing these two structures was to compare the effect of adding structure to both interfaces to a case which possesses glide symmetry. It has already been shown in Chapter 5 that the dispersion of glide-symmetric surfaces leads to the degeneracy of modes at the first Brillouin zone boundary.

If at first the dispersion presented in Figure 8.2(a) for the non-glide system is considered, similarities can be seen with the single structured interface system. The lowest order mode, indicated by the solid blue line, shows the crossing of the MA_1 mode with one of the CM modes. However, in this system, there now exists

two cantilever modes for every cantilever resonance, due to both interfaces being structured. The displacements for these two modes are shown in Figure 8.3(a-b).

In 8.3(a) the cantilever resonances on each face are anti-symmetric around the mirror plane, while in 8.3(b) they are now symmetric about the mirror plane. In contrast to the single structured interface system, there is a diffracted section of the cantilever dispersion around A. The remaining dispersion curves are similar to the systems in the Chapter 6, where there are a pair of anti-symmetric modes with the field configuration shown in Figure 8.3(c-d). There is also a symmetric pair shown in Figure 8.3(e-f).

The dispersion of the glide-symmetric system is displayed in Figure 8.2(b). The effect of the glide symmetry is immediately obvious, by comparing this dispersion with the non-glide system. At the first Brillouin zone there now exist three pairs of degenerate modes: one for the cantilever modes, Figure 8.4(a-b); one for the modified anti-symmetric modes, Figure 8.4(c-d); and the final pair relates to the modified symmetric pair, Figure 8.4(e-f). For each of the three cases, the degeneracy arises because the two standing wave solutions with periodicity twice the grating pitch have identical field distributions when considered from the opposite faces. Thus they are the same energy. This is clear in Figure 8.4 which illustrate that by translating one by half a period and reflecting along the mirror plane, the field distribution of the other mode in the pair is obtained. A further effect of the glide symmetry is that for both the cantilever and anti-symmetric pairs of modes, around $k_g/2$ the dispersion becomes near-linear, due to the removal of the band gap. A similar feature was shown in Chapter 5, albeit the linear region of the dispersion was over a much broader frequency range.

In future such samples may be manufactured and their dispersion verified experimentally, as to the authors knowledge direct measurement of the dispersion of surface acoustics wave on a glide-symmetric metamaterial has not yet been done.

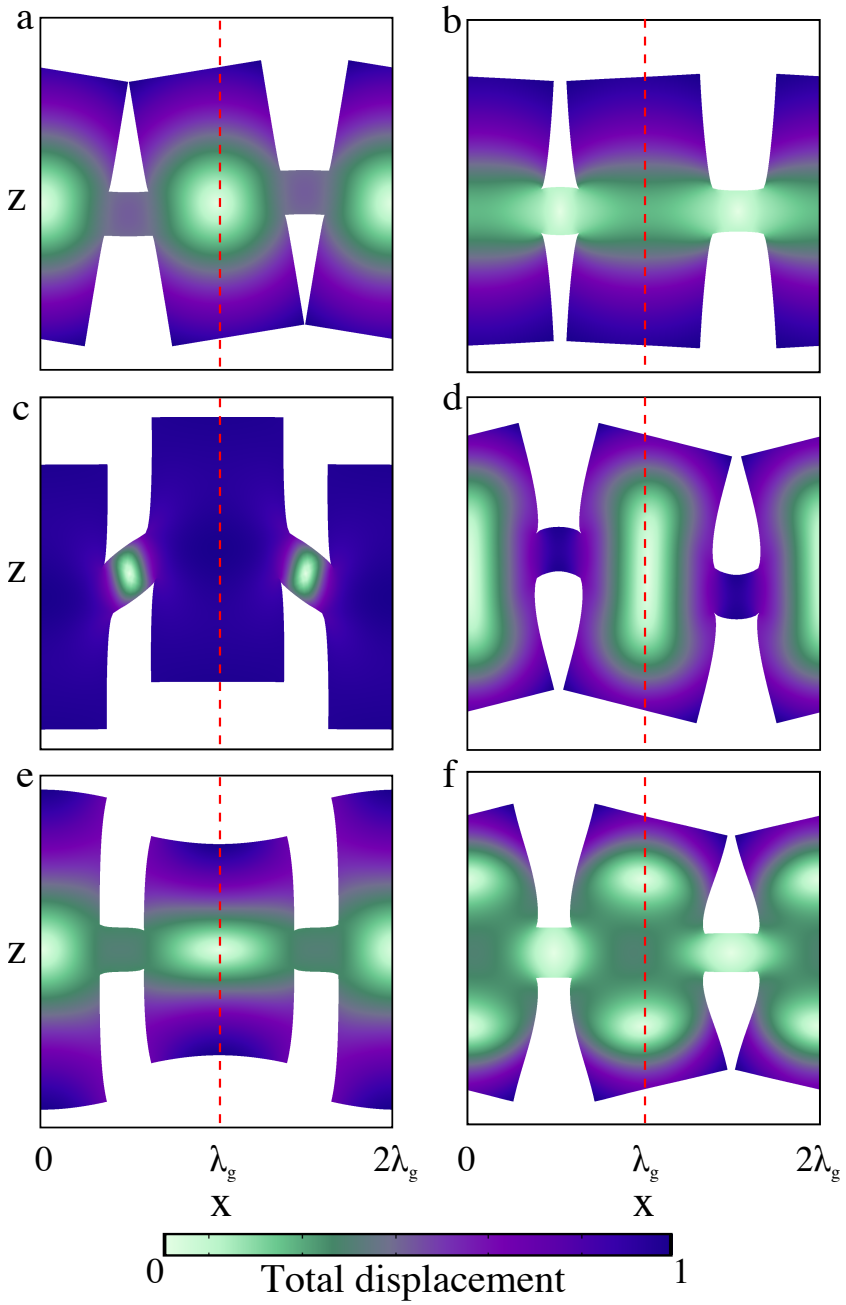

Fig. 8.3 Total displacement ($A = \sqrt{u^2 + w^2}$) of the modes supported on an acrylic plate with grooves on both interfaces. Note: A has been normalised to the maximum value. a) anti-symmetric cantilever mode, b) symmetric cantilever mode c-d) Modified anti-symmetric coupled Scholte modes. e-f) Modified symmetric coupled Scholte modes. The physical displacement shown has been exaggerated for clarity.

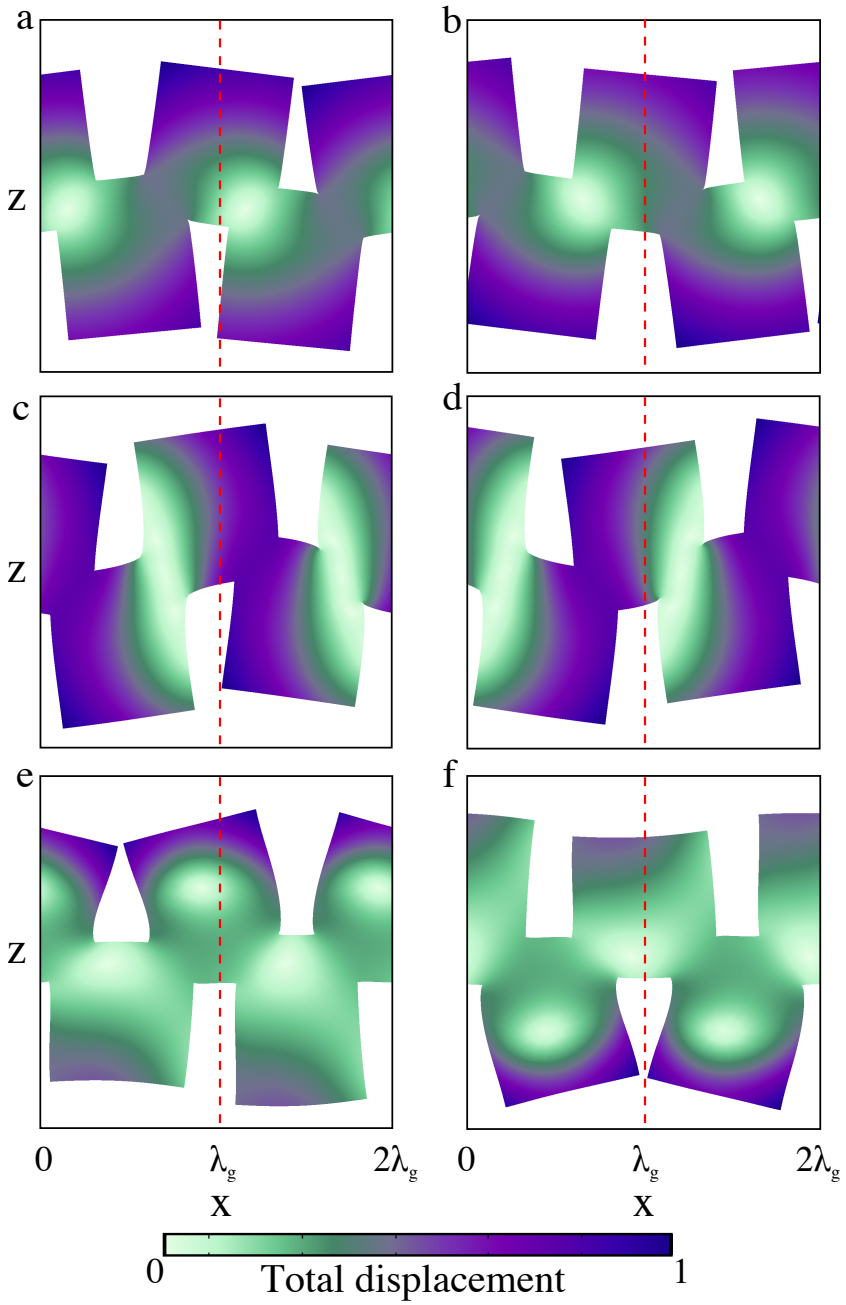

Fig. 8.4 Total displacement ($A = \sqrt{u^2 + w^2}$) of the modes supported on an acrylic plate with glide-symmetric grooves. Note: A has been normalised to the maximum value. a) anti-symmetric cantilever mode, b) symmetric cantilever mode c-d) Modified anti-symmetric coupled Scholte modes. e-f) Modified symmetric coupled Scholte modes. The physical displacement shown has been exaggerated for clarity.

8.3 Underwater Bigrating

So far, we have only considered underwater acoustic structures where the periodicity is in one direction. Now the non-radiative dispersion of bigratings (perpendicular intersecting grooves) on soft-solid and hard-solid metasurfaces will be explored.

The unit cell used in this initial investigation is presented in Figure 8.5. Here, in both the y and x directions 1 mm wide grooves of 3 mm depth, are spaced 5 mm apart. Creating a surface of perpendicular intersecting grooves. The resulting surface is a square array of pillars on a backing plate. Here, $\lambda_g = 6$ mm. The soft-solid material used is acrylic of parameters $\rho = 1190$ kgm^{-1}, $E = 4.5$ GPa and $\nu = 0.35$. For the hard-solid aluminium was chosen with $\rho = 2700$ kgm^{-1}, E = 70 GPa and $\nu = 0.35$.

The band diagram for both the acrylic and aluminium system are shown in Figure 8.6(a-b). It is immediately clear from initial observations that there is an abundance of modes for acrylic, while the band structure of aluminium present three modes over the frequency range displayed. Due to the lower ρ and E, the pillar resonances

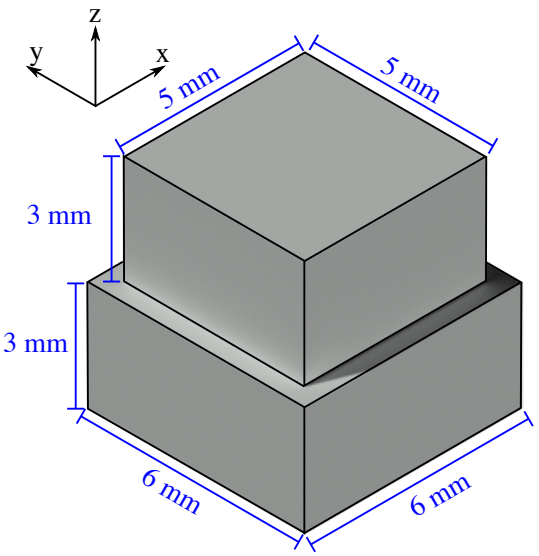

Fig. 8.5 The unit cell for the underwater bigrating investigated. The structure comprises of a 5 mm × 5 mm × 3 mm pillar on a backing plate of a 6 mm × 6 mm × 3 mm.

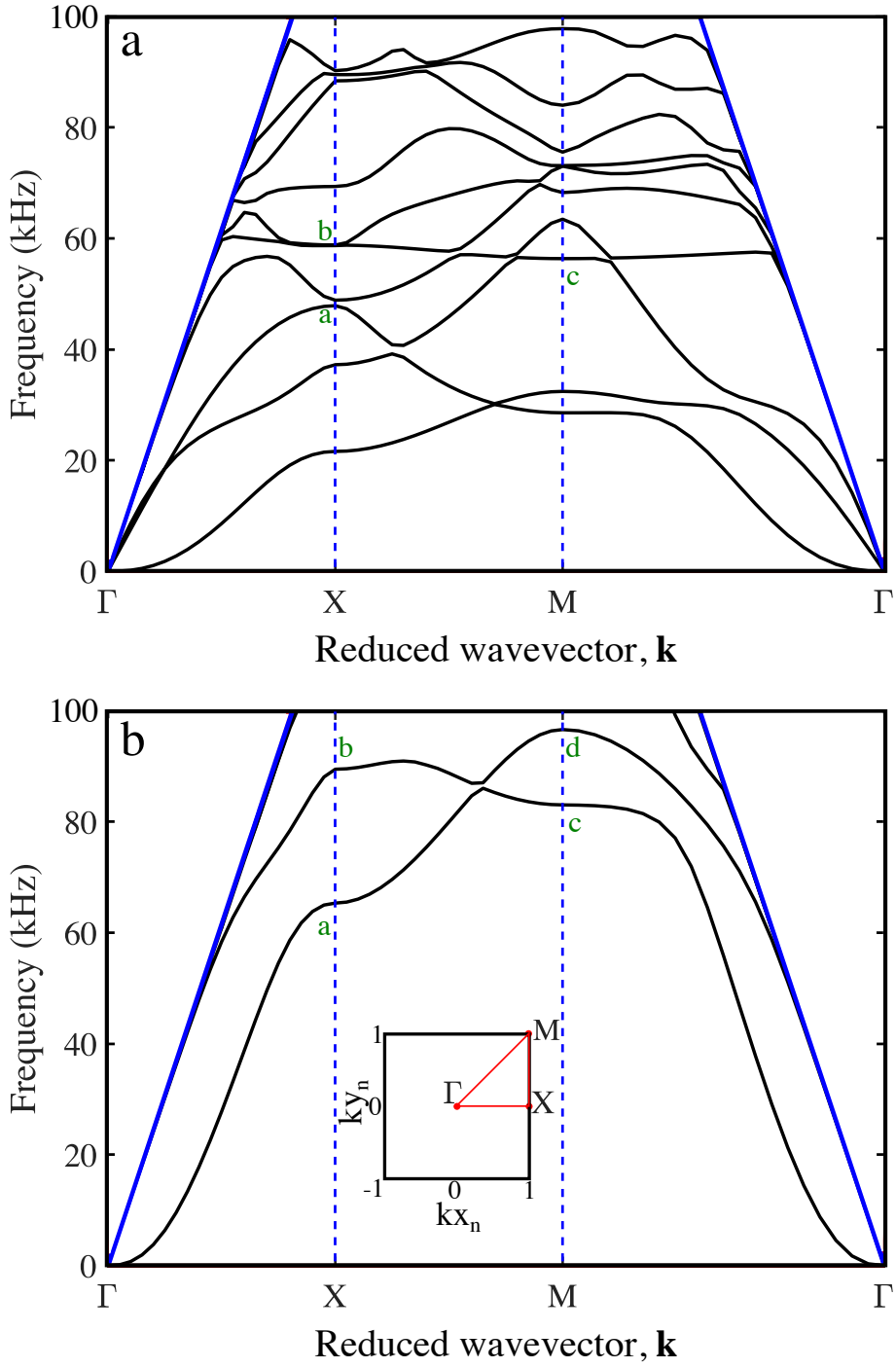

Fig. 8.6 The band structure for both acrylic (a) and aluminium (b) bigratings. The inset in (b) shows the contour in momentum space for which the band structure was plotted. Here, kx_n and ky_n are the wavevectors normalised to $k_g/2$ in the respective direction. For acrylic, the lowest ten eigenvalues were solved.

occur at a lower frequency than in aluminium. One should note that in the model for the acrylic system that the lowest ten eigenvalues were solved. Now, we will consider some of the modes. For mode a the displacement fields in Figure 8.7(a) show an anti-symmetric wave propagating in the backing plate in the x-direction; however, the fundamental cantilever mode is oscillating in the y-direction. Now we can see a relatively flat mode which couples weakly to the sound lines. At the X and M points, this mode is labelled b and c respectively. By investigating the total displacement field, this mode can be identified as a torsional mode seen in Figure 8.7(b-c), where the pillar is oscillating in a twisting motion about the centre, and there is little displacement in the backing plate. In the one-dimension groove structure seen in Chapter 6, these two modes were not excitable as the pillars are infinite in the y-direction.

At the X point for the aluminium bigrating, there are two modes within the frequency range displayed. The lower in frequency, located around a in Figure 8.6, is the fundamental cantilever mode, where the pillar oscillates in the same direction as the propagating wave in the backing plate. The second mode, located at b, is one of the modified anti-symmetric Scholte modes. At the M point, the mode of the fields at c, show that this mode in Figure 8.7(d) is the fundamental cantilever mode oscillating in the y-directions, while the mode at d is the fundamental cantilever mode oscillating in the x-directions.

Clearly there are many further modes one could discuss and an exploration of such bigrating structures would need to explore the influence of the variation in groove depth and pitch. Further possibilities lie with hexagonal gratings (essentially trigratings) with three sets of grooves at 60 degrees to each other. Such structures may well exhibit novel properties such as Dirac points if correctly fabricated. There is here much that could be done.

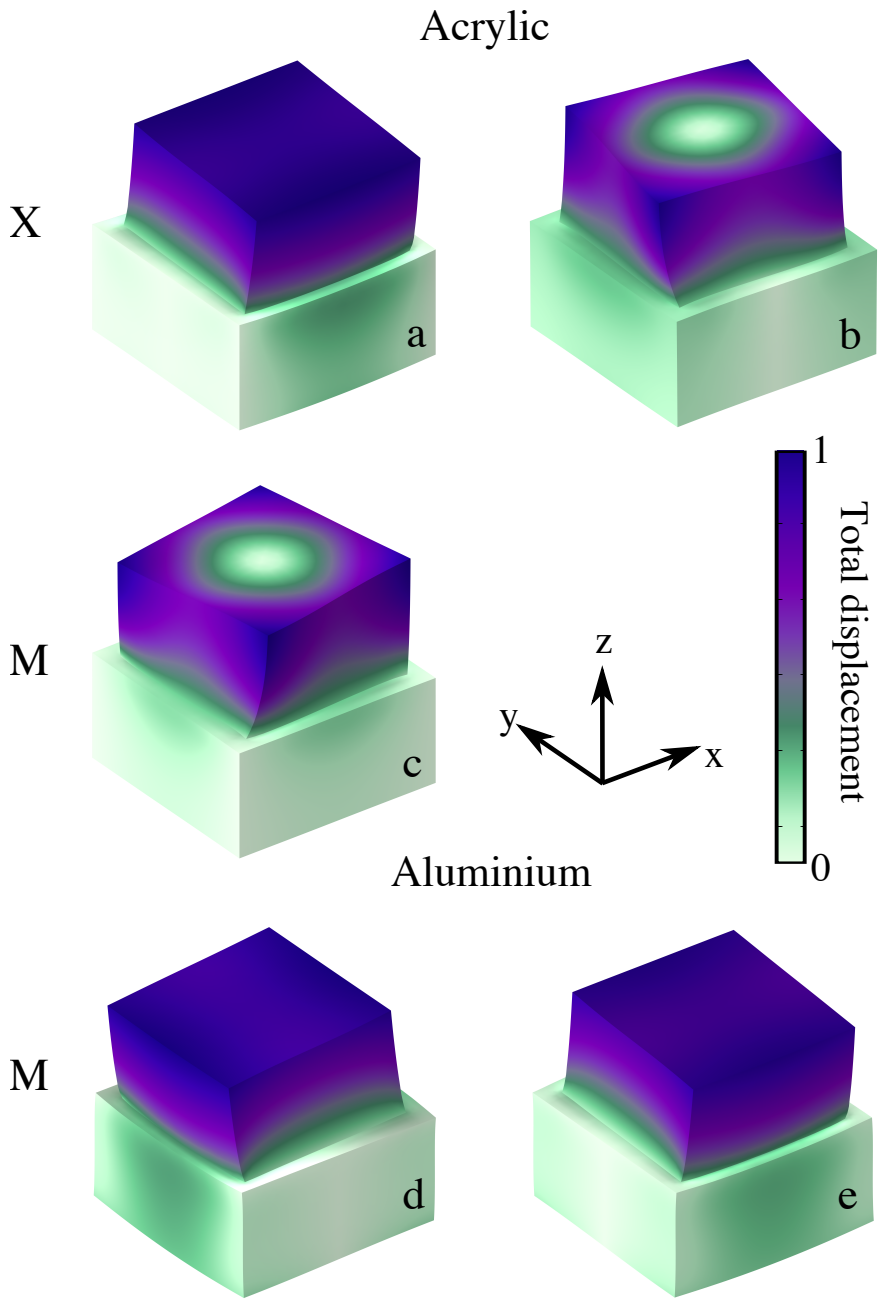

Fig. 8.7 Total displacement fields for selected modes at various points on the band structures in Figure 8.6. a-c) Acrylic modes. d-e) Aluminium modes. a-b) Total displacement fields at the X point. c-e) Total displacement fields at the M point.

8.4 Radiative Scan Measurements

In this section, a potential experimental technique for obtaining the radiative dispersion of metasurfaces will be described. In this method, a point source is placed at some distance above a sample. Then a two-dimensional scan of the detector (Brüel & Kjær Probe Microphone Type 4182, with a tip diameter of 1.24 mm) in the region between the source and sample is performed. Here we emphasise that the probe microphone was placed such that it did not obstruct the incident radiation. A schematic of the setup is shown in Figure 8.8. Here, in the x-z plane, the source emits semi-circular wavefronts (shown as the blue lines). In the desired scan region, these wavefronts propagate in the negative z-direction. Due to the spherical nature of the point source, the incident radiation contains sound waves of multiple angles of incidences (θ). When the wavefronts reach the sample, they are reflected and propagate in positive z, shown by the red lines in 8.8. Depending on the sample of interest, the reflected wave will be attenuated at some angles at some frequencies, which should allow us to obtain the reflectivity spectrum.

Two different methods of obtaining the reflectivity spectrum just for near normal-incidence radiation will be presented. The first will be a self normalisation where the incident signal normalises the reflected signal. The second involves a second surface scan where a mirror replaces the sample so that the sample's reflection data can be normalised to that of the mirror.

In order to test this method, we used the phase resonance sample used in Chapter 4, as the near normal-incidence reflectivity spectrum has already been characterised via the method presented in Section 3.4. The time-domain data for a two-dimensional surface scan is shown in Figure 8.9. For the measurement shown, a source was placed 270 mm above the sample surface. The scan region is 580 mm $\times$ 260 mm, and x_{res} = z_{res} = 5 mm. One should note that the x-length of the sample is less than of

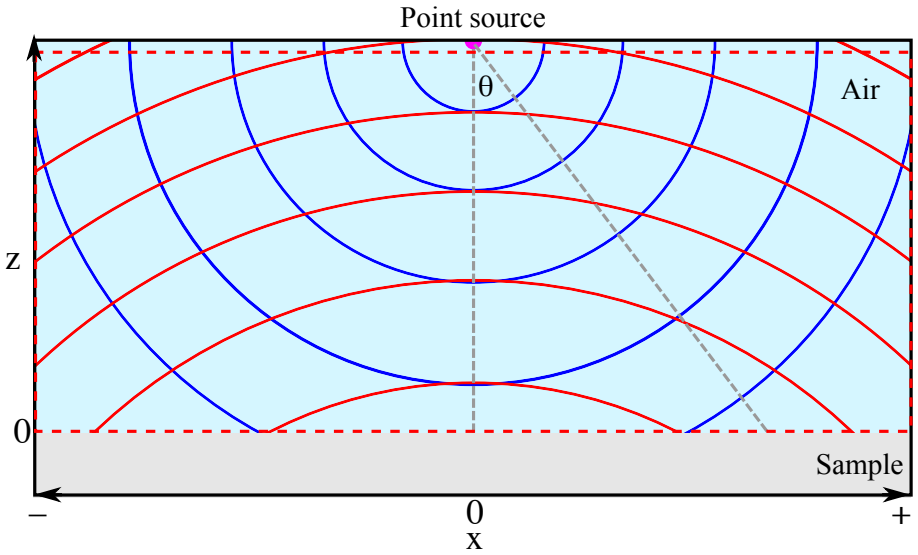

Fig. 8.8 Schematic of the experimental setup used. Here, a point source is placed above a sample. Due to the point-like nature of the source, spherical wavefronts are emitted and propagate in the −z direction (shown by the blue lines). The sound waves then interact wit the sample at z = 0 and reflect in the +z direction. By using a point source, multiple θ can be measured instantaneously.

the scan area, at 450 mm. However, absorber was placed next to the sample to reduce unwanted reflections. In order to achieve a point-like source, a 2 mm thick aluminium plate of dimensions 450 mm × 450 mm with a 5 mm hole in the centre was placed above the scan region. To avoid standing waves forming the source was placed close to the plate surface. The pulse emitted from the speaker propagates through the hole and diffracts on the opposite side resulting in spherical wavefronts. The incident radiation can be seen in Figures 8.9(a-c), while the reflect pulse and the ringing incident radiation are shown in Figures 8.9(d-f). Unexpectedly, in Figures 8.9(a-b), faint wavefronts can be seen to travel along the bottom of the plate at a velocity faster than the speed of sound. These are radiative plate modes of the thin aluminium plate.

Using the Fourier analysis presented in Section 3.6, the iso-frequency contours presented in Figure 8.10 can be obtained. Considering the radiative dispersion for the experimental sample obtained in Chapter 4, we know that as the frequency of

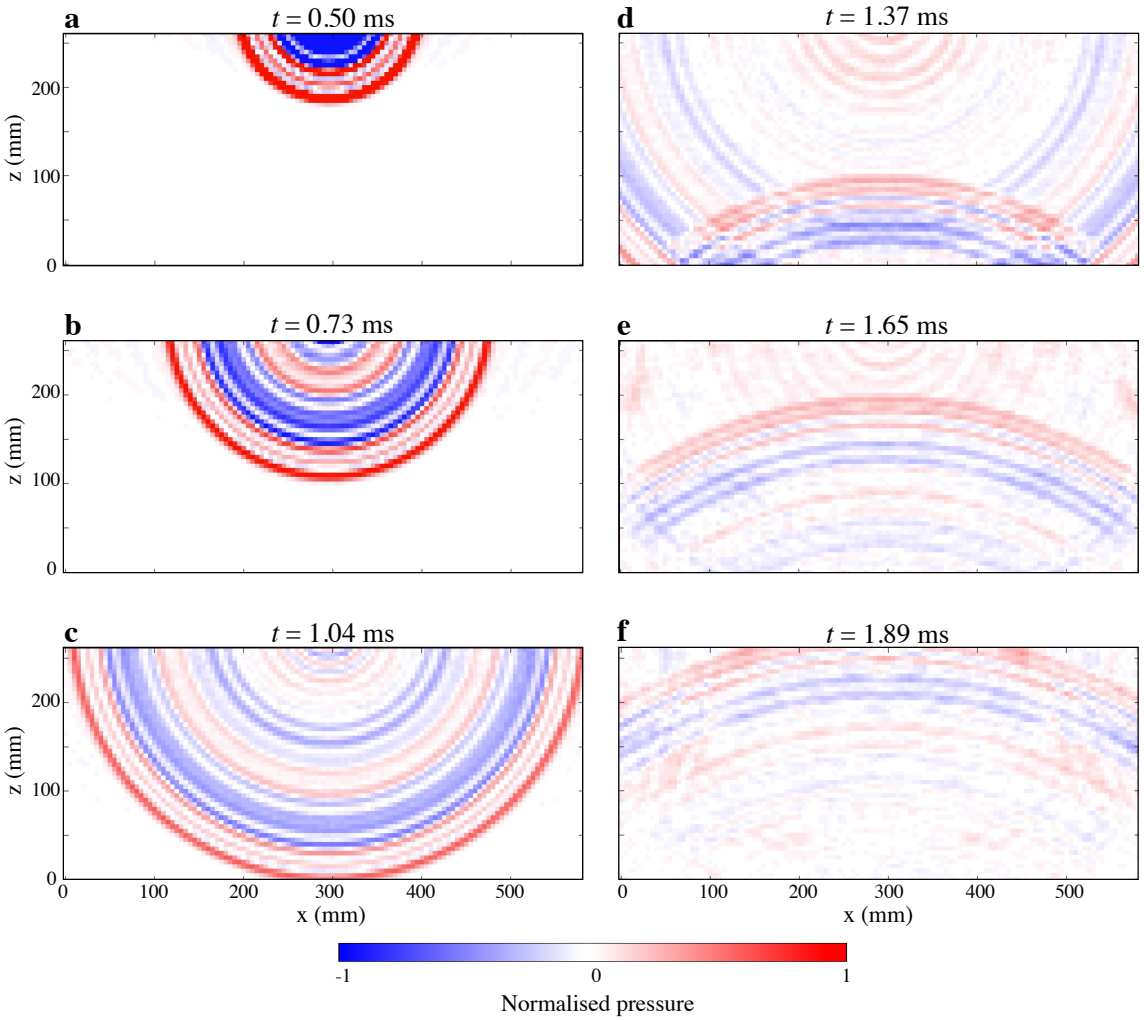

Fig. 8.9 Time-domain experimental results, showing the propagation of sound waves from the source located at z = 270 mm. Here, the pressure field has been normalised to an arbitrary value so that the reflected waves could be shown more clearly. Note: due to how the scans are performed, x = 0 is located at the extreme left of the figure.

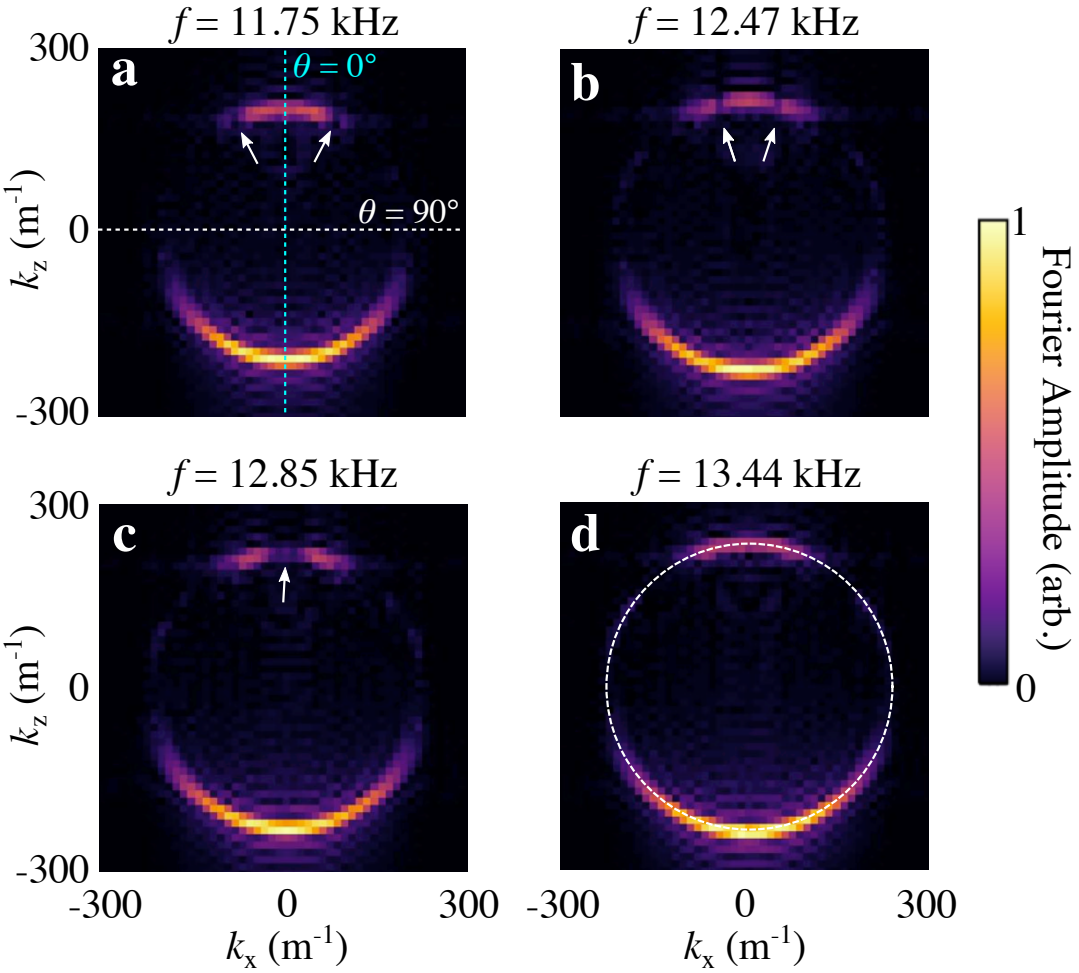

Fig. 8.10 Experimental iso-frequency contours for various frequencies of a radiative scan for the phase resonance sample seen in Chapter 4. The dashed blue line in (a) at $k_x = 0$ represents normal-incidence and normal reflection data. The dashed white in (a) at $k_z = 0$ represents grazing incidence. The white arrows in (a-c) represent the minimum related to mode A of the phase resonant sample (see Chapter 4). The dashed white line in (d) is the sound line ($k_0 = \sqrt{k_x^2 + k_z^2}$, in two-dimensions). Note that the data has not had a window function applied as this reduced the resolution of the peaks.

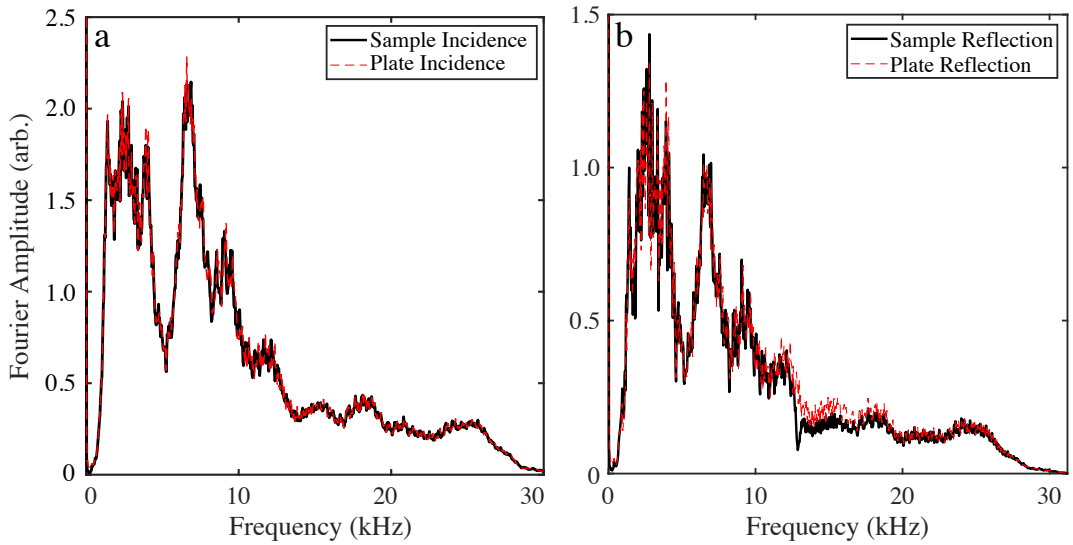

Fig. 8.11 Experimental near normal-incidence frequency spectrum. To avoid the detector being in the path of the incidence radiation, it was moved slightly out of plane. a) Incident radiation. b) reflected radiation.

the exciting radiation is increased to that of the resonance frequency of mode A (two outer grooves out of phase with the central groove), the angle of incidence needed to excited the mode goes from off-normal to near normal-incidence. The iso-frequency contours show this feature, which has been highlighted in the reflected data ($k_z > 0$) by the white arrows in Figures 8.10(a-c). It can be seen that as the frequency increases, the k_x component of the minima reduce until at 12.85 kHz the two minima meet at $k_x = 0$, which agrees with what was discussed in Chapter 4. One obvious limitation of this method presents itself within the iso-frequency contours, the angle range of the reflected radiation is poor, $\theta_{max} \approx 25°$. This is remedied by moving the source closer to the sample; however, this reduces the resolution in k_z.

From here onwards, we will only consider near normal-incidence. If we consider data along at k_x, we can see in the Fourier spectrum we obtain two peaks at $\pm k_z = k_0$. By integrating over the widths of these peaks for all frequencies, we can obtain the incident and reflected signals as a function of frequency. Figure 8.11 shows the result for both the phase resonance sample and also a metallic plate which acts as a mirror

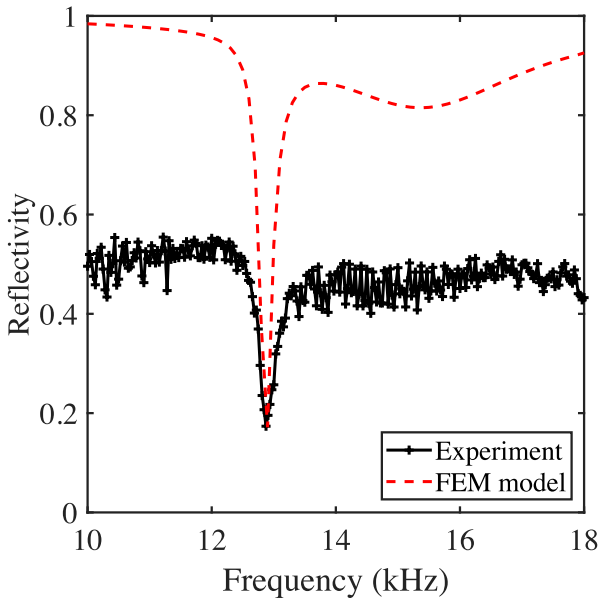

Fig. 8.12 Experimental near normal-incidence reflectivity (black-solid line), obtained from the self-normalisation method, here, the reflected radiation was normalised to the incident radiation. FEM model of the expected response from the phase resonance sample (red dashed line).

for normalisation. The incident spectrum for both cases in 8.11(a) are similar. In the reflection data, there is a clear difference between the sample and plate measurement around 13 kHz in the sample data.

The near normal-incidence reflectivity of a self-normalised measurement can be seen in Figure 8.12. It is immediately apparent that there is a significant difference between the experimental and FEM model data, being that reflectivity is too low over the frequency range shown, only reaching a maximum value of 0.55. However, the minimum associated with the phase resonance can be seen at 12.9 kHz. One possible reason for the low reflectivity is that the analysis ignores the third-dimension (y-direction) completely. One possible explanation for this is the detector placement. If the microphone was placed so that the probe obstructed the path of the incident radiation, less radiation would reach the surface to be reflected back onto the microphone. Therefore, there would be a reduction in intensity between the incident and the reflected signals. There is also interference effects present in the data, shown

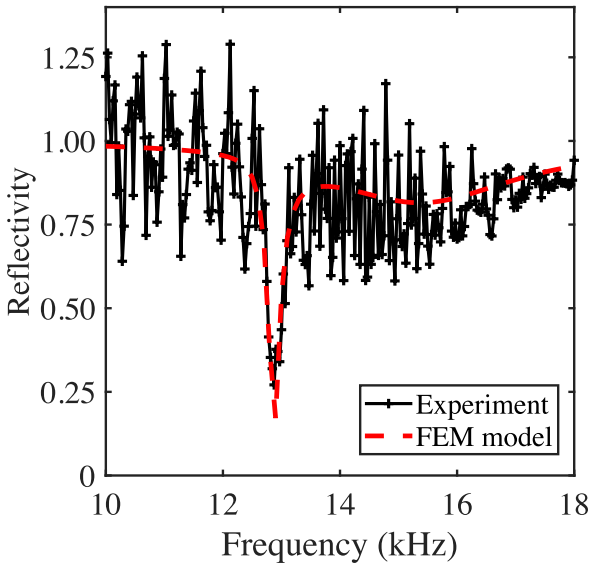

Fig. 8.13 Experimental near normal-incidence reflectivity (black-solid line), obtained from the mirror normalisation method, the reflected radiation from the sample was normalised to the reflected radiation from a mirror. FEM model of the expected response from the phase resonance sample (red dashed line).

by the fast oscillation in the data. This interference likely arises from standing waves forming somewhere in the experimental setup.

The near normal-incidence reflectivity of the second method, where a mirror measurement normalises the reflected wave is shown in Figure 8.13. As with the self-normalisation method, the minimum at 12.9 kHz can be seen. However, the maximum reflectivity now is greater than unity; this is due to some strong interference in the measurements. It was shown in the previous case that standing waves are able to form in the system leading to fast oscillations. When performing both scans, the distance from the source to the sample surface must remain unchanged. Any difference in distance will render the normalisation ineffective and present additional features. It appears in this data, that while the scan was performed in the same plane, the source to sample distance has changed ever so slightly. We can see in Figure 8.11(b) that in both the sample and plate measurements, there is a fast oscillation present. If these fast oscillations occur at the same frequencies (which would happen

in the ideal case), during the normalisation process, they will cancel. However, when there is a slight difference between the two measurements, the oscillations occur at different frequencies for each measurement. Therefore, they now constructively and destructively interfere, which we see as the strong oscillations in Figure 8.13. In airborne measurements, one solution to remove this potential variation between sample and mirror measurements would be to use the unstructured side of the sample as the mirror; this is possible as the materials used for sample fabrication are acoustically-rigid. However, this was not possible with the phase resonance sample due to the reverse of the sample being uneven in texture.

8.5 Conclusions

In this chapter, a few preliminary models and experiments have been shown to extend the work presented in this thesis.

Following on from the result in Chapter 6, the effect on the band structure of adding periodic structure to both interfaces was explored. By introducing glide-symmetry into the system, degenerate modes at the first Brillouin zone boundary were shown to exist.

Similar to the previous idea, the effect of adding 2D periodic structure to create a bigrating onto one of the interfaces of underwater plate has been explored. Both acrylic (soft) and aluminium (hard) bigratings were modelled FEM showing a vast difference in the band structures. Due to the additional freedom, torsional modes of the pillars are now supported on the surface.

Finally, a technique for obtaining the reflectivity spectrum (radiative dispersion) through scanning techniques was suggested. Using two separate normalisation methods: one self-normalisation and the other a mirror normalisation, initial experimental

results were shown for near normal-incidence radiation. However, interference effects were dominant in both sets of measurements.

It is clear from these three examples of possible studies that there are many more which could be undertaken. For example, can one utilise 2D meander surfaces to give much more isotropic slow-wave structures. What happens if we use partially covered meander structures with tapered tape covering? Will this give us 'rainbow trapping' of sound? Could this easily be achieved by fabricating a meander structure where the height varies linearly along the sample? Is it possible to create slow-sound acoustic waveguides by structuring either side of the channel with meander structures, or is it merely that the thermoviscous losses would dominate attenuating the sound wave rapidly? Can we create phase resonances in a structured underwater plate by having multiple different sized pillars per unit cell? Also, what happens to the dispersion relation if the backing plate has both soft and hard-solid pillars? Do the pillars act independently or do the pillars couple through the backing plate? All of these questions have yet to be answered, and could potentially lead to exciting discoveries for acoustic metamaterials.

Chapter 9

List of Publications and Conferences

9.1 Publications

- J. G. Beadle, T. Starkey, J. A. Dockrey, J. R. Sambles, and A. P. Hibbins. The acoustic phase resonances and surface waves supported by a compound rigid grating. *Scientific Reports*, 8(1):10701, 2018.

- J. G. Beadle, I. R. Hooper, J. R. Sambles, and A. P. Hibbins. Broadband, slow sound on a glide-symmetric meander-channel surface. *The Journal of the Acoustical Society of America* 145(5):3190-3194, 2019.

9.2 Conferences

- American Physics Society Division of Fluid Dynamics (APS DFD), Denver USA. 19$^{\text{th}}$ - 21$^{\text{st}}$ November 2017 - "*Broadband, slow sound on a glide-symmetric metasurface*".

- Institute of Acoustics: Acoustics, Milton Keynes UK. 13th - 14st May 2019 - "*Broadband, slow sound on a glide-symmetric metasurface*".

- Underwater Acoustics Conference and Exhibition, Hersonissou Greece. - 1th - 5st July 2019 - "*Modified coupled-Scholte modes on a thin acrylic monograting*".

9.3 Posters

- Acoustics Metamaterials Meeting, Exeter UK. 16th - 17st April 2018 - "*Broadband, slow sound on a glide-symmetric metasurface*".

- Symposium on Acoustic Materials and Metamaterials, Birmingham UK. 20th September 2018. - "*Broadband, slow sound on a glide-symmetric metasurface*". Best poster award.

References

[1] L. Brillouin. Wave propagation in periodic structures: Electric filters and crystal lattices. *Dover Publications*, 1953.

[2] G. Floquet. Sur les équations différentielles linéaires à coefficients périodiques. *Annales Scientifiques de l'École Normale Supérieure*, 12:47–88, 1883.

[3] R. Martínez-Sala, J. Sancho, J. V. Sánchez, V. Gómez, J. Llinares, and F. Meseguer. Sound attenuation by sculpture. *Nature*, 378(6554):241, 1995.

[4] M. Sigalas and E. N. Economou. Band structure of elastic waves in two dimensional systems. *Solid State Communications*, 86(3):141–143, 1993.

[5] J. V. Sánchez-Pérez, D. Caballero, R. Mártinez-Sala, C. Rubio, J. Sánchez-Dehesa, F. Meseguer, J. Llinares, and F. Gálvez. Sound attenuation by a two-dimensional array of rigid cylinders. *Physical Review Letters*, 80:5325–5328, 1998.

[6] F. R. Montero de Espinosa, E. Jiménez, and M. Torres. Ultrasonic band gap in a periodic two-dimensional composite. *Physical Review Letters*, 80:1208–1211, 1998.

[7] M. Kafesaki and E. N. Economou. Multiple-scattering theory for three-dimensional periodic acoustic composites. *Phys. Rev. B*, 60:11993–12001, 1999.

[8] T. Miyashita. Sonic crystals and sonic wave-guides. *Measurement Science and Technology*, 16(5):R47–R63, 2005.

[9] A. Khelif, B. Djafari-Rouhani, J. O. Vasseur, P. A. Deymier, P. H. Lambin, and L. Dobrzynski. Transmittivity through straight and stublike waveguides in a two-dimensional phononic crystal. *Physical Review B*, 65(17):174308, 2002.

[10] T. Miyashita. Full band gaps of sonic crystals made of acrylic cylinders in air–numerical and experimental investigations–. *Japanese Journal of Applied Physics*, 41(5S):3170, 2002.

[11] A. Khelif, B. Djafari-Rouhani, J. O. Vasseur, and P. A. Deymier. Transmission and dispersion relations of perfect and defect-containing waveguide structures in phononic band gap materials. *Physical Review B*, 68(2):024302, 2003.

[12] M. Kafesaki, M. M. Sigalas, and N. García. Frequency modulation in the transmittivity of wave guides in elastic-wave band-gap materials. *Physical Review Letters*, 85:4044–4047, 2000.

[13] A. Khelif, A. Choujaa, S. Benchabane, B. Djafari-Rouhani, and V. Laude. Guiding and bending of acoustic waves in highly confined phononic crystal waveguides. *Applied Physics Letters*, 84(22):4400–4402, 2004.

[14] F. Cervera, L. Sanchis, J. V. Sánchez-Pérez, R. Martínez-Sala, C. Rubio, F. Meseguer, C. López, D. Caballero, and J. Sánchez-Dehesa. Refractive acoustic devices for airborne sound. *Physical Review Letters*, 88:023902, 2001.

[15] B. C. Gupta and Z. Ye. Theoretical analysis of the focusing of acoustic waves by two-dimensional sonic crystals. *Physical Review E*, 67(3):036603, 2003.

[16] L. S. Chen, C. H. Kuo, and Z. Ye. Acoustic imaging and collimating by slabs of sonic crystalsmade from arrays of rigid cylinders in air. *Applied Physics Letters*, 85(6):1072–1074, 2004.

[17] Z. Liu, X. Zhang, Y. Mao, Y. Y. Zhu, Z. Yang, C. T. Chan, and P. Sheng. Locally resonant sonic materials. *Science*, 289(5485):1734–1736, 2000.

[18] N. Fang, D. Xi, J. Xu, M. Ambati, W. Srituravanich, C. Sun, and X. Zhang. Ultrasonic metamaterials with negative modulus. *Nature Materials*, 5(6):452, 2006.

[19] S. H. Lee, C. M. Park, Y. M. Seo, Z. G. Wang, and C. K. Kim. Acoustic metamaterial with negative density. *Physics Letters A*, 373(48):4464–4469, 2009.

[20] S. H. Lee, C. M. Park, Y. M. Seo, Z. G. Wang, and C. K. Kim. Composite acoustic medium with simultaneously negative density and modulus. *Physical Review Letters*, 104(5):054301, 2010.

[21] Z. Liang and J. Li. Extreme acoustic metamaterial by coiling up space. *Physical Review Letters*, 108(11):114301, 2012.

[22] M. Yang, S. Chen, C. Fu, and P. Sheng. Optimal sound-absorbing structures. *Materials Horizons*, 4(4):673–680, 2017.

[23] C. Zwikker and C.W. Kosten. *Sound absorbing materials*. Elsevier, 1949.

[24] Michael R. Stinson. The propagation of plane sound waves in narrow and wide circular tubes, and generalization to uniform tubes of arbitrary cross-sectional shape. *The Journal of the Acoustical Society of America*, 89(2):550–558, 1991.

[25] G. P. Ward, A. P. Hibbins, J. R. Sambles, and J. D. Smith. Acoustic transmission through compound subwavelength slit arrays. *Physical Review B*, 94(2):1–7, 2016.

[26] C. E. Bradley. Time harmonic acoustic bloch wave propagation in periodic waveguides. part i. theory. *The Journal of the Acoustical Society of America*, 96(3):1844–1853, 1994.

[27] N. Sugimoto and T. Horioka. Dispersion characteristics of sound waves in a tunnel with an array of helmholtz resonators. *The Journal of the Acoustical Society of America*, 97(3):1446–1459, 1995.

[28] T. Wu, T. J. Cox, and Y. W. Lam. A profiled structure with improved low frequency absorption. *The Journal of the Acoustical Society of America*, 110(6):3064–3070, 2001.

[29] V. Romero-García, G. Theocharis, O. Richoux, A. Merkel, V. Tournat, and V. Pagneux. Perfect and broadband acoustic absorption by critically coupled sub-wavelength resonators. *Scientific Reports*, 6:19519, 2016.

[30] V. Romero-García, G. Theocharis, O. Richoux, and V. Pagneux. Use of complex frequency plane to design broadband and sub-wavelength absorbers. *The Journal of the Acoustical Society of America*, 139(6):3395–3403, 2016.

[31] N. Jiménez, V. Romero-García, V. Pagneux, and J-P. Groby. Rainbow-trapping absorbers: Broadband, perfect and asymmetric sound absorption by subwavelength panels for transmission problems. *Scientific Reports*, 7(1):1–12, 2017.

[32] L. Rayleigh. On waves propagated along the plane surface of an elastic solid. *Proceedings of the London Mathematical Society*, 1(1):4–11, 1885.

[33] R. Stoneley. Elastic waves at the surface of separation of two solids. *Proceedings of the Royal Society of London. Series A, Containing Papers of a Mathematical and Physical Character*, 106(738):416–428, 1924.

[34] J. G. Scholte. The range of existence of Rayleigh and Stoneley waves. *Geophysical Supplements to the Monthly Notices of the Royal Astronomical Society*, 5(5):120–126, 1947.

[35] C. B. Scruby, K. R. Jones, and L. Antoniazzi. Diffraction of elastic waves by defects in plates: Calculated arrival strengths for point force and thermoelastic sources of ultrasound. *Journal of Nondestructive Evaluation*, 5(3-4):145–156, 1986.

[36] P. G. Malischewsky. Comparison of approximated solutions for the phase velocity of Rayleigh waves (comment on 'characterization of surface damage via surface acoustic waves'). *Nanotechnology*, 16(6):995, 2005.

[37] L. Bergmann. *Ultrasonics and their scientific and technical applications*. G. Bell and Sons Ltd., 1938.

[38] M. Rahman and T. Michelitsch. A note on the formula for the Rayleigh wave speed. *Wave Motion*, 43(3):272–276, 2006.

[39] G. D. Meegan, M. F. Hamilton, Y. A. Il'inskii, and E. A. Zabolotskaya. Nonlinear Stoneley and Scholte waves. *The Journal of the Acoustical Society of America*, 106(4):1712–1723, 1999.

[40] K Sezawa and K Kanai. The range of possible existence of Stoneley waves and some related problems. *Bulletin of the Earthquake Research Institute*, 17:1–8, 1939.

[41] P. Chadwick and D. A. Jarvis. Interfacial waves in a pre-strained neo-hookean body: I. biaxial states of strain. *The Quarterly Journal of Mechanics and Applied Mathematics*, 32(4):387–399, 1979.

[42] M. A. Dowaikh and R. W. Ogden. Interfacial waves and deformations in pre-stressed elastic media. *Proceedings of the Royal Society of London. Series A: Mathematical and Physical Sciences*, 433(1888):313–328, 1991.

[43] P. C. Vinh and P. T. H. Giang. Uniqueness of Stoneley waves in pre-stressed incompressible elastic media. *International Journal of Non-Linear Mechanics*, 47(2):128–134, 2012.

[44] P. C. Vinh and P. T. H. Giang. On formulas for the velocity of Stoneley waves propagating along the loosely bonded interface of two elastic half-spaces. *Wave Motion*, 48(7):647–657, 2011.

[45] P. C. Vinh, P. G. Malischewsky, and P. T. H. Giang. Formulas for the speed and slowness of Stoneley waves in bonded isotropic elastic half-spaces with the same bulk wave velocities. *International Journal of Engineering Science*, 60:53–58, 2012.

[46] S. R. Seshadri. Leaky rayleigh waves. *Journal of Applied Physics*, 73(8):3637–3650, 1993.

[47] S. Nazarian. In situ determination of soil deposits and pavement systems by spectral analysis of surface waves method (PhD thesis). *Austin, Texas: University of Texas*, 1984.

[48] C. B. Park, R. D. Miller, and J. Xia. Multichannel analysis of surface waves. *Geophysics*, 64(3):800–808, 1999.

[49] J. R. Chamuel and G. H. Brooke. Transient Scholte wave transmission along rough liquid–solid interfaces. *The Journal of the Acoustical Society of America*, 83(4):1336–1344, 1988.

[50] F. Padilla, M. de Billy, and G. Quentin. Theoretical and experimental studies of surface waves on solid–fluid interfaces when the value of the fluid sound velocity is located between the shear and the longitudinal ones in the solid. *The Journal of the Acoustical Society of America*, 106(2):666–673, 1999.

[51] C. Glorieux, K. Van de Rostyne, K. Nelson, W. Gao, W. Lauriks, and J. Thoen. On the character of acoustic waves at the interface between hard and soft solids and liquids. *The Journal of the Acoustical Society of America*, 110(3):1299–1306, 2001.

[52] J. Zhu and J. S. Popovics. Analytical study of excitation and measurement of fluid-solid interface waves. *Geophysical research Letters*, 33(9), 2006.

[53] F. B. Jensen and H. Schmidt. Shear properties of ocean sediments determined from numerical modelling of Scholte wave data. In *Ocean Seismo-Acoustics*, pages 683–692. Springer, 1986.

[54] M. H. Ritzwoller and A. L. Levshin. Estimating shallow shear velocities with marine multicomponent seismic data. *Geophysics*, 67(6):1991–2004, 2002.

[55] T. Bohlen, S. Kugler, G. Klein, and F. Theilen. 1.5 d inversion of lateral variation of Scholte-wave dispersion. *Geophysics*, 69(2):330–344, 2004.

[56] O. Diachok, A. Caiti, P. Gerstoft, and Henrik Schmidt. *Full field inversion methods in ocean and seismo-acoustics*, volume 12. Springer Science & Business Media, 2013.

[57] F. Jenot, M. Ouaftouh, M. Duquennoy, and M. Ourak. Interferometric detection of acoustic waves at air-solid interface applications to non-destructive testing. *Journal of Applied Physics*, 97(9):094905, 2005.

[58] H. Lamb. On waves in an elastic plate. *Proceedings of the Royal Society of London. Series A, Containing papers of a mathematical and physical character*, 93(648):114–128, 1917.

[59] E. Lehfeldt and P. Höller. Lamb waves and lamination detection. *Ultrasonics*, 5(4):255–257, 1967.

[60] D. F. Ball and D. Shewring. Some problems in the use of Lamb waves for the inspection of cold-rolled steel sheet and coil. *Non-destructive Testing*, 6(3):138–145, 1973.

[61] M. G. Silk and K. F. Bainton. The propagation in metal tubing of ultrasonic wave modes equivalent to Lamb waves. *Ultrasonics*, 17(1):11–19, 1979.

[62] Y. Bar-Cohen and A. K. Mal. Characterization of composite laminates using combined LLW and PBS methods. In *Review of Progress in Quantitative Nondestructive Evaluation*, pages 1555–1560. Springer, 1991.

[63] K. Okada. Ultrasonic measurement of anisotropy in rolled materials using surface wave. *Japanese Journal of Applied Physics*, 25(S1):197, 1986.

[64] J. Degrieck, N. F. Declercq, and O. Leroy. Ultrasonic polar scans as a possible means of non-destructive testing and characterisation of composite plates. *Insight-Non-Destructive Testing and Condition Monitoring*, 45(3):196–201, 2003.

[65] D. E. Chimenti. Guided waves in plates and their use in materials characterization. *Applied Mechanics Reviews*, 50(5):247–284, 1997.

[66] A. Sommerfeld. *Über die Ausbreitung der Wellen in der drahtlosen Telegraphie*. Verlag der Königlich Bayerischen Akademie der Wissenschaften, 1909.

[67] J. C. Slater. *Theory of the magnetron oscillator*. Radiation Laboratory, Massachusetts Institute of Technology, 1941.

[68] H. M. Barlow and A. L. Cullen. Surface waves. *Proceedings of the IEE-Part III: Radio and Communication Engineering*, 100(68):329–341, 1953.

[69] J. B. Pendry, L. Martin-Moreno, and F. J. Garcia-Vidal. Mimicking surface plasmons with structured surfaces. *Science*, 305(5685):847–848, 2004.

[70] A. R. Wenzel. Propagation of waves along an impedance boundary. *The Journal of the Acoustical Society of America*, 55(5):956–963, 1974.

[71] U. Ingard. On the reflection of a spherical sound wave from an infinite plane. *The Journal of the Acoustical Society of America*, 23(3):329–335, 1951.

[72] S-I. Thomasson. Reflection of waves from a point source by an impedance boundary. *The Journal of the Acoustical Society of America*, 59(4):780–785, 1976.

[73] R. Raspet and G. E. Baird. The acoustic surface wave above a complex impedance ground surface. *The Journal of the Acoustical Society of America*, 85(2):638–640, 1989.

[74] L. Kelders, J. F. Allard, and W. Lauriks. Ultrasonic surface waves above rectangular-groove gratings. *The Journal of the Acoustical Society of America*, 103:2730–2733, 1998.

[75] L. Kelders, W. Lauriks, and J. F. Allard. Surface waves above thin porous layers saturated by air at ultrasonic frequencies. *The Journal of the Acoustical Society of America*, 104:882–889, 1998.

[76] K. M. Ivanov-Shits and F. V. Rozhin. Investigation of surface waves in air. *Sov. Phys. Acoust*, 5:510–512, 1959.

[77] Z. He, H. Jia, C. Qiu, Y. Ye, R. Hao, M. Ke, and Z. Liu. Nonleaky surface acoustic waves on a textured rigid surface. *Physical Review B*, 83(13):132101, 2011.

[78] Y. Ye, M. Ke, Y. Li, T. Wang, and Z. Liu. Focusing of spoof surface-acoustic-waves by a gradient-index structure. *Journal of Applied Physics*, 114(15):154504, 2013.

[79] J. Christensen, A. I. Fernandez-Dominguez, F. de Leon-Perez, L. Martin-Moreno, and F. J. Garcia-Vidal. Collimation of sound assisted by acoustic surface waves. *Nature Physics*, 3(12):851, 2007.

[80] L. Schwan, O. Umnova, and C. Boutin. Sound absorption and reflection from a resonant metasurface : homogenization model with experimental validation. *Wave Motion*, 72:154–172, 2017.

[81] J. Zhu, Y. Chen, X. Zhu, F. J. Garcia-Vidal, X. Yin, W. Zhang, and X. Zhang. Acoustic rainbow trapping. *Scientific Reports*, 3:1728, 2013.

[82] H. Jia, M. Lu, X. Ni, M. Bao, and X. Li. Spatial separation of spoof surface acoustic waves on the graded groove grating. *Journal of Applied Physics*, 116(12):124504, 2014.

[83] H. Jia, M. Lu, Q. Wang, M. Bao, and X. Li. Subwavelength imaging through spoof surface acoustic waves on a two-dimensional structured rigid surface. *Applied Physics Letters*, 103(10):103505, 2013.

[84] C. Li, M. Ke, S. Zhang, S. Peng, C. Qiu, and Z. Liu. Guiding spoof surface acoustic waves on a monolayer array of rigid cylinders in water. *Journal of Physics D: Applied Physics*, 49(12):125304, 2016.

[85] Y. Xie, W. Wang, H. Chen, A. Konneker, B. I. Popa, and S. A. Cummer. Wavefront modulation and subwavelength diffractive acoustics with an acoustic metasurface. *Nature Communications*, 5:5553, 2014.

[86] K. Tang, C. Qiu, M. Ke, J. Lu, Y. Ye, and Z. Liu. Anomalous refraction of airborne sound through ultrathin metasurfaces. *Scientific Reports*, 4:6517, 2014.

[87] Y. Li, X. Jiang, R. Q. Li, B. Liang, X. Y. Zou, L. L. Yin, and J. C. Cheng. Experimental realization of full control of reflected waves with subwavelength acoustic metasurfaces. *Physical Review Applied*, 2(6):064002, 2014.

[88] Y. Li, X. Jiang, B. Liang, J. C. Cheng, and L. Zhang. Metascreen-based acoustic passive phased array. *Physical Review Applied*, 4(2):024003, 2015.

[89] G. Memoli, M. Caleap, M. Asakawa, D. R. Sahoo, B. W. Drinkwater, and S. Subramanian. Metamaterial bricks and quantization of meta-surfaces. *Nature Communications*, 8:14608, 2017.

[90] J. Mei, G. Ma, M. Yang, Z. Yang, W. Wen, and P. Sheng. Dark acoustic metamaterials as super absorbers for low-frequency sound. *Nature Communications*, 3:756, 2012.

[91] A. Merkel, G. Theocharis, O. Richoux, V. Romero-García, and V. Pagneux. Control of acoustic absorption in one-dimensional scattering by resonant scatterers. *Applied Physics Letters*, 107(24):244102, 2015.

[92] V. Leroy, A. Strybulevych, M. Lanoy, F. Lemoult, A. Tourin, and J. H. Page. Superabsorption of acoustic waves with bubble metascreens. *Physical Review B*, 91(2):020301, 2015.

[93] Y. Li and B. M. Assouar. Acoustic metasurface-based perfect absorber with deep subwavelength thickness. *Applied Physics Letters*, 108(6):063502, 2016.

[94] L. E. Kinsler, A. R. Frey, A. B. Coppens, and J. V. Sanders. *Fundamentals of Acoustics*. Wiley-VCH, 4th edition, 1999.

[95] G. Kirchhoff. Ueber den einfluss der wärmeleitung in einem gase auf die schallbewegung. *Annalen der Physik*, 210:177 – 193, 2006.

[96] L. Rayleigh. *The Theory of Sound—Volume 2*. Macmillan, London, 2nd edition, 1877.

[97] T. Yazaki, Y. Tashiro, and T. Biwa. Measurements of sound propagation in narrow tubes. *Proceedings of the Royal Society A: Mathematical, Physical and Engineering Sciences*, 463(2087):2855–2862, 2007.

[98] L. E. Kinsler, A. R. Frey, A. B. Coppens, and J. V. Sanders. *Fundamentals of acoustics*. Wiley-VCH, 4th edition, 1999.

[99] A. H. Nayfeh. Effect of the acoustic boundary layer on the wave propagation in ducts. *The Journal of the Acoustical Society of America*, 54(6):1737–1742, 1973.

[100] Y. Aurégan, R. Starobinski, and V. Pagneux. Influence of grazing flow and dissipation effects on the acoustic boundary conditions at a lined wall. *The Journal of the Acoustical Society of America*, 109(1):59–64, 2001.

[101] G. Kooijman, A. Hirschberg, and J. Golliard. Acoustical response of orifices under grazing flow: Effect of boundary layer profile and edge geometry. *Journal of Sound and Vibration*, 315(4):849 – 874, 2008.

[102] G. P. Ward, R. K. Lovelock, A. Murray, A. P. Hibbins, J. R. Sambles, and J. D. Smith. Boundary-layer effects on acoustic transmission through narrow slit cavities. *Physical Review Letters*, 115(4):1–5, 2015.

[103] M. Molerón, M. Serra-Garcia, and C. Daraio. Visco-thermal effects in acoustic metamaterials: from total transmission to total reflection and high absorption. *New Journal of Physics*, 18(3):033003, 2016.

[104] X. Olny and C. Boutin. Acoustic wave propagation in double porosity media. *The Journal of the Acoustical Society of America*, 114(1):73–89, 2003.

[105] F. C. Sgard, X. Olny, N. Atalla, and F. Castel. On the use of perforations to improve the sound absorption of porous materials. *Applied Acoustics*, 66(6):625–651, 2005.

[106] D. G. Rabus, M. Hamacher, and H. Heidrich. Active and passive microring resonator filter applications in GaInAsP/InP. *Conference Proceedings. 2001 International Conference on Indium Phosphide and Related Materials. 13th IPRM (Cat. No. 01CH37198)*, pages 477–480, 2001.

[107] S. Vargas and C. Vázquez. New optical filter employing multireflection mirror to provide design flexibility for wdma. *LEOS 2000. 2000 IEEE Annual Meeting Conference Proceedings. 13th Annual Meeting. IEEE Lasers and Electro-Optics Society 2000 Annual Meeting (Cat. No. 00CH37080)*, 2:480–481, 2000.

[108] A. Yariv. Universal relations for coupling of optical power between microresonators and dielectric waveguides. *Electronics Letters*, 36(4):321–322, 2000.

[109] V. M. García-Chocano, S. Cabrera, and J. Sánchez-Dehesa. Broadband sound absorption by lattices of microperforated cylindrical shells. *Applied Physics Letters*, 101(18):184101, 2012.

[110] M. Yang, C. Meng, C. Fu, Y. Li, Z. Yang, and P. Sheng. Subwavelength total acoustic absorption with degenerate resonators. *Applied Physics Letters*, 107(10):104104, 2015.

[111] N. Jiménez, W. Huang, V. Romero-García, V. Pagneux, and J-P. Groby. Ultra-thin metamaterial for perfect and quasi-omnidirectional sound absorption. *Applied Physics Letters*, 109(12):121902, 2016.

[112] H. Long, Y. Cheng, J. Tao, and X. Liu. Perfect absorption of low-frequency sound waves by critically coupled subwavelength resonant system. *Applied Physics Letters*, 110(2):023502, 2017.

[113] P. J. Crepeau and P. R. McIsaac. Consequences of symmetry in periodic structures. *Proceedings of the IEEE*, 52(1):33–43, 1964.

[114] A. Hessel, M. H. Chen, R. C. M. Li, and A. A. Oliner. Propagation in periodically loaded waveguides with higher symmetries. *Proceedings of the IEEE*, 61(2):183–195, 1973.

[115] A. Mock, L. Lu, and J. O'Brien. Space group theory and fourier space analysis of two-dimensional photonic crystal waveguides. *Physical Review B*, 81(15):155115, 2010.

[116] R. Quesada, D. Martín-Cano, F. J. García-Vidal, and J. Bravo-Abad. Deep-subwavelength negative-index waveguiding enabled by coupled conformal surface plasmons. *Optics Letters*, 39(10):2990–2993, 2014.

[117] R. Mittra and S. Laxpati. Propagation in a wave guide with glide reflection symmetry. *Canadian Journal of Physics*, 43(2):353–372, 1965.

[118] R. Kieburtz and J. Impagliazzo. Multimode propagation on radiating travelling-wave structures with glide-symmetric excitation. *IEEE Transactions on Antennas and Propagation*, 18(1):3–7, 1970.

[119] M. Ebrahimpouri, E. Rajo-Iglesias, Z. Sipus, and O. Quevedo-Teruel. Low-cost metasurface using glide symmetry for integrated waveguides. In *2016 10th European Conference on Antennas and Propagation (EuCAP)*, pages 1–2. IEEE, 2016.

[120] M. Ebrahimpouri, O. Quevedo-Teruel, and E. Rajo-Iglesias. Design guidelines for gap waveguide technology based on glide-symmetric holey structures. *IEEE Microwave and Wireless Components Letters*, 27(6):542–544, 2017.

[121] Miguel Camacho, Rhiannon C Mitchell-Thomas, A. P. Hibbins, J. R. Sambles, and O. Quevedo-Teruel. Designer surface plasmon dispersion on a one-dimensional periodic slot metasurface with glide symmetry. *Optics Letters*, 42(17):3375–3378, 2017.

[122] M. Camacho, R. C. Mitchell-Thomas, A. P. Hibbins, J. R. Sambles, and O. Quevedo-Teruel. Mimicking glide symmetry dispersion with coupled slot metasurfaces. *Applied Physics Letters*, 111(12):121603, 2017.

[123] P. Padilla, L. F. Herrán, A. Tamayo-Domínguez, J. F. Valenzuela-Valdés, and O. Quevedo-Teruel. Glide symmetry to prevent the lowest stopband of printed corrugated transmission lines. *IEEE Microwave and Wireless Components Letters*, 28(9):750–752, 2018.

[124] S. Guenneau, A. Movchan, G. Pétursson, and S. A. Ramakrishna. Acoustic metamaterials for sound focusing and confinement. *New Journal of Physics*, 9(11):399, 2007.

[125] G. L. Huang and C. T. Sun. Band gaps in a multiresonator acoustic metamaterial. *Journal of Vibration and Acoustics*, 132(3):031003, 2010.

[126] M. S. Kushwaha, P. Halevi, L. Dobrzynski, and B. Djafari-Rouhani. Acoustic band structure of periodic elastic composites. *Physical Review Letters*, 71(13):2022, 1993.

[127] I.A. Viktrov. Rayleigh and Lamb waves: physical theory and applications. *Springer*, 1967.

[128] R. N. Bracewell. *The Fourier transform and its applications*, volume 31999. McGraw-Hill New York, 1986.

[129] J. O. Smith. Mathematics of the discrete fourier transform (dft). *Center for Computer Research in Music and Acoustics (CCRMA), Department of Music, Stanford University, Stanford, California*, 2002.

[130] The Mathworks, Inc., Natick, Massachusetts. *MATLAB version 9.6.0.1065788 (R2019a)*, 2015.

[131] O. C. Zienkiewicz, R. L. Taylor, P. Nithiarasu, and J. Z. Zhu. *The finite element method*, volume 3. McGraw-hill London, 1977.

[132] COMSOL AB. COMSOL Multiphysics{®}.

[133] Dortmund Data Bank. Available at: www.ddbst.com [Accessed 09/03/2020].

[134] S. G. Johnson. Notes on perfectly matched layers (PMLs). *Lecture notes, Massachusetts Institute of Technology, Massachusetts*, 29, 2008.

[135] L. Zhou and G. A. Kriegsmann. Complete transmission through a periodically perforated rigid slab. *The Journal of the Acoustical Society of America*, 121(6):3288–99, 2007.

[136] B. Hou, J. Mei, M. Ke, W. Wen, Z. Liu, J. Shi, and P. Sheng. Tuning Fabry-Perot resonances via diffraction evanescent waves. *Physical Review B*, 76(5), 2007.

[137] X. Wang. Theory of resonant sound transmission through small apertures on periodically perforated slabs. *Journal of Applied Physics*, 108(6), 2010.

[138] T.W. Ebbesen, H. J. Lezec, H. F. Ghaemi, T. Thio, and P. A. Wolff. Extraordinary optical transmission through sub-wavelength hole arrays. *Nature*, 86(6):1114–7, 1998.

[139] D. C. Skigin and R. A. Depine. Resonances on metallic compound transmission gratings with subwavelength wires and slits. *Optics Communications*, 262(2):270–275, 2006.

[140] H. Zhang, L. Fan, J. Qu, and S. Zhang. Sound transmission properties assisted by the phase resonances of composite acoustic gratings. *Journal of Applied Physics*, 119(8), 2016.

[141] A. N. Fantino, S. I. Grosz, and D. C. Skigin. Resonant effects in periodic gratings comprising a finite number of grooves in each period. *Physical Review E*, 64:016605, 2001.

[142] A. P. Hibbins, J. R. Sambles, and C. R. Lawrence. Excitation of remarkably nondispersive surface plasmons on a nondiffracting, dual-pitch metal grating. *Applied Physics Letters*, 80(13):2410–2412, 2002.

[143] A. Barbara, J. Le Perchec, S. Collin, C. Sauvan, J-L. Pelouard, T. López-Ríos, and P. Quémerais. Generation and control of hot spots on commensurate metallic gratings. *Optics Express*, 16(23):19127–35, 2008.

[144] M. Tabib-Azar, P. S. Pathak, G. Ponchak, and S. LeClair. Nondestructive superresolution imaging of defects and nonuniformities in metals, semiconductors, dielectrics, composites, and plants using evanescent microwaves. *Review of Scientific Instruments*, 70(6):2783–2792, 1999.

[145] W. E. Kock and F. K. Harvey. Refracting sound waves. *The Journal of the Acoustical Society of America*, 21(5):471–481, 1949.

[146] T. Frenzel, J. David Brehm, T. Bückmann, R. Schittny, M. Kadic, and M. Wegener. Three-dimensional labyrinthine acoustic metamaterials. *Applied Physics Letters*, 103(6):061907, 2013.

[147] Y. Xie, B. I. Popa, L. Zigoneanu, and S. A. Cummer. Measurement of a broadband negative index with space-coiling acoustic metamaterials. *Physical Review Letters*, 110(17):175501, 2013.

[148] Y. F. Zhu, X. Y. Zou, R. Q. Li, X. Jiang, J. Tu, B. Liang, and J. C. Cheng. Dispersionless manipulation of reflected acoustic wavefront by subwavelength corrugated surface. *Scientific Reports*, 5:10966, 2015.

[149] X. D. Fan, Y. F. Zhu, B. Liang, J. C. Cheng, and L. Zhang. Converting a monopole emission into a dipole using a subwavelength structure. *Physical Review Applied*, 9(3):034035, 2018.

[150] R. C. Mitchell-Thomas, J. R. Sambles, and A. P. Hibbins. High index metasurfaces for graded lenses using glide symmetry. In *2017 11th European Conference on Antennas and Propagation (EUCAP)*, pages 1396–1397. IEEE, 2017.

[151] J. V. Sanders, A. B. Coppens, A. R. Frey, and L. E. Kinsler. Fundamentals of Acoustics. *John Wiley & Sons*, 1999.

[152] J. G. Beadle, I. R. Hooper, J.R. Sambles, and A. P. Hibbins. Broadband, slow sound on a glide-symmetric meander-channel surface. *The Journal of the Acoustical Society of America*, 145(5):3190–3194, 2019.

[153] S. M. Ivansson. Sound absorption by viscoelastic coatings with periodically distributed cavities. *The Journal of the Acoustical Society of America*, 119(6):3558–3567, 2006.

[154] G. W. Milton and A. V. Cherkaev. Which elasticity tensors are realizable? *Journal of Engineering Materials and Technology*, 117(4):483–493, 1995.

[155] A. Martin, M. Kadic, R. Schittny, T. Bückmann, and M. Wegener. Phonon band structures of three-dimensional pentamode metamaterials. *Physical Review B*, 86(15):155116, 2012.

[156] A. N. Norris. Acoustic cloaking theory. *Proceedings of the Royal Society A: Mathematical, Physical and Engineering Sciences*, 464(2097):2411–2434, 2008.

[157] Y. Chen, M. Zheng, X. Liu, Y. Bi, Z. Sun, P. Xiang, J. Yang, and G. Hu. Broadband solid cloak for underwater acoustics. *Physical Review B*, 95(18):180104, 2017.

[158] J. Chen, J. Liu, and X. Liu. Broadband underwater acoustic carpet cloak based on pentamode materials under normal incidence. *AIP Advances*, 8(8):085024, 2018.

[159] Z. Sun, X. Sun, H. Jia, Y. Bi, and J. Yang. Quasi-isotropic underwater acoustic carpet cloak based on latticed pentamode metafluid. *Applied Physics Letters*, 114(9):094101, 2019.

[160] F. B. Cegla, P. Cawley, and M. J. S Lowe. Material property measurement using the quasi-Scholte mode—a waveguide sensor. *The Journal of the Acoustical Society of America*, 117(3):1098–1107, 2005.

[161] E. Pistone, K. Li, and P. Rizzo. Noncontact monitoring of immersed plates by means of laser-induced ultrasounds. *Structural Health Monitoring*, 12(5-6):549–565, 2013.

[162] O. Önen. Dispersion and sensitivity analysis of quasi-Scholte wave liquid sensing by analytical methods. *Journal of Sensors*, 2017, 2017.

[163] A. E. Takiy, S. C. G. Granja, R. T. Higuti, C. Kitano, L. Elvira, O. F. Martinez-Graullera, and F. M. de Espinosa. Theoretical analysis and experimental validation of the Scholte wave propagation in immersed plates for the characterization of viscous fluids. pages 1614–1617, 2013.

[164] GoodFellow. Polymethylmethacrylate material information [online]. Available at: http://www.goodfellow.com/E/Polymethylmethacrylate.html [Accessed 09/03/2020].

[165] Q. Qi. Attenuated leaky rayleigh waves. *The Journal of the Acoustical Society of America*, 95(6):3222–3231, 1994.

[166] T. V. Zharnikov and D. E. Syresin. Repulsion of dispersion curves of quasidipole modes of anisotropic waveguides studied by finite element method. *The Journal of the Acoustical Society of America*, 137(6):EL396–EL402, 2015.

[167] W. C. Young, R. G. Budynas, A. M. Sadegh, et al. Roark's formulas for stress and strain. *McGraw-Hill New York*, 7, 2002.